NORTHWESTERN UNIVERSITY

Development of clinical visible-light optical coherence tomography

A DISSERTATION

SUBMITTED TO THE GRADUATE SCHOOL
IN PARTIAL FULFILLMENT OF THE REQUIREMENTS

For the degree

DOCTOR OF PHILOSOPHY

Field of Biomedical Engineering

BY

Ian Rubinoff

EVANSTON, ILLINOIS

August 2022

Abstract

Development of clinical visible-light optical coherence tomography

Ian Rubinoff

Optical coherence tomography (OCT) images the retina noninvasively with micrometer-scale volumetric resolutions. It is an invaluable resource in the clinic for identifying, monitoring, and treating blindness-causing diseases. By shortening illumination wavelengths to the visible range, visible-light OCT (vis-OCT) improves image resolution, provides new scattering contrasts, and enables oxygen saturation (sO_2) measurements, expanding the potential for clinical care. In this dissertation, I develop vis-OCT technological improvements that bridge the gap between the laboratory and clinic. First, I develop a scanning algorithm robust against eye motions that visualizes anatomical features like Bruch's membrane and inner plexiform layer (IPL) with unprecedented detail. Both features, previously inaccessible in vivo, are locations of interest in diseases like macular degeneration and glaucoma, respectively. Next, I define a framework of signals, noises, and systemic biases influencing sO_2 measurements called spectral contaminants (SCs). I build upon this framework to develop a new retinal sO_2 algorithm that senses, adapts to, and removes SCs in the human retina. This technique enables accurate sO_2 measurements in 18 human volunteers with repeatability < 2.5%. Accurate and repeatable sO_2 measurements provide the potential to sense retinal diseases at the metabolic level before vision loss occurs. Finally, I address fundamental noise and speed limitations in vis-OCT by implementing a detection scheme called balanced detection (BD). BD increases signal-to-noise ratios up to 25.6 dB and increases imaging speeds 5-fold. Together, these advances satisfy the necessary image quality, speed, and sO_2 reliability to translate vis-OCT to the clinic.

Acknowledgements

In 2015, two years prior to the start of my PhD at Northwestern, I could not imagine that I would be where I am today. At that time, was barely treading water academically and was struggling to find my place as a student, engineer, and person. In the Spring of 2015, I took a signal processing course taught by Chao Zhou, which introduced me to all things Fourier-transform-related. For the first time, I found my academic passion, and more importantly, professional mentors who believed in me. In addition to Professor Zhou, I received enormous support from the teaching assistant for this course, Omid, who worked tirelessly to help me debug my circuits, figure out tough problems, and teach me best engineering practices. With my interest sparked and my skills sharpened, I joined Professor Zhou's lab as an undergraduate researcher. Here, I studied optical coherence tomography, which would later become the topic of my PhD research and this dissertation. I am eternally thankful to Professor Zhou, Omid, and my undergraduate advisor Bill Best for giving me support when I needed it most and encouraging me to pursue my PhD.

Next, I would like to thank my PhD advisor, Hao Zhang. In an uphill battle applying to PhD programs, you believed in my potential when very few others did. You provided me with an incredible opportunity to prove myself, and this opportunity changed my life. This opportunity extended throughout the five years of my PhD, where you encouraged me to dig deeper and find new solutions to problems, even when they conflicted with your own ideas. I am a better researcher and better person because of it. Our work together consisted of significant up-and-downs, stresses and excitements. You taught me how to deal with failures and successes professionally and not let them affect my long-term goals. Simply stated, I would not be where I am today without your guidance.

I would like to thank my committee members, Robert Linsenmeier, Cheng Sun, and Mark Johnson. Each in your own way assisted my research, taught me important lessons, and made my time at Northwestern more fruitful.

Dr. Linsenmeier provided me with the necessary education and equipment to start oximetry experiments, which would become critical to a major research project. In fact, we considered the oximetry project a complete failure until you told us we misinterpreted readings from the blood-gas machine! This dissertation would be half as long if you had not been there.

Dr. Sun attended all of my lab's group meetings and provided excellent feedback on my research. Thank you for supporting my work and being a voice of reason, even when Dr. Zhang did not agree with my theories. I also appreciate the time we spent at a recent conference, where you spoiled us with great food and drinks!

Dr. Johnson provided me with invaluable academic and life lessons, even if I did not realize them at the time. Even though your class was a constant struggle for me, you were fair, honest, and an excellent teacher. You taught me the critical importance of not overthinking science and starting with basic principles. This mindset helped inform the new method I developed for retinal oximetry.

Next, I'd like to thank my colleagues from the Functional Optical Imaging Lab (FOIL), whose intellectual and emotional support helped me every day. None of this dissertation would be possible without you. My education as a PhD student did not end with classes. I owe so much of my knowledge to you, from formal lessons to casual discussions to heated debates. Although the list extends well beyond this, I'd like to specifically thank those I worked closely with, including Roman Kuranov, Yuanbo Wang, Yang Zhang, Xiao Shu, Ki-Hee Song, Janel Davis, Brian Soetikno, Lisa Beckmann, David Miller, and Raymond Fang. You made the PhD experience worthwhile.

Last but not least, I'd like to thank my parents, whose constant love and support and belief in my potential made me who I am today. Your positive impact on my life is immeasurable.

List of Abbreviations

1D	One-dimensional
2D	Two-dimensional
3D	Three-dimensional
ADS	Adaptive spectroscopic
AW	Anterior wall
ANOVA	Analysis of variance
BM	Bruch’s Membrane
CFZ	Cell-free zone
CNR	Contrast to noise ratio
COST	Cone outer segment tips
ENL	Equivalent number of looks
FA	Fixed attenuation
FT	Fourier transform
FOV	Field of view
FWHM	Full-width at half-maximum
GCL	Ganglion cell layer
ILM	Inner limiting membrane
INL	Inner nuclear layer
IPL	Inner plexiform layer
IRB	Institutional review board
K	Wavenumber
LCA	Longitudinal chromatic aberration

LCI	Low-coherence inferometry
LI	Linear interpolation
MC	Monte carlo
MFP	Mean free path
NA	Numerical Aperture
NIR-OCT	Near-infrared optical coherence tomography
OCT	Optical coherence tomography
OCTA	Optical coherence tomography angiography
ONH	Optic nerve head
ONL	Outer nuclear layer
OPL	Outer plexiform layer
ORL	Outer retinal layers
PD	Photodetector
PSD	Power spectral density
PS-OCT	Polarization-sensitive optical coherence tomography
PW	Posterior wall
RBC	Red blood cell
RGCs	Retinal ganglion cells
RIN	Relative intensity noise
RNFL	Retinal nerve fiber layer
ROI	Region of interest
ROST	Rod outer segment tips
RPE	Retinal pigment epithelium

SC	Spectral Contaminant
SD-OCT	Spectral-domain optical coherence tomography
SDBG	Spectrally dependent background
SDR	Spectrally dependent roll-off
SLD	Superluminescent diode
SNR	Signal-to-noise ratio
SNFR	Signal-to-noise-floor ratio
sO_2	Oxygen saturation
SR	Speckle reduction
SS-OCT	Swept-source optical coherence tomography
SSADA	Split-spectrum amplitude decorrelation algorithm
SSF	Scattering scaling factor
STFT	Short-time Fourier Transform
TD-OCT	Time-domain optical coherence tomography
VIS-OCT	Visible-light optical coherence tomography
W	Packing factor

OCT-Specific Terminology

A-line: One-dimensional (1D) profile of an imaged sample plotting amplitude as a function of depth. Also known as ‘axial-line’ referring to the axial (depth) dimension.

A-line rate: Frequency of A-line acquisition. Inverse of the time it takes to acquire one A-line.

B-scan: Two-dimensional (2D) profile of an imaged sample plotting depth and axial dimensions. A B-scan is composed of a series of adjacent A-lines.

Bandwidth: Range of wavelengths detected by an OCT system. Typically evaluated at the full-width-at-half-maximum (FWHM) of a gaussian spectrum.

Fringe: Oscillating pattern typically seen in the interference between two waves

SDA-line: Spectrally Dependent A-line

Spectrometer: Device composed of a linear array of pixels detecting different wavelengths.

Volume: Three-dimensional (3D) profile of an imaged sample plotting two later and one depth dimension. A volume is composed of a series of adjacent B-scans.

Table of Contents

Chapter 6 Adaptive spectroscopic visible-light optical coherence tomography for human retinal oximetry 169

List of Figures

and Google Scholar searching the terms “visible light optical coherence tomography”, “vis-OCT”, “visible light OCT”, and “white-light OCT”. Figure and caption replicated with permission from Lisa Beckmann.

Fig. 2.1 Illustrations of speckle-reduction scanning protocols. (a) Overall illustration of the relationship between the B-scan axis and the orthogonal axis in the modulated raster scan; (b) Detailed illustration of the A-line acquisition sequence in the modulated raster scan. d is the distance between two adjacent A-lines along the orthogonal axis. The arrows 1, 2, and 3 highlight the trajectory of galvanometer motion; (c) Overall illustration of the relationship between the B-scan axis and the orthogonal axis in the modulated circular scan; (d) Detailed illustration of the A-line acquisition sequence in the modulated circular scan.

Figure 2.2. Speckle reduction test in the model mouse eye. (a) Change of averaged CNR as a function of d in the modulated raster scan; (b) Change of averaged CNR as a function of d in the modulated circular scan; (c) An srB-scan image of the model mouse eye acquired using modulated raster scan with d = 0 µm. The structures corresponding to the two tape and one paper layers are highlighted by the arrows; (d) Magnified view of the region highlighted by the box in panel (c); (e) An srB-scan image of the model mouse eye acquired using modulated raster scan with d = 6 µm. (f) Magnified view of the region highlighted by the box in panel (e); (g) An srB-scan image of the model mouse eye acquired using modulated circular scan with d = 0 µm; (h) Magnified view of the region highlighted by the box in panel (g); (i) An srB-scan image of the model mouse eye acquired using modulated circular scan with d = 6 µm; (j) Magnified view of the region highlighted by the

box in panel (i). All images are plotted with identical color bar; (k) Fitted pixel intensity histograms within the tape layer 1 acquired by modulated raster scans with d = 0 µm and d = 6 µm; (l) Fitted pixel intensity histograms within the tape layer 1 acquired by modulated circular scans with d = 0 µm and d = 6 µm.

Figure 2.3. Speckle reduction test in mouse retina using modulated raster scan. (a) Reference raster B-scan image. Three ROIs from IPL, ONL, and ORL are highlighted by a1, a2, and a3, respectively. The size of each ROI is 140 µm (lateral) × 20 µm (axial); (b) The corresponding srB-scan image. The same three ROIs are highlighted by b1, b2, and b3. (a1), (a2), and (a3) are the magnified views of the three highlighted ROIs in panel a. (b1), (b2), and (b3) are the magnified views of the three highlighted ROIs in panel b. CNR and ENL values are calculated from all the selected ROIs. All images are plotted with identical color bar.

Figure 2.4. Speckle reduction test in mouse retina using modulated circular scan. (a) Reference circular B-scan image. Three ROIs from IPL and two vessels are highlighted by a1, a2, and a3, respectively. The size of each ROI is 140 µm (lateral) × 20 µm (axial); (b) The corresponding srB-scan image. The same three ROIs are highlighted by b1, b2, and b3. CNR and ENL values are calculated from all the selected ROIs. All images are plotted with identical color bar.

Figure 2.5. Speckle reduction test in human retina using modulated raster scan. (a) Reference raster B-scan image. Three ROIs from NFL, GCL, and ORL are highlighted by a1, a2, and a3, respectively. The size of each ROI is 430 μm (lateral) × 23 μm (axial); (b) The corresponding srB-scan image. The same three ROIs are highlighted by b1, b2, and b3. (a1), (a2), and (a3) are the magnified views of the

three highlighted ROIs in panel a. (b1), (b2), and (b3) are the magnified views of the three highlighted ROIs in panel b. CNR and ENL values are calculated from all the selected ROIs. The bottom three anatomical layers ROST, RPE, and BM are highlighted in panel b3. The arrows in a3 and b3 highlight the same blood vessel shadow. All images are plotted with identical color bar.

Figure 2.6. Comparing directly averaged B-scan with srB-scan images from human retina. (a) Image scan from the same location as shown in Fig. 2.5b after averaging 8 B-scans; (b) Magnified view of the outer retina region as highlighted in panel a; (c) Two A-lines from the positions highlighted by 1 and 2 in panel b; (d) Magnified view of the same outer retina region from the srB-scan shown in Fig. 2.5b. Five anatomical layers are labeled; (e) Two A-lines from the positions highlighted by 3 and 4 in panel d. All plotted A-lines are averaged three times laterally to reduce variation. All images are plotted on the same contrast scale as used in Figure 5.

Figure 2.7. Speckle reduction test in human retina using modulated circular scan. (a) Reference circular B-scan image. Three ROIs from NFL, GCL, and ORL are highlighted by a1, a2, and a3, respectively. The size of each ROI is 900 µm (lateral) × 40 µm (axial); (b) The corresponding srB-scan image. The same three ROIs are highlighted by b1, b2, and b3. (a1), (a2), and (a3) are the magnified views of the three highlighted ROIs in panel a. (b1), (b2), and (b3) are the magnified views of the three highlighted ROIs in panel b. CNR and ENL values are calculated from all the selected ROIs. The bottom four anatomical layers COST (cone outer segment tips), ROST, RPE, and BM are highlighted in panel b3. All images are plotted with identical color bar.

Figure 2.8. Speckle reduction test in human retina in clinical environment using modulated raster scan. (a) Reference raster B-scan image; (b) The corresponding srB-scan image; (c) Magnified view of the region highlighted in panel a; (d) Magnified view of the region highlighted in panel b. The five anatomical layers: IS/OS, COST, ROST, RPE, and BM are labeled. All images are plotted with identical color bar.

Figure 3.1. (a) Wavelength-to-pixel mapping ($\lambda[j]_{map}$) in vis-OCT spectrometer; (b) k spacing calculated from $\lambda[j]_{map}$ (red dashed line) in (a) and linear k spacing (solid blue line) for same wavelength range. Green dot indicates the mean value of $\Delta k[j]_{map}$ coinciding with a constant $k[j]_{lin}$; (c) Illustration of spectrometer pixel array (rectangles) and focal spots (green dots, shorter wavelengths [pixels 1-5]; red dots, longer wavelength [pixels 2044-2048]). Sine waves below array plotted as a function of $\Delta k[j]_{map}$ (red dashed line) and $k[j]_{lin}$ (solid blue line).

Figure 3.2. (a) Simulated FSR (blue dots) and SDR for uniform focal spot sizes incident on pixel array. SDR wavelengths are identified by colorbar. (b) SDR (red dashed line) and equivalent simulation (solid blue line) at 1-mm depth in (a); (c) Simulated FSR (blue dots) and SDR for spot sizes varying quadratically with pixel index; (d) SDR (red dashed line) and equivalent simulation (solid blue line) at 1 mm depth in (c).

Figure 3.3. (a) Measured FSR (blue dots) and SDR from a commercial vis-OCT spectrometer. The color of each SDR curve reflects the central wavelength of its

sub-band as shown by the color bar; (b) SDR at 1 mm imaging depth as a function of the central wavelength of each sub band.

Figure 3.4. (a) Measured spectra (solid lines) of oxygenated blood at different depths with reported spectrum of oxygenated hemoglobin (red dashed line); (b) Spectra of oxygenated blood at different depths after SDR correction.

Figure 4.1. Influence of grating dispersion on interference fringe (a) Digitized relative k rates of a spectrometer. Colored dots represent locations of pixel segments in (c-e); (b) illustration of Dirac comb sampling by pixel array with period Δx; (c) Interference fringe plotted at the location of the yellow dot in panel a; (d) Interference fringe plotted at the location of the green dot in panel a; (e) Interference fringe plotted at the location of the orange dot in panel a.

Figure 4.2. Simulated SDBGs in vis-OCT. (a) Simulated background SDA-lines with LI; (b) predicted SDBG bias (blue line) and simulated SDBG bias (red dashed line) with LI from z = 500 μm to 800 μm; (c) simulated background SDA-lines without LI; (d) predicted SDBG bias (blue line) and simulated SDBG bias (red dashed line) without LI from z = 500 μm to 800 μm

Figure 4.3. Measured SDBGs in vis-OCT. (a) Measured background SDA-lines with LI; (b) predicted SDBG bias (blue line) and measured SDBG bias (red dashed line) with LI from z = 500 μm to 800 μm; (c) measured background SDA-lines without LI; (d) predicted SDBG bias (blue line) and measured SDBG bias (red dashed line) without LI from z = 500 μm to 800 μm

Figure 4.4. Simulated background SDA-lines with LI after (a) no, (b) two-fold, (c) four-fold, and (d) six-fold up-sampling.

Figure 4.5. SDBG correction in the human retina. (a) B-scan image with one artery (red box) and one vein (blue box); scale bars are 250 μm (lateral) and 50 μm (axial); (b) measured blood spectrum in the artery before SDBG correction; (c) measured SDBG bias in the artery; (d) measured blood spectrum in the artery after SDBG correction; € measured blood spectrum in the vein before SDBG correction; (f) measured SDBG bias in the vein; (g) measured blood spectrum in the vein after SDBG correction

Figure 4.6. RMSE of simulated sO_2 measurements with respect to the ground truth as a function of SNFR.

Figure 4.7. SDBGs in vis-OCT using spline interpolation. (a) Simulated background SDA-lines with spline interpolation; (b) Measured background SDA-lines with spline interpolation

Figure 5.1 (A) Illustration of OCT illumination of a weakly scattering medium. Incident photons (green arrow) create a focal spot (green oval) and detection aperture in the tissue; (B) Magnified illustration of the highlighted region in the panel A, showing the paths of Class I (green arrow), Class II (yellow arrow), and Class III photons (red arrow); (C) Illustration of vis-OCT illumination of a retinal blood vessel (RBC) containing red blood cells (RBC); (D) Magnified illustration of the highlighted region in panel C, showing the paths of Class I photons (green arrow).

Figure 5.2 Illustration of tissue and imaging geometry in Monte Carlo simulation. Downward arrows (from left to right) highlight the interface depths of the vessel wall, cell free zone, and blood, respectively; fourth arrow highlights depth of the vessel center.

Figure 5.3 (A) Simulated photon packet path (green line) and scattering events (green stars) in the blood vessel; (B) Proportions of detected singly-scattered photon packets; (C) Histogram showing the number of scattering events of the detected Class I and Class II photons; (D) Distributions of the number of scattering events at different depths in blood; (D) The average number of scattering events at different depths in blood

Figure 5.4 (A) A simulated A-line at the center of the vessel, showing the anterior wall (AW), cell-free zone (CFZ), blood maximum (BM), blood signal decay (BSD), and posterior wall (PW); The red-dashed line highlights measurement depth range starting at z_0 and ranging Δz; (B) Measured SSF values from A-line in the panel A as a function of different z_0 and Δz.

Figure 5.5 (A) Simulated A-line at the center of the vessel after thresholding the number of detected scattering events in blood. Lighter shades indicate a lower threshold of detected scattering events; (B) The SSF value as a function of detected scattering threshold.

Figure 5.6 (A) The SSF values as a function of optical detection radius and angle; (B) SSF as a function of numerical aperture (NA), which is the diagonal of the matrix in the panel A; (C) Simulated A-line at center of vessel for different NAs;

lighter shades indicate lower NA; (D) Normalized distributions of scattering events in blood for different NAs.

Figure 5.7 (A) vis-OCT B-scan of fully oxygenated blood in a tube phantom; (B) A vis-OCT A-line at the center of tube phantom (yellow-dashed line) in the panel A; (C) Measured attenuation spectrum of fully oxygenated blood; (D) Measured sO_2 and SSF values at different pre-set oxygenation levels.

Figure 5.8 (A) Vis-OCT B-scan image of a human retina, where a vein is labeled by 1 and an artery is labeled by 2; (B) Vis-OCT A-line of the vein from the highlighted position in the panel A; (C) Vis-OCT A-line of the artery from the highlighted position in the panel (A); (D) Measured attenuation spectrum from the highlighted vein in the panel A; (E) Measured attenuation spectrum from the highlighted artery in the panel A.

Figure 6.1. Illustration of the human retina composed of inner-limiting-membrane (ILM), Retinal Nerve Fiber Layer (NFL), blood vessels (BV; red is the artery, blue is vein), red blood cells (RBC), ganglion cell layer (GCL), nuclear layers (NL) representing the outer nuclear layer to the outer nuclear layer, photoreceptor layers (PRL) containing rods and cones, and the retinal pigment epithelium and Bruch's membrane (RPE/BM). Number 1 highlights the photon path of a specular reflection; 2 highlights the photon path of backscattering without blood attenuation; 3 highlights the photon path backscattering from red blood cells. A scanning beam (SB) is composed of visible-light wavelengths (green, yellow, and red illustrate different spectral bands of the beam).

Figure 6.2. Flow chart overview of Ads-vis-OCT processing for retinal oximetry. Arrow direction highlights the input and output of each step.

Figure 6.3. Spectroscopic normalizations in the human retina. (A) vis-OCT B-scan of healthy human retina; vessels labeled V1-V4 were identified as vein, artery, vein, and vein, respectively; (B) Measured spectra in V1 with no normalization (yellow), normalization by NFL (green), normalization by the anterior vessel wall (blue), and normalization by the start of signal decay in blood (z_d) (purple), respectively; predicted spectrum for sO_2 = 99.6% (gray dashed line); (C) Bias for each normalization with respect to predicted spectrum at five wavelengths; (D & E) Same analysis for V2 and sO_2 = 56.5%; (F & G) Same analysis for V3 and sO_2 = 61.3%; (H & I) Same analysis for V4 and sO_2 = 62.5 %

Figure 6.4. Oximetry map of the optic disk. (A) sO_2 measurements in 17 vessels in the optic disk from a healthy 23-year-old. The sO_2 values pseudo-colored and overlaid onto the fundus image. Scale bar: 300 μm; (B) Bar chart plots sO_2 measurements from panel A in individual arteries (red bar) and veins (blue) numbered from 1 to 17, as well as average sO_2 in all arteries and all veins; (C) B-scan from the position highlighted by the yellow dashed line in panel A. Scale bars: 150 μm.

Figure 6.5. Oximetry map of the optic disk. (A) sO_2 measurements in 17 vessels in the optic disk from a healthy 23-year-old. The sO_2 values pseudo-colored and overlaid onto the fundus image. Scale bar: 300 μm; (B) Bar chart plots sO_2 measurements from panel A in individual arteries (red bar) and veins (blue) numbered from 1 to 17, as well as average sO_2 in all arteries and all veins; (C) B-

scan from the position highlighted by the yellow dashed line in panel A. Scale bars: 150 μm.

Figure 6.6. Capillary tube phantom for *ex-vivo* vis-OCT oximetry. (A) Glass capillary tube pulled to an inner diameter of ~ 200 μm (arrow); (B) Tube inserted in a homemade well under ~ 500 μm of immersion oil.

Figure 6.7. Results of vis-OCT oximetry in *ex vivo* phantom and comparison to *in vivo* human eye. (a) vis-OCT sO_2 measurements in phantom plotted against sO_2 measurements from blood-gas machine; (b) Distributions of spectral fit R^2 and best fit W in phantom; (c) Distributions of best fit W in phantom compared to human eye; (d) Distributions of best fit R^2 in phantom compared to human eye

Figure 6.8. Coefficient of variation ratio between slope and depth averaging methods for estimating attenuation coefficient. Exponential decay model from Eq. 6.14 is used for calculations. α_1 is attenuation coefficient estimated by slope method; β_1 is proportional to α_1 and estimated by depth averaging method.

Figure 6.9. Simulation of LCA in human eye and influence on vis-OCT retinal oximetry. (a) CFS in human eye simulated by Zemax software; (b) Transfer function of the LCA on vis-OCT SDA-lines. Colors depict central wavelength of STFT window; (c) Simulated LCA contribution to measured spectrum after Ads-OCT processing; (d) Simulated sO_2 measurement without LCA correction when focus at 550 nm is 50 μm above the anterior vessel wall; (e) Simulated sO_2 measurement without LCA correction when focus at 550 nm is 50 μm below the

anterior vessel wall; (f) Simulated sO_2 measurement with LCA correction for all focus positions

Figure 6.10. SDA-lines features. (a) SDA-lines from vein in human retina (after SDBG correction). Color bar represents central wavelength of STFT window. z_d indicates depth of normalization where SDA-lines start to decay in amplitude; (b) Magnified B-scan where SDA-lines in (a) were measured. SDA-lines were averaged laterally within yellow dashed lines

Figure 6.11. Spectral stability analysis in human retinal vessels. (a) Spectral stability matrix (SSM) for vessel V3 from Fig. 6.3. Green box highlights lowest mean-squared-error (MSE) and black box highlights highest MSE; (b) Spectra in V3 after nine depth perturbations for the lowest MSE (blue lines) and highest MSE (black lines), respectively. (c) SSM for vessel V2 from Fig. 6.3. Green box highlights MSE and black box highlights highest MSE. (d) Spectra in V4 after nine depth perturbations for the lowest MSE (red lines) and highest MSE (black lines)

Figure 7.1. (A) Schematic of BD-vis-OCT system. SCL: supercontinuum laser; DM: dichroic mirror; BB: beam block; P: polarizer; BPF: bandpass filter; SSF: spectral shaping filter; CL: collimating lens; PC: polarization controller; FC: fiber coupler; FD: fiber delay; TS: translation stage; M: mirror; DC: dispersion compensation; AD: air delay; SRA: spectrometer A; SRB: spectrometer B; GS: galvanometric scanner; L: lens; MS: microelectromechanical scanner; DL: diode laser; FT: fixation target; (B) reference arm spectra; (C) spectrometer wavenumber (k) maps; (D) Signal roll-offs normalized with respect to the first depth

measurement in SRB. Circle, square, and triangle show actual measurements for SRA, SRB and balanced detection (BD); corresponding lines show best fits

Figure 7.2. Flowchart for BD vis-OCT. The sequence follows arrows from top to bottom.

Figure 7.3. Spectrometer noises in 100 continuous camera exposures for the camera pixel 500 without calibration (A), with calibration (B), and after subtraction between spectrometer B (SRB) and A (SRA) (C); (D) Standard deviations of noises across the entire camera array; (E) Calibration map relating pixels in SRB to pixels in SRA. The map is nonlinear and displayed after fitting by a third-order polynomial; (F) Correlation coefficient as a function of shifting the map in (E). (G) Average ratio of standard deviation between SRA and the difference of SRA and SRB as a function of shifting the map in (E). Higher ratio indicates better noise suppression. In (F) & (G), pixel shift = 0 represents the optimal calibration map.

Fig. 7.4. (A) Single detection and (B) balanced detection B-scans of phantom eye at lowest camera amplification level. Red and green boxes highlight measurement locations of CNR. Red and green dashed lines highlight locations of A-lines plotted in (C); (D-F) Following same layout as (A-C) but for maximum camera amplification level. B-scans magnified to show detail. Scale bars 50 μm (vertical) × 225 μm (horizontal).

Figure 7.5. Small field-of-view vis-OCT images of the retina of a healthy 47-year-old male (Eye 1); (A) En-face image near the fovea for SD; (B) En-face projection near the fovea for BD; (C) Magnified view of area highlighted by the red dashed

box in panel A; red stars highlight small blood vessels; (D) Magnified view of the area highlighted by the green dashed box in panel B; green stars highlight small blood vessels; (E) B-scan image from the location highlighted by the dashed line in panel A; (F) B-scan image from the location highlighted by the dashed line in panel B; Red and green A-lines overlay their respective locations; stars near A-line 1 highlight blood attenuation; red and green arrows highlight locations of PSNFR and PSNR measurement; solid red and green boxes highlight locations of CNR measurement. Scale bars in (A) & (B) are 275 μm (isometric); scale bars in (C) & (D) are 150 μm (isometric); scale bars in (E) & (F) are 60 μm (vertical) × 225 μm (horizontal). NFL: nerve fiber layer; GCL: ganglion cell layer; IPL: inner plexiform layer; INL: inner nuclear layer; OPL: outer plexiform layer; ELM: external limiting membrane; IS/OS: inner segment/outer segment; COST: cone outer segment tips; ROST: rod outer segment tips; RPE: retinal pigment epithelium; BM: Bruch's membrane.

Fig. 7.6. Medium FOV vis-OCT images of the retina of a healthy 24-year-old male (Eye 2); (A) En-face image near the fovea for SD; (B) En-face image near the fovea for BD; (C) Magnified view of the region highlighted by the red dashed box in panel A; (D) Magnified view of the region highlighted by the green dashed box in panel B; (E) B-scan image from the location highlighted by the dashed line in panel A; (F) B-scan image from the location highlighted by the dashed line in panel B; Red and green A-lines overlay their respective locations; stars near A-line 2 highlight blood attenuations; red and green arrows highlight locations of SNFR measurement; solid red and green boxes highlight locations of CNR measurement. Scale bars in (A) & (B): 275 μm (vertical) × 325 μm (horizontal); scale bars

in (C) & (D): 150 µm (vertical) × 175 µm; scale bars in (E) & (F): 50 µm (vertical) × 275 µm (horizontal).

Figure 7.7. (A-D) Large FOV scans in 24-year-old male (Eye 2); (A) En face projection for SD; (B) En face projection for BD; (C) High-density speckle reduction (HDSR) scan at location of red dashed line in (A); (D) High-density speckle reduction (HDSR) scan at location of green dashed line in (B). Red and green dashed boxes in (C) & (D) labeled 1-3 highlight regions for magnification in SD and BD, respectively. Magnifications for respective boxes are shown below. Red and green stars in boxes 1 & 2 highlight blood vessels. Scale bars in (A) & (B): 350 µm (vertical)× 500 µm (horizontal); scale bars in (C) & (D): 100 µm × 700 µm; scale bars in magnification boxes 1-3: 40 µm × 100 µm.

Figure 7.8. Resolution measurement for BD and SD; (A) Point spread functions (PSF) from specular reflection at ILM. The solid green line represents PSF from BD, and the red dashed line represents PSF from SD. Both PSFs overlap and have a measured full-width and half maximum (FWHM) of 1.7 μm. (B) (B) Location of PSF for SD (highlighted by red arrow); (C) Location of PSF for BD (highlighted by green arrow)

Figure 7.9. (A-F) Small field-of-view vis-OCT images of the retina of a healthy 24-year-old male (Eye 2); (A) *En face* projection near fovea for single detection; (B) *En face* projection near fovea for balanced detection; (C) Magnification from red dashed box in (A); (D) Magnification from green dashed box in (B); (E) B-scan from the location of the dashed line in (A); (F) B-scan from the location of the dashed line in (B); Red and green A-lines overlay their respective locations Scale

bars in (A & B) are 275 μm (isometric); scale bars in (C & D) are 150 μm (isometric); scale bars in (E & F) are 60 μm (vertical) × 225 μm (horizontal). NFL: nerve fiber layer; GCL: ganglion cell layer; IPL: inner plexiform layer; INL: inner nuclear layer; OPL: outer plexiform layer; ELM: external limiting membrane; IS/OS: inner segment/outer segment; COST: cone outer segment tips; ROST: rod outer segment tips; RPE: retinal pigment epithelium; BM: Bruch's membrane

Figure 7.10. (A-F) Small field-of-view vis-OCT images of the retina of a healthy 27-year-old female (Eye 3); Figure layout and scale bars are same as in Fig. 7.9.

Figure 7.11. (A-F) Small field-of-view vis-OCT images of the retina of a healthy 25-year-old male (Eye 5); Figure layout and scale bars are same as in Fig. 7.9.

Figure 7.12. (A-F) Medium field-of-view vis-OCT images of the retina of a healthy 25-year-old male (Eye 4); (A) *En face* projection near fovea for single detection; (B) *En face* projection near fovea for balanced detection; (C) Magnification from red dashed box in (A); (D) Magnification from green dashed box in (B); (E) B-scan from the location of the dashed line in (A); (F) B-scan from the location of the dashed line in (B); Scale bars in (A & B) are 365 μm (horizontal) × 275 μm (vertical); scale bars in (C & D) are 200 μm ×150 μm; scale bars in (E&F) are 50 μm × 275 μm. B-scans magnified to show detail. NFL: nerve fiber layer; GCL: ganglion

Figure 7.13. (A-D) High-definition speckle reduction (HDSR) vis-OCT image of the retina of a healthy 27-year-old female (Eye 3). (A) B-scan for SD; (B) B-scan for BD; (C) Magnification from red dashed box in (A); (D) Magnification from

List of Tables

Chapter 1

Introduction

1.1 BACKGROUND

Optical coherence tomography (OCT) measures the echo-time-delays of photons backscattered from a sample [1, 2]. By converting each time-delay to a discrete distance, OCT can localize how deep photons traveled in the sample. Since the number of photons returning from a particular depth is related to the sample's optical scattering and absorption properties, OCT can generate a depth-intensity profile related to its physical structure. In this sense, OCT is an optical analog of ultrasound imaging, which measures the echo-time delays of sound rather than light. There are two main benefits to using light, rather than sound, for imaging. First, light can travel long distances in air, allowing for non-contact imaging. Second, light travels significantly faster than sound, allowing for increased discrimination between echo-time delays, and, therefore, increased depth resolutions. Ultrasound reaches millimeter-scale depth resolutions, while OCT reaches micrometer-scale depth resolutions, an increase of at least three orders of magnitude [3].

1.1.1 Low Coherence Interferometry

Light travels too quickly to directly measure distances with micrometer-scale precision. Therefore, researchers employed an optical technique called low-coherence interferometry (LCI) to encode depth precision in the interference of broadband light [2, 4, 5]. Briefly, an interferometer splits and recombines light, defined as two electromagnetic fields, from a common source. The recombined light is a superposition of the split electromagnetic waves, generating interference according to their phase difference. Fig. 1.1 illustrates a Michelson interferometer, the most common configuration used in OCT. Following the path from the light source, complex electric field $E(t)$, where t is time, propagates forward in time towards a beam splitter. $E(t)$ is partially transmitted along Path 1 and orthogonally reflected along Path 2. $E_1(t)$ denotes the electric field propagating along Path 1 and $E_2(t)$ denotes the electric field propagating along Path 2. $E_1(t)$ and $E_2(t)$ then back-reflect off mirrors (M1 & M2) and return to the beam splitter along their respective paths. $E_1(t)$ now transmits through the beam splitter and $E_2(t)$ reflects, superimposing the waves along Path 3. The electric field along Path 3 is $E_3(t) = E_1(t) + E_2(t)$.

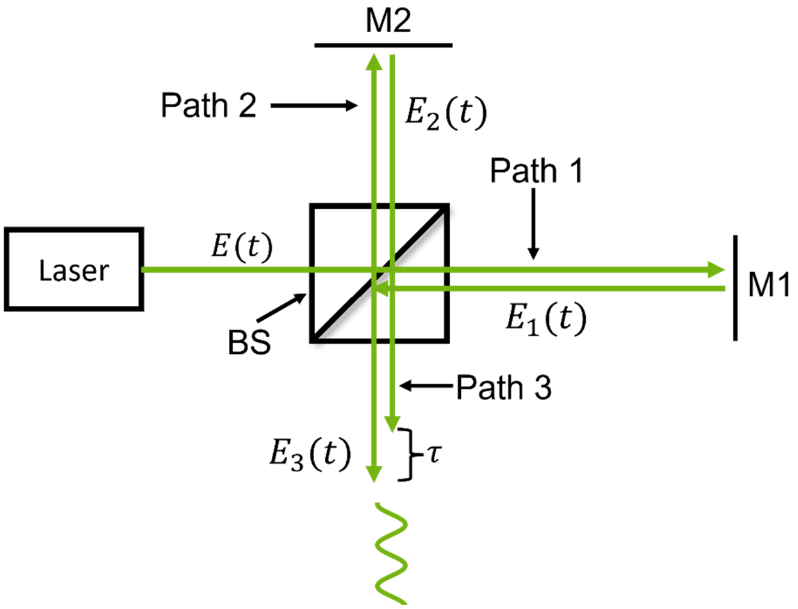

Figure 1.1. Michelson interferometer using beam splitter (BS) to split electric field $E(t)$ into $E_1(t)$ and $E_2(t)$ and recombine them into $E_3(t)$. (M1) Mirror 1; (M2) Mirror 2; (τ) Time delay between $E_1(t)$ and $E_2(t)$ caused by difference in Path 1 and Path 2.

The intensity of $E(t)$ at time t is defined as

$$I(t) = E(t)E^*(t) = |E(t)|^2 \tag{1.1}$$

where * denotes the complex conjugate. Equation 1.1 can be extracted from cross-correlation of $E(t)$ with itself, also known as the auto-correlation [4, 6]. We can write the time-averaged auto-correlation

$$\Gamma(t) = \lim_{t\to\infty} \frac{1}{T}\int_{-T/2}^{T/2} E(t)E^*(t+\tau)dt = \langle E(t)E^*(t+\tau)\rangle \tag{1.2}$$

where τ is time delay between the electric fields, T is total measurement time, and brackets $\langle ... \rangle$ are shorthand representation for temporal averaging. Equation 1.2 becomes Equation 1.1 when $\tau = 0$.

Returning to the interferometer in Fig. 1.1, we note that $E_1(t)$ and $E_2(t)$ originate from $E(t)$. Therefore, $E_1(t)$ and $E_2(t)$ are simply time delayed representations of $E(t)$. If Path 1 = Path 2, the intensity measured along Path 3 is represented by Equation 1.1. If Path 1 ≠ Path 2 (e.g., the mirrors along the paths are different distances from the center of the beam splitter) the intensity along Path 3 is represented by Equation 1.2. Under this condition $\tau = \frac{2\Delta z}{c}$, where Δz is the difference in distances from the beam splitter to each respective mirror, c is the speed of light in air and the '2' indicates forward and backwards propagation along each respective path. Therefore, we can write [7] the electric field intensity along Path 3 as

$$\Gamma_3(t) = \langle\big(E_1(t){+}E_2(t+\tau)\big)\big(E_1^*(t){+}E_2^*(t+\tau)\big)\rangle$$

$$= \langle E_1(t)E_1^*(t)\rangle + \langle E_2(t+\tau)E_2^*(t+\tau)\rangle + \langle E_1(t)E_2^*(t+\tau)\rangle + \langle E_1^*(t)E_2(t+\tau)\rangle \tag{1.3}$$

Assuming a photo sensing device measures the real-valued intensity of electric fields, we get

$$I_3(\tau) = I_1 + I_2 + 2Re\{\langle E_1^*(t)E_2(t+\tau)\rangle\}$$

$$= I_1 + I_2 + 2\sqrt{I_1 I_2}Re\{e^{-ik_0c\tau}\}|\gamma_{12}| \tag{1.4}$$

where I_1 and I_2 are the time-averaged intensities of $E_1(t)$ and $E_2(t)$, respectively; $Re\{\dots\}$ is the real value operator; k_0 is the central wavenumber of the spectrum, such that $k_0 = \frac{2\pi}{\lambda_0}$ and λ_0 is the central wavelength of the spectrum; and $|\gamma_{12}|$ is the degree of temporal coherence between $E_1(t)$ and $E_2(t)$, varying between 0 and 1, which will be detailed shortly hereafter. The third additive term in Equation 1.4 is called the cross-term due to the interactions of the two delayed fields. The cross-term has three critical components: (1): $2\sqrt{I_1 I_2}$, which is a constant that scales the cross-term, (2): $Re\{e^{-ik_0c\tau}\}$, which is a sinusoidal modulation the cross-term, and (3): $|\gamma_{12}|$, which describes ability to resolve the cross term at a given τ.

Two electromagnetic fields can only resolve the cross-term when they are temporally coherent, or when $|\gamma_{12}| > 0$. In other words, $|\gamma_{12}|$ is the correlation coefficient of two electromagnetic fields evaluated at time delay τ. When two fields are highly correlated, $|\gamma_{12}| \rightarrow 1$; when they are uncorrelated $|\gamma_{12}| \rightarrow 0$. Herein lies the foundation of OCT: we can manipulate an interferometer's design to resolve interference only within certain τ, generating a parameter for depth precision.

The degree of temporal coherence $|\gamma_{12}|$ is directly related to the bandwidth of interfering light. Perfectly coherent light ($|\gamma_{12}| = 1$ for all τ) is composed of only one wavelength (e.g., infinitely narrow bandwidth $\delta\lambda$). $E_1(t)$ and $E_2(t)$ are therefore two sine waves of the same frequency, with any temporal delay τ yielding a constant phase shift between the two fields. Looking at Equation 1.4, we see how setting $|\gamma_{12}|$ to 1 in the cross-term yields $2\sqrt{I_1 I_2}\, Re\{e^{-ik_0 c\tau}\} = 2\sqrt{I_1 I_2}\cos{(k_0 c\tau)}$. Hence, for any τ, the cross-term oscillates between 0 and $2\sqrt{I_1 I_2}$, giving rise to the characteristic interference 'fringe' pattern [5, 8].

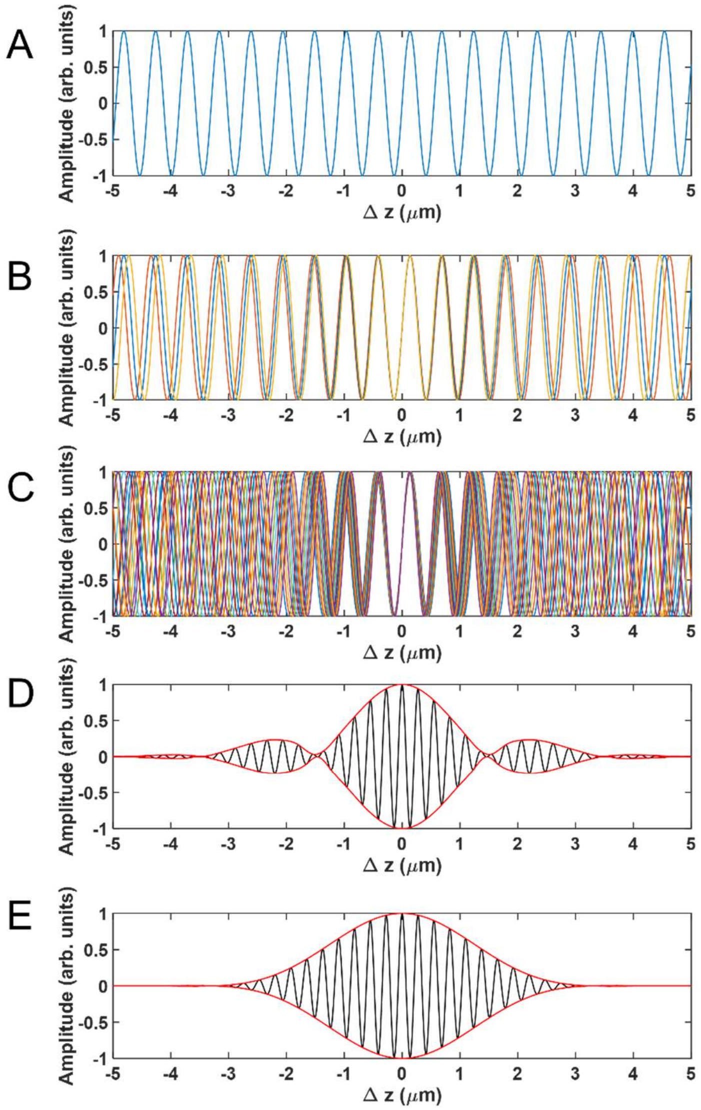

Figure 1.2. (A) Sine wave of wavelength 550 nm; (B) Sine waves of wavelengths 540 nm (orange), 550 nm (blue), 560 nm (yellow); (C) Sine waves of wavelengths 500 nm – 600 nm (various colors); (D) Autocorrelation of (C) in black and envelope in red. (E) Autocorrelation of (C) when wavelength distribution made gaussian

Fig. 1.2A plots a sine wave with wavelength 550 nm evaluated at $\Delta z = \pm 5$ μm along its propagation path. Like the example above, Fig. 1.2A represents perfectly coherent light. As light's bandwidth increases (e.g., bandwidth $\Delta\lambda \gg \delta\lambda$), interference must now consider the phases of each wavelength in the spectrum. Fig 2B overlays wavelengths of 540 nm, 550 nm, and 560 nm across the same range. All the waves have the same phase at $\Delta z = 0$. Looking at the plot, the waves overlap and appear to form a single sine wave near $\Delta z = 0$. As distance increases from $\Delta z = 0$, the discrepancy between each of the wavelengths becomes more apparent. Fig. 1.2C overlays wavelengths of 500 nm – 600 nm in 10 nm intervals, representing a $\Delta\lambda$ = 100 nm. In Fig. 1.2C, the effect described in Fig. 1.2B becomes more exaggerated. After only a few µm, the waves no longer share a single phase. The waves overlap almost randomly, making the broadband light incoherent. Broadband light can be considered as the superposition of all wavelengths with bandwidth $\delta\lambda$ across the range $\Delta\lambda$. Therefore, we can compute the autocorrelation of Fig. 1C to estimate the cross-term from Equation 1.4 for broadband light. We plot this (normalized to maximum of 1) in Fig. 1.2D for $\Delta z = c\tau$ in the range $\pm$ 5 µm. Looking at Fig. 1.2D, we see a high frequency fringe (black) with a low frequency envelope (red). The fringe is $\cos(k_0 c\tau)$ and the envelope is $|\gamma_{12}|$. Hence, for broadband light, $|\gamma_{12}|$ is a narrow-width envelope that attenuates interference with increasing Δz.

The rapid decay of $|\gamma_{12}|$ with Δz in broadband light makes it 'low-coherence'. Therefore, a low-coherence interferometer (LCI) is a spatial filter that measures with a precision determined by the width of $|\gamma_{12}|$. Typically, this precision is measured as the full-width-at-half-maximum (FWHM) of $|\gamma_{12}|$, which, for visible-light, is 1-2 μm. The 'side-lobe' effect seen in Fig. 1.D comes from the equal distribution of amplitudes across bandwidth $\Delta\lambda$, whose Fourier transform (FT) is the *sinc* function. The relationship between $|\gamma_{12}|$ and the FT is detailed later in Section 1.1.3. To this end, researchers typically use broadband light with a gaussian distribution across $\Delta\lambda$. Fig. 1.2E shows the same autocorrelation as Fig. 1.2D, except when the wavelengths are distributed with a gaussian profile. Here, envelope $|\gamma_{12}|$ is gaussian and the side-lobes disappear. For a broadband gaussian spectrum, the FWHM of $|\gamma_{12}|$ is called the coherence length

$$l_c = \frac{2ln2}{\pi n}\frac{\lambda_c^2}{\Delta\lambda_{FWHM}}, \tag{1.5}$$

where n is refractive index ($n = 1$ in air) and $\Delta\lambda_{FWHM}$ denotes the FWHM bandwidth. For a given l_c, we estimate that we can only resolve interference when the paths are matched within $\pm\frac{l_c}{2}$. If, for example, we were to move M2 a length $L > l_c$, we would need to match this distance by moving M1 the same length. By shifting M1 and M2 in conjunction, we can resolve the cross-term at different distances from the beam splitter. Therefore, LCI allows for depth precision (l_c) along multiple physical distances from the beam splitter.

The analysis above describes LCI for mirrors in Path 1 and 2, and, therefore, a single τ. Assuming a mirror is an infinitely thin, perfect reflector, we can model its depth profile, by the distance-shifted delta function $\delta(z - c\tau)$. The LCI response to the delta function is the cross-term in Equation 1.4. A semi-transparent, non-infinitely thin sample, like tissue, can be modeled as sum of reflectors along its depth: $\sum_{m=1}^{j} R_m\delta(z - c\tau_m)$, where m is the reflection layer, R_m is the reflectivity of the m^{th} layer, and τ_m is the time delay of the m^{th} layer. By placing such a sample in Path 1, rather than a mirror, as depicted in Fig. 1.3, we measure the cross-term for each respective layer in the sample. By shifting the location of M2 (now called reference mirror, RM) and sensing interference along Path 3 in time with a photodetector (PD), we can reconstruct a depth profile of the sample. In LCI, the path with the sample is called the sample arm and the path with the mirror is the called the reference arm.

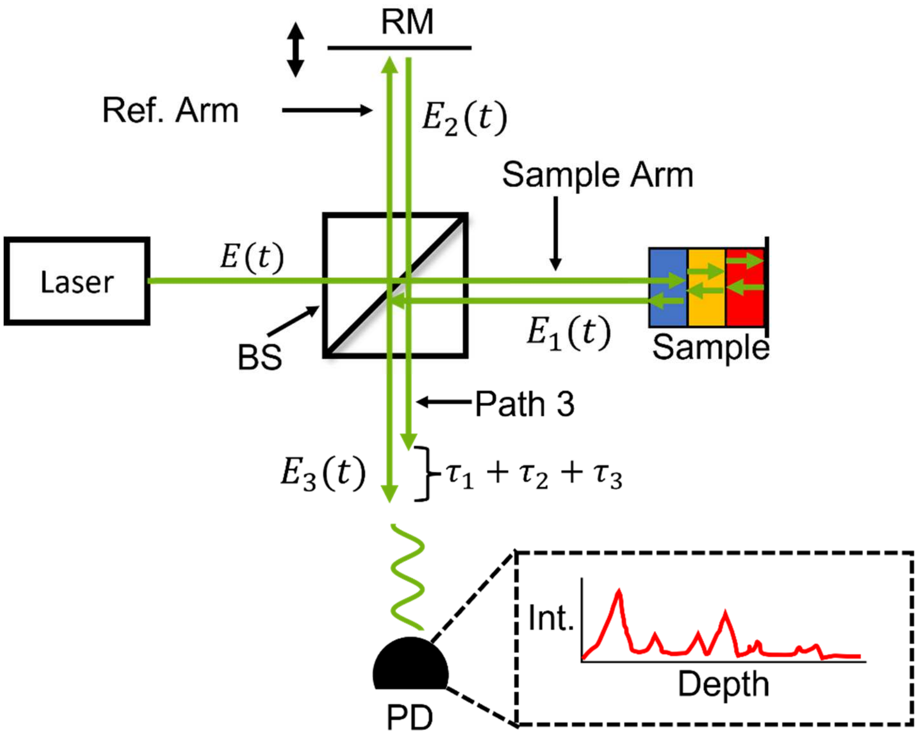

Figure 1.3. LCI system using beam splitter (BS) to split electric field $E(t)$ into $E_1(t)$ and $E_2(t)$ and recombine them into $E_3(t)$; (RM) Reference mirror, which moves along double-sided arrow; (τ_m) Time delays between $E_1(t)$ and $E_2(t)$ caused by sample; (PD) Photodetector, which measures $E_3(t)$ at different positions of RM.

The signal measured by the photodetector in Path 3 is

$$I_{PD}(\tau_m) = I_{samp} + I_{ref} + \sum_{m=1}^{j}\left[2\sqrt{I_{samp}I_{ref}R_m}Re\{e^{-ik_0c\tau_m}\}|\gamma_{12}| \otimes \delta(z - c\tau_m)\right] \quad (1.6)$$

where $\otimes$ is the convolution operator and I_{samp} and I_{ref} are the total powers coming from the sample and reference arms, respectively. By removing the non-signal carrying components in post-processing and converting to distance, we get

$$I_{PD}(\Delta z_m) = \sum_{m=1}^{j}\sqrt{I_{samp}I_{ref}R_m}\delta(z - 2\Delta z_m) \otimes |\gamma_{12}| \quad (1.7)$$

which is a simple convolution of each sample layer with $|\gamma_{12}|$. This is also a low-pass filter operation, so a narrower $|\gamma_{12}|$ will resolve higher spatial frequencies along the sample depth than a broader $|\gamma_{12}|$. Critically, $I_{PD}(\Delta z_m)$ is proportional to the reflectance properties of each sample layer, $\sqrt{R_m}$. In tissues, $\sqrt{R_m}$ is proportional to their optical scattering and absorption properties. Therefore, each depth profile (called 'A-line') plots a tissue's optical properties as a function of depth. By scanning multiple depth profiles along a line, the system can image a cross-sectional frame (B-scan). By scanning multiples B-scans, the system can image a three-dimensional (3D) volume. Since LCI creates images from the optical properties of tissues, it is entirely non-invasive and requires no external imaging contrasts.

1.1.2 Time-Domain Optical Coherence Tomography

The first demonstration of LCI for tomographic imaging was in 1991 by Huang et. al [1], who named such a technique 'optical coherence tomography' (OCT). They performed the first *in vivo* imaging of the human retina with OCT, paving the way for the most impactful imaging device in eye care today. The version of OCT demonstrated in 1991 has been described above. This version is called time-domain OCT (TD-OCT), owing to the acquisition of different tissue layers at different times.

The practical application of TD-OCT for *in vivo* imaging is limited by the signal acquisition process. As depicted in Equations 1.6 & 1.7, the reference arm mirror moves to image each sample depth. Therefore, velocity and mass of the mirror limit the speed of A-line acquisition (A-line rate). Any sample motions or mirror vibrations faster than the A-line rate can severely detract from image quality. This is particularly significant when imaging the living human eye [5]. Researchers overcame the limitations of depth scanning by developing spectral-domain OCT (SD-OCT) in the late 1990's and early 2000's [5]. SD-OCT is perhaps the most significant OCT advance since its original development and has been fundamental towards clinical adoption.

1.1.3 Spectral Domain Optical Coherence Tomography

Equations 1.6 & 1.7 show that the autocorrelation of electric fields in the sample and reference arms sense each depth in an OCT A-line. The autocorrelation shares mathematical similarity with the convolution and therefore can be easily described by Fourier analysis. In particular, it can be shown [6] that $FT\{f(x) \otimes g(x)\} = F(\omega)G(\omega)$, where x and ω Fourier domain conjugates. This well-known identity relates the convolution of two functions to the multiplication of their spectra by Fourier transform (FT). A similar identity can be applied to the autocorrelation using the Wiener-Khinchin theorem [7]. Looking at Equation 1.2, the autocorrelation can be related to the convolution by reversing the sign of t in $E^*(t+\tau)$, demonstrating

$$\Gamma(t) = \lim_{t\to\infty}\frac{1}{T}\int_{-T/2}^{T/2} E(t)E^*(t+\tau)dt = E(t)\otimes E^*(-t). \tag{1.8}$$

It can be further shown that the FT of $f(-x)$ is $F^*(\omega)$. Therefore,

$$FT\{E(t)\otimes E^*(-t)\} = FT\{E(t)\}^2 = FT\{I_3(\tau)\} = S(k), \tag{1.9}$$

where $S(k)$ is the power spectral density (PSD) [6, 7] and k is the Fourier domain conjugate of τ. The PSD of light can be measured in a spectrometer, which diffracts light into different spectral components and focuses them onto a pixel array. Hence, the interference of two electric fields for any time delay can be measured in a spectrometer and computed with a FT. When low-coherence light is used, a FT of the spectrometers signal is the A-line. Critically, the PSD is time-independent, meaning a full, depth-resolved A-line can be acquired without moving the reference mirror. The total signal measured on the spectrometer [5] is approximately

$$S_{total}(k) = FT\{\Gamma_3(t)\} =$$

$$S_{samp}(k) + S_{ref}(k) + \sum_{m=1}^{j}\sqrt{S_{samp}(k)S_{ref}(k)R_m}\cos(kc\tau_m). \tag{1.10}$$

where $S_{samp}(k)$ and $S_{ref}(k)$ are the wavenumber-dependent powers returning from sample and reference arms, respectively. By removing the non-signal carrying components in post-processing and converting to distance, we get

$$S_{total}(k) = \sum_{m=1}^{j}\sqrt{S_{samp}(k)S_{ref}(k)R_m}\cos(2k\Delta z_m). \tag{1.11}$$

From Equation 1.11, it becomes clear that $S_{total}(k)$ is a summation of sinusoids, with frequency encoding depth in the sample. An inverse FT of Equation 1.11

yields an A-line proportional to that in Equation 1.7. The key relationship between TD-OCT and SD-OCT is that which converts $\delta(z - 2\Delta z_m)$ to cos $(2k\Delta z_m)$.

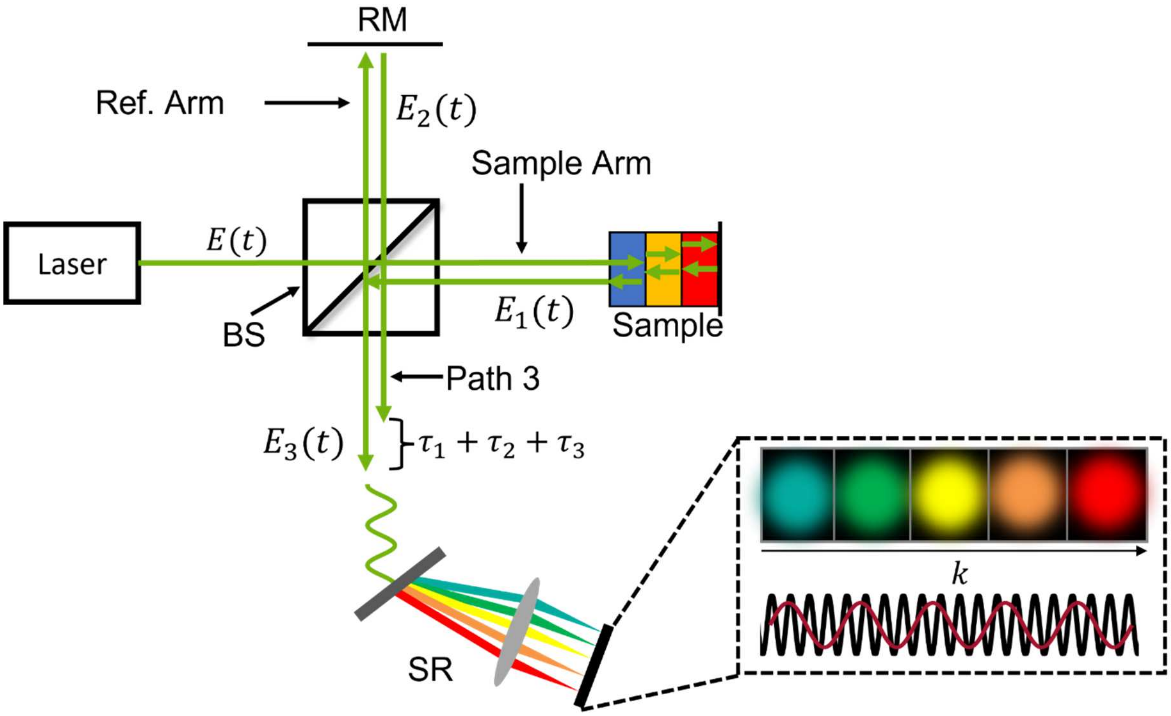

Figure 1.4. LCI system using beam splitter (BS) to split electric field $E(t)$ into $E_1(t)$ and $E_2(t)$ and recombine them into $E_3(t)$; (RM) Reference mirror, which moves along double-sided arrow; (τ_m) Time delays between $E_1(t)$ and $E_2(t)$ caused by sample; (SR) Spectrometer, which measures $E_3(t)$ for different k.

Fig. 1.4 illustrates an SD-OCT system with spectrometer detection. In such a system, the A-line rate is determined not by the motion of the mirror but by the inverse of the exposure time of the spectrometer. By shifting speed limitation from physical inertia to the electronic properties of a camera, A-line rate can be increased significantly in SD-OCT, as compared with TD-OCT. In the future, improvements to camera technology will allow for lower exposure times, and therefore higher A-line rates. Today, SD-OCT remains the most popular form of OCT for research and in the clinic. Nevertheless, there are still major limitations to spectrometer detection in SD-OCT. A significant portion of this dissertation addresses these limitations.

1.1.4 Swept-Source Optical Coherence Tomography

Finally, the most recently developed version of OCT is swept-source OCT (SS-OCT). Signal formation in SS-OCT is mathematically identical to SD-OCT. However, instead of detecting $S_{total}(k)$ on a spectrometer, it decomposes $S_{total}(k)$ in time. The laser source in SS-OCT 'sweeps' across the light spectrum as a function of time, generating the PSD, $S_{total}(k(t))$. By encoding k in time, SS-OCT can measure $S_{total}(k(t))$ using a photodetector (PD). Since PDs can detect light many orders of magnitude faster than spectrometers, SS-OCT shifts A-line rate limitations from the spectrometer exposure time to the laser sweep rate without needing to move the reference arm mirror. Laser sweep rates can be at least an order of magnitude faster than state-of-the-art spectrometer exposure times [5]. There are numerous other advantages of SS-OCT over SD-OCT that can be found in the literature [5]. However, the high costs of the technologies used SS-OCT are still prohibitive for widespread adoption, especially in the clinic. Moreover, swept lasers do not presently exist in the visible-light wavelength range, limiting the presence of SS-OCT within this dissertation.

1.1.5 Visible-light Optical Coherence Tomography

Until recently, nearly all research and clinical OCT systems imaged with near-infrared light (NIR), which contains wavelengths between 800 nm and 1300 nm. NIR light is weakly attenuated by retinal tissues and is invisible to humans, making it a desirable candidate for clinical imaging. For the last 30 years, technical improvements to NIR technology pushed the boundaries of image quality and speed [5]. However, recent development of visible-light OCT (vis-OCT), operating between 510 nm and 610 nm, has the potential to provide new information inaccessible by NIR systems. First, vis-OCT can visualize fine retinal structures with depth resolutions near 1 μm, a significant improvement over other ophthalmic NIR-OCTs [9]. This is due to the squared relationship between coherence length (l_c) and wavelength (see Equation 1.5). For example, when using the same FWHM bandwidths ($\Delta\lambda_{FWHM}$), vis-OCT centered at 560 nm has a four-fold resolution increase over NIR-OCT centered at 1020 nm. Second, tissues increasingly scatter and absorb visible light compared with NIR light [10], which, previously assumed to be a limitation, is now found to improve tissue contrasts. Third, visible light is highly sensitive to the oxygen-dependent attenuations of blood, enabling measurement of oxygen saturation (sO_2), a potential early biomarker for a variety of retinal diseases [11]. Such capabilities open a new window for vision care in the clinic, where early detection of retinal disease can prevent irreversible blindness. A detailed history of vis-OCT development can be found in Shu et. al [9].

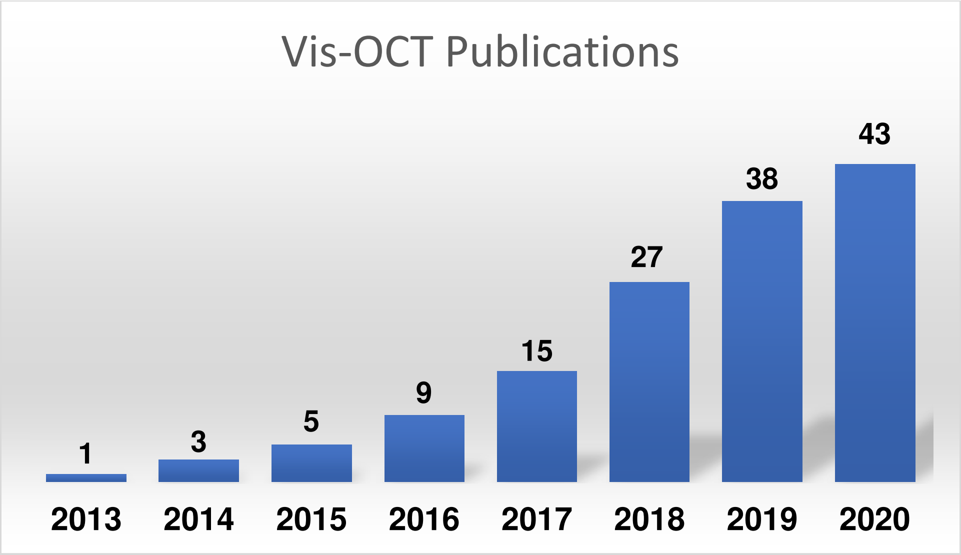

Figure 1.5 Number of vis-OCT publications (peer-reviewed journals and published conference abstracts) per years since initial introduction in 2013. This data for this figure were generated from a systematic review of the English literature in PubMed and Google Scholar searching the terms "visible light optical coherence tomography", "vis-OCT", "visible light OCT", and "white-light OCT". Figure and caption replicated from with permission from Lisa Beckmann.

Although the use of visible-light in LCI and OCT dates back to the development of these technologies, broader use of vis-OCT began only in the last decade. Fig. 1.5 plots the number of vis-OCT publications since 2013, as documented by scientific publication aggregators like Google Scholar. Since 2013, the number of vis-OCT publications has grown almost exponentially. Such growth can be attributed to the first demonstration of vis-OCT retinal oximetry by Yi et. al [11] in 2013. Retinal oximetry is perhaps vis-OCT's most novel and impactful application and provides a wealth of information about retinal disease previously inaccessible in the clinic. This renewed interest in vis-OCT within the research community has led to new investigations and technological advances improving retinal oximetry and discovering previously unexplored applications. Recent applications include full, *in vivo*, 3D visualization of Schlemm's canal and its response to pressure changes in mice [12]; quantifying nerve fiber bundle loss *in vivo* in mice after optic nerve damage [13]; visualizing of discrete ganglion cell bodies in rats [14]; measuring Bruch's membrane and IPL sub-lamination thickness in human retinas [15, 16]; quantifying changes in optical scattering properties of the nerve-fiber layer in mice [17]; and measuring sO_2 in large and small retinal blood vessels in animal models and humans. A handful of these advances are made in this dissertation [18-20].

1.1.6 Spectroscopic visible-light optical coherence tomography

A benefit to using a broadband light source in OCT is that provides spectroscopic information on light-tissue interactions. Unlike spatial information, which encodes one intensity value for a given τ_m, and is limited by coherence length, spectroscopic information encodes many wavelength-dependent intensities for a given τ_m. Such intensities may be sensitive to energy or spatial differences across wavelengths, which occur on scales much smaller than the coherence length. Therefore, spectroscopic provides the potential to 'see' information beyond the resolution of the OCT system. Briefly, SD-OCT can measure spectroscopic information by applying a short-time Fourier transform (STFT) (also referred to as short-frequency Fourier transform), which decomposes the SD-OCT signal into different spectral locations. This can be represented by applying a k-dependent window, such that

$$S_{total}(k_2 - k_1) = \sum_{m=1}^{j} \sqrt{S_{samp}(k_2 - k_1) S_{ref}(k_2 - k_1) R_m} \cos(2(k_2 - k_1)\Delta z_m), \qquad (1.12)$$

where $k_2 - k_1$ represent the continuous k range bounded by k_2 and k_1, such that $k_2 - k_1 < \frac{2\pi}{\Delta\lambda}$, the full wavenumber bandwidth of the light source. By computing the Fourier transform of Equation 1.12, we arrive at the spectrally-dependent A-line

$$I(\Delta z_m, k_2 - k_1) \sum_{m=1}^{j} \sqrt{I_{samp} I_{ref} R_{m,k_2-k_1}} \delta(z - 2\Delta z_m) \otimes |\gamma_{12}|_{k_2-k_1} \qquad (1.13)$$

where R_m and $|\gamma_{12}|$ become sensitive to the region $k_2 - k_1$. If we evaluate Equation 1.13 for different spectral windows, R_{m,k_2-k_1} will encode spectrally-dependent information at Δz_m. However, owing to the narrowed bandwidth $k_2 - k_1 < \frac{2\pi}{\Delta\lambda}$, the effective coherence length for $|\gamma_{12}|_{k_2-k_1}$ will increase, decreasing the resolution and depth precision of the A-line. In other words, the uncertainty principle dictates that increasing spectroscopic precision decreases depth precision, and vice-versa. The uncertainty trade-off is an important factor for performing depth-resolved spectroscopy like attenuation measurements.

Spectroscopic OCT has been used to investigate chromophore concentrations [8, 21], external contrasts [22], tissue damages [17], and blood-oxygen saturation (sO_2) [11, 19]. Within this dissertation, we focus on the application of spectroscopic vis-OCT for sO_2 measurement. Notably, Equation 1.13 is a highly simplified version of the A-line and fails to account for spectroscopic information imposed by sources other than R_{m,k_2-k_1}. Failure to account for such information can lead to unreliable measurements and is a major focus of Chapter 6.

1.2 LIMITATIONS OF VIS-OCT

Vis-OCT has the potential to transform retinal monitoring in the clinic but has so far failed to reach this goal. These limitations can be divided into three categories: imaging speed, image quality, and reliability of oxygen saturation (sO_2) measurements. Below, we define these limitations.

1.2.1 Imaging Speed and Image Quality

Vis-OCT uses an SD-OCT configuration with spectrometer detection. In SD-OCT, A-line rate is inversely proportional to the spectrometer's exposure time. However, there are intrinsic trade-offs to reducing the exposure time. We can investigate these trade-offs using the signal-to-noise ratio (SNR) [23] in SD-OCT

$$SNR = t_e\sqrt{\frac{S_{ref}(k)S_{samp}(k)}{\sigma_{rd}^2+\sigma_s^2+\sigma_{RIN}^2}}. \tag{1.14}$$

Signal (numerator) is adapted from Equation 1.11 and is equal to $t_e\sqrt{S_{ref}(k)S_{samp}(k)}$, where $S_{ref}(k)$ is the total power returning from the reference arm; $S_{ref}(k)$ is the total power returning from the sample arm; and t_e is the spectrometer camera's exposure time. Noise (denominator) is equal to $\sqrt{\sigma_{rd}^2 + \sigma_s^2 + \sigma_{RIN}^2}$, where σ_{rd}^2 is the variance of readout and dark noise, which describes electronic noises in the spectrometer camera; σ_s^2 is variance of shot noise, which describes the stochastic nature of light hitting the detector; and σ_{RIN}^2 is the variance of the relative intensity noise, or RIN, which describes fluctuations in the light source intensity. $\sigma_{rd}^2 = \alpha$, a constant; $\sigma_s^2 = \beta t_e(S_{ref}(k) + S_{samp}(k))$, where β is a constant; and $\sigma_{RIN}^2 = \xi t_e\left(S_{ref}(k) + S_{samp}(k)\right)^2$, where ξ is a constant. For tissue imaging, light reflected from the reference arm mirror is orders of magnitudes more intense than that backscattered in the sample arm, adding the assumption $S_{ref}(k) \gg S_{samp}(k)$. Inputting the noises and the assumption into SNR, we get

$$SNR = t_e\sqrt{\frac{S_{ref}(k)S_{samp}(k)}{\alpha+\beta t_e S_{ref}+\xi t_e S_{ref}^2}} \tag{1.15}$$

Next, we assume $S_{ref}(k)$ is sufficiently high, such that optical noises in the system are much greater than the electronic noises in the camera (e.g., σ_s^2 & $\sigma_{RIN}^2 \gg \sigma_{rd}^2$), allowing us to greatly simplify the equation to

$$SNR = t_e\sqrt{\frac{S_{samp}(k)}{\beta t_e+\xi t_e S_{ref}}} = \sqrt{\frac{t_e S_{samp}(k)}{\beta+\xi S_{ref}}}. \tag{1.16}$$

Equation 1.16 lets us investigate two critical conditions for SD-OCT operation: Condition 1, where the laser source has negligible RIN, making $\sigma_s^2 \gg \sigma_{RIN}^2$ and $SNR = \sqrt{\frac{t_e S_{samp}(k)}{\beta}}$; and Condition 2, where the laser source has significant RIN, making $\sigma_{RIN}^2 \gg \sigma_s^2$ and $SNR = \sqrt{\frac{t_e S_{samp}(k)}{\xi S_{ref}(k)}}$. Assuming $S_{samp}(k)$ and t_e are fixed for a given experiment, we see that Condition 1 approaches a constant, which is the maximum SNR possible for the SD-OCT system. This is called the ‘shot-noise limit’, owing to shot noise being the limiting factor in the SNR. Conversely, SNR under Condition 2 does not approach a constant, and instead scales inversely with

$S_{ref}(k)$. This means that for all $S_{ref}(k)$, Condition 1 reaches a higher maximum SNR than Condition 2 ($\sqrt{\frac{t_e S_{samp}(k)}{\beta}} > \sqrt{\frac{t_e S_{samp}(k)}{\xi S_{ref}(k)}}$).

In Equation 1.14, $S_{ref}(k)$ is necessary for generating interference and therefore signal. In Equation 1.16, we neglect the influence of σ_{rd}^2 by assuming sufficiently high $S_{ref}(k)$. Therefore, in SD-OCT, we are incentivized to maximize $S_{ref}(k)$ as much as physically possible. This strategy is effective under Condition 1, where SNR will not scale with $S_{ref}(k)$, but fails under Condition 2, which scales inversely with $S_{ref}(k)$. Critically, most modern NIR SD-OCT systems use light from super luminescent diodes (SLDs), which have negligible RIN, allowing for operation under Condition 1. However, SLDs do not generate broadband visible light. Therefore, vis-OCT relies on supercontinuum light sources (SCs), which generates broadband visible light through high energy optical pulses [23]. SCs have significant RIN, making vis-OCT operate under Condition 2. Therefore, vis-OCT systems work with an intrinsic SNR disadvantage. Looking at Equation 1.16, we can increase SNR by either increasing $S_{samp}(k)$ or t_e. For vis-OCT ophthalmic applications, we cannot increase $S_{samp}(k)$ beyond a set limit (typically $250\ \mu$W) due to phototoxicity and comfort in the retina. Therefore, we and other researchers increased t_e [24, 25]. Our vis-OCT systems previously operated with $t_e = 40\ \mu s$, equivalent to a 25 kHz A-line rate. A typical vis-OCT ophthalmic volume is typically composed of a minimum density of 512 A-lines × 256 B-scans, meaning vis-OCT required scan times ≥ 5 seconds. Considering breathing motions, head motions, and eye motions, including involuntary saccades, an acquisition time of

≥ 5 seconds is particularly onerous for patients in the clinic. Furthermore, a visible-light scanning beam may be distracting or uncomfortable to patients, exaggerating these motions. Simply stated, under Condition 2, clinical vis-OCT cannot simultaneously guarantee high image quality and high imaging speed. Without sufficient speed or image quality, vis-OCT cannot access its resolution or functional imaging advantages.

Chapters 2-6 use vis-OCT systems under Condition 2 and are therefore subject to the above limitations. In Chapter 2, we partially overcome the speed limit by presenting a more efficient scan pattern. However, this comes at the trade-off of scanning smaller fields-of-view in the retina. In Chapter 7, which is the most recent work in this dissertation, we finally address the root cause of speed and image quality limitations, RIN. In this chapter, we develop a detection scheme that almost entirely removes RIN, allowing high-speed, high-quality ophthalmic vis-OCT in the clinic for the first time.

1.2.2 sO_2 Reliability

Vis-OCT is sensitive to the oxygen dependent absorption and scattering coefficients of blood. This enables inverse measurement of sO_2 by measuring the depth-resolved attenuation of blood at different wavelengths. However, such analysis is susceptible to contaminating signals and noises called spectral contaminants (SCs). Within the scope of this dissertation, we define SCs as any signal or noise not originating from the oxygen-dependent attenuation of blood. As will be investigated in this dissertation, SCs can originate from the vis-OCT system hardware, data processing, or different layers of the imaged sample. SCs detract from the accuracy and repeatability of sO_2, particularly across different vis-OCT systems and human eyes. Unfortunately, previous applications failed to correct for SCs, leading to unreliable sO_2 measurements. This dissertation, particularly Chapter 6, models and corrects for each SC source *in vivo* for the first time.

1.3 SCOPE OF THE DISSERTATION

The work presented in this dissertation identifies, addresses, and overcomes the major limitations for clinical translation of vis-OCT. Above, we defined two categories limiting clinical translation of vis-OCT: imaging speed, image quality, and reliability of sO_2 measurements. Each chapter in this dissertation, outlined below, details a new vis-OCT technical improvement that addresses one or all categories. Many of these improvements begin with new theoretical frameworks for vis-OCT hardware and signal processing. The overarching philosophy of this dissertation is to understand, define, and validate our methods, beginning with basic physical laws. By the end of Chapter 7, we provide critical new information on the operation of vis-OCT and effectively demonstrate structural and functional vis-OCT imaging in humans.

1.4 OUTLINE OF THE DISSERTATION

Chapter 2 describes a new scan pattern for vis-OCT that removes speckle noise in human retinal images [24]. By modulating the scanning beam orthogonal to the imaging path, we acquire a set of decorrelated speckle noises at a local imaging location. By averaging the decorrelated noises, we reveal the true sample structure without sacrificing image resolution. This method provides a significant speed advantage over traditional averaging techniques and is robust against blurring from sample motions. Such speed advantage is critical for vis-OCT, which typically scans slower than NIR OCTs to maintain sufficient image quality. This work reveals fine structures in the human retina, such as Bruch's membrane, a locus for macular degeneration, and inner plexiform layer (IPL), a locus for glaucoma, with unprecedented clarity. A follow up study in the clinic [26] uses this scan pattern to investigate IPL lamination thicknesses in healthy and glaucomatous eyes. The researchers find that the central lamination of the IPL thins significantly in glaucomatous eye compared with healthy eyes.

Chapter 3 presents a theoretical and experimentally validated definition of spectrally-dependent roll-off (SDR) in vis-OCT [27]. Roll-off describes image signal attenuation with depth caused by the hardware detection. Specifically, vis-OCT uses spectrometer detection, which is composed of a linear array camera that measures interfering light at different wavelengths. Each pixel-element of the spectrometer integrates light across a finite region, acting as a low-pass filter for the interference spectrum. Since image depth is the Fourier transform conjugate of the interference spectrum (units in optical frequency, or wavenumber), such low-pass filtering attenuates the image with increasing depth. In nearly all vis-OCT systems, the interference is projected nonlinearly on the spectrometer, mapping different spatial frequencies to different pixels. Therefore, each spectrometer element applies a different low-pass filter function, which we call SDR. In vis-OCT spectroscopic imaging, SDR causes non-uniform, wavelength-dependent attenuations in images. Such attenuations influence quantitative spectroscopic measurements, such as sO_2, and must be corrected.

Chapter 4 presents another artifact caused by spectrometer detection. Here, we derive and experimentally validate the existence of the spectrally-dependent background (SDBG) in vis-OCT [28]. As described in Chapter 3, the vis-OCT image is reconstructed by Fourier transform of the interference spectrum detected by the spectrometer. To reconstruct the sharpest image, the spectrometer should detect interference as a linear function of optical frequency, or wavenumber. However, as also described in Chapter 3, the spectrometer samples the interference nonlinearly. To achieve best image quality, we numerically resample the interference spectrum to be linear in wavenumber. An unintended consequence of resampling is that it scales image background noise. Since the level of scaling is determined by the resampling rate, some spectral components will have amplified background noises relative to others. This imposes an additive bias on the image signal that changes with different wavelength components, called SDBG. Therefore, SDBG, like SDR, influences quantitative spectroscopic vis-OCT measurements like sO_2. We found that SDBG can impose greater than 10% bias on the measured sO_2 in the human retina.

Chapters 3 & 4 define SDR and SDBG, two alterations of the spectroscopic vis-OCT signal. They are representative of a larger group of signals and noises that contaminate quantitative spectroscopic measurements. We call these spectral contaminants, or SCs. Within the scope of this dissertation, we focus on SCs influencing of retinal sO_2. There are two main consequences of uncorrected SCs: error in measuring blood's oxygen-dependent spectrum, and incorrect assumptions of blood's optical properties. The former influences the physical measurements, while the latter results in improper regression modeling of these measurements. Together, they result in high sO_2 errors and uncertainties that are often unpredictable and nonlinear. We address both problems in Chapter 5 & 6.

We address modeling of blood's optical properties in Chapter 5 [29]. Briefly, we measure sO_2 by fitting vis-OCT measurements to a linear combination of the known oxygenated and deoxygenated absorption and scattering spectra of blood, respectively [30]. The known spectra are taken from the literature and assumed to be representative of the vis-OCT measurements. Following theoretical assumptions in the literature, we and other groups previously applied a scaling factor between 0.20 and 0.40 to the known scattering coefficients of blood to account for hematocrit-dependent optical scattering effects [11]. From here on, we refer to this factor as the scattering scaling factor, or SSF. Through a combination of numerical modeling, simulation, empirical measurements, and SC removal, we determined such SSF values were incorrect, disproving fundamental assumptions of how vis-OCT senses the optical properties of blood. Instead, we find the SSF is between 0.02 and 0.10, significantly lower than the previously assumed value. We found that the lower SSFs are the result of vis-OCT's high sensitivity to multiple forward scattering in blood.

Chapter 6 presents adaptive spectroscopic vis-OCT, or Ads-vis-OCT, a new algorithm that identifies and removes SCs by conforming sO_2 measurements to the unique properties of each blood vessel [20]. Here, we introduce the first comprehensive model of retinal oximetry in vis-OCT, which includes SCs from the vis-OCT system, image processing, retinal tissues, and blood itself. We validate our model by simulation and well-controlled *ex vivo* measurements. Then, we use Ads-vis-OCT to measure sO_2 the retinas of 18 healthy human volunteers. In humans, we measure repeatable sO_2 values in vessels as small as 37 µm and as large as 168 µm. This method is shown to be more accurate and repeatable than other widely used vis-OCT sO_2 methods.

Chapter 7 presents a transformative advance in vis-OCT speed and image quality. Here, we develop a new vis-OCT system detecting interference with two spectrometers called ‘balanced detection’ (BD) [31]. BD addresses the key limiting factor in vis-OCT image quality, relative intensity noise, or RIN, which is a type of noise associated with visible-light lasers. RIN becomes pronounced with increased imaging speed, fundamentally limiting how fast vis-OCT can acquire images in the clinic. For the first time, we implement a highly accurate subpixel cross-calibration between the two spectrometers to sense and cancel out the influence of RIN. BD increases image SNR up to 25.6 dB and performs the fastest ever vis-OCT human retinal imaging.

Finally, Chapter 8 summarizes this dissertation and presents areas for future work.

Chapter 2

Speckle reduction in visible-light optical coherence tomography using scan modulation

2.1 MOTIVATION

Vis-OCT offers a near 1 μm depth resolution but fails to visualize micrometer-scale retinal structures due to presence of speckle noise. In the past, researchers averaged different tissue locations across multiple frames to reduce the influence of speckle. However, this method is unreliable in clinical vis-OCT due to low scanning speeds and fast eye motions. A technique that can reduce speckle while avoiding motion artifacts is necessary to visualize fine features in the retina.

2.2 SUMMARY

We present a technique to reduce speckle in visible-light optical coherence tomography (vis-OCT) that preserves fine structural details and is robust against sample motion. Specifically, we locally modulate B-scans orthogonally to their axis of acquisition. Such modulation enables acquisition of uncorrelated speckle patterns from similar anatomical locations, which can be averaged to reduce speckle. To verify the effectiveness of speckle reduction, we performed in-vivo retinal imaging using modulated raster and circular scans in both mice and humans. We compared speckle-reduced vis-OCT images with the images acquired with unmodulated B-scans from the same anatomical locations. We compared contrast-to-noise ratio (CNR) and equivalent number of looks (ENL) to quantify the image quality enhancement. Speckle-reduced images showed up to a 2.35-dB improvement in CNR and up to a 3.1-fold improvement in ENL with more discernable anatomical features using eight modulated A-line averages at a 25-kHz A-line rate.

2.3 INTRODUCTION

Optical coherence tomography (OCT) is a scattering-based imaging technology that acquires high-resolution 3D images of biological samples *in vivo* [1]. Following its initial report in 1991, OCT has become the “gold standard” for noninvasive retinal imaging. Today, it is an essential technology in labs and clinics for studying and managing a wide variety of retinal diseases [32]. Advances in optoelectronics in the last 25 years has led to improved resolution, signal-to-noise ratio, and imaging field of view in OCT [5]. However, speckle, an image artifact caused by the self-interference of coherent light at random phases, remains a significant source of reduced image quality [33]. This is of particular salience in retinal imaging, where speckle noise can obscure fine structures in the outer retina, such as the retinal pigment epithelium (RPE) and Bruch’s membrane (BM). Minute pathological changes in these structures may be strongly associated with the progressions of several retinal diseases, including macular degeneration [34] and central serous retinopathy (CSR) [35].

To improve imaging quality, researchers developed several methods to suppress speckle artifacts in OCT. These methods can be separated into two categories: digital filtering [36] and incoherent averaging [37]. Digital filtering, while simple to implement and effective in reducing the grainy appearance of speckle, causes blurring that degrades image resolution and prevents the delineation of fine anatomical features. Incoherent averaging, on the other hand, samples photons that have undergone statistically different scattering events, thereby generating uncorrelated speckle patterns. Uncorrelated patterns from similar structural locations can be averaged to remove speckle and reveal original anatomical information. The physical basis of incoherent averaging method makes it ideal for situations where the study of fine anatomical features is required. However, manipulating image acquisition to obtain uncorrelated speckle patterns can be challenging. First, different scattering events must be probed without losing the structural integrity of the location of interest. Second, multiple acquisitions at a particular location are required to generate enough patterns suitable for averaging. Samples with strong motion can pose a challenge to averaging, especially in human eyes. Multiple approaches were developed to achieve incoherent averaging of speckle while retaining high image quality. The most basic technique is to average consecutive B-scans in a raster pattern, either from the same location or from a slightly offset position [38]. The former relies on small sample movement to modify scattering events, while the latter directly modifies scattering events across consecutive separated B-scans. More advanced techniques for spatial averaging include modulating the scanning beam after every A-line with a translational offset [39] or angular offset [40]. In particular, translational offset has been shown to be more robust against sample motion than B-scan averaging. Both scan modulations were previously implemented with additional hardware and moving parts. Other techniques include multi-wavelength averaging [41, 42], modulation of light wave front [43], and non-local, software-based averaging [44].

Recent development of visible-light optical coherence tomography (vis-OCT) has generated new capabilities for retinal imaging, including visualization of fine structures with ultra-high resolution and spectroscopic analysis of blood-oxygen concentration (sO_2) [9, 18, 45]. Speckle, which distorts both structural and spectral information [46], can undermine these new benefits. To reduce speckle in vis-OCT using incoherent averaging, there are some unique challenges. First, there is strong optical absorption and scattering in tissue in the visible-light spectral range, reducing the amount of photons that can be collected per unit time. This is coupled with high relative intensity (RIN) from the supercontinuum laser source [9]. To achieve high signal-to-noise ratio (SNR), a prolonged camera exposure is required, therefore reducing scanning speed. Second, since eyes are sensitive to visible light illumination, vis-OCT often suffers from increased retinal motion. Finally, preservation of structure-dependent spectroscopic information requires anatomically localized sampling of scattering events.

A method for speckle reduction that is both structurally localized and robust against retinal motion is optimal for vis-OCT. Furthermore, it is ideal for a speckle reduction technique to be easily implementable in clinical settings to increase usability, reduce likelihood of malfunction, and cause no additional discomfort to patients. A straightforward approach is to perform B-scan averaging. However, eye motion in vis-OCT makes B-scan averaging unreliable due to blurring, even with post-acquisition image registration. To overcome this challenge, we modulated the scanning trajectory orthogonally to the direction of the B-scan images during data acquisition. This method enabled sampling of different speckle patterns while maintaining high anatomical similarity between modulations. We implemented scanning modulation by directly controlling the galvanometer scanners without additional hardware.

2.4 METHODS

We modulated both raster and circular scans, which are commonly used in vis-OCT [9], to test our speckle reduction method. Fig. 2.1 illustrates the modulated raster scan (Figs. 2.1a and 2.1b) and modulated circular scan (Figs. 2.1c and 2.1d). As shown in Figs. 2.1a and 2.1c, we define the B-scan axis as the direction along which a traditional cross-sectional image would be acquired without modulation. We define the orthogonal axis as the direction orthogonal to the B-scan axis on the 2D scanning plane. Movement along the orthogonal axis (arrow 1 in Figs. 2.1b and 2.1d) occurs in n equidistant steps, where n is the number of speckle-uncorrelated A-lines to be locally averaged. Each translation of the galvanometer (red dots in Figs. 2.1b and 2.1d) is discrete, synchronized with the spectrometer camera exposure, and implemented entirely via software control without additional hardware or moving parts. This avoids a complex synchronization procedure or risk for desynchronization between the beam path and camera exposure when using an external scanner [39]. The centroids of each spot generating an A-line are separated by a distance d along the orthogonal axis (Fig. 2.1b). After n translations in this direction, the beam is shifted along the B-scan axis (arrow 2 in Figs. 2.1b and 2.1d), followed by a reversed scan along the orthogonal axis (arrow 3 in Figs. 2.1b and 2.1d). Such modulation superimposes a rectangular wave on the B-scan axis, where each rising and falling edge of each rectangle contains n speckle-uncorrelated A-lines. While other modulation shapes, such as sinusoidal or triangular are possible, we chose rectangular to best preserve lateral resolution along the B-scan axis.

During acquisition, several parameters, including *n*, *d,* and imaging field of view are adjustable. We investigated how to obtain an optimal *d* in section 2.5.1.

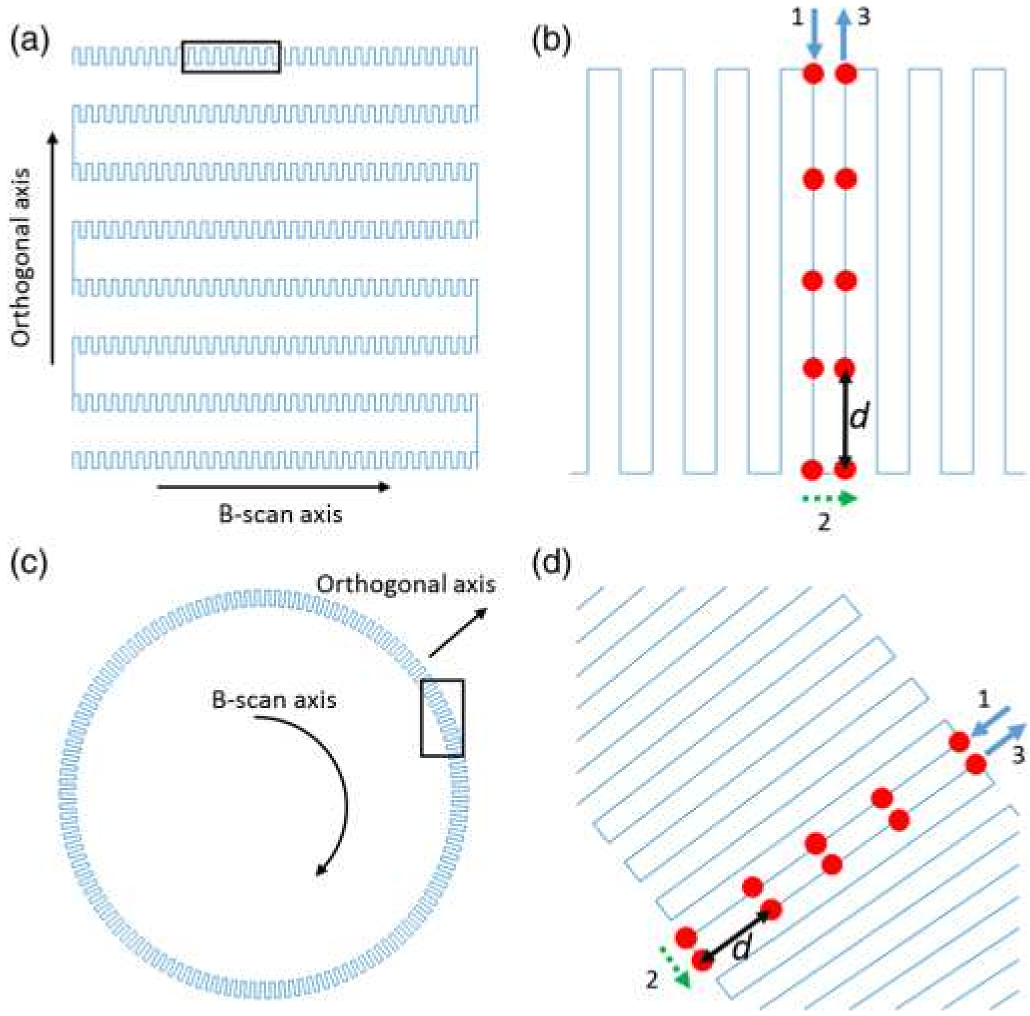

Fig. 2.1 Illustrations of speckle-reduction scanning protocols. (a) Overall illustration of the relationship between the B-scan axis and the orthogonal axis in the modulated raster scan; (b) Detailed illustration of the A-line acquisition sequence in the modulated raster scan. d is the distance between two adjacent A-lines along the orthogonal axis. The arrows 1, 2, and 3 highlight the trajectory of galvanometer motion; (c) Overall illustration of the relationship between the B-scan

axis and the orthogonal axis in the modulated circular scan; (d) Detailed illustration of the A-line acquisition sequence in the modulated circular scan.

We averaged all n A-lines in the orthogonal direction along each rectangular edge (Figs. 1b and 1d) to generate a single speckle reduced A-line (srA-line). For a desired sampling density of m srA-lines per speckle-reduced B-scan (srB-scan), the total number of camera acquisitions per srB-scan is $n \times m$. Each consecutive srA-line in an srB-scan can then be calculated as

$$srA_j = \frac{1}{n}\sum_{i=1}^{n} A_{ij} \;\; for\; j = 0, 1, 2, \ldots m-1, \tag{2.1}$$

where i is the index of each set of n A-lines about the edge of a rectangle; j is the index of each consecutive edge of a rectangle; and A_{ij} is the i+j×n^{th} A-line in a full B-scan acquisition.

Since an srB-scan increases imaging time over normal B-scan acquisition by a factor of n, it is important to collectively limit n, m, and the number of total srB-scans to prevent overly long imaging time. First, all sampling numbers were selected in powers of 2 to support fast GPU data processing. Next, we limited all imaging experiments to 8192 total A-lines per srB-scan. Given a camera exposure time of 40 μs, which is required for sufficiently high SNR, an srB-scan could be acquired in 327 ms, an upper limit for reducing bulk motion artifacts (satisfying Nyquist criterion of 500 ms for eye microsaccades of ~ 1 Hz) [47]. Furthermore, we chose to limit the total image acquisition time to ~ 5 s to prevent patient fatigue and discomfort. This limited the total amount of srB-scans per acquisition to 16 (5.25 s total acquisition time). In our experimental human imaging system (Section

2.4.3), we maximized lateral sampling density in a raster scan without spot overlap, where m = 1024 srA-lines and n = 8 averages. The parameters n, m, and d can be easily modified for different experimental conditions.

The srB-scan image is the physical equivalent of averaging n spatially separated B-scans, each of m A-lines. However, in direct B-scan averaging, each A-line at a particular lateral position is delayed temporally by the scanner's fly back time. This results in a total sampling period of $n \times m \times t$, where t is the camera exposure time for each A-line. In our method, modulation removes the wait for scanner fly back, thereby reducing the total sampling period to $n \times t$ for each srA-line. Using our experimental parameters (m = 1024, n = 8, t = 40 μs), we reduced the sampling period from 328 ms to 320 μs for each *sr*A-line and increased the *sr*A-line rate from 3 Hz to 3,125 Hz. Constant, involuntary retinal motions [47] can occur at frequencies up to 90 Hz with amplitudes up to 40 arc seconds (equivalent 0.011 μm change in sampling location per 40 μs camera exposure in the human retina). This leaves possibility of only 0.088 μm of movement during an *sr*A-line, which is insignificant when compared with the micron-order lateral and axial resolutions in OCT. Therefore, the improved *sr*A-line rate is highly significant.

2.4.1 Metrics to evaluate image quality improvement

We used contrast-to-noise ratio (CNR) and equivalent number of looks (ENL) [48] to evaluate image quality improvement after speckle reduction. CNR measures how well the sample feature can be discerned from the surrounding background. Mean intensity and variance from both the image background and sample feature are included to account for two separate noise components: intrinsic OCT background noise and speckle. Since the optical properties of different features vary, we calculated CNR in confined region of interests (ROIs) as

$$CNR = 10log_{10}\frac{\mu_i-\mu_b}{\sqrt{\sigma_i^2+\sigma_b^2}}, \tag{2.2}$$

where μ_i is the mean intensity of the i^{th} ROI; μ_b is the mean intensity of the background outside of the sample structure; σ_{i}^2 is the variance of the i^{th} ROI; and σ_b^2 is the variance of the background outside of the sample feature.

ENL is the squared inverse of the speckle contrast and measures the smoothness and homogeneity within a ROI. We calculated ENL as

$$ENL = \frac{\mu_i^2}{\sigma_i^2}, \tag{2.3}$$

where μ_i is the mean intensity of the i^{th} ROI and σ_i^2 is the variance of the i^{th} ROI. An increase in ENL serves as a strong indicator for the reduction of speckle.

We compared CNR and ENL in srB-scans with a ‘reference’ B-scan from the same location as an srB-scan. A reference B-scan included 8192 A-lines acquired along the B-scan axis with a 40 μs camera exposure. Every 8 consecutive A-lines were averaged, resulting in a final sampling density of 1024 averaged A-lines per reference B-scan. This operation was equivalent to acquiring an srB-scan without modulating the scanner along the orthogonal axis. Because of high sampling density along the B-scan axis, averaged speckle patterns were still highly correlated, preventing reduction of speckle. However, suppression of the noisy background in the reference B-scan was equivalent to that in an srB-scan due to averaging along the same the same number of A-lines at the same camera exposure time. We compared the CNR and ENL values between the reference B-scan and sr-Bscans to evaluate the effectiveness of speckle reduction.

2.4.2 Data Acquisition

We tested our speckle reduction protocol in both mouse and human retinas using two prototype systems developed at Northwestern University. In addition, we further tested our speckle reduction method in humans in a clinical setting using a commercial vis-OCT system (Aurora X1, Opticent Health), where optical engineering expertise was unavailable. We directly implemented the modulated scanning protocol in that system without additional calibration, alignment, or changes to the photographer's workflow.

2.4.2 Mouse Imaging

For mouse imaging, we used the system described in our previous work [49]. In brief, a $1/e^2$ spot size of ~ 5.7 μm was incident on the retina. We controlled the total illumination power to 1.2 mW on the cornea in all instances. For a raster scan, we used m = 1024, n = 8, and d = 6.3 μm. A field of view (FOV) of 1.4 × 1.4 mm^2 was used in all mouse retina images, equivalent to ~ 1.4 μm separation between srA-lines along the B-scan axis. For a circular scan, we used n = 8 and d = 5.4 μm. The circle circumference was 1.8 mm, equivalent to ~ 1.8 μm separation between srA-lines along the B-scan axis. Improved from our previous system, we adopted a commercial spectrometer (Blizzard SR, Opticent Health) with a 2048-pixel line scan camera covering 510 nm - 610 nm, which provided an axial resolution of ~ 1 μm in tissue. We used an A-line rate of 25 kHz in all rodent experiments.

All rodent experimental procedures were approved by the Northwestern University IACUC and conformed to the Association for Research in Vision and Ophthalmology (ARVO) Statement on Animal Research. We anesthetized adult C57Bl6/J mice (n = 8) with an intraperitoneal injection (10 mL/kg body weight) of a ketamine/xylazine cocktail (ketamine: 11.45 mg/mL; xylazine: 1.7 mg/mL). Each mouse was then placed on a custom-made animal holder and immobilized for imaging. The body temperature was maintained with a heat lamp. To dilate the pupil, we applied a drop of 1% tropicamide hydrochloride ophthalmic solution. Throughout imaging, we applied one drop of commercial artificial tears after each image acquisition to prevent corneal dehydration. After the imaging session concluded, the mouse was allowed to recover under heat lamp and was returned to the animal housing facility.

2.4.3 Human Imaging

Human imaging was performed using two vis-OCT systems. First, images were acquired in the Ophthalmology Department at Northwestern Memorial Hospital using an experimental system reported in our previous work [45]. We controlled the illumination power to be less than 250 μW on the cornea in all our human studies. A $1/e^2$ spot size of ~ 6.3 μm was incident on the retina. For a raster scan, we used n = 8, d = 7 μm, and m = 1024. The FOV was 6.8 × 6.8 mm^2, leading to a d ~ 6.6 μm separation between srA-lines along the B-scan axis. For a circular scan, we used n = 8 and d = 5.9 μm. The circle circumference was 18.3 mm, equivalent to ~ 18-μm separation between srA-lines along the B-scan axis. Similar to our mouse system, we upgraded to a commercial spectrometer (Blizzard SR, Opticent Health). The A-line rate was 25 kHz in all human imaging tests.

To verify the efficacy of our method outside lab environment, we further conducted human imaging in the Department of Ophthalmology at New York University (NYU) Langone Medical Center. A clinical vis-OCT system (Aurora X1, Opticent Health) was used to acquire all images. It offered an axial resolution of ~ 1 µm and we controlled the spectrometer exposure time to be 40 µs. We used the same raster scanning parameters as those in the Northwestern system, but reduced the FOV to 5×5 mm^2. We implemented the speckle-reduction acquisitions in Aurora X1 entirely via a software update without any additional calibration or hardware modifications. Clinical photographers acquired retinal images without any changes to their normal workflow.

All human imaging procedures in the respective imaging locations were approved by the Northwestern University Institutional Review Board (IRB) and NYU IRB, and adhered to the tenets of the Declaration of Helsinki. Healthy volunteers without known eye diseases provided informed consent before imaging (Northwestern site: n = 3; NYU site: n = 6).

2.4.4 Initial Calibration for Orthogonal Spot Separation

A calibration procedure was needed for coarse determination of optimal spot separation, *d*, along the orthogonal axis. Since CNR is associated with the ability to discern features from noise, we used it as the primary indicator for image quality. In theory, an increased *d* increases decorrelation of the speckle patterns between adjacent orthogonal A-lines. After averaging, speckle is maximally reduced when the averaged patterns are entirely uncorrelated [39]. However, if d is too large, we will lose structural similarity between orthogonal A-lines, which can result in image blurring. We investigated the impact of modulation distance on CNR by imaging a model mouse eye using both raster and circular scans. The model eye was made from a silica bead (diameter: 3.15 mm). We attached two layers of tape and paper with an ink pattern to the bottom of the bead to simulate the retinal layers. Using the rodent vis-OCT system, we reached a $1/e^2$ spot size of ~ 5.5 µm on the tape layers through the bead. We then varied the d value from 0 to 13.75 µm in 16 steps and acquired an srB-scan after each step. We calculated CNR from 3 ROIs in the top tape layer and averaged them to determine the impact of the d value on image quality.

2.5 RESULTS

2.5.1 Initial Calibration for Orthogonal Spot Separation

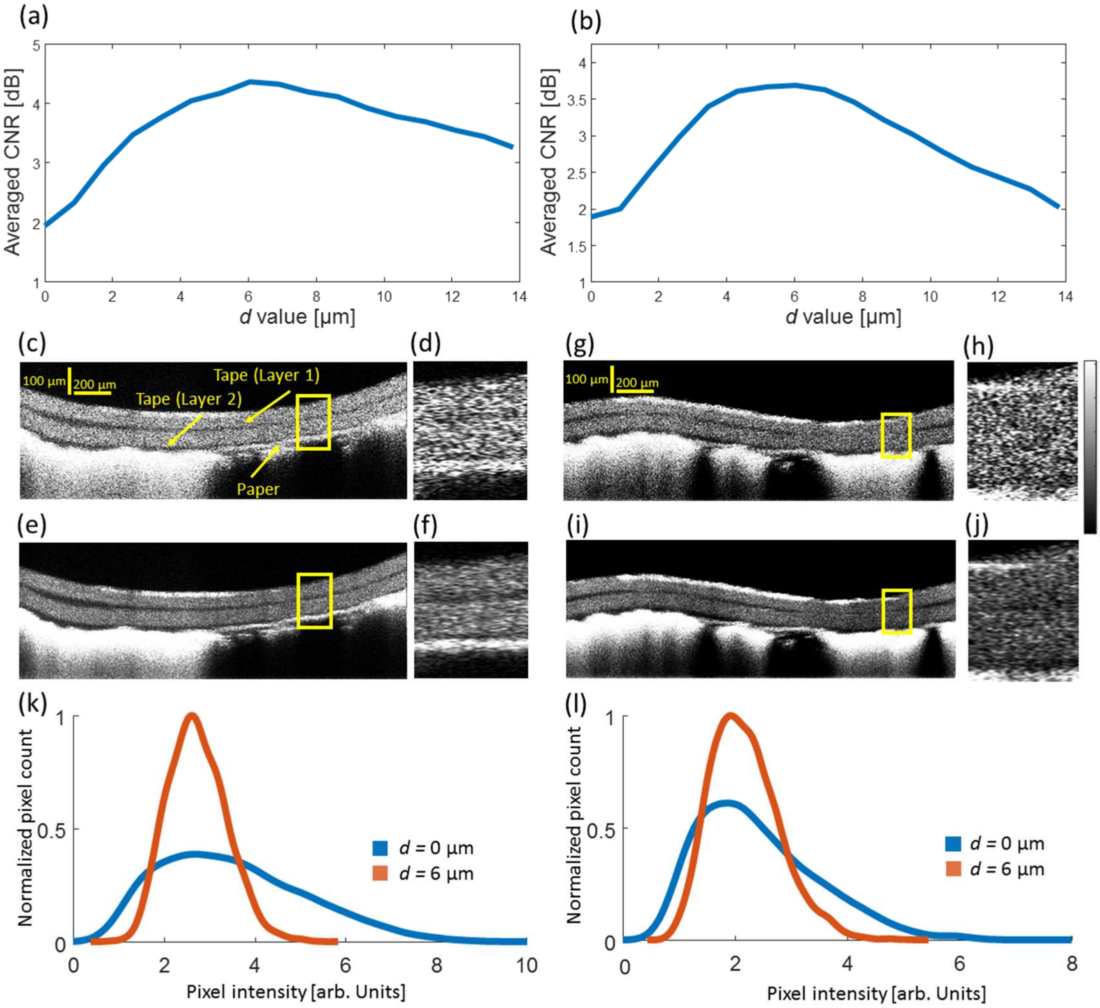

Figure 2.2. Speckle reduction test in the model mouse eye. (a) Change of averaged CNR as a function of d in the modulated raster scan; (b) Change of averaged CNR as a function of d in the modulated circular scan; (c) An srB-scan image of the model mouse eye acquired using modulated raster scan with d = 0 µm. The structures corresponding to the two tape and one paper layers are highlighted by the arrows; (d) Magnified view of the region highlighted by the box in panel (c); (e) An srB-scan image of the model mouse eye acquired using modulated raster scan with d = 6 µm. (f) Magnified view of the region highlighted by the box in panel (e); (g) An srB-scan image of the model mouse eye acquired using modulated circular scan with d = 0 µm; (h) Magnified view of the

region highlighted by the box in panel (g); (i) An srB-scan image of the model mouse eye acquired using modulated circular scan with d = 6 µm; (j) Magnified view of the region highlighted by the box in panel (i). All images are plotted with identical color bar; (k) Fitted pixel intensity histograms within the tape layer 1 acquired by modulated raster scans with d = 0 µm and d = 6 µm; (l) Fitted pixel intensity histograms within the tape layer 1 acquired by modulated circular scans with d = 0 µm and d = 6 µm.

The results to identify an optimal *d* value are shown in Fig. 2.2. Figs. 2.2a and 2.2b, respectively, show how CNR values vary as a function of *d* in imaging the model eye using modulated raster and circular scans. When *d* is increased from 0 to 13.75 µm in both scans, CNR reaches its maximum at *d* = 6 µm. Figs. 2.2c and 2.2e show raster srB-scans with *d* = 0 µm and *d* = 6 µm, respectively. Figs. 2.2d and 2.2f show magnified views of the two highlighted images (yellow boxes in Figs. 2.2c and 2.2e). The srB-scan with *d* = 6 µm (Fig. 2.2f) shows a smoother intensity distribution within each layer and much improved discrimination between the tape and the paper layers, as compared with the unmodulated scan (Fig. 2.2d). Figs. 2.2g-2.2j show the similar comparison in the circular scan, where the speckle-reduced circular scan with *d* = 6 µm demonstrates improvement in image quality.

Figs. 2.2k and 2.2l, respectively, show the pixel intensity histograms from the tape layer 1 (highlighted in Fig. 2.2c) in the raster and circular scans. In both scan patterns, the intensity histograms changed from a broad, right-skewed distribution when *d* = 0 µm to a lower-variance, nearly centrosymmetric distribution when *d* = 6 µm. These results agree with the expected change in pixel intensity distribution from Rayleigh distribution to Poisson distribution after speckle reduction [43].

From Figs. 2.2a and 2.2b, we used a -0.25-dB drop in CNR to determine the range of acceptable *d* values, which gives $d_{\min} = 5.1$ µm and $d_{\max} = 7.8$ µm. This range is helpful for human retinal imaging, where the eye shape, optical properties, and scanning location may differ among subjects. We also noted that the optimal *d* = 6 µm is approximately equal to the estimated spot size of ~ 5.5 µm on the retina. This suggests that adjacent spots along the orthogonal axis should be as close as possible without spatial overlap. This result is consistent with the notion that spatial overlapping provides correlated speckle patterns. This result also suggests that it is acceptable to estimate the optimal *d* using the OCT focal spot size on the sample. These considerations are not expected to change in the living human eye, where local movement during a single *sr*A-line (0.088 µm) is significantly less than *d*.

We adjusted the *d* value within the identified range in rodent and human imaging to accommodate different eye conditions. Since we control the *d* value by the galvanometer angle, we identified optimal angular step size along the orthogonal axis in different experimental conditions. For mouse imaging, the optimal angular step sizes were 0.175^{o} and 0.15^{o}, which correspond to *d* values of 6.3 µm and 5.4 µm, respectively, in raster and circular scans. For human imaging, the optimal angular step sizes were 0.025^{o} and 0.02^{o}, which correspond to d values of 7 µm and 5.9 µm, respectively, in raster and circular scans.

2.5.2 Speckle Reduction in the Mouse Retina

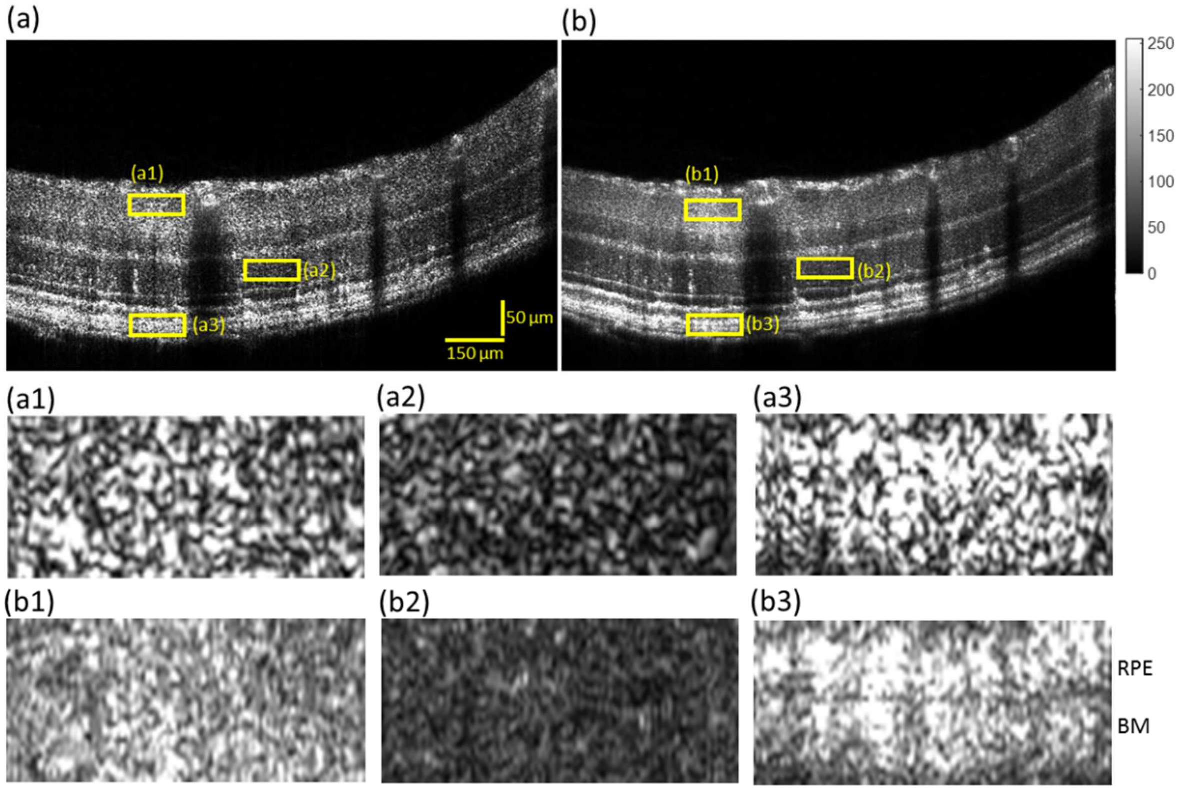

Figure 2.3. Speckle reduction test in mouse retina using modulated raster scan. (a) Reference raster B-scan image. Three ROIs from IPL, ONL, and ORL are highlighted by a1, a2, and a3, respectively. The size of each ROI is 140 µm (lateral) × 20 µm (axial); (b) The corresponding srB-scan image. The same three ROIs are highlighted by b1, b2, and b3. (a1), (a2), and (a3) are the magnified views of the three highlighted ROIs in panel a. (b1), (b2), and (b3) are the magnified views of the three highlighted ROIs in panel b. CNR and ENL values are calculated from all the selected ROIs. All images are plotted with identical color bar.

Fig. 2.3 shows the speckle reduction results in a mouse retina using raster scan. Figs. 3a is the reference B-scan image and Fig. 2.3b is the srB-scan image. The imaged retina in the srB-scan has a smoother, less grainy appearance that provides a clearer differentiation between anatomical layers. We selected six ROIs from the inner plexiform layer (IPL, highlighted by a1 and b1), outer nuclear layer (ONL, highlighted by a2 and b2), and ORL (highlighted by a3 and b3) to quantify quality improvement. Figs. 2.3a1-2.3a3 and Figs. 2.3b1-2.3b3 show the magnified views of the six selected ROIs and Table 2.1 shows the quantitative comparisons of CNR and ENL values from these ROIs. Speckle-reduction is particularly helpful in the ORL, where a small gap near RPE and BM layers is revealed (Fig. 2.3b3), which is not visible in the reference B-scan image (Fig. 2.3a3). The capability to differentiate RPE and BM may add significant value to various preclinical studies using mouse models.

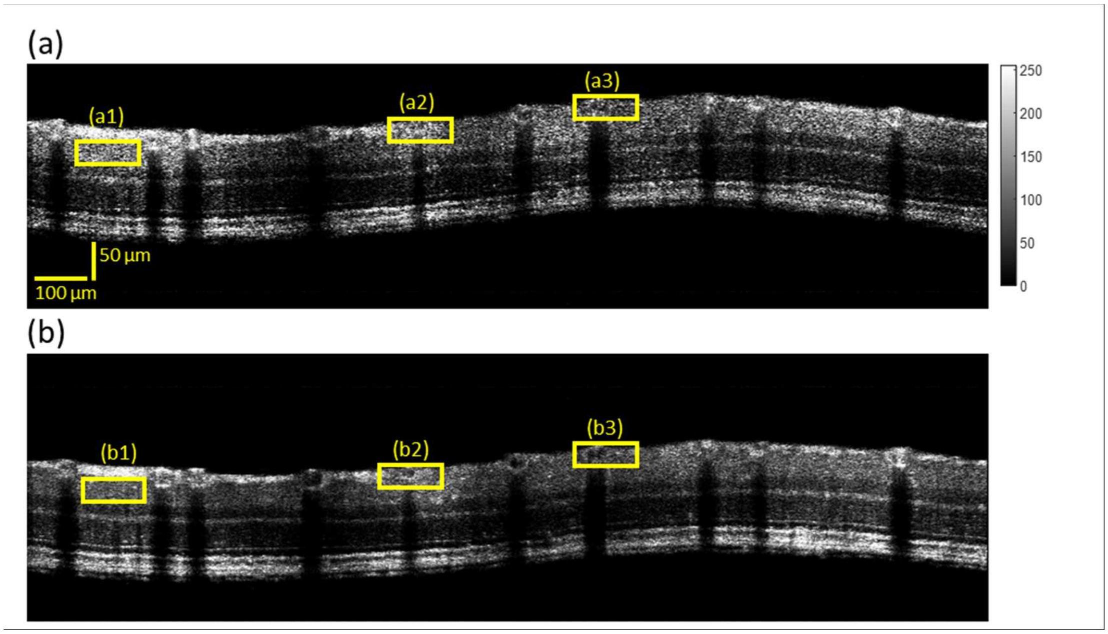

Figure 2.4. Speckle reduction test in mouse retina using modulated circular scan. (a) Reference circular B-scan image. Three ROIs from IPL and two vessels are highlighted by a1, a2, and a3, respectively. The size of each ROI is 140 µm (lateral) × 20 µm (axial); (b) The corresponding srB-scan image. The same three ROIs are highlighted by b1, b2, and b3. CNR and ENL values are calculated from all the selected ROIs. All images are plotted with identical color bar.

Fig. 2.4 shows the speckle reduction results in a mouse retina using circular scan. Figs. 2.4a and 2.4b are the reference B-scan and srB-scan images, respectively. Again, the srB-scan image improved the overall image quality with better differentiated fine anatomical features. We also selected six ROIs from IPL (highlighted by a1 and b1) and retinal blood vessels (RBV, highlighted by a2, b2, a3, and b3, respectively) for quantitative evaluation.

Scan Type	ROI	CNR (dB) Ref. B-scan	CNR (dB) srB-scan	ENL Ref. B-scan	ENL srB-scan
Raster	IPL	2.03	4.38	3.94	12.21
Raster	ONL	1.63	3.47	3.38	8.56
Raster	ORL	1.83	3.15	2.76	5.07
Circular	IPL	2.32	4.16	4.74	12.74
Circular	Vessel 1	1.63	3.53	3.36	8.6
Circular	Vessel 2	2.00	3.11	6.11	9.97

Table 2.1. Image quality metric values from the ROIs in the mouse retina shown in Figs. 2.3 & 2.4.

Table 2.1 compares CNR and ENL values from the selected ROIs in both raster and circular scans. In each scan mode, we see increased metric values from the ROIs in the srB-scan images. For raster scans, the ROIs in the IPL, ONL, and ORL show 2.35 dB, 1.84 dB, and 1.32 dB respective improvements in CNR, and 3.1, 2.53, and 1.84 times respective improvements in ENL. For circular scans, the ROIs in the IPL and two vessels how 1.84 dB, 1.90 dB, and 1.11 dB respective improvement in CNR, and 2.69, 2.56, and 1.63 times respective improvements in ENL. CNR and ENL improvements for the ORL in the raster scan and second vessel in the circular scan are slightly lower than other improvements. This is because some of the image background is unavoidably included in the ROI, artificially contributing low pixel intensities to μ_i in the metrics.

2.5.3 Speckle reduction in the human retina

We accomplished speckle reduction in the human retina using both the laboratorial prototype [45] and a clinical vis-OCT system. Unlike mouse imaging, in which retinal motion can be minimized and images can be acquired over an extended period, human imaging usually suffers from severe retinal motions and image acquisition needs to complete within few seconds. For vis-OCT, retinal motion can be much stronger as described in the introduction.

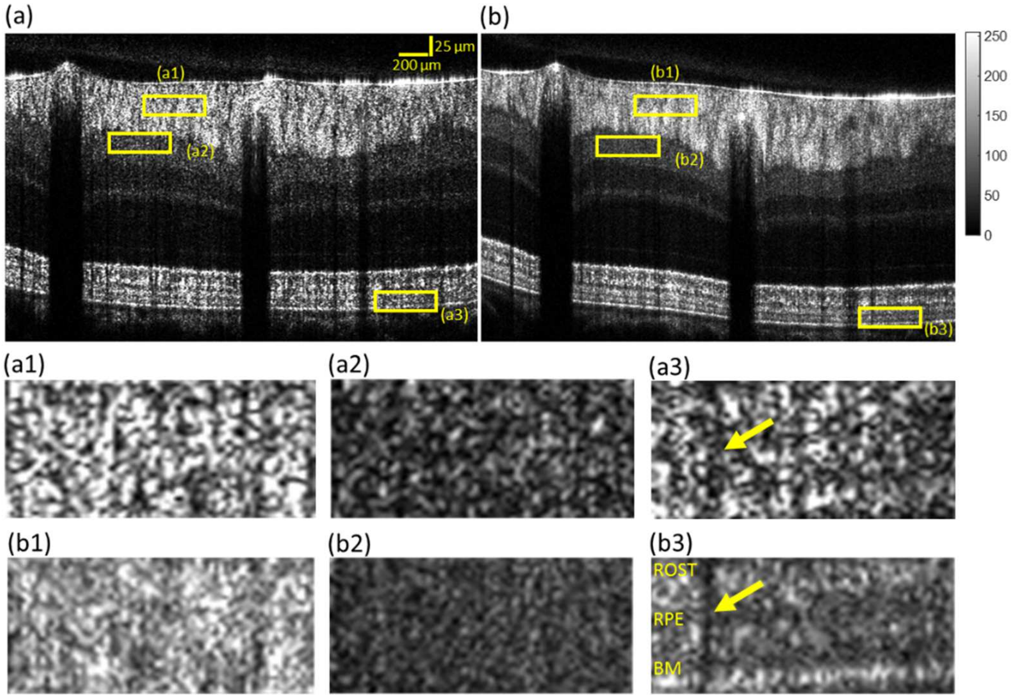

Figure 2.5. Speckle reduction test in human retina using modulated raster scan. (a) Reference raster B-scan image. Three ROIs from NFL, GCL, and ORL are highlighted by a1, a2, and a3, respectively. The size of each ROI is 430 μm (lateral) × 23 μm (axial); (b) The corresponding srB-scan image. The same three ROIs are highlighted by b1, b2, and b3. (a1), (a2), and (a3) are the magnified views of the three highlighted ROIs in panel a. (b1), (b2), and (b3) are the magnified views of the three

highlighted ROIs in panel b. CNR and ENL values are calculated from all the selected ROIs. The bottom three anatomical layers ROST, RPE, and BM are highlighted in panel b3. The arrows in a3 and b3 highlight the same blood vessel shadow. All images are plotted with identical color bar.

Fig. 2.5 shows the speckle reduction results using raster scan in a human retina (22 year old male volunteer). Figs. 2.5a and 2.5b are reference B-scan and srB-scan images superior to the optic disk, respectively. The sr-Bscan is smoother and less grainy in appearance than the reference B-scan, increasing visibility of the retinal layers. Improved image quality here is consistent with that in the mouse retina (Fig. 2.3b). We selected six ROIs from the nerve fiber layer (NFL, highlighted by a1 and b1), ganglion cell layer (GCL, highlighted by a2 and b2), and outer retina layers (ORL, highlighted by a3 and b3) to quantify quality improvement. Figs. 2.5a1-2.5a3 and Figs. 2.5b1-2.5b3 show the magnified views of the six selected ROIs and Table 2.2 shows the quantitative comparisons of CNR and ENL values from these ROIs. Of particular note is increased clarity in ORL in the srB-scan (Fig. 2.5b3). Unlike the reference B-scan (Fig. 2.5a3), the shape and boundaries of the rod outer segment tips (ROST), RPE, and BM become clearly discernable from one another. The thickness of BM is measured as ~ 3 μm and is resolved in the whole image without blur or distortion. The average measured thickness of BM in the human eye is ~ 2-5 μm [50], which is consistent with our measurement. The distinct separation between the BM and the RPE shown in Fig. 2.5a3 may open up new window to investigate macular degeneration, where initial pathological alterations are hypothesized to start from BM [50, 51]. Lastly, we note a shadow caused by a small blood vessel as highlighted by the arrows in both the reference B-scan (Fig. 2.5a3) and srB-scan (Fig. 2.5b3) image in ORL. It is measured as 2 pixels laterally, or ~

14 μm in width. This feature is better resolved in the srB-scan image, indicating that lateral resolution has been well-preserved after speckle reduction.

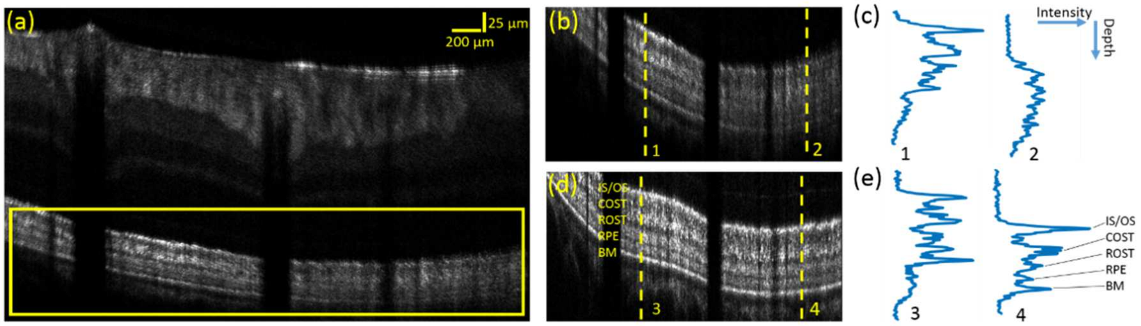

Figure 2.6. Comparing directly averaged B-scan with srB-scan images from human retina. (a) Image scan from the same location as shown in Fig. 2.5b after averaging 8 B-scans; (b) Magnified view of the outer retina region as highlighted in panel a; (c) Two A-lines from the positions highlighted by 1 and 2 in panel b; (d) Magnified view of the same outer retina region from the srB-scan shown in Fig. 2.5b. Five anatomical layers are labeled; (e) Two A-lines from the positions highlighted by 3 and 4 in panel d. All plotted A-lines are averaged three times laterally to reduce variation. All images are plotted on the same contrast scale as used in Figure 5.

Repetitive B-scan averaging is not trivial due to retinal motion, which often leads to image blurring even after registration. We overcame this challenge and show that our speckle reduction method is robust against retinal motion in Fig. 2.6. We acquired 8 repeated raster B-scans (each containing 1024 A-lines) from same anatomical location and volunteer as shown in Figs. 5a and 5b. All the B-scans were axially and laterally registered using an FFT-based cross-correlation algorithm [52]. The averaged B-scan image (Fig. 2.6a) shows blurred anatomical layers in both the inner retina and outer retina due to motion. Fig. 2.6b shows a magnified view of the region highlighted by the box in Fig. 2.6a. Two A-lines from the locations highlighted by lines 1 and 2 in Fig. 2.6b are shown in Fig. 2.6c. A-line 1 reveals five anatomical layers in the outer retina, notably with reduced contrast near the RPE. A-line 2 fails to resolve any anatomical features. Since vis-OCT offers and axial resolution of near 1 µm, small misalignments in B-scan averaging may lead to much severer blurring. The image quality shown in Fig. 2.6a is representative of most averaged B-scan images acquired by vis-OCT using similar scan parameters. Fig. 2.6d shows a magnified view of the same anatomical position from an srB-scan image, where all anatomical layers are clearly resolved across the whole image. The same A-line locations from Fig. 2.6b are highlighted in Fig. 2.6d (by 3 and 4). Fig. 2.6e shows A-line 3 and A-line 4, confirming that all outer retinal layers are well resolved despite retinal motion.

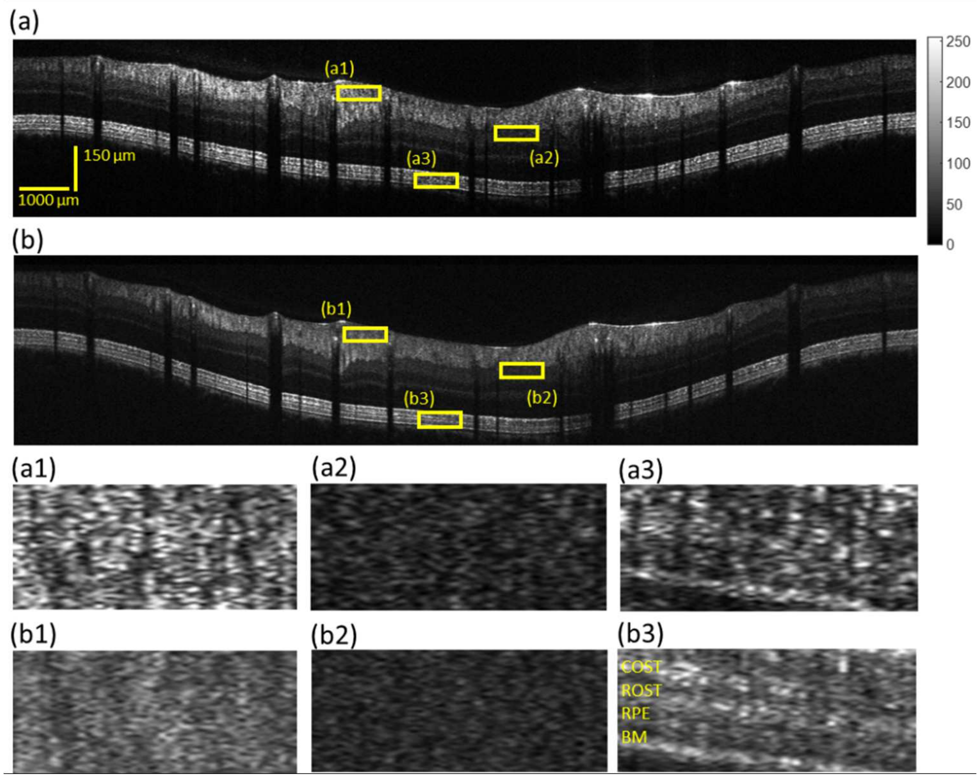

Figure 2.7. Speckle reduction test in human retina using modulated circular scan. (a) Reference circular B-scan image. Three ROIs from NFL, GCL, and ORL are highlighted by a1, a2, and a3, respectively. The size of each ROI is 900 µm (lateral) × 40 µm (axial); (b) The corresponding srB-scan image. The same three ROIs are highlighted by b1, b2, and b3. (a1), (a2), and (a3) are the magnified views of the three highlighted ROIs in panel a. (b1), (b2), and (b3) are the magnified views of the three highlighted ROIs in panel b. CNR and ENL values are calculated from all the selected ROIs. The bottom four anatomical layers COST (cone outer segment tips), ROST, RPE, and BM are highlighted in panel b3. All images are plotted with identical color bar.

We also demonstrate speckle reduction in circular scan in the human retina (Fig. 2.7). Figs. 2.7a and 2.7b show a reference B-scan image and an srB-scan image, acquired at the same anatomical location, respectively. We selected six ROIs from the same locations as in Fig. 2.5, including the NFL (highlighted by a1 and b1), GCL (highlighted by a2 and b2), and ORL (highlighted by a3 and b3) to quantify quality improvement. Figs. 2.7a1-2.7a3 and Figs. 2.7b1-2.7b3 show magnified views of the six selected ROIs and Table 2.2 shows the quantitative comparisons of the CNR and ENL values from these ROIs. Similar to the ORL in the raster srB-scan (Fig. 2.6b3), the ORL in the circular srB-scan (Fig. 2.7b3) shows distinct separation between BM, RPE, and ROST. In the reference B-scan image (Fig. 2.7a3), however, boundaries of these anatomical layers are not easily differentiated due to speckles. To the best of our knowledge, this is the first demonstration of speckle-reduced imaging in a circular pattern using localized scan modulation in the human retina.

Scan Type	**ROI**	**CNR (dB) Ref. B-scan**	**CNR (db) srB-scan**	**ENL Ref. B-scan**	**ENL srB-scan**
Raster	NFL	2.39	4.64	4.19	12.01
Raster	GCL	2.31	4.31	5.92	16.12
Raster	ORL	1.90	3.76	3.76	9.47
Circular	NFL	2.85	4.93	6.15	17.03
Circular	GCL	1.99	3.91	10.50	22.13
Circular	ORL	1.76	3.40	4.52	8.20

Table 2.2. Image quality metric values from the ROIs in the human retina shown in Figs. 2.5 & 2.7.

Table 2.2 compares the CNR and ENL values from the selected ROIs in the human retina for both raster and circular scans. In each instance, we see increased metric values in the srB-scan ROIs. Raster scans show an improvement in CNR of 2.25 dB, 2.00 dB, and 1.86 dB, in the NFL, GCL, and ORL, respectively. Corresponding ENL improvements are 2.87, 2.72, and 2.52 times. Circular scans show an improvement in CNR of 2.08 dB, 1.92 dB, and 1.64 dB, in the NFL, GCL, and ORL, respectively. Here, corresponding ENL improvements are 2.77, 2.11, and 1.81 times. Again, we attribute the slightly lower metric value increases in the ORL to the unavoidable inclusion of image background in the ROI, artificially contributing low pixel intensities to μ_i in the metrics.

2.5.3 Speckle Reduction in Clinical Environment

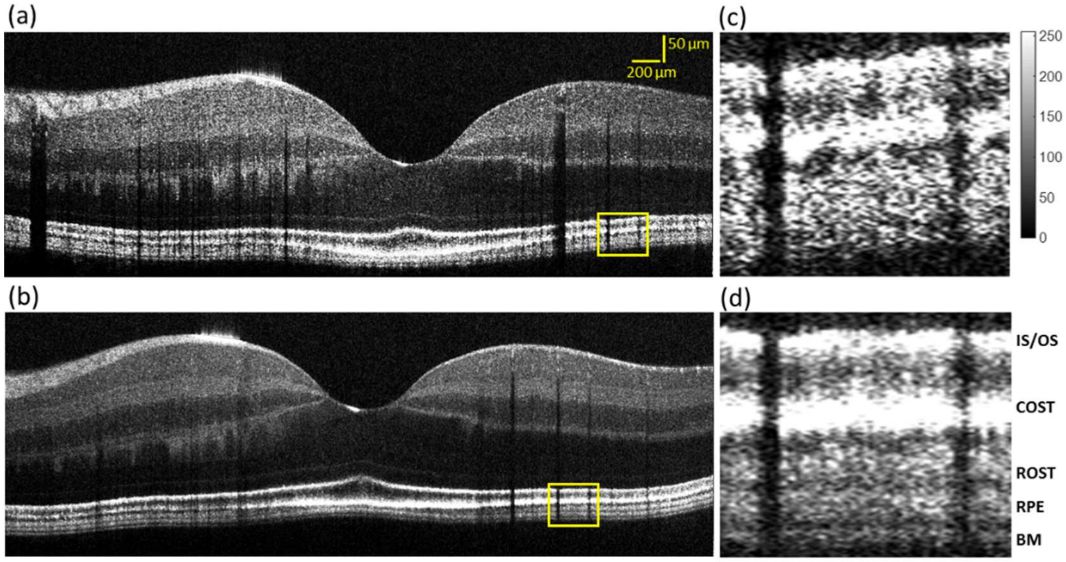

Figure 2.8. Speckle reduction test in human retina in clinical environment using modulated raster scan. (a) Reference raster B-scan image; (b) The corresponding srB-scan image; (c) Magnified view of the region highlighted in panel a; (d) Magnified view of the region highlighted in panel b. The five anatomical layers: IS/OS, COST, ROST, RPE, and BM are labeled. All images are plotted with identical color bar.

A clinical photographer without technical knowledge of the scanning protocol independently verified speckle reduction in the human retina using a commercial vis-OCT system. The photographer acquired images using the same procedure as acquiring normal raster scan images and received no additional training. Quality improvement in the clinical speckle-reduced images were comparable to the lab tests (Section 2.5.3). Figs. 8a and 8b show a reference B-scan and a srB-Scan of the macula from a 37-year old female volunteer. In the reference B-scan image, speckle particularly distorts the ORL as shown in Fig. 2.8c, preventing the delineation of fine anatomical structures, such as the RPE and BM. As a comparison, all five outer retinal layers, including the RPE and BM, are clearly resolved in the magnified srB-scan image as shown in Fig. 2.8d. Quantitatively, the improvements in CNR and ENL from similar ROIs are comparable with what we achieved in lab tests.

2.6 DISCUSSION

This study implemented, calibrated, and tested *in vivo* a scanning modulation technique for the reduction of speckle in vis-OCT retinal images. We addressed unique engineering constraints of vis-OCT, including slower image acquisition, intrinsically reduced SNR, and need to preserve structurally localized, high-detail retinal information. These constraints contrast with NIR OCT, where high SNR can be achieved at faster imaging speeds [5], B-scan averaging is more feasible, and lower resolutions are less affected by small image blurring. In our human imaging tests, where motions were high, B-scan averaging in vis-OCT proved unreliable for producing high quality images at an A-line rate of 25 kHz. Our technique for rectangular modulation of the scanning beam reliably produced speckle-reduced images in live mouse and human retinas without image blurring.

The ultimate target of vis-OCT retinal imaging is in the clinic, where increased resolution and spectroscopic analysis can improve the study and diagnosis of retinal diseases [9]. Therefore, a primary design constraint for our speckle-reduction technique was usability by a clinical photographer in clinical environment, where advanced vis-OCT engineering skills are unavailable. It is unreasonable to expect a clinical photographer to make optical adjustments to the system or troubleshoot technical issues that arise. Our technique was implemented in a clinical vis-OCT system at NYU Langone Medical Center simply via a software update. No additional optical calibrations were made to the clinical system and no changes were made to the photographers' imaging protocol. Critically, the photographers achieved comparable image quality (Figure 8) to experts in a controlled lab environment. Specifically, clinical images showed delineation of RPE and BM (Figures 8b and 8d). Micrometer-scale basal linear and basal laminar deposits between RPE and BM are thought to be early indicators of macular degeneration, a leading cause of blindness among older adults [51]. A future study in which these morphological changes are observed *in vivo* in the clinic may open a new window for the diagnosis and managing of this disease. Such capabilities have been previously unavailable in clinical NIR OCT systems due to reduced axial resolution. Presently, NIR OCT is limited to imaging larger scale drusen [51], which are developed only at a more advanced stage of macular degeneration.

Szkulmowski et al. performed averaging of offset A-lines in NIR OCT using a resonant scanner [39]. One hardware challenge expressed in this study was fringe washout. In addition to adding hardware complications to the system, the resonant scanner is continuously moving during a single camera exposure. The axial component of the scanner velocity imparts Doppler shifts to the interference fringe, thereby decaying image SNR [53]. To overcome this challenge, Szkulmowski et al. suggested minimizing camera exposure time (demonstrated at 5 μs) to reduce the effects of fringe washout. Such reduction of camera exposure time would severely compromise image quality in vis-OCT, which typically requires camera exposures ≥ 40 μs to achieve sufficiently high SNR in the human retina. Our scanning technique does not introduce additional fringe washout, as the scanning beam moves in discrete steps and is static during each camera exposure. Szkulmowski et al. experienced ~ 6 dB loss to pSNR [39] in scan-optimized images at an exposure time of 20 μs, which they attribute to fringe washout. We did not experience any pSNR drops in our scan-optimized images at an exposure time of 40 μs. Although our discrete scanning trajectory is optimized for vis-OCT, it is expected to provide superior image quality in all OCT systems with higher exposure times when using the same sampling parameters as a resonance mirror-based technique.

Our scanning technique also addresses the trajectory limits of a single resonant mirror shown in Szkulmowski et al. Using discrete, software-based control of XY galvanometer scanners, we enable multiple modulation waveforms across multiple coordinate systems (e.g. Cartesian and polar). There is promise for applying circular scan modulation for circumpapillary retinal oximetry, where speckle in blood may disrupt true spectroscopic signal. The velocity of blood (e.g. ~ 0.014 μm/μs for a 100 μm diameter human retinal artery [54]) is not high enough to completely uncorrelate the local scattering structure of erythrocytes during consecutive A-lines (period of $40\mu s$). Therefore, A-line averaging across a regular circular scan is not perfectly efficient for reducing the effects of speckle. By scanning a larger volume, our modulated circular scan is expected acquire more uncorrelated speckle patterns in blood using the same number of A-lines as a regular scan. Furthermore, the modulated scan pattern is not expected to disrupt the SNR of the blood signal since it does not induce additional fringe washout.

Next, by selecting a rectangular waveform, we (1) best preserve lateral resolution along the B-scan axis and (2) take full advantage of the space available along the orthogonal axis for speckle pattern decorrelation. In comparison, a resonant scanner can only oscillate along a single axis. Furthermore, the resonant scanner uses a sinusoidal waveform, in which each mirror deflection along the orthogonal axis also carries a component along the B-scan axis. In this case, averaging consecutive A-lines will decrease lateral resolution along the B-scan axis. Additionally, the sinusoidal trajectory makes orthogonal step size, d, nonlinear across each scan of the orthogonal axis. Our findings suggest that image quality is optimized when d is approximately equal to the focused spot diameter along the orthogonal axis. Precise optimization is not possible with a nonlinear trajectory. Szkulmowski et al. partially overcame this by only acquiring A-lines along the pseudo-linear region of each sinusoidal period. However, this is still less efficient that scanning with a rectangular wave, in which all space along the orthogonal axis is linear and can be fully utilized.

Acquisition of A-lines along the orthogonal axis increases imaging time by a factor of $n = 8$. This limits the total number of srB-scans per acquisition to 16 for an imaging time of ~ 5 s. Naturally, 16 raster srB-scans are not feasible to reconstruct a high detail *en face* image of the human retina. A potential solution is to decompose each srB-scan with $n = 8$ into 8 regular B-scans along the orthogonal axis, each of 1024 A-lines. If the spacing between each srB-scan is made to be d, then we can decompose 16 srB-scans into 128 equidistant B-scans. By reducing the number of srA-lines per srB-scan to 4096 at $n = 8$, we can decompose the full raster scan into 512 A-lines x 256 B-scans, and so on. Since each decomposed B-scan originates from the rectangular wave scan pattern, the user may view regular B-scans or srB-scans at a location of interest in the *en face* image. Rather than choosing between a high quality *en face* image or high quality B-scans, the user may adjust scanning parameters to acquire both simultaneously.

2.7 CONCLUSION

We showed that our orthogonal modulation protocol significantly reduced speckle for both raster and circular scans in vis-OCT without additional hardware. This protocol was robust against retinal motions. Furthermore, we showed that speckle-reduced vis-OCT imaging does not require additional training for a clinical photographer to operate, allowing smooth clinical translation. We designed this orthogonal modulation protocol to be compatible with arbitrary scanning trajectories and demonstrated such capability in circular scans for the first time.

In the mouse retinas, we showed that up to a 2.35-dB (116%) improvement in CNR and 3.1-fold increase in ENL can be achieved. We recognized that an anesthetized and stabilized mouse retina had negligible motion, allowing for simple B-scan averaging, and further conducted human retinal imaging. Consistently improved image qualities after speckle reduction are shown in human retinas using both an experimental and a clinical vis-OCT system and provide comparable results. Here, we showed that up to a 2.25-dB (94%) improvement in CNR and 2.87-fold increase in ENL can be achieved. We also showed that reducing speckle via direct B-scan averaging is not as reliable for preserving the fine features due to retinal motion. Our speckle-reduction method offered a local sampling rate of 3,125 Hz (Section 2.4), which is well beyond the motion frequency.

2.8 SUBLAYER ANALYSIS OF HUMAN RETINAL INNER PLEXIFORM LAYER

We guide the reader to a recent study by Ghassabi et. al [15] that uses the speckle-reduction methods outlined in Chapter 2 to visualize the micrometer-scale sublayers of the inner plexiform layer (IPL). In humans, the IPL is a well-organized laminar structure containing synaptic connections between axons of bipolar cells and axons of ganglion cells. In glaucoma, increased pressure in the eye leads to optic nerve damage and ganglion cell loss. Ganglion cell damage may be visible in the synaptic connections of the IPL before ganglion cell or nerve fiber layer dropout. Increased depth resolution, scattering contrasts, and motion resistive speckle reduction in vis-OCT offer the potential to observe this for the first time. Ghassabi et. al used vis-OCT to image nine healthy and five glaucomatous subjects and measure IPL sublayers, which were divided into three sublayers. They found statistically significant IPL thinning in glaucomatous eyes as compared with healthy eyes. Furthermore, they found thinning was associated with the central of the three IPL sublayers, suggesting connection specific losses. This is first report of such findings in the living human retina.

Chapter 3

Spectrally dependent roll-off in visible-light optical coherence tomography

3.1 MOTIVATION

Vis-OCT reconstructs images by Fourier transform of interference patterns detected by a spectrometer. The finite size of the spectrometer's sensing components acts as a low-pass filter for spatial frequencies in the interference. This low pass filter is evident as a decay in image signal with increased depth. The decay rate can change for different wavelengths, artificially inducing spectroscopic features in the image that do not originate from the sample itself.

3.2 SUMMARY

Recent development of visible-light optical coherence tomography (vis-OCT) has introduced new applications for noninvasive spectroscopic imaging. However, the measured spectra may be altered by spectrally dependent roll-off (SDR). We formulated a mathematical model for SDR that accounted for nonuniform wavenumber spacing, optical aberrations, and misalignments in the spectrometer. We simulated SDR based on this model and found strong agreement with measurements from a vis-OCT system. We verified that SDR altered spectroscopic measurements of fully oxygenated blood. We corrected these alterations by normalizing each spectrally dependent A-line by the measured SDR of the spectrometer. Our investigations of SDR are critical for informing OCT spectrometer design, alignment, and spectroscopic measurements.

3.3 INTRODUCTION

Optical coherence tomography (OCT) [1] uses low-coherence interferometry to resolve backscattered photons in biological tissue. Such capability enables noninvasive cross-sectional imaging at microscopic resolution. This has led to valuable clinical applications, particularly in the retina [2]. Visible-light OCT (vis-OCT) [3] is an emerging OCT technology that uses the visible-light wavelength range to achieve ultrahigh axial resolution and perform spectroscopic analysis of tissue, such as measuring retinal oxygen saturation (sO_2) [4]. Presently, vis-OCT builds on spectral-domain OCT (SD-OCT) technology to obtain structural and spectral information. SD-OCT uses a spectrometer to spatially disperse the interfered beam across multiple wavelengths and focus them onto a 1D array camera. A Fourier transform (FT) of interference across the full spectrum enables reconstruction of ultrahigh-resolution image. Applying the Short-Time Fourier transform (STFT) across a series of sub-band windows enables extraction of depth-resolved spectral information at an axial resolution trade-off.

Accurate spectral measurements must account for spectral alterations not associated with light-tissue interaction. One potential source of spectral alteration is OCT signal roll-off [5], which is caused by low-pass filtering by the finite sampling elements of the spectrometer. Decay of the structural image with depth, which we refer to as full-spectrum roll-off (FSR), has been thoroughly investigated and modeled [6-9]. However, the spectral dependence of signal roll-off, referred to as spectrally dependent roll-off (SDR), has been observed but is not well characterized [10-12]. A quantitative analysis of SDR is critical for spectroscopic OCT.

We investigate the origins of SDR and its impacts on spectroscopic vis-OCT. For the first time, we establish an analytical model for SDR. Next, we introduce simulations to test our model using vis-OCT reconstruction software. Then, we measure FSR and SDR of our vis-OCT system. Finally, we investigate the influence of SDR on measured spectra of fully oxygenated blood and correct for the known SDR. These investigations build the foundation for understanding spectroscopic OCT.

3.4 THEORY

In SD-OCT, interference can be considered a function of wavenumber $k = 2\pi/\lambda$, where λ is wavelength, since the depth-resolved OCT signal is the Fourier transform of the k domain interference fringe. The interference fringe can be expressed as

$$S(k) = \int_0^{z_{max}} 2\sqrt{S_{samp}(k,z)S_{ref}(k)}\cos(kz)dz, \tag{3.1}$$

where z is the round-trip depth of each collected photon; $S_{samp}(k,z)$ is the power spectrum of light back scattered at depth z; $S_{ref}(k)$ is the reference arm power spectrum; z_{max} is the maximum imaging depth. We neglect the DC and autocorrelation terms in Eq. 3.1 since they are removed after post-processing [13]. In SD-OCT, a grating-based spectrometer disperses $S(k)$ across a 1-D detector array. The array contains pixels of width Δx indexed $j = 1, 2, \dots, N$, where N is number of pixels. Dispersion of the spectrum in space closely follows the grating equation [7]. We use coordinate x to denote the spatial position of the dispersed interference spectrum, $S(x)$. $S(x)$ starts at 0 and ends at $N\Delta x$ (neglecting gap between pixels). The spectrometer's impulse response is approximated by convolution of the two finite sampling elements

$$H(x,j) = G(x,j) \otimes R(x,j). \tag{3.2}$$

The first convolution term represents the spatial distribution of the Gaussian beam with respect to the center of each pixel as

$$G(x,j) = \frac{2\sqrt{ln2}}{a_j\sqrt{\pi}} exp\left(-4ln2\left(\frac{x-(j-1)\Delta x-\frac{\Delta x}{2}}{a_j}\right)^2\right), \tag{3.3}$$

where $a_j$is the full-width-at-half-maximum (FWHM) spot size of the beam at pixel j. Note that a_j is assumed constant at a single pixel, but may vary across different pixels due to spectrometer optics aberrations or misalignments. The second term is the rectangular shape of each pixel's integration surface,

$$R(x,j) = \begin{cases} 1, (j-1)\Delta x - \frac{\Delta x}{2} \leq x \leq (j-1)\Delta x + \frac{\Delta x}{2} \\ 0, elsewhere \end{cases}. \tag{3.4}$$

The fringe is measured by integrating $S(x)$ about $H(x,j)$ for each pixel at index j as

$$S[j] = \sum_{j=1}^{N} \int_0^{N\Delta x} S(x)H(x,j)dx\,. \tag{3.5}$$

Eq. 3.5 represents sampling the convolution of the spectrometer's finite elements at each pixel index. This can be written as

$$S[j] = [S(x) \otimes G(x,j) \otimes R(x,j)]\Omega(x,j), \tag{3.6}$$

where $\Omega(x,j)$ is Dirac's comb of period Δx. Following interpolation of $S[j]$ to linear k domain and taking the discrete Fourier transform (DFT), the 1D depth-resolved OCT signal (A-line) is expressed as

$$A[i] = \mathrm{D}FT\{S[j]\} = \big[S[i]G[i]R[i]\big] \otimes \Omega[i] = S[i]G[i]R[i], \tag{3.7}$$

where i is the index of each sampled imaging depth, $S[i]$, $G[i]$, $R[i]$, and $\Omega[i]$ are the DFT's of the fringe, Gaussian beam, Rectangle, and Dirac's comb functions, respectively. Convolution with $\Omega[i]$ is omitted at the end, as this term represents imaging depths outside of the Nyquist-limited imaging range. Only $S[i]$ contains depth information from the sample. Thus, $S[i]$ is modulated with depth by the term $G[i]R[i]$, which is the FSR. The normalized FSR is

$$F[i] = exp\left(-\frac{(a_{eff}i)^2}{4ln2}\right) sinc(\Delta x i), \tag{3.8}$$

which attenuates $S[i]$ with depth. a_j is simplified to an effective constant term, $a_{eff} = \sqrt{\frac{N}{\sum_{j=1}^{N}\frac{1}{a_j^2}}}$, using first terms of the Taylor series expansion of the Gaussian function [7].

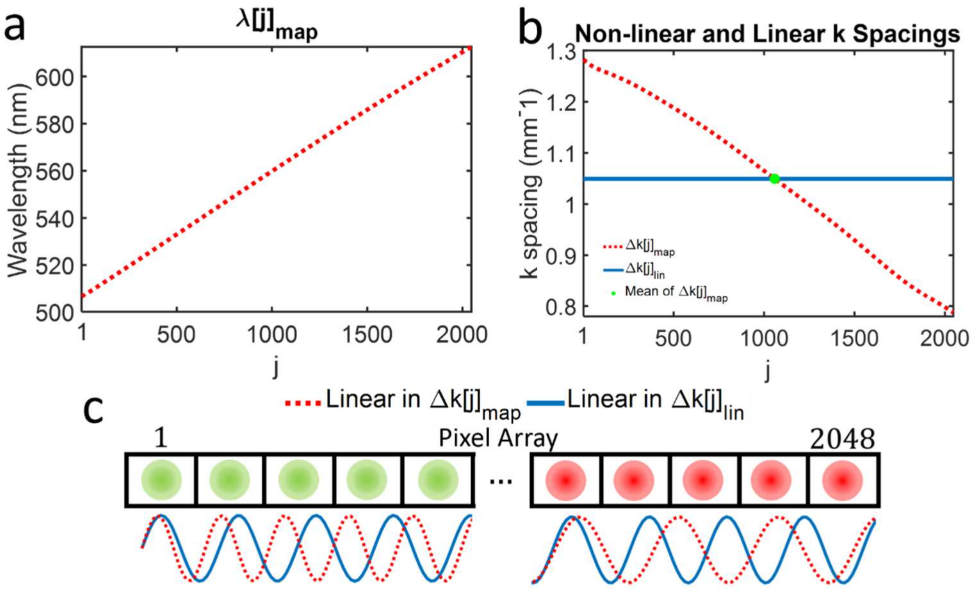

Figure. 3.1. (a) Wavelength-to-pixel mapping ($\lambda[j]_{map}$) in vis-OCT spectrometer; (b) k spacing calculated from $\lambda[j]_{map}$ (red dashed line) in (a) and linear k spacing (solid blue line) for same wavelength range. Green dot indicates the mean value of $\Delta k[j]_{map}$ coinciding with a constant $k[j]_{lin}$; (c) Illustration of spectrometer pixel array (rectangles) and focal spots (green dots, shorter wavelengths [pixels 1-5]; red dots, longer wavelength [pixels 2044-2048]). Sine waves below array plotted as a function of $\Delta k[j]_{map}$ (red dashed line) and $k[j]_{lin}$ (solid blue line).

We investigated the spectral dependence of spectrometer sampling. In practice, x is highly linear in the λ domain according to the grating equation [7, 9]. However, $S(k)$ in Eq. 3.1 must be linearized in the k domain, creating a mismatch with spectrometer sampling. Fig. 3.1a shows wavelength-to-pixel mapping, $\lambda[j]_{map}$, for a vis-OCT spectrometer (Blizzard SR, Opticent Health). The spectrometer covers λ_1=506 nm to λ_2=613 nm, corresponding to and has N = 2048 pixels. The spacing between the centers of adjacent pixels of the spectrometer in the k domain, $\Delta k[j]_{map}$, is shown in Fig. 3.1b (red dashed line). The k spacing between pixels is not constant and monotonically decreases with pixel index. In contrast, linear k domain mapping on an N-pixel array with the same spectral range,

$$\lambda[j]_{k\_lin} = \frac{\left(\frac{2\pi}{\lambda_2} - \frac{2\pi}{\lambda_1}\right)}{N} j, \tag{3.9}$$

has constant k spacing of $\Delta k[j]_{lin} = \left|\frac{\left(\frac{2\pi}{\lambda_2} - \frac{2\pi}{\lambda_1}\right)}{N}\right|$. However, the means of $\Delta k[j]_{map}$ and $\Delta k[j]_{lin}$ are the same (green dot in Fig. 3.1b). We illustrate sampling of $S(x)$ in Fig. 3.1c. The top panel in Fig. 3.1c illustrates a 1D-spectrometer pixel array (rectangles numbered from 1 to 2048) with optical focal spots (green and red spots). The solid blue sine wave (below pixel array) represents a hypothetical $S(x)$ with one frequency dispersed linearly with $\Delta k[j]_{lin}$, while the red dashed sine wave shows the same function dispersed linearly with $\Delta k[j]_{map}$. The linear-in-k $S(x)$ is of uniform frequency across the whole array. However, the non-linear-in-k $S(x)$ is a higher frequency than the linear-in-k version at the beginning of the array (green spots, shorter wavelengths), following the sparser-than-mean k spacing. Likewise, at the end of the array (red spots, longer wavelengths), the non-linear-in-k $S(x)$ is a lower frequency than the linear-in-k version, following denser-than-mean k spacing in Fig. 3.1b. Therefore, in general, an OCT spectrometer disperses $S(x)$ at higher frequencies for shorter wavelengths and at lower frequencies for longer wavelengths. An equivalent representation of this effect is to scale finite sampling elements, $G(x, j)$ and $R(x, j)$, by the k spacing of the spectrometer. Indeed, despite not changing their physical dimensions, the focal spots and pixels 'expand' and 'contract' relative to the mean k spacing. We refer to the mean-normalized version of $\Delta k[j]_{map}$ as $\Delta k^{*}[j]_{map}$.Decomposing $F[i]$ into spectrally-localized pixel range j_{start} to j_{end} (and equivalent λ_{start} to λ_{end}) yields the SDR:

$$F[i,\Delta j] = \exp\left(-\frac{\left(a_{eff}[\Delta j]\Delta k^{*}_{eff}[\Delta j]_{map} i\right)^{2}}{4ln2}\right) sinc\left(\Delta x \Delta k^{*}_{eff}[\Delta j]_{map} i\right), \tag{3.10}$$

where Δj is the STFT range j_{start} to j_{end}; $a_{eff}[\Delta j]$ is the effective spot size localized to Δj; and $\Delta k^{*}_{eff}[\Delta j]_{map}$ is the effective (by same principle as a_{eff}), mean-normalized k spacing localized to Δj. Both $a_{eff}[\Delta j]$ and $\Delta k^{*}_{eff}[\Delta j]$ are constant only across Δj. Since $a_{eff}[\Delta j]$ and $\Delta k^{*}_{eff}[\Delta j]_{map}$ vary with different Δj, different wavelengths intrinsically decay at different rates.

3.5 SIMULATION

We simulated SDR for Blizzard SR from 523 nm to 591 nm. $S(x)$ was a sine wave of varying frequencies, representing different imaging depths. We generated $S(x)$ as a function of the measured $\Delta k[j]_{map}$ and upsampled it to simulate continuous space. We simulated impulse responses of the spectrometer according to Eqs. 3.1-3.5 for a constant spot size $a_j = a_{eff}$= 8.8 μm and pixel width Δx=10 μm. We calculated $S[j]$ according to Eq. 3.5 and interpolated from linear in $k[j]_{map}$ to linear in $k[j]_{lin}$. We took DFT of the full spectrum with a Gaussian window and discrete STFT using 24 Gaussian-windows spaced equidistantly from 523 nm to 591 nm in k. Each window had the same bandwidth (FWHM) in k, corresponding to an ~13-nm bandwidth centered at 556 nm.

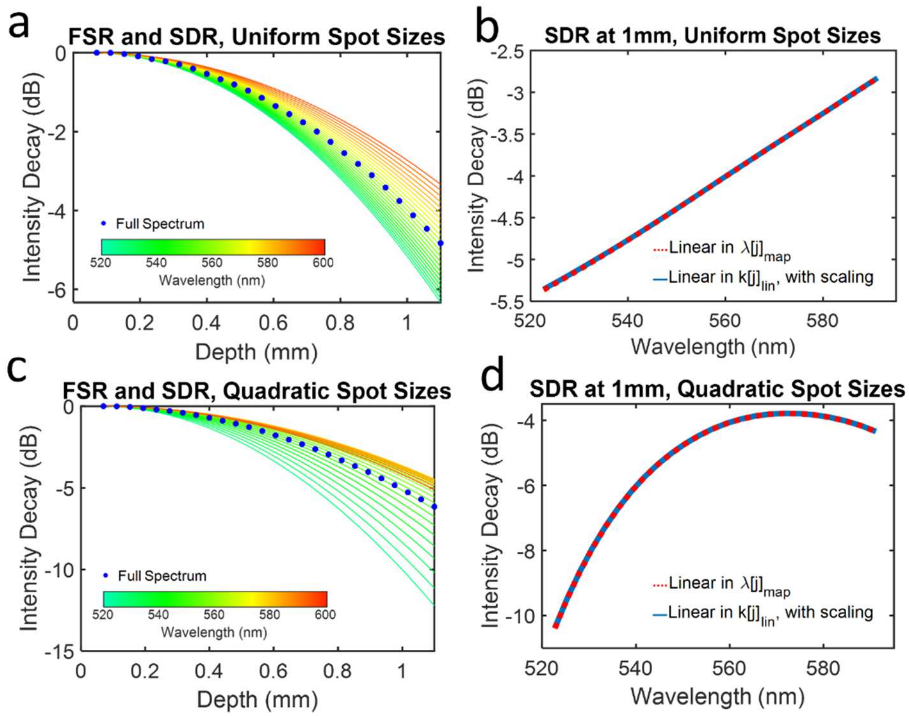

Fig. 3.2. (a) Simulated FSR (blue dots) and SDR for uniform focal spot sizes incident on pixel array. SDR wavelengths are identified by colorbar. (b) SDR (red dashed line) and equivalent simulation (solid blue line) at 1-mm depth in (a); (c) Simulated FSR (blue dots) and SDR for spot sizes varying quadratically with pixel index; (d) SDR (red dashed line) and equivalent simulation (solid blue line) at 1 mm depth in (c).

Simulated SDR for depths up to 1.1 mm are shown in Fig. 3.2a. Note that SDR is more rapid for shorter wavelengths than for longer wavelengths. Furthermore, SDR near the center of the spectrum follow the FSR (blue dots) closely. These trends are explained by the spectrometer's $\Delta k[j]_{map}$ (Fig. 3.1b). The simulated SDR at 1 mm is plotted in Fig. 3.2b (red dashed line). SDR is -5.4 dB at 523 nm and -2.8 dB at 591 nm, a 2.6-dB difference between the two sub-bands.

We verified Eq. 3.10 by generating $S(x)$ as a function of $k[j]_{lin}$ rather than $\Delta k[j]_{map}$. Then, we applied scaling factor $\Delta k^{*}[j]_{map}$. We replicated the rest of the simulation, except for the interpolation step, as previously described. Identical results to the previous simulation were achieved (plotted as solid blue line in Fig. 3.2b).

Additionally, we simulated influence of non-uniformly focused spot sizes (a_j not constant) on SDR. We simulated spherical aberration influence on SDR by varying $a[j]$ quadratically from 8.8 μm to 18.6 μm across the pixel array, with the minimum value at the central pixel of the array. The normalized roll-offs for depths up to 1.1 mm are plotted in Fig. 3.2c. Unlike in Fig. 3.2a, transition of SDR between shorter wavelengths (green) and longer wavelengths (orange) is less uniform. Shorter wavelengths decay more rapidly than longer wavelengths. Additionally, the FSR (blue dots) is biased closely towards the longer wavelength sub-bands. SDR at 1 mm depth is illustrated in Fig. 3.2d. Here, SDR is -10.4 dB at 523 nm and –4.3 dB at 591 nm, a 6.1-dB difference. Notably, SDR at 1-mm depth, shown in Fig. 3.2d (red dashed line), does not follow a perfectly quadratic shape centered at the central sub-band, as one might expect. Rather, it follows the multiplication of spectrally varying $a[j]$, with $k^*[j]_{map}$, as predicted by Eq. 3.10.

3.6 EXPERIMENTAL RESULTS

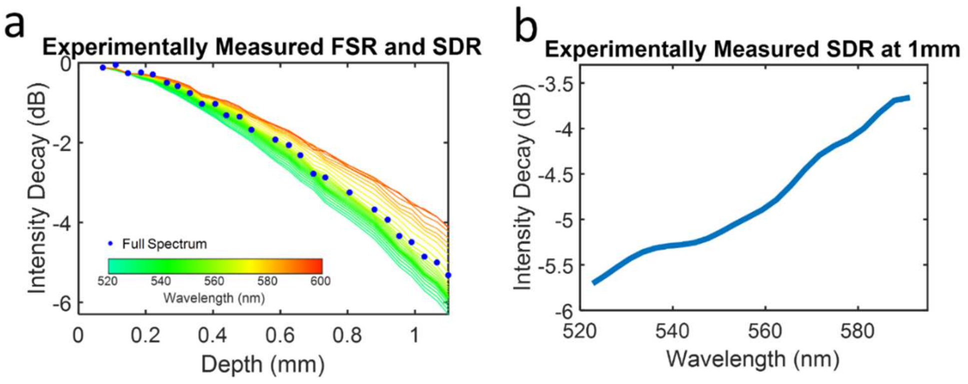

Figure 3.3. (a) Measured FSR (blue dots) and SDR from a commercial vis-OCT spectrometer. The color of each SDR curve reflects the central wavelength of its sub-band as shown by the color bar; (b) SDR at 1 mm imaging depth as a function of the central wavelength of each sub band.

We experimentally verified our simulation in the Blizzard SR spectrometer. Briefly, we aligned a mirror in the sample arm of a vis-OCT Michelson interferometer near the zero-delay position. The reference arm was tuned in ~40 μm increments to an imaging depth of 1.1 mm. For each depth, we recorded 5000 background spectra from the sample and reference arms, followed by 5000 interference fringes at 25 kHz acquisition rate. We subtracted and divided each fringe by its DC component and digitally compensated for dispersion mismatch. Following interpolation to the linear k domain, we took the DFT and discrete STFT of the interference signal for each depth position using the same bands described in the simulation. Each A-line was averaged 5000 times for each recorded fringe. Experimentally measured SDRs shown in Figs. 3a and 3b follow trend similar to our simulation for uniform spot sizes (Figs. 2a and 2b). SDR for shorter wavelengths (green) are more rapid than longer wavelengths (orange). SDR for sub-bands near the center of the full spectrum (yellow) follow the FSR (blue dots) closely. Measured SDR is -5.7 dB at 523 nm and -3.7 dB at 591 nm, showing a 2.0-dB difference. We noted that longer wavelengths decay more rapidly than the simulation for uniform spot sizes (-3.7 dB measured vs. -2.8 dB predicted at 591 nm), indicating that $a_{eff}[\Delta j]$ is larger at longer wavelengths. Potentially, a small tilt in the camera may have caused defocusing at longer wavelengths.

We investigated the influence of SDR on vis-OCT measured spectra of blood in glass tubes (100-μm inner diameter). Briefly, we oxygenated bovine blood (Sigma Aldrich) with hematocrit 47 % to > 99% sO_2 (measured with Rapidlab 248, Siemens Healthcare Diagnostics) by exposing it to a constant stream of oxygen. Then, we secured the tube in a homemade well filled with immersion oil (refractive index = 1.52) 300 µm below the oil surface. We coated the inner wall of the tube with heparin and phosphate-buffered saline to prevent blood clotting. We filled the tube with oxygenated blood and flowed it at ~0.03 mm/s to prevent clotting. An objective lens with 39-mm effective focal length (LSM03-vis, Thorlabs) focused 1.25 mW of light onto the tube. We imaged the tube using a 512 x 512 raster scan. We adjusted the reference arm to acquire images with the tube top wall positioned 0.120 mm, 0.375 mm, 0.725 mm, and 1.025 mm from the zero-delay. Before processing the fringes, we normalized by the DC spectrum and numerically compensated for dispersion mismatch. We applied STFTs to the normalized fringes to reconstruct spectrally dependent A-lines (SDA-lines). We took the natural logarithm of the SDA-lines following reference [5] to measure the hemoglobin spectrum. For each depth, we spatially averaged the spectra in the tube across 50 B-scans (~50,000 image pixels). Pixels were selected from the same location in the tube from each image to ensure a fair comparison.

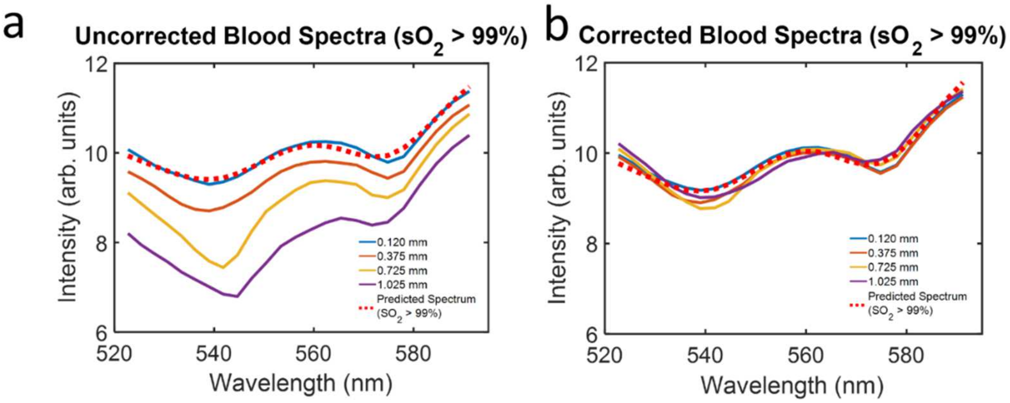

Fig. 3.4. (a) Measured spectra (solid lines) of oxygenated blood at different depths with reported spectrum of oxygenated hemoglobin (red dashed line); (b) Spectra of oxygenated blood at different depths after SDR correction.

The measured blood spectra at selected depths are plotted in Fig. 3.4a, alongside that of reported oxygenated hemoglobin [14]. The spectrum at 0.120 mm (blue solid line) closely matches the reported spectrum. However, increasing depth alters the measured spectra. Specifically, shorter wavelengths decay more rapidly than longer ones, consistent with Figs. 3.2 & 3.3. We corrected this by dividing each SDA-line by measured SDR (Fig. 3.3). The measured SDR was fitted with a 4th order polynomial to extrapolate all depths. Fig. 3.4b shows the blood spectra at different depths after SDR correction. Comparing with Fig. 3.4a, all spectra have approximately same mean intensity and closely match the reported spectrum. We quantified the impact of SDR correction by fitting each measured spectrum from Figs. 3.4a and 3.4b to the reported spectrum. We confirmed that SDR correction significantly reduced mean-squared-error of fitting at larger depths with minor influence from error propagation at shorter depths. We also note that SDR correction doesn’t increase SNR of the spectrum.

3.7 CONCLUSION

In summary, we presented an analytical model that describes SDR as a function of the nonlinear k spacing in a grating-based spectrometer and nonuniform spot sizes on the detector array. We validated our model using numerical simulation. We measured SDR from a commercial vis-OCT spectrometer and found agreement with our simulation and model. Finally, we verified the influence of SDR on vis-OCT measured spectrum of oxygenated blood. Together, these results suggest that our model and simulation can better inform spectrometer design, diagnose misalignments, or enhance spectroscopic measurements. First, predicted SDR for uniform spot sizes (Fig. 3.2a) can be a target in designs or alignments. Deviation from expected SDR can inform the nature of aberration or misalignment. This approach is superior to simply minimizing the FSR, which does not contain spectrally dependent information. In another application, one may shape the laser spectrum for higher power at shorter wavelengths to ensure SNR is comparable along all wavelengths. This can be especially useful in vis-OCT, where biological tissues are highly attenuating. Finally, since k spacing varies more rapidly with λ for shorter wavelengths than longer ones, SDR is intrinsically more severe in vis-OCT than NIR OCT, assuming similar bandwidths. Since SDR is associated with multiplication of $k^*[j]_{map}$ and spot size on the pixel array, influence of aberrations or misalignments on SDR are exaggerated in the visible-light spectral range. Therefore, careful spectrometer design and alignment is likely most critical for vis-OCT.

If zero-delay imaging is challenged, such as in human eyes due to motions [15], a correction using measured SDR must be applied. Correction is limited to depths with sufficiently high SNR. We believe that the best solution is the hardware design. A linear-in-k spectrometer [9] or a linear-in-k swept-source [13] (presently only available in NIR) will largely remove influences of SDR due to highly uniform k space sampling.

Chapter 4

Intrinsic spectrally-dependent background in visible-light optical coherence tomography

4.1 MOTIVATION

Vis-OCT reconstructs images by Fourier transform of interference patterns detected by a spectrometer. However, most vis-OCT spectrometers do not project spatial frequencies linearly across the detector array. This requires numerical resampling to linearize the interference. Image background noise changes with the resampling rate. Different wavelengths experiencing different resampling rates impose a spectroscopic bias in the image.

4.2 SUMMARY

Visible-light optical coherence tomography (vis-OCT) enabled new spectroscopic applications, such as retinal oximetry, as a result of increased optical

absorption and scattering contacts in biological tissue and improved axial resolution. Besides extracting tissue properties from back-scattered light, spectroscopic analyses must consider spectral alterations induced by image reconstruction itself. We investigated an intrinsic spectral bias in the background noise floor, which is hereby referred to as the spectrally-dependent background (SDBG). We developed an analytical model to predict the SDBG-induced bias and validated this model using numerically simulated and experimentally acquired data. We found that SDBG systemically altered the measured spectra of blood in human retinal vessels in vis-OCT, as compared to literature data. We provided solutions to quantify and compensate for SDBG in retinal oximetry. This work is particularly significant for clinical applications of vis-OCT.

4.3 INTRODUCTION

Optical coherence tomography (OCT) [1] detects back-scattered light to image biological tissue at microscopic resolutions noninvasively. In spectral-domain OCT (SD-OCT) [55], three-dimensional (3D) images are reconstructed using the Discrete Fourier transform (DFT) of a sampled interference spectrum. Visible-light OCT (vis-OCT) [9] is a rapidly evolving SD-OCT technology that operates within the visible-light wavelength range to increase axial resolution and spectroscopic tissue contrast, as compared with near-infrared OCT (NIR-OCT). These benefits enabled new spectroscopic vis-OCT applications, including oximetry [18, 21], detection of tissue ultrastructure [56], and investigating various neuropathologies [57, 58]. Spectroscopic vis-OCT computes a series of short-time Fourier

Transforms (STFT) using moving spectral windows with reduced bandwidth across the entire spectral interference fringes. Performing STFT enables the reconstruction of a series of sub-band spectral images with a reduced axial resolution.

To accurately extract tissue spectral information, it is essential to eliminate influence from the OCT image reconstruction itself. In most SD-OCTs, a grating-based spectrometer samples the interference fringe according to the grating equation and spectrometer optics [59]. It is typical for such spectrometers to sample almost linearly in the wavelength (λ) space, which is inversely proportional to the wavenumber (k) space. Since axial depth (z) is the Fourier conjugate of k, non-uniformly sampled frequencies in the k domain will result in a broadened point-spread-function in the z domain. Thus, optimal axial resolution requires the interference fringe to be interpolated linearly in k space [55, 60]. We found that linear-in-k interpolation generates spectrally-dependent background (SDBG), an intrinsic bias of the vis-OCT background noise floor that can alter spectroscopic measurements.

The prevalence of linear-in-k interpolation in SD-OCT makes the systemic nature of the SDBG highly significant towards the spectroscopic OCT research community. Various background biases have been previously reported [61-65]. For example, in polarization-sensitive OCT (PS-OCT) the noise floor may vary in different polarization channels and, therefore, comparing the polarization channels may require noise floor correction to achieve more accurate PS-OCT data [62]. Although researchers previously recognized the existence of SDBG and applied empirical corrections [63, 65], a thorough investigation of SDBG's origin, influence on spectroscopic vis-OCT, and correction techniques have yet to be conducted.

In this work, we first theoretically derive the systemic bias of SDBG caused by linear-in-k interpolation of the interference fringe. We simulate SDBG in our vis-OCT system and compare it with experimentally acquired SDBG. Then, we establish a minimum fringe upsampling rate in spectroscopic vis-OCT that removes many depth-dependences of the SDBG, increasing simplicity of SDBG correction. Finally, we investigate the influence of SDBG on vis-OCT retinal oximetry and apply an SDBG correction strategy. This work establishes important principles and consequences of widely-used data processing in spectroscopic vis-OCT and all other SD-OCTs, informing a broad range of biophotonic applications.

4.3 ORIGIN AND DERIVATION OF SDBG

4.3.1 Wavenumber dispersion in spectrometer detection

In SD-OCT, the noise-free interference fringe (neglecting the DC component) can be written as

$$S(k)_{int} = \int_0^{z_{max}} 2\sqrt{S_{samp}(k,z)S_{ref}(k)}\cos(kz)dz, \tag{4.1}$$

where z is the round trip depth of the collected back-scattered photons from the zero-delay; z_{max} is the maximum round trip imaging depth [5]; $S_{samp}(k,z)$ is the power spectrum of the back-scattered light from the depth z; and $S_{ref}(k)$ is the power spectrum of the reference arm. $S(k)_{int}$ is spatially dispersed onto a one-dimensional (1D) pixel array in the spectrometer as a function of $k(x)$ across the range from k_{start} to k_{end}, which is determined by the grating equation and spectrometer optics [59]. Here, x is the spatial coordinate along the 1D array ranging from 0 to $N\Delta x$, where N is the the total number of pixels and Δx is the width of each pixel.

The spatial dispersion of the spectrometer is represented by $\delta k = \left|\frac{dk(x)}{dx}\right|$, which we refer to as the k spacing. It is also important to consider a hypothetical uniform dispersion across the same spectral range, $\delta k_{lin} = \frac{|k_{end} - k_{start}|}{N\Delta x}$, which is constant. The dimensionless ratio, $\delta k_{rel} = \frac{\delta k}{\delta k_{lin}}$, referred to as relative k spacing, describes how the spectrometer deviates from ideal uniform k dispersion across each pixel. Indeed, a larger δk_{rel} indicates more k-space bandwidth per unit pixel Δx, while a smaller δk_{rel} indicates less k-space bandwidth per unit pixel. The interference fringe in the Eq. 4.1 sampled by the 1D pixel array (without considering spectrometer roll-off [27]) can be written as

$$S[j]_{int} = \sum_{j=1}^{N} S(x\delta k_{rel})_{int}\, \theta(x - j\Delta x), \tag{4.2}$$

where $j = 1, 2, \dots N$ is the array pixel index, and $\theta(x - j\Delta x)$ is the Dirac comb function with a period Δx. The spectrometer pixel array samples with a uniform period in x, but the fringe is a function of δk_{rel} . Such a non-uniform sampling of the k space results in a phase nonlinearity in $S[j]_{int}$ [66], which distorts $S[j]_{int}$ and reduces image axial resolution. For optimal image reconstruction, the phase of $S[j]_{int}$ must be made linear-in-k, which we will discuss in Section 4.3.2.

Quantifying δk_{rel} for a spectrometer is valuable for understanding the distortion of $S[j]_{int}$. In this work, we measured δk_{rel} digitally sampled by the spectrometer: Δk_{rel}. From here on, δk_{rel} refers to the k spacing in the continuous domain, while Δk_{rel} refers to the k spacing in the discrete domain. Briefly, we found the k distribution on the pixel array $k[j]_{map}$ using spectral calibration lamps [27, 66]. Next, we obtained the sampled δk, defined as Δk, by calculating the absolute change in $k[j]_{map}$ with j. Hence, the sampled δk_{lin} is

$$\Delta k_{lin} = \left|\frac{k[N]_{map} - k[1]_{map}}{N}\right|. \tag{4.3}$$

From this information, we obtained the sampled δk_{rel}, defined as $\Delta k_{rel} = \frac{\Delta k}{\Delta k_{lin}}$.

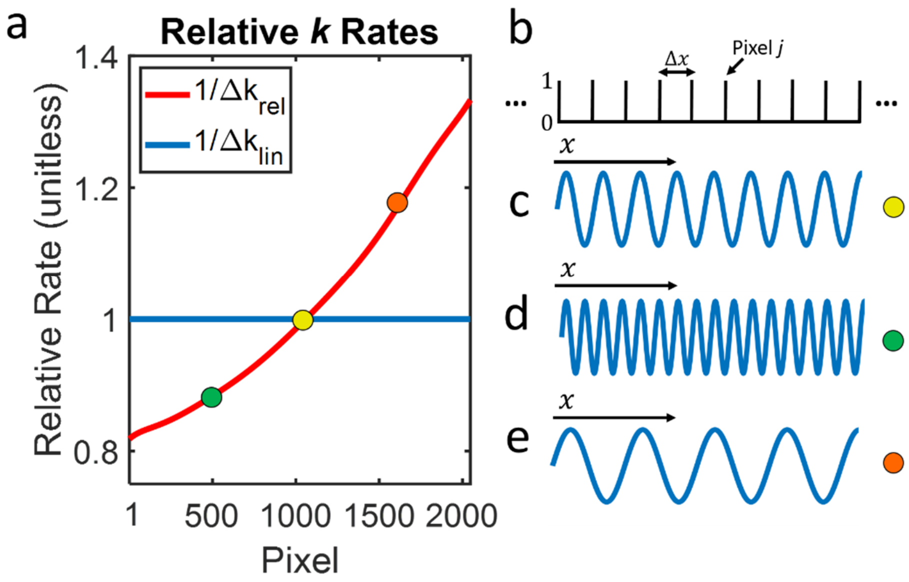

Fig. 4.7. Influence of grating dispersion on interference fringe (a) Digitized relative k rates of a spectrometer. Colored dots represent locations of pixel segments in (c-e); (b) illustration of Dirac comb sampling by pixel array with period Δx; (c) Interference fringe plotted at the location of the yellow dot in panel a; (d) Interference fringe plotted at the location of the green dot in panel a; (e) Interference fringe plotted at the location of the orange dot in panel a.

In Fig. 4.1a, we plot measured $\frac{1}{\Delta k_{rel}}$ and $\frac{1}{\Delta k_{lin}}$ as a function of pixel j for a commercial vis-OCT spectrometer (Blizzard SR, Opticent Health, Evanston, IL). Briefly, the spectrometer collimates light from a single-mode fiber output. The collimated light is diffracted by a transmission grating. The diffracted light is focused by on a 2048-pixel camera (OctoPlus, Teledyne E2V, UK) placed at the focal plane of the diffracted light. The spectral detection range is from 506 nm to 613 nm. We measured the full spectrum roll-off as -4.8 dB/mm and confirmed that aberrations at the focal plane were minimized by measuring the spectrally-dependent roll-off (SDR). [27].

From Fig. 4.1a, is evident that $\frac{1}{\Delta k_{rel}}$ is smaller for shorter wavelengths and larger for longer wavelengths. Physically, this can be considered as a compression of the k-space for shorter wavelengths and an expansion of the k-space for longer wavelengths, as shown in Figs. 4.1b-4.1e. Fig. 4.1b shows a segment of the Dirac Comb from Eq. 4.2, representing sampling by 10 pixels with a period of Δx. Fig. 4.1c shows a single sine wave, representing a segment of $S(x\delta k_{rel})_{int}$, where $\frac{1}{\delta k_{rel}} = \frac{1}{\delta k_{lin}}$ (highlighted by the yellow dot in Fig. 4.1a). All sine waves are plotted along the same x-axis from Fig. 4.1b. Fig. 4.1d shows the same $S(\delta k_{rel})_{int}$ as in Fig. 4.1c, but for a segment where $\frac{1}{\delta k_{rel}} < \frac{1}{\delta k_{lin}}$ (highlighted by the green dot in Fig. 4.1a). This condition causes a compression of the k-space. Therefore, more cycles of $S(x\delta k_{rel})_{int}$ are observed comparing with Fig. 4.1c. Since the pixel array samples with uniform period Δx, which is independent of δk_{rel}, dispersing more k-space per pixel comes at the expense of acquiring fewer k-space samples. As shown in Eq. 4.2, $S(x\delta k_{rel})_{int}$ experiences a relatively sparse discrete sampling rate when $\frac{1}{\delta k_{rel}} < \frac{1}{\delta k_{lin}}$. In this way, we show that the k-space sampling rate is proportional to $\frac{1}{\delta k_{rel}}$ (and estimated by $\frac{1}{\Delta k_{rel}}$). Fig. 4.1e shows $S(x\delta k_{rel})_{int}$ for a segment where $\frac{1}{\delta k_{rel}} > \frac{1}{\delta k_{lin}}$ (highlighted by the orange dot in Fig. 4.1a), where expanded k-space results in a relatively dense k-space sampling rate when $\frac{1}{\delta k_{rel}} > \frac{1}{\delta k_{lin}}$. Other than the spectral distortions described above, uniform sampling by the pixel array itself does not introduce any new distortions (not considering aliasing and roll-off).

4.3.2 Linear-k interpolation and resampling

A linear-in-k version of $S[j]_{int}$ can be estimated by digitally redistributing the locations of k-space samples. Specifically, $S[j]_{int}$ is interpolated to linear-in-k by calculating unknown values of $S[j]_{int}$ from an estimated continuous version of itself. Due to its simplicity and computational efficiency, a popular SD-OCT fringe interpolation is linear interpolation (LI) [67], which is the focus of our analysis. However, the mathematical principles and fundamental conclusions derived here remain valid for other interpolations, such as cubic spline. A discrete LI consists of three steps: up-sampling, low-pass filtering, and down-sampling [6].

As shown above, $S[j]_{int}$ is initially down-sampled at shorter wavelengths and up-sampled at longer wavelengths according to $\frac{1}{\delta k_{rel}}$. Phase distortion of $S[j]_{int}$ can be removed by an inverse operation. Therefore, $S[j]_{int}$ is resampled at a rate inverse to $\frac{1}{\delta k_{rel}}$, which is in the up-sampling and down-sampling steps in LI.

As illustrated in Fig. 4.1, LI results in an expansion of shorter wavelengths and compression of longer wavelengths exactly inverse to their original distortions. This can be described mathematically as

$$S[j]_{int\_lin} = \sum_{j=1}^{N} S\left(x\frac{\delta k_{rel}}{\delta k_{rel}}\right)_{int} \theta(x - j\Delta x) = \sum_{j=1}^{N} S(x)_{int}\, \theta(x - j\Delta x). \tag{4.4}$$

From Eq. 4.5, the noise-free interference fringe is resampled linearly in k and x, canceling sampling-based distortions. Finally, the low-pass filtering step in LI uses a triangle function

$$t[j] = \begin{cases} 1 - \frac{|j|}{\xi}, |j| \leq \xi \\ 0, \quad elsewhere \end{cases}, \tag{4.5}$$

where ξ is the order of interpolation [68]. We show the influence of Eq. 4.5 in Section 4.4.3.

4.3.3 Noise in SD-OCT

In SD-OCT, the additive noise consists of shot noise, dark noise, readout noise, and relative intensity noise (RIN) and is assumed to be Gaussian distributed at each pixel [23]. Unlike sampled fringe $S[j]_{int}$, the additive noise is not correlated with k. Therefore, we modify representation of the signal detected by the spectrometer to

$$S[j]_{total} = S[j]_{int} + e[j]_{noise}, \tag{4.6}$$

where $e[j]_{noise}$ is the additive noise in SD-OCT.

We confirmed the Gaussian noise distribution by acquiring images using our vis-OCT system (40 μs exposure time, 5000 A-lines, 0.15 μW laser power from reference arm) without any sample in the sample arm. After normalizing the detected noise by the spectral shape of the light source (NKT Photonics, SuperK 150 MHz), we found that our measured noise followed the Gaussian distribution with a mean near 0 and a standard deviation (σ) of 0.79 [arb. Units]. Additionally, it has been shown in SD-OCT that a supercontinuum laser source contributes pink RIN noise [23]. In our experimental measurements in Section 4.4, we demonstrate that although pink noises exist, SDBG bias and the general spectral profile of the background is dominated by the white noise component.

4.3.2 Interpolation of noise in SD-OCT

To understand how interpolation leads to SDBG, we must consider a complete representation of the SD-OCT signal

$$S[j]_{total\_lin} = S[j]_{int\_lin} + e[j]_{noise\_lin} = LI\{S[j]_{int}\} + LI\{e[j]_{noise}\}, \tag{4.7}$$

where $S[j]_{total\_lin}$ is the linearly interpolated signal detected by the spectrometer; $S[j]_{int\_lin}$ is the linearly interpolated interference fringe; $e[j]_{noise\_lin}$ is the linearly interpolated noise; and LI is the linear interpolation operator. $S[j]_{int}$ and $e[j]_{noise}$ are interpolated independently.

A useful property of white noise is that its autocorrelation is proportional to the Dirac delta function. First, we denote the autocorrelation of $e[j]_{noise}$ as $\phi[j]_{noise_{ee}}$. To investigate $\phi[j]_{noise_{ee}}$ in the same way as the sampled interference fringe, we write $\phi[j]_{noise_{ee}}$ as

$$\phi[j]_{noise_{ee}} = \sum_{j=1}^{N}[e(x) * e(x)]\ \theta(x - j\Delta x) = \sum_{j=1}^{N}\sigma^2\delta(x)\theta(x - j\Delta x) = \sigma^2\delta[j], \qquad (4.8)$$

where $e(x)_{noise}$ is the SD-OCT noise as a function of continuous space x; $*$ is the continuous convolution operator; σ^2 is the variance of the noise; and $\delta(x)$ and $\delta[j]$ are the continuous and discrete Dirac delta functions, respectively. Eq. 4.8 is valid because $e[j]_{noise}$ is a wide-sense stationary signal [6]. Unlike the interference fringe, neither $e[j]_{noise}$ nor $e(x)$ are correlated with k . As such, from the perspective of the spectrometer array, $e(x)$, $e[j]_{noise}$, and $\phi[j]_{noise_{ee}}$ are all assumed linear with the pixel index. However, interpolating $S[j]_{int}$ still necessitates linear-in-k interpolation of $e[j]_{noise}$. Similar to Eq. 4.4, we can write the interpolated noise as

$$e[j]_{noise\_lin} = \sum_{j=1}^{N} e\left(\frac{x}{\delta k_{rel}}\right)_{noise}\ \theta(x - j\Delta x). \qquad (4.9)$$

Now, we can write the autocorrelation of the interpolated noise, as

$$\phi[j]_{noise\_lin_{ee}} = \sum_{j=1}^{N}\left[e\left(\frac{x}{\delta k_{rel}}\right) * e\left(\frac{x}{\delta k_{rel}}\right)\right]\ \theta(x - j\Delta x) = \sum_{j=1}^{N}\sigma^2\delta\left(\frac{x}{\delta k_{rel}}\right)\theta(x - j\Delta x) = \Delta k_{rel}\sigma^2\delta[j]. \qquad (4.10)$$

Indeed, expansion or compression by δk_{lin} does not linearize k domain sampling for $e[j]_{noise}$ like it does for $S[j]_{int}$. Eq. 11 shows that the amplitude of $\phi[j]_{noise\_lin_{ee}}$ is determined by δk_{rel} and scaled by Δk_{rel}.

4.3.4 SDBG in the reconstructed depth spectrum

Since we are interested in the depth-resolved spectral signatures of vis-OCT signals, we need to investigate the STFT of $S[j]_{total\_lin}$ as

$$STFT\{S[j]_{total\_lin}\} = \sum_{r=1}^{R_{total}}\left(DFT\{S[\Delta j_r]_{\mathrm{int}\_lin}\} + DFT\{e[\Delta j_r]_{noise\_lin}\}\right), \tag{4.11}$$

where r is the STFT sub-band spectral window and Δj_r are the sample indexes under the full-width-half-maximum (FWHM) bandwidth of spectral sub-band window r. $S[\Delta j_r]_{int\_lin}$ and $e[\Delta j_r]_{noise\_lin}$ are the windowed versions of $S[j]_{int\_lin}$ and $e[j]_{noise\_lin}$, respectively. We can compute STFT of $\phi[j]_{noise\_lin_{ee}}$ as

$$STFT\{\phi[j]_{noise\_lin_{ee}}\} = \sum_{r=1}^{R_{total}} \frac{1}{j_{end}-j_{start}} \sum_{j=j_{start}}^{j_{end}-1} \Delta k_{rel}\sigma^2\delta[j]e^{\frac{-i2\pi jz}{j_{end}-j_{start}}} \sim \Delta k_{rel_r}\sigma^2, \tag{4.12}$$

where z is the transformed index of j representing the depth; i is the complex number; j_{start} and j_{end} are the first and last indexes of Δj_r, respectively; and Δk_{rel_r} is the windowed version of Δk_{rel}. Applying the Wiener-Khinchen theorem, the DFT of $\phi[j]_{noise\_lin_{ee}}$ for each sub-band is the power spectral density (PSD) of $e[j]_{noise\_lin}$ under each sub-band, referred to as $\Phi[j]_{noise\_lin_{ee}}$ [6]. Since the result of Eq. 12 is a positive constant for each r, we can relate the PSD to its amplitude spectrum (spectrally dependent A-line or SDA-line: $A[z, \Delta j_r]_{noise\_lin}$) using

$$A[z, \Delta j_r]_{noise\_lin} = \sqrt{\Phi[j]_{noise\_lin_{ee}}} \sim \sqrt{\Delta k_{rel_r}}\sigma. \tag{4.13}$$

Then Eq. 11 can be rewritten as

$$STFT\{S[j]_{total}\} = A[z, \Delta j_r]_{int\_lin} + A[z, \Delta j_r]_{noise\_lin}, \qquad (4.14)$$

where $A[z, \Delta j_r]_{int\_lin}$ is an SDA-line reconstructed from the fringe. SDBG is therefore a bias of the noise floor proportional to $\sqrt{\Delta k_{rel_r}}$.

4.4 RESULTS

4.4.1 Simulated SDBG

We simulated SDBG for the Blizzard SR spectrometer by generating a Gaussian white noise ($e[j]_{noise}$) and processing it following an STFT spectroscopic vis-OCT reconstruction procedure [9]. Briefly, we generated $e[j]_{noise}$ with $N = 2048$ pixels and an SD of 0.79 (arb. units, same as measured in Section 4.3.3). Then, we up-sampled $e[j]_{noise}$ six times using FT zero-padding [67] and linearly resampled to obtain $e[j]_{noise\_lin}$. Finally, we applied STFTs using $R_{total} = 24$ Gaussian windows spaced equidistantly in the k space from 523 nm to 591 nm. Each sub-band had the same FWHM bandwidth, corresponding to a 13-nm FWHM bandwidth for a sub-band centered at 556 nm. We repeated this processing 5000 times with and without the LI step and averaged all the respective $A[z, \Delta j_r]_{noise_{lin}}$.

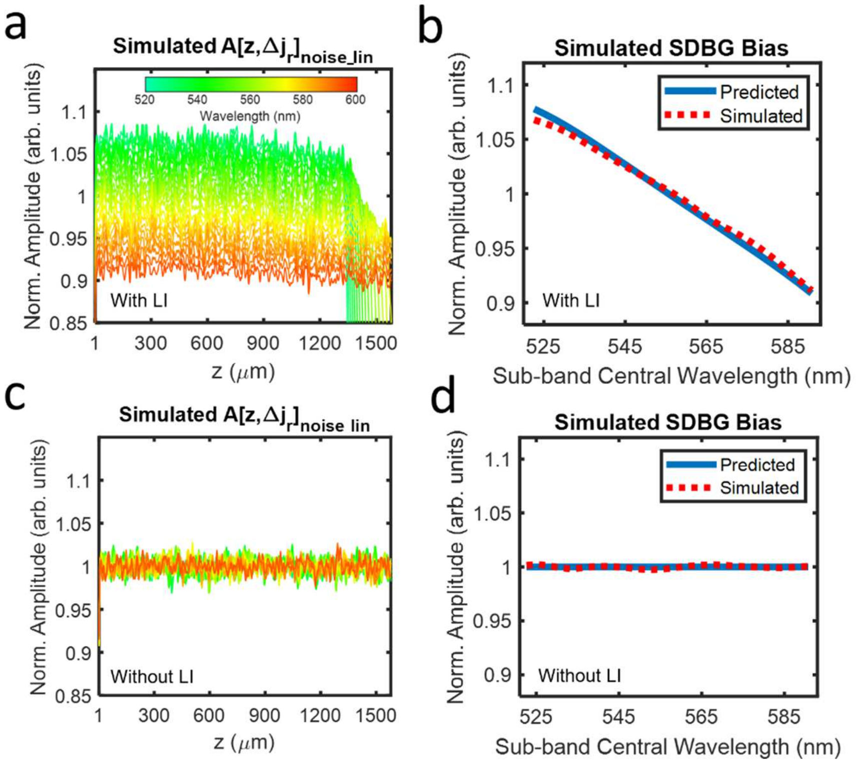

Figure. 4.8. Simulated SDBGs in vis-OCT. (a) Simulated background SDA-lines with LI; (b) predicted SDBG bias (blue line) and simulated SDBG bias (red dashed line) with LI from z = 500 µm to 800 µm; (c) simulated background SDA-lines without LI; (d) predicted SDBG bias (blue line) and simulated SDBG bias (red dashed line) without LI from z = 500 µm to 800 µm

Fig. 4.2a shows the simulated $A[z, \Delta j_r]_{noise\_lin}$ with LI after normalizing by its average spectral amplitude $\left(\frac{\sum_{r=1}^{R} A[z,\Delta j_r]_{noise\_lin}}{r}\right)$ and average depth amplitude between z = 500 µm and z = 800 µm $\left(\frac{\sum_{z=500\ \mu m}^{800\ \mu m} A[z,\Delta j_r]_{noise\_lin}}{300\ \mu m}\right)$. From here on, all $A[z, \Delta j_r]_{noise\_lin}$ are plotted after this normalization. The simulated $A[z, \Delta j_r]_{noise\_lin}$ has 24 background values, each representing the r^{th} STFT sub-band. We color-code the central wavelength of each sub-band, as shown by the color bar. Although all $A[z, \Delta j_r]_{noise\_lin}$ are approximately constant with z, the mean amplitude from shorter (green) wavelengths are higher than those from longer (orange) wavelengths. We visualize the simulated SDBG bias in Fig. 4.2b (red dashed line), which we approximate as the depth-averaged $A[z, \Delta j_r]_{noise\_lin}$ between 500 μm and 800 μm:

$$\mathrm{SDBG} \approx A[\Delta j_r]_{noise\_lin} = \frac{\sum_{z=500\ \mu m}^{800\ \mu m} A[z, \Delta j_r]_{int\_lin}}{300\ \mu m} \tag{4.15}$$

The blue line in Fig. 4.2b shows the SDBG bias predicted by the spectrometer's $\frac{1}{\sqrt{\Delta k_{rel_r}}}$, which agrees well with the simulated $A[\Delta j_r]_{noise\_lin}$. Fig. 4.2b and all plotted $A[\Delta j_r]_{noise\_lin}$ are normalized by their average spectral amplitude, as done in Fig. 4.2a. We noted that there is a small difference between the SDBG biases at the shortest wavelengths, although this difference is < 1% of the predicted value. This difference may be caused by σ not being perfectly constant with sub-band center wavelength or a minute depth-dependence of $A[z, \Delta j_r]_{noise\_lin}$, which is discussed in Section 4.4.3. Fig. 4.2c illustrates the simulated $A[z, \Delta j_r]_{noise\_lin}$ after the same respective processing and analysis as Figs. 4.2a, without the LI of $e[j]_{noise}$. Fig. 4.2d illustrates the simulated $A[\Delta j_r]_{noise\_lin}$ calculated from Fig. 4.2c and the predicted SDBG bias. It is clear that all the noises have the same amplitude, regardless of their center wavelengths. This matches the predicted SDBG bias since $e[j]_{noise}$ is not correlated with k and no k distortion is present.

4.4.2 Experimentally measured SDBG

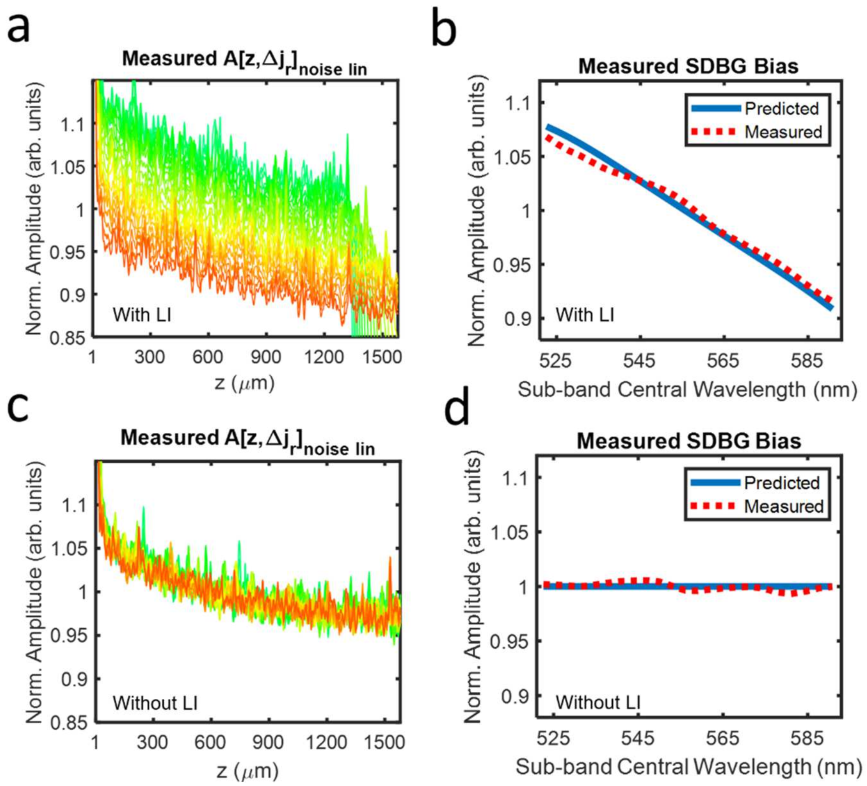

Figure. 4.9. Measured SDBGs in vis-OCT. (a) Measured background SDA-lines with LI; (b) predicted SDBG bias (blue line) and measured SDBG bias (red dashed line) with LI from z = 500 µm to 800 µm; (c) measured background SDA-lines without LI; (d) predicted SDBG bias (blue line) and measured SDBG bias (red dashed line) without LI from z = 500 µm to 800 µm

We applied the same analysis from Section 4.4.1 to experimentally acquired $e[j]_{noise}$ using our vis-OCT system. Fig. 4.3a shows the $A[z, \Delta j_r]_{noise\_lin}$ from the measured $e[j]_{noise}$, plotted using the same colorbar in Fig. 4.2a. The experimental $A[z, \Delta j_r]_{noise\_lin}$ in Fig. 4.3a has a similar, monotonic spectral bias to that of the simulated version (Fig. 4.2a). We confirmed this trend by measuring $A[\Delta j_r]_{noise\_lin}$ (Fig. 4.3b, red dashed line). Similar to the simulated $A[\Delta j_r]_{noise\_lin}$, the experimental $A[\Delta j_r]_{noise\_lin}$ (also for depths $500\ \mu m$ – $800\ \mu m$) decreases approximately linearly with increasing central wavelength. Unlike the simulated $A[z, \Delta j_r]_{noise\_lin}$, the experimental $A[z, \Delta j_r]_{noise\_lin}$ (Fig. 4.3a) is not approximately constant with depth. Instead, its amplitudes are higher at shorter depths and decay exponentially with depth, which may be caused by two experimental conditions. First, the noise distribution from a supercontinuum laser is pink [23], which contains a higher proportion of low-frequency noises. Second, imperfect normalization of the light source spectral shape can propagate a low-frequency component into interference fringe. As shown in Eq. 10, the SDBG bias is contingent on the spectroscopic processing of white noise. To this end, it was important to directly measure $A[z, \Delta j_r]_{noise\_lin}$ to monitor any inconsistencies with the model. Since the measured SDBG bias was in strong agreement with our mathematical model and simulation, we concluded, to a reasonable approximation, that background noise in our vis-OCT system was dominated by a white noise process and interpolation. We did note small differences (~ 2% error) between the measured $A[\Delta j_r]_{noise\_lin}$ and predicted SDBG bias, which was likely explained by the lower noise frequencies, normalization of the light source shape, or σ not being perfectly constant across spectral locations, which may be caused by different excess noises or efficiencies of the spectrometer elements [25]. Since supercontinuum laser sources may vary in power, spectral shape, repetition rate, and RIN noise, it is important that researchers directly measure the SDBG. They may also directly investigate light-dependent influences by comparing the SDBG with the light source on and off.

Finally, Figs. 3c and 3d illustrate the measured $A[z, \Delta j_r]_{noise\_lin}$ and $A[\Delta j_r]_{noise\_lin}$, respectively, without LI. As predicted, the spectral dependence of the background noise floor is not present. Furthermore, depth decay of the background still existed, since the frequency distribution of the background noise is not influenced by interpolation.

4.4.3 Influence of interference fringe up-sampling

To this point, to simplify the calculation of SDBG, we did not extend the analysis to the filter in Eq. 5. Indeed, the convolution of $t[j]$ with $e[j]_{noise}$ adds additional depth-dependence and spectral dependence to the SDBG. The STFT of $t[j]$ for LI is

$$T[z, \Delta j_r] = sinc^2\left[\frac{z\Delta k_{rel_r}}{\pi}\right], \tag{4.16}$$

where ξ from Eq. 5 is set to 1 since the total number of samples in each sub-band does not change. The multiplication of Δk_{rel} with z signifies the scaling of the k domain after resampling. Therefore, true SDA-line can be written as

$$STFT\{S[j]_{total}\} = A[z, \Delta j_r]_{int\_lin}T[z, \Delta j_r] + A[z, \Delta j_r]_{noise\_lin}T[z, \Delta j_r] \tag{4.17}$$

which adds the spectrally-dependent roll-off (SDR) [27] component to the signal and noise, according to Eq. 16. It has been shown that uniformly up-sampling $S[j]_{total}$ before the interpolation step reduces A-line amplitude decay with depth [67]. This is because up-sampling compresses SDA-lines, but not the depth-resolved interpolation filter. Compression of imaging depths relative to the interpolation filter exposes them to less decay by the $sinc^2$ function than without compression (no up-sampling).

If $S[j]_{total}$ is up-sampled at a high enough rate, the SDR induced by the interpolation filter becomes small enough to be negligible for most applications. This is also why there is no visually noticeable decay by the $sinc^2$ function in Fig. 4.3. However, to our knowledge, an optimal up-sampling rate for spectroscopic vis-OCT has not been determined. An optimal up-sampling rate should be established since researchers may apply low upsampling rates to increase processing speeds without considering the spectroscopic consequences.

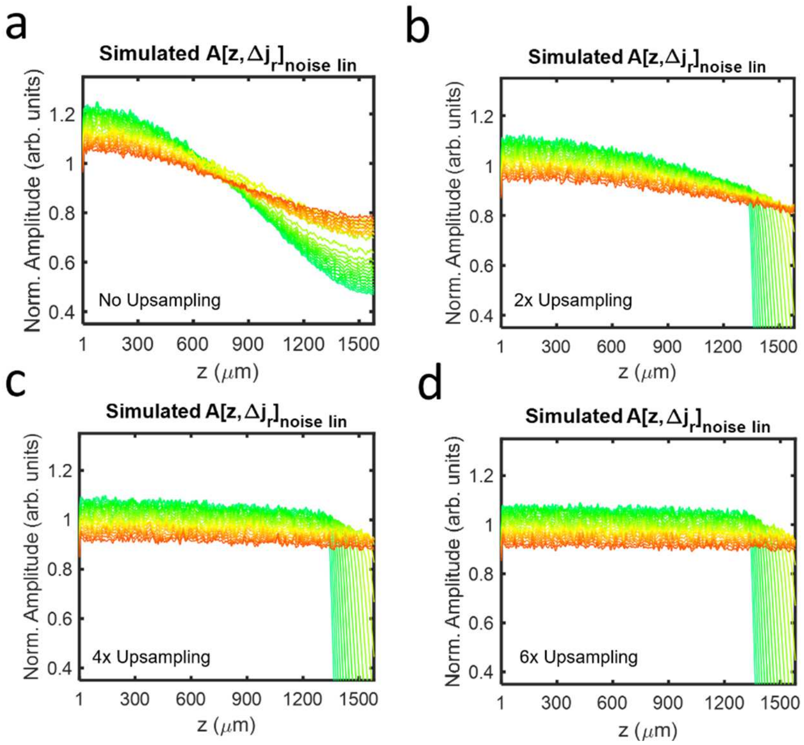

Figure. 4.10. Simulated background SDA-lines with LI after (a) no, (b) two-fold, (c) four-fold, and (d) six-fold up-sampling.

We investigate a minimum upsampling rate for spectroscopic vis-OCT in Fig. 4.4, which uses the simulation from Fig. 4.2a, except that we varied the up-sampling rates before interpolation. We compared $A[z, \Delta j_r]_{noise\_lin}T[z, \Delta j_r]$ corresponding to upsampling rates of 1, 2, 4, and 6. In Fig. 4.4a, $A[z, \Delta j_r]_{noise\_lin}T[z, \Delta j_r]$ is influenced by the depth-independent amplitude scaling in Eq. 13 and the depth-dependent interpolation filter in Eq 16. Each noise component decays with depth, where shorter wavelengths decay more rapidly than longer ones. Such decay adds two additional influences to the noise floor: decay with depth and different depth decay rates with different wavelengths. These influences further complicate the alterations of spectroscopic vis-OCT measurements, since the assumption of a constant SDBG bias shown in Eq. 13 is no longer satisfied. This also complicates the SDBG correction, which is described in Section 4.4.4. As shown in Figs. 4.4b and 4.4c, the influence of the interpolation filter is reduced with increased upsampling but cannot be completely removed. Under six-fold up-sampling (Fig. 4.4d), $A[z, \Delta j_r]_{noise\_lin}T[z, \Delta j_r]$ only shows minute decay with depth, which suggests that $S[j]_{total}$ should be up-sampled at least six times. At this point, Eq. 4.17 can be simplified back to Eq. 4.14. Finally, we note that $T[z, \Delta j_r]$ is also multiplicative with the signal-carrying SDA-lines in Eq. 4.17. Up-sampling $S[j]_{total}$ by six-fold will reduce SDR of the signal-carrying SDA-lines in the same way as the background shown in Fig. 4.4.

4.4.4 Correcting SDBG in vis-OCT oximetry in humans

Influence of SDBG on spectroscopic analysis can be corrected experimentally by subtracting $A[z, \Delta j_r]_{int\_lin}$ from Eq. 14 as

$$A[z, \Delta j_r]_{int\_lin} = STFT\{S[j]_{total}\} - A[z_0, \Delta j_r]_{noise\_lin} \quad (4.18)$$

where z_0 is the depth of the spectroscopic calculation. Practically, this can be accomplished by selecting a depth region where the spectroscopic image is completely attenuated. Since the experimental SDBG was shown to decay with depth, we fit an exponential curve to each $A[z, \Delta j_r]_{noise\_lin}$ in the selected depth region. We then used the fitted values at z_0 to estimate $A[z_0, \Delta j_r]_{noise\_lin}$. We note that zero-padding the fringe at least 6-fold greatly simplifies this correction, since the depth decays of the SDBG are minimized and nearly uniform across all spectral sub-bands. Insufficient zero-padding, as exemplified in Fig. 4.4a, introduces additional complications: (1) The assumption of simple exponential decay is lost according to Eq. 16; and (2) Each sub-band experiences a unique, spectrally-dependent decay, leaving them more susceptibility to errors from direct measurement or depth-fitting of the SDBG. If the spectroscopic image is not completely attenuated, it is an acceptable alternative to acquire only the background signal, as shown in Fig. 4.3a, and directly calculate $A[z_0, \Delta j_r]_{noise\_lin}$. However, this will also require the researcher to account for any other modifications made in the spectroscopic image processing, which is discussed in Section 4.5.

To demonstrate the importance of SDBG correction, we measured the vis-OCT spectrum of blood in human retinal vessels. Briefly, we imaged the retina of a healthy 23-year-old volunteer with a vis-OCT system described in [24]. Human imaging was approved by the Northwestern University Institutional Review Board and adhered to the Declaration of Helsinki. The optical power incident on the cornea was 250 μW. We measured the spectrum inside the retinal blood vessels using STFT sub-bands $r = 3$ to $r = 23$ (528 nm to 588 nm). We applied standard OCT processing, including removal of the spectrum DC component, 6-fold zero-padding, compensation for dispersion mismatch, and correction for the system roll-off. We averaged ~ 500 pixels in each vessel from 16 B-scans (8192 A-lines per B-scan) to reduce the background and speckle noise fluctuations.

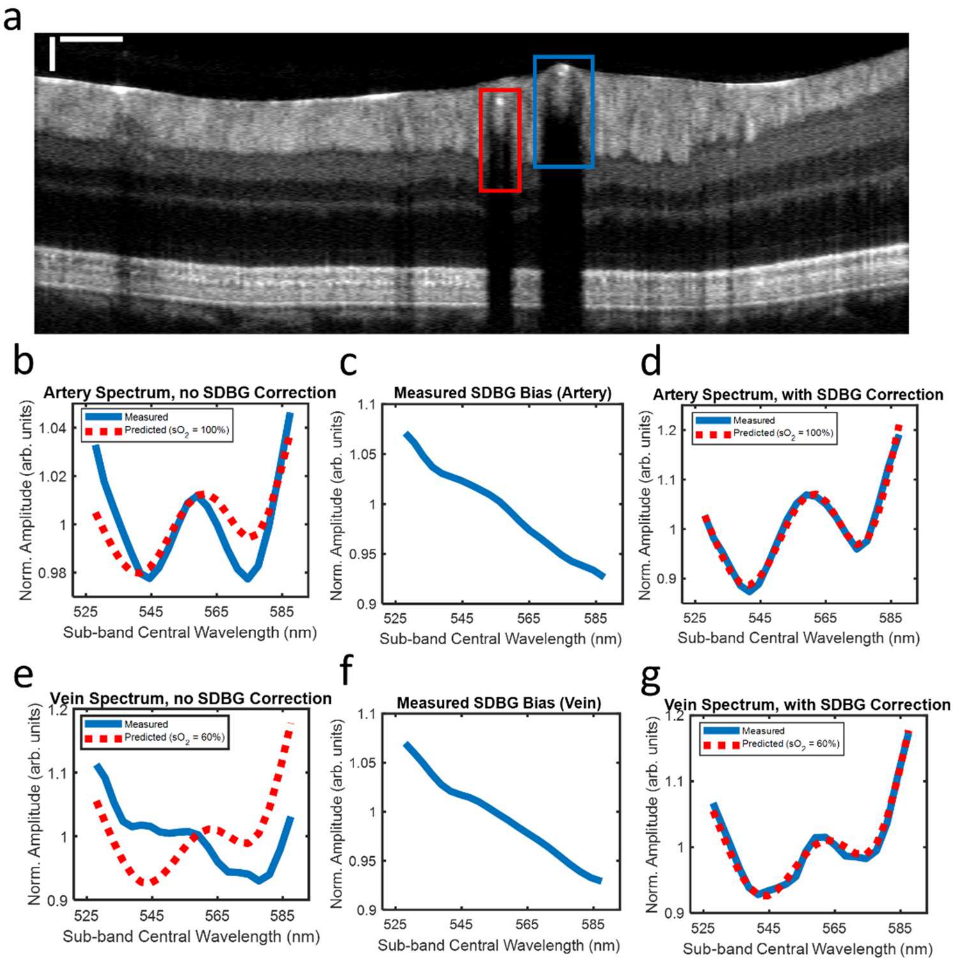

Figure. 4.11. SDBG correction in the human retina. (a) B-scan image with one artery (red box) and one vein (blue box); scale bars are 250 μm (lateral) and 50 μm (axial); (b) measured blood spectrum in the artery before SDBG correction; (c) measured SDBG bias in the artery; (d) measured blood spectrum in the artery after SDBG correction; € measured blood spectrum in the vein before SDBG

correction; (f) measured SDBG bias in the vein; (g) measured blood spectrum in the vein after SDBG correction

We calculated the influence of SDBG in an artery (red box) and vein (blue box), as highlighted in Fig. 4.5a, near the optic disk. The spectrum was detected at an average distance of ~40 μm below the anterior vessel wall and is plotted in blue in Fig. 4.5b. All spectra are plotted after normalizing by their respective mean amplitudes. The red dashed-line in Fig. 4.5b is the predicted spectrum from the literature [30] for oxygen concentration (sO_2) = 100%. Note how the blue spectrum is tilted downwards with increasing wavelength and does not well match the literature spectrum. Fig. 4.5c shows the measured $A[z_0, \Delta j_r]_{noise\_lin}$. It matches well with those simulated and experimental SDBGs shown in Figs. 4.2b and 4.3b. The downwards tilt in the measured spectrum in Fig. 4.5b follows the trend of $A[z_0, \Delta j_r]_{noise\_lin}$ in Fig. 4.5c.

Fig. 4.5d shows the same spectral calculation in Fig. 4.5b after SDBG correction. We corrected the spectrum using $A[z_0, \Delta j_r]_{noise\_lin}$ from Fig. 4.5c. After correction, the spectrum matches well ($R^2 = 0.98$) with the literature spectrum (sO_2 = 100%). Fig. 4.5e shows the measured spectrum (blue line) without SDBG correction in the vein and literature spectrum (red dashed-line) for sO_2 = 60%. Again, the measured spectrum differs from the literature spectrum with a tilt downwards at longer wavelengths. Fig. 4.5f shows the measured $A[z_0, \Delta j_r]_{noise\_lin}$. Fig. 4.5g shows the SDBG corrected spectrum, which well agrees with the literature spectrum (R^2 = 0.98).

4.4.5 Metric to evaluate the influence of SDBG on spectroscopic OCT measurements

We recognized that the influence of SDBG also depends on the amplitude of the spectroscopic signal relative to the noise floor. To quantify SDBG's influence on retinal oximetry in vessels similar to the ones in Fig. 4.5, we simulated oxygen-dependent spectra for $sO_2 = 0$ to 100% and SDBGs for different signal-to-noise-floor-ratios (SNFRs). We define SNFR as

$$SNFR = \frac{\sum_{r=1}^{R} A[z_0,\Delta j_r]_{int\_lin}/r}{\sum_{r=1}^{R} A[z_0,\Delta j_r]_{noise\_lin}/r}, \tag{4.19}$$

which is the ratio between the mean spectral amplitudes from the structure of interest and the noise floor. We calculated sO_2 from the simulated spectra and calculated the root-mean-squared-error (RMSE) between the calculated sO_2 and the ground truth. Figure 4.12 illustrates RMSE from the computer-generated ground truth when SNFR varies from 3 to 100 (sO_2 values for SNFRs below 3 could not be quantified). Indeed, the error of sO_2 is severely compromised by SDBG until SNFR > 55 (RMSE < 2%). For our vis-OCT setup, we found that typical SNFR in locations used for sO_2 were no higher than 4.5, which was limited by the rapid attenuation of blood. The SNFRs in Fig. 4.5a were 2.05 and 1.77 for the artery and vein, respectively. The sO_2 could not be calculated in these vessels until the SDBG was corrected. Therefore, we conclude that SDBG correction is critical for human retinal oximetry. The influence of SDBG correction will be different depending on specific applications. We recommend readers to simulate an accuracy metric similar to that shown in Fig. 4.6 to quantify the influence of the SDBG in a specific application.

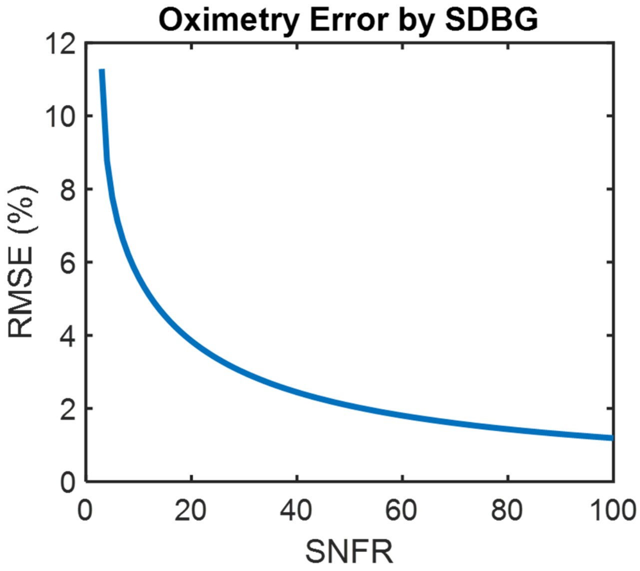

Figure 4.12. RMSE of simulated sO_2 measurements with respect to the ground truth as a function of SNFR.

4.5 DISCUSSION

We thoroughly investigated a systemic SDBG in spectroscopic SD-OCT. We developed a mathematical model to show that SDBG is caused by linear-in-k interpolation of the white noise. We validated the model using simulated and experimental SDBGs in vis-OCT. We demonstrated the importance of up-sampling the fringe before LI. We corrected SDBG in human spectroscopic vis-OCT and found that correcting SDBG was critical for measuring an accurate blood spectrum in humans. Finally, we showed the influence of SDBG in spectroscopic SD-OCT under different SNFR levels.

Potentially most insidious are cases where measured spectra agree with their literature models but are still subject to SDBG bias. Indeed, the SDBG amplitude derived here monotonically decreases with wavelength. Such shape is inconveniently correlated with the reported $\lambda^{-\alpha}$ scattering and backscattering spectra of many biological tissues, where α is a constant [18, 69]. As such, perceived scattering properties of tissue may be altered by the SDBG. This is relevant in a model of light-tissue interaction where the scattering coefficient or elements of the scattering coefficient a fitted parameter [63].

We note that δk_{rel} varies more in visible-light spectral range than in NIR spectral range. To this end, the SDBG is likely influence spectroscopic vis-OCT applications the most. Using a linear-in-k spectrometer [70] or swept-source [5] (not currently available in visible light), rather than a grating-based spectrometer, will greatly reduce the influence of SDBG since δk_{rel} becomes nearly constant. In this work, we performed all STFT analysis using sub-bands with uniform bandwidths in k space. Varying sub-bands' bandwidths in the STFT to compensate for SDBG remains an open question. However, doing so will alter the amplitudes and resolutions of $A[z, \Delta j_r]_{int\_lin}$. Finally, we recognize that in spectroscopic OCT, the interference fringe is often divided by the source spectrum, $\sqrt{S_{samp}(k,z)S_{ref}(k)}$ from Eq. 4.1, for normalization purposes. As such, the measured SDBG may be altered by $\sqrt{S_{samp}(k,z)S_{ref}(k)}$, depending on normalization method and SDBG amplitude. However, such normalization does not alter the analysis concluded in this work, nor does it alter the proposed SDBG correction.

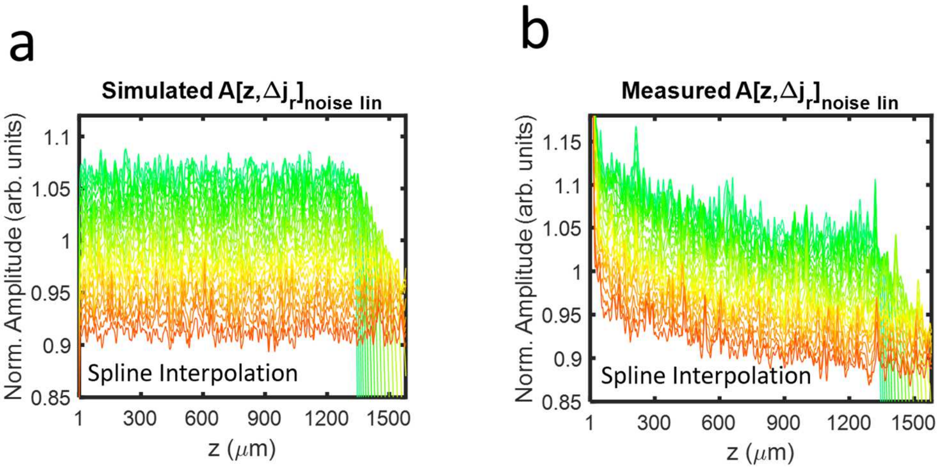

Figure. 4.7. SDBGs in vis-OCT using spline interpolation. (a) Simulated background SDA-lines with spline interpolation; (b) Measured background SDA-lines with spline interpolation.

Finally, while this work focused on LI, more advanced interpolations, such as spline, which trade speed and simplicity for better roll-offs, are of interest to researchers based on application. We confirmed that our SDBG analysis is consistent with other interpolations. Fig. 4.7a illustrates the SDBG for simulated noise using spline interpolation and Fig. 4.7b illustrates the SDBG for measured noise using spline interpolation. The plots were generated using the same methods that generated Figs. 4.2a & 4.3a, respectively. Indeed, the SDBGs generated using spline interpolation are nearly identical to those generated using LI. This is because the SDBG bias is principally dependent on the resampling of white noise shown in Eq. 4.13. Since spline interpolation has less roll-off than LI [6], it required only 2-fold up-sampling to reach the constant bias derived in Eq. 4.13 and shown in Fig. 4.7a, as opposed to 6-fold for LI, as shown in Fig. 4.4. Researchers can use the tools provided in this work to assess which interpolation technique best fits their application of spectroscopic OCT.

4.6 CONCLUSION

In conclusion, we demonstrated that spectroscopic SD-OCT signals are intrinsically biased by the spectrometer's k spacing after linear-in-k interpolation. We investigated this phenomenon in vis-OCT and found strong agreements between mathematical model, simulation, and experiment. We found that correction of the SDBG is important for retinal oximetry, a primary application for vis-OCT. By establishing and verifying the principles of the SDBG, this work informs researchers towards making accurate spectroscopic OCT measurements.

Chapter 5

Multiple forward scattering reduces the measured scattering coefficient of blood in visible-light optical coherence tomography

5.1 MOTIVATION

OCT is traditionally considered to be sensitive to photons single-backscattered in a sample. Previous vis-OCT sO_2 models relied on this assumption to predict the optical properties of blood. However, the extreme forward scattering of blood in the visible-light wavelength range breaks this assumption, leading to sensitivity to multiple scattered photons. This changes how vis-OCT detects the optical properties of blood and impacts sO_2 measurements.

5.1 SUMMARY

Optical properties of blood encode oxygen-dependent information. Noninvasive optical detection of these properties is increasingly desirable to extract biomarkers for tissue health. Recently, visible-light optical coherence tomography (vis-OCT) demonstrated retinal oxygen saturation (sO_2) measurements by inversely measuring the oxygen dependent absorption and scattering coefficients of whole blood. However, vis-OCT may be sensitive to optical scattering properties of whole blood different from those reported in literature. Incorrect assumptions of such properties can add additional uncertainties or biases into vis-OCT's sO_2 model. This work investigates whole blood's scattering coefficient measured by vis-OCT. Using Monte Carlo simulation of a retinal vessel, we determined that vis-OCT almost exclusively detects multiple-scattered photons in whole blood. Meanwhile, photons mostly forward scatter in whole blood within the visible spectral range, allowing photons to maintain ballistic paths and penetrate deeply, leading to a reduction in the measured scattering coefficient. We defined a scattering scaling factor (SSF) to account for such a reduction and found that SSF varied with measurement conditions, such as numerical aperture, depth resolution, and depth selection. We further experimentally validated SSF in *ex vivo* blood phantoms pre-set sO_2 levels and in the human retina, both of which agreed well with our simulation.

5.2 INTRODUCTION

Optical coherence tomography (OCT) enabled noninvasive three-dimensional (3D) retinal imaging at micrometer-scale volumetric resolutions [1, 4]. Since its first report 30 years ago, OCT has become the clinical gold standard for diagnosing and monitoring nearly all major ocular diseases [5, 71].

OCT's sensitivity to optical scattering and absorption provides imaging contrast between tissues and may be used to probe tissue health [72-75]. These capabilities extend to whole blood (further referred to as blood), where absorption and scattering are wavelength-dependent and oxygen-dependent [30, 76-78]. Applying short-time Fourier transforms (STFTs), OCT can measure wavelength-dependent attenuations of blood with micrometer-scale depth resolution, enabling measurement of oxygen saturation (sO_2) in discrete blood vessels [8, 9, 21, 63, 79]. Studies suggested that alterations in retinal sO_2 can be a sensitive biomarker for blindness-causing diseases, including glaucoma and diabetic retinopathy [80, 81]. Hence, accurate and noninvasive retinal sO_2 measurement can improve the clinical management of these diseases.

Blood's optical absorption properties are 2-3 orders of magnitude higher in the visible spectral range than the near-infrared (NIR) spectral range [30], enabling recently developed visible-light OCT (vis-OCT) [9] to overcome the fundamental optical contrast limit in NIR OCTs [79, 82]. In 2013, Yi et al. showed that vis-OCT is sensitive to retinal sO_2 in rodents. Later on, vis-OCT retinal oximetry was demonstrated in rodents [83-86] and humans [87, 88].

Vis-OCT relies on the reported optical properties of whole blood to estimate sO_2. In the visible spectral range, Mie theory predicts an average absorption coefficient (μ_a) near 150 cm^{-1} and an average scattering coefficient (μ_s) near 3000 cm^{-1} [30, 89]. However, a wide range of experimentally measured values have been reported, suggesting uncertainty in the measured optical properties of blood, and potentially reducing the reliability of vis-OCT oximetry [76-78, 89-92]. For example, some measured μ_s values are ~ 1/3 of the Mie theory prediction [11, 76, 91]. Researchers attributed such a reduction in μ_s to the blood's 'packing factor', which describes correlated optical interactions between densely packed RBCs and their hematocrit-dependence [76, 91]. Our group previously used the packing factor (denoted as W) to scale μ_s in the vis-OCT inverse fitting model for sO_2 measurement [11]. Specifically, our group found that the model's goodness of fit (R^2) maximized when W was between 0.2 and 0.4. This W value was consistent with the definition of the packing factor, which scales μ_s by ~ 1/3 at physiological hematocrit [76]. Several other vis-OCT retinal oximetry works also used this W range to scale μ_s [11, 83, 87, 93].

However, reported vis-OCT oximetry methods accounted for blood's μ_s differently, among which significant discrepancies exist [11, 65, 74, 84, 85, 94-96]. Since vis-OCT oximetry fits the measured spectrum to the literature-reported μ_a and μ_s, deviations between the measured and reported μ_s can introduce sO_2 measurement error. Therefore, accurate and consistent quantification of sO_2 benefits from a systemic investigation on how vis-OCT measures μ_s.

We systemically investigated measuring optical scattering properties of blood detected by vis-OCT. First, we performed Monte Carlo (MC) simulations of a retinal blood vessel and photon detection by vis-OCT. MC simulation is not susceptible to systemic biases present in practical OCT detection or image reconstruction [22, 28, 97] and, therefore, provides a fundamental understanding of light-tissue interaction. For each photon packet exiting the tissue, we monitored the number of scattering events and optical pathlength traveled in tissue to investigate the impact of multiple scattering on the vis-OCT signal. We reconstructed simulated vis-OCT A-lines to establish a direct relationship between multiple scattering and the measured μ_s. Then we established the scattering scaling factor (SSF), a generalized scaling coefficient for μ_s. Since multiple scattering influenced the measured μ_s, we further investigated photon detection by different numerical apertures (NA's), because NA acts as a geometric filter in detecting multiply scattered photons. Second, we compared our simulation results to experimental vis-OCT imaging of *ex vivo* blood phantoms. We found excellent agreement between the simulated and experimentally measured values across pre-set oxygenation levels. Finally, we validated our SSF analysis in human retina vis-OCT imaging and found a strong agreement with our simulated results. Validated by simulation, *ex vivo* blood phantom imaging, and *in vivo* human retinal imaging, we provide evidence that vis-OCT measured μ_s is smaller than the reported packing factor but higher than the reduced scattering coefficient (μ_s') [97, 98]. This work sets the foundation for a unified theory of vis-OCT-measured optical properties of blood and more robust retinal oximetry.

5.2 DETECTING SCATTERED LIGHT WITH OCT

Most OCT's use NIR (800 nm – 1300 nm) illumination, where biological tissues have lower optical scattering coefficients (μ_s < 100 cm^{-1}), lower optical absorption coefficients (μ_a < 1 cm^{-1}), and moderately high scattering anisotropy ($0.7 < g < 0.9$) [99]. Such optical properties yield mean-free-paths (MFPs) of several hundred micrometers in tissue, meaning photons can travel deep into tissues before being multiply scattered. Since OCT's axial resolution is dominated by light's coherence length and not geometrical optics, OCT can use a low NA to image deeply penetrating photons across several hundred micrometers with axial resolutions < 10 μm [100]. Another benefit of imaging weakly scattering tissues with a low NA is high sensitivity to single-scattered or ballistic photons [101]. In this work, we define ballistic photons as Class I photons [97], which satisfy

$$|2z_{max} - D| \leq \frac{l_c}{2}, \tag{5.1}$$

where z_{max} [μm] is the maximum depth a photon travels in the tissue with respect to the OCT's zero delay; D [μm] is the total optical path traveled by the photons with respect to the OCT's zero delay; and l_c [μm] is the coherence length. Essentially, a Class I photon travels straight, allowing only a slight deviation within l_c. We define Class II photons as photons that do not travel in a straight line before being detected by the OCT, which satisfy

$$|2z_{max} - D| > \frac{l_c}{2}. \tag{5.2}$$

Finally, we define those photons undetectable by the OCT system as Class III photons.

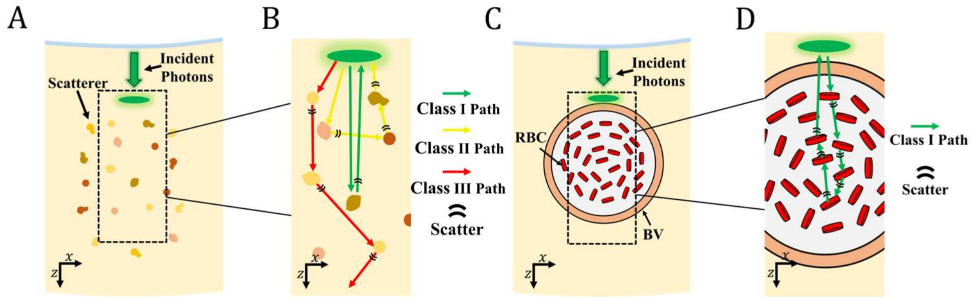

Figure 5.1 (A) Illustration of OCT illumination of a weakly scattering medium. Incident photons (green arrow) create a focal spot (green oval) and detection aperture in the tissue; (B) Magnified illustration of the highlighted region in the panel A, showing the paths of Class I (green arrow), Class II (yellow arrow), and Class III photons (red arrow); (C) Illustration of vis-OCT illumination of a retinal blood vessel (RBC) containing red blood cells (RBC); (D) Magnified illustration of the highlighted region in panel C, showing the paths of Class I photons (green arrow).

Figs. 5.1A & 5.1B illustrate OCT imaging in a weakly scattering tissue (e.g. $\mu_s < 100\ \mathrm{cm}^{-1}$ and $0.7 < g < 0.9$) using a low NA (e.g. < 0.2). Fig. 5.1A shows a global illustration of tissue with optical properties within the NIR spectral range. The OCT sample arm focuses light on a spot in the tissue (illustrated by the green oval), which creates an A-line at that location. Due to the low NA, incident photons (green arrow) are nearly perpendicular to the tissue surface. Since the focus spot creates a conjugate point with the sample arm detector, it also acts as a geometric projection of the detector itself [102]. Only photons collected within the spot and the solid angle defined by the illumination NA will contribute to the A-line.

Fig. 5.1B is a magnified illustration of Fig. 5.1A in the black-dashed box. The green, yellow, and red arrows respectively illustrate representative paths of Class I, Class II, and Class III photons. The black bands represent scattering events. The Class I photon travels deeply into the tissue, scatters once, reverses direction, and returns along almost the same path in the z-direction (also referred to as backscattering). The Class II photons are scattered multiple times and travel significantly along the x-direction before returning to the detector. The Class III photons are scattered multiple times deeply in the tissue and do not return to the detector. Under the conditions of $\mu_s < 100$ cm^{-1} and $0.7 < g < 0.9$, photons can travel tens or hundreds of μm along the x-direction after each scattering event. Therefore, multiply scattered photons are increasingly likely to be Class III rather than Class II photons since they will travel too far from the detector before being absorbed by tissue or escaping the tissue. Meanwhile, most detected photons are likely to be Class I photons (green arrow in Fig. 5.1B) since they do not have the opportunity to travel outside the detection region.

When most photons are Class I and single scattered, the OCT A-line can be modeled by the Beer-Lambert Law [103].

$$A(z)^2 \propto e^{-2(\mu_a+\mu_s)z}, \tag{5.3}$$

where $A(z)^2$ [arbitrary unit] is the A-line intensity; z [mm] is the depth in the tissue; and the coefficient 2 in the exponential term indicates round trip in tissue. Eq. 5.3 has been thoroughly derived and experimentally validated for Class I photons [73].

Vis-OCT imaging of blood represents a special scenario that deviates from the assumptions described in Figs. 1A & 1B. The reported μ_s for oxygenated and deoxygenated blood states are > 3000 cm^{-1} and the W-scaled μ_s are near 1000 cm^{-1} [76]. Both these μ_s values are over an order of magnitude greater than μ_s values (< 100 cm^{-1}) typical of most tissues within NIR spectral range. Furthermore, blood is more highly forward scattering ($g \geq 0.98$) than most tissues ($0.7 < g < 0.9$). Therefore, photons are likely to travel only a few μm or less along the x-direction after each scattering event. Assuming normal incidence of light on a vessel (Fig. 5.1C), photons can be multiply scattered and still satisfy the Class I condition. Fig. 5.1D illustrates such a path following the green arrow. We hypothesize that the path shown in Fig. 5.1D is a common, if not dominant, detection scenario in blood imaging using vis-OCT. A Class I photon that travels deeper than its single scatter assumption is equivalent to reducing its μ_s in Eq. 5.3. Therefore, the Beer-Lambert Law may be rewritten as

$$A(z)^2 \propto e^{-2(\mu_a + SSF\mu_s)z}, \quad 5.4$$

where SSF [dimensionless] is the scattering scaling factor, which is < 1 and scales μ_s to account for the increased detection of photons deeper in tissue. The SSF is a generalized scaling factor and incorporates any other reductions of μ_s, including W.

5.3 VIS-OCT OXIMETRY

Oxygenated and deoxygenated blood have distinct wavelength-dependent μ_a and μ_s, allowing estimation of sO_2. An STFT [104] can reconstruct spectrally-dependent A-lines, which can be modeled by

$$\log(A(\lambda,z)^2) \propto -2[sO_2\mu_{aHbO_2}(\lambda) + (1 - sO_2)\mu_{aHb}(\lambda) + SSF \times sO_2\mu_{sHbO_2}(\lambda) + SSF \times (1 - sO_2)\mu_{sHb}(\lambda)]z, \quad (5.5)$$

where λ [nm] is the central wavelength of the selected STFT sub-band; sO_2 [dimensionless, between 0 and 1] is the oxygen saturation in blood; the subscripts

HbO_2 and Hb denote oxygenated or deoxygenated hemoglobin, respectively; and SSF [dimensionless] is the scattering scaling factor. We used 21 STFT sub-bands ranging from 528 nm to 588 nm equidistant in wavenumber, with an average full-width-at-half-max (FWHM) bandwidth of 11 nm.

5.4 METHODS

5.4.1 MC simulation parameters

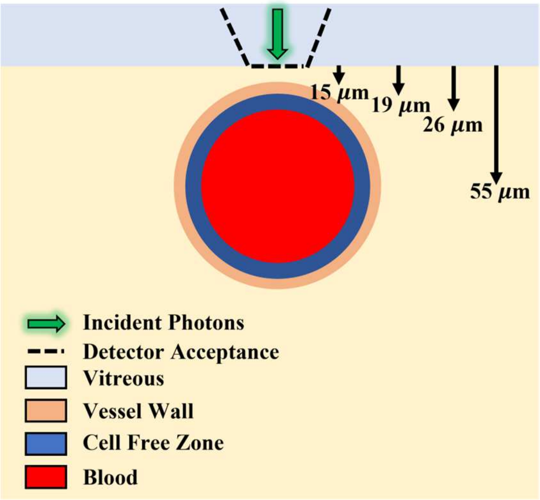

Figure 5.2 Illustration of tissue and imaging geometry in Monte Carlo simulation. Downward arrows (from left to right) highlight the interface depths of the vessel wall, cell free zone, and blood, respectively; fourth arrow highlights depth of the vessel center.

We simulated vis-OCT detection and reconstruction in a retinal blood vessel using MC simulation [75, 89, 97, 98, 105-109]. Fig. 5.2 shows the multi-layered 3D model of a blood vessel embedded in the retina. We modeled the blood vessel using an infinitely long cylinder located 55 μm below the vitreous-retina interface. The vessel has three concentric layers: blood, cell-free zone (CFZ) [35, 36], and the vessel wall. The CFZ is a thin layer consisting primarily of plasma between the blood and the vessel wall. It arises from the difference in viscosity between RBCs and plasma and is described by the Fahraeus Lindqvist (FL) effect [110]. The CFZ has been previously observed in OCT images [111] and is noticeable in our vis-OCT data. Table 5.1 summarizes the optical and geometrical parameters. We extracted the properties of the retina [89, 107], vessel wall [89], and CFZ [112] from the literature. We used the theoretical optical properties of blood previously derived by Faber et al. [30, 89]. To increase the speed of our simulation, we used the average μ_a and μ_s between 520 nm and 600 nm (center wavelength 560 nm). Although there is still uncertainty in the exact values of μ_a, μ_s, and g [76], our values are well within the reported range [76-78, 89-92]. To account for correlated optical interactions between densely packed RBCs, we scaled blood's μ_s using the packing factor $W = (1 - H)^2$, where H is hematocrit [dimensionless]. Assuming a hematocrit of 45% [113], we have $W = 0.3025$.

Table 5.1. Optical properties of tissues used in Monte Carlo simulation.

	μ_s $[cm^{-1}]$	μ_a $[cm^{-1}]$	g [dimensionless]	Thickness $[\mu m]$
Retina	319	9	0.97	NA
Vessel Wall	284	4	0.84	4
Cell Free Zone	0.8	0.4	0.7	6
Blood	3415.5	176.1	0.984	68

5.4.2 MC simulation algorithm

MC simulation of photon propagation in biological tissue has been widely reported [75, 89, 97, 98, 105-109, 114]. We followed the algorithm of simulation photon transport in multi-layered tissues (MCML) [98]. Briefly, we launch a photon packet towards the retina and blood vessel, as illustrated in Fig 2. The photon packet's launching position is at the vitreous-retina interface (Fig. 5.2) at the lateral center of the vessel. The initial direction vector is along the z-axis. Upon tissue entry, we generated the step size (s) following the Poisson distribution

$$s = \frac{-\ln(\xi)}{\mu_t} \tag{5.6}$$

where $\mu_t = \mu_a + \mu_s$ and ξ [dimensionless] is a random variable following an even distribution between 0 and 1. After traveling distance s, the photon packet interacts with tissue and deposits a fraction $\frac{\mu_a}{\mu_t}$ of its weight. At each interaction location, the photon packet is scattered by an angle θ relative to its current propagation direction determined by the Henyey-Greenstein phase function [114].

$$p(\theta) = \frac{1}{4\pi} * \frac{1-g^2}{\left(1+g^2-2g\cos(\theta)\right)^{\frac{3}{2}}} \tag{5.7}$$

At the interface between two media, the photon packet either reflects or transmits with probabilities according to the Fresnel's equations [115]. Upon entering a new tissue region, μ_t is adjusted accordingly. The simulation continues until the photon packet exits the retina into the vitreous or the optical path distance traveled is greater than 2000 μm, well beyond the depth of the blood vessel.

If the photon packet exits the retina into the vitreous, we recorded the remaining weight of the photon packet, the optical pathlength traveled within the tissue, the total number of scattering events in all tissue regions, the total number of scattering events in blood, the exiting position, and the exit angle. We simulated 10^{10} photon packets for each A-line. We implemented the simulation in MATLAB 2020 using parallel computing on a PC with a 3.4-GHz Intel Core i7-6800K CPU and 64-GB RAM. The simulation of an A-line took approximately 120 hours to complete.

5.4.3 Photon detection

To simulate OCT detection, we geometrically filtered photons exiting the retina [109] (black-dashed lines in Fig. 5.2). We determined photon acceptance aperture and angle according to the

$$NA = n \cdot sin\left(\tan^{-1}\frac{D}{2f}\right), \tag{5.8}$$

NA of the light incident on the retina. We tested the NA value from 0.015 to 0.094, which follows the optical properties of normal human eyes [116]. We calculated the NA as

where n [dimensionless] = 1.35 is the refractive index; D [cm] is the $1/e^2$ diameter of the collimated beam incident on the cornea; f [cm] = 1.8 cm is the focal length of a normal eye [117]; and $\tan^{-1}\frac{D}{2f}$ is the acceptance angle with respect to normal incidence. We used the NA to calculate the focal spot beam waist

$$w = n\frac{2\lambda}{\pi NA}, \tag{5.9}$$

where λ = 560 nm is the central wavelength of the vis-OCT probing light. For simplicity, we detect photons using a uniform circle with a radius of w. In the results, we use an NA = 0.05, equivalent to a 2.9° acceptance angle and a detection diameter of $2w = 7.0\ \mu$m unless otherwise specified.

5.4.4 Vis-OCT A-line reconstruction

We reconstructed simulated vis-OCT A-lines using the recorded photon weights and optical path distances in the simulation. We only used photons detected under the acceptance conditions. Adopting the methods in Kirillin et al. [109], we reconstructed the OCT A-line as

$$A(z) = \sum_{i=1}^{N_{photons}} W_i \exp\left(-\left(\frac{2z-D_i}{l_c}\right)^2\right), \tag{5.10}$$

where W_i [dimensionless] is the photon weight; D_i [cm] is the optical path distance; and l_c [μm] is the axial resolution. We set the distance between adjacent z positions as 1 μm and used an axial resolution of 9 μm defined by the l_c of the STFT sub-band window centered at 558 nm with an FWHM bandwidth of 11 nm [100]. We used this sub-band window size for spectroscopic A-line reconstruction in our experimental studies.

5.4.4 Experimental measurements of *ex vivo* blood samples

We used the vis-OCT system operating from 510 to 610 nm described by Beckmann et al. [12] to image *ex vivo* blood samples in phantom vessels. The imaging objective in the sample arm had an NA of 0.05 [118], consistent with our simulation and human imaging. Briefly, we constructed a vessel phantom by pulling a glass capillary tube to have an inner diameter of 200 μm and embedded and stabilized the tube in a plastic well. To reduce the influence of specular reflections, we added immersion oil to the well until the tube was covered. We prepared whole bovine blood (Quadfive, Ryegate, MT) of hematocrit 45% of oxygen levels ranging from 45% to > 99%. To oxygenate the blood, we added a constant stream of pure oxygen and stirred the blood with a magnetic stir bar. To deoxygenate the blood, we added sodium dithionite [119] to the solution and stirred. We repeated these processes until reaching the desired oxygen level. We monitored blood's partial pressure of oxygen (pO_2), partial pressure of carbon dioxide (pCO_2), pH, and temperature using a blood-gas analyzer (Rapidlab 248, Siemens Healthcare Diagnostics, Malvern, PA) and estimated the corresponding sO_2 [120]. Before loading the tube with blood, we flushed it with a phosphate-buffered saline and heparin solution to reduce clotting or sedimentation. Finally, we loaded the tube with blood and flowed it at 0.3 mm/s using a syringe pump (Fusion 100, Chemyx, Inc. Stafford, TX). We aligned the tube to be in focus and near the system zero-delay and illuminated it with 1.20 mW of power. Finally, we acquired data consisting of 512 A-lines × 256 B-scans with imaging range 1 mm × 1 mm at a 25 kHz A-line rate.

5.4.5 Experimental measurements of human retinal vessels

For human imaging, we used the system described by Rubinoff et al. [121]. We used Eq. 5.8 to estimate an NA of 0.05 in the retina, similar to the simulation and *ex vivo* measurements. All human imaging procedures were approved by Northwestern Institutional Review Board (IRB) and adhered to the Tenets of Helsinki. We illuminated the retina with 250 μW of power and acquired human retinal images consisting of 8192 A-lines × 16 B-scans repeated across a 3.8 mm field of view at a 25 kHz A-line rate.

5.5 RESULTS

5.5.1 Contribution from multiple forward scattering in vis-OCT blood signal

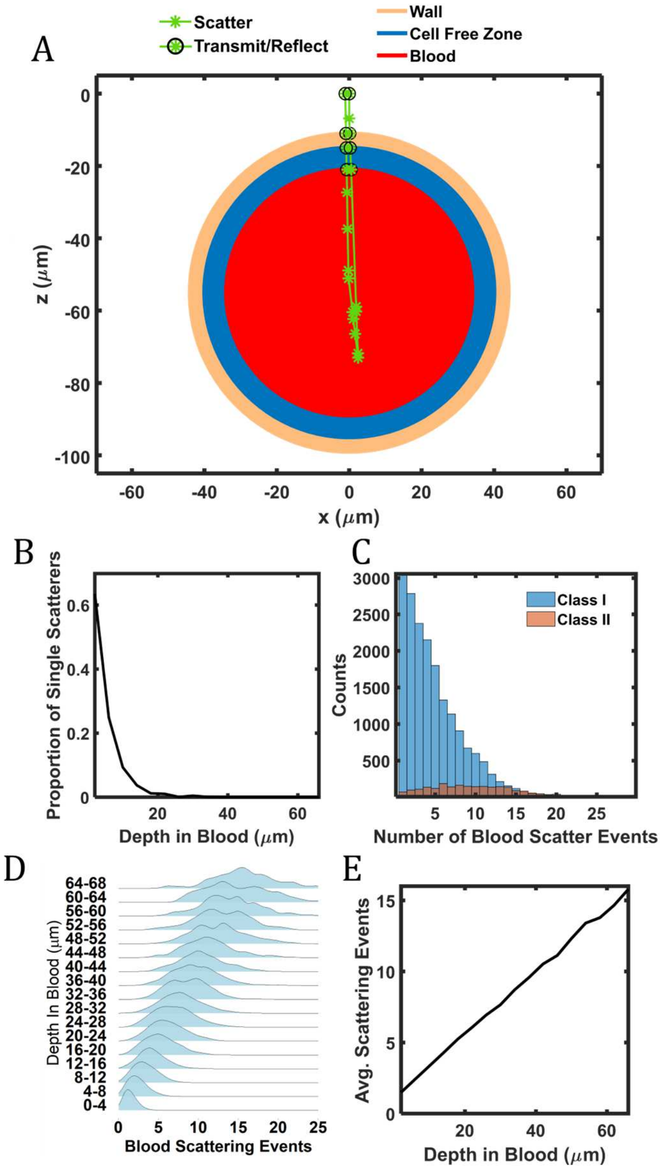

Figure 5.3 (A) Simulated photon packet path (green line) and scattering events (green stars) in the blood vessel; (B) Proportions of detected singly-scattered photon packets; (C) Histogram showing the number of scattering events of the detected Class I and Class II photons; (D) Distributions of the number of scattering events at different depths in blood; (D) The average number of scattering events at different depths in blood.

We investigated how blood's scattering properties influence the detection of photons in vis-OCT. Fig. 5.3A plots a detected photon packet path from our MC simulation. The concentric rings plot the outer boundaries of each vessel layer. The photon packet launched from the origin followed the path of the green line. The green asterisk (*) highlights a scattering event, and a circled asterisk highlights a transmission or reflection across tissue regions. The photon packet in Fig. 5.3A was scattered 11 times inside the blood vessel. Notably, the photon packet travels mainly along the z-axis, consistent with a high scattering anisotropy ($g = 0.987$). This allows the photon packet to backscatter to nearly the same x-position as it launched, similar to the illustration in Fig. 5.1D. Despite the multiple scattering events, we classified this photon packet to be Class I. Based on the optical properties shown in Table 5.1, the calculated MFP in blood is 8.5 μm; however, the photon packet travels 60 μm into the vessel (Fig. 5.3A).

To assess whether the multiple scattering observed in Fig. 5.3A was a frequent occurrence, we measured the proportion of all detected singly scattered photons packets that entered the blood region (Fig. 5.3B). Within the first 10 μm in blood, about 50% of photon packets are singly scattered, which is consistent with the predicted MFP near 8.5 μm. The proportion drops rapidly, where almost no detected photons are singly scattered after 17 μm into the blood region (2 MFPs). Considering that measurements deeper than 8.5 μm are necessary to provide sufficient attenuation contrast, it is reasonable to assume that retinal oximetry measurements are dominated by multiply scattered photons (excluding capillaries that may not generate multiple scattering due to low RBC counts).

Fig. 5.3C plots the detected Class I and Class II photons that entered the blood region. To improve the precision of the photon packet classification, we used l_c = 1.4 μm, the estimated vis-OCT full band resolution, rather than l_c = 9 μm, the STFT resolution. As shown in Fig. 5.3C, Class I photons dominate. Figs. 3B & 3C collectively demonstrate that most detected photons are both Class I and multiply scattered photons. This observation is further emphasized by Fig. 5.3D, which plots the fitted histograms of scattering events in blood from detected photons for different depths. The histograms are normalized with respect to their maximum values to show detail. The distributions show that, other than at the shallowest depths, photons are always multiple scattered. The average value of scattering events increases, and their distributions broaden as photon packets propagate deeper. Fig. 5.3E shows that the average value of scattering events is always > 1 and increases linearly with depth. Such a linear increase is consistent with the notion that a photon packet travels nearly along the same direction after each scattering event. The slope of this line corresponds to 1 blood scattering event for a photon step of 8.9 μm, consistent with the calculated MFP.

5.5.2 Measuring the SSF value

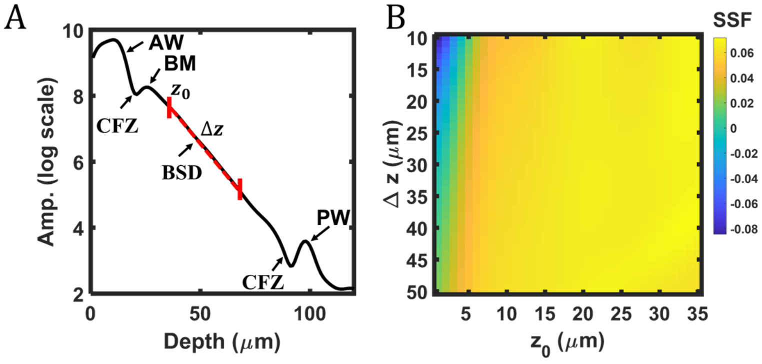

Figure 5.4 (A) A simulated A-line at the center of the vessel, showing the anterior wall (AW), cell-free zone (CFZ), blood maximum (BM), blood signal decay (BSD), and posterior wall (PW); The red-dashed line highlights measurement depth range starting at z_0 and ranging Δz; (B) Measured SSF values from A-line in the panel A as a function of different z_0 and Δz.

Fig. 5.4A plots the simulated A-line on a natural logarithm scale (referred to as 'log'). and illustrates the depth selection procedure for SSF measurement. From left to right, the first peak represents the anterior wall (AW) of the vessel, which is slightly convolved with the retinal tissue above it. Beneath the AW is a valley representing the cell-free zone (CFZ). The valley is smaller than expected from a completely 'scattering-free' region due to the limited 9-μm axial resolution. Beneath the CFZ is the blood maximum (BM), representing the start of blood signal decay (BSD) in the A-line. The distinct peak at the BM is collectively contributed by the finite MFP in blood, the size of the CFZ, and the limited 9-μm axial resolution. The depth location of BM in the A-line is about 10 μm deeper than the physical start of the vessel lumen and about 20 μm deeper than the AW peak. The blood signal decay (BSD) follows the BM and is consistent with log-scale decay described by the Beer-Lambert law [103]. When measuring the optical properties of blood *in vivo*, it is critical to start at least from the BM rather than assuming BSD occurs at the boundary of the AW and vessel lumen. Finally, the last peak represents the posterior wall (PW) of the vessel.

To measure the scattering coefficient, we modeled the BSD using a modified Eq. 5.5

$$\log(A(z)) = -2\left[\mu_{aHbO_2}(avg) + SSF \times \mu_{sHbO_2}(avg)\right]z. \tag{5.11}$$

We include only the oxygenated coefficients since the simulated sO_2 was 100%. The term 'avg' indicates that simulation used optical properties that were the average value between 520 nm and 600 nm. The double pass Beer-Lambert law does not need to be squared in the simulated A-line since it is not the product of interference between the sample and the reference electromagnetic fields. Although there are a handful of ways to extract $\mu_{sHbO_2}(avg)$ from this equation, we elected to compute a depth-average of Eq. 5.11, which we empirically found robust against noise [121]. The starting measurement depth is z_0 and the depth range is Δz. The full region of measurement is highlighted by the red dashed line. We first normalized $A(z)$ by its amplitude at z_0, which shifted the coordinate system to z_0 = 0. The average intensity becomes

$$\frac{1}{\Delta z}\int_0^{\Delta z} \log(A(z))\,dz = -\frac{2}{\Delta z}\left[\mu_{aHbO_2}(avg) + SSF \times \mu_{sHbO_2}(avg)\right]\frac{\Delta z^2}{2} = \left[\mu_{aHbO_2}(avg) + SSF \times \mu_{sHbO_2}(avg)\right]\Delta z. \tag{5.12}$$

Dividing by Δz, we are left only with the linear combination of $\mu_{aHbO_2}(avg)$ and $SSF \times \mu_{sHbO_2}(avg)$. By subtracting $\mu_{aHbO_2}(avg)$, whose value is from the literature, we are left with $SSF \times \mu_{sHbO_2}(avg)$, which can be compared with the literature μ_s value used in the simulation. The SSF can be calculated as

$$SSF = \frac{\frac{1}{\Delta z^2}\int_0^{\Delta z}\log\big(A(z)\big)dz-\mu_{aHbO_2}(avg)}{\mu_{sHbO_2}(avg)}. \tag{5.13}$$

Fig. 5.4B shows the SSF under various combinations of z_0 and Δz, where $z_0 = 0$ at the start of the vessel lumen. For z_0 between 0 μm and 5 μm, SSF $\leq$ 0, which is caused by choosing a depth before BM and is physically impossible. At $z_0 = 10$ μm, the approximate location of BM, SSF = 0.05-0.06, with slight variation for different Δz. For z_0 between 11 μm and 25 μm, SSF = 0.060-0.068. For $z_0 > 25$ μm, SSF is slightly greater than 0.07, which may be biased by the CFZ near the PW. Therefore, we selected $z_0 = 17$ μm and $\Delta z = 33$ μm, a range where the SSF = 0.064. The measured SSF is approximately 5-fold smaller than the literature packing factor W = 0.3025. Here, $\mu_{sHbO_2} = 0.064 \times \mu_{sHbO_2}(avg)$ = 222 cm^{-1}, which is similar to the absorption coefficient $\mu_{aHbO_2}(avg)$ = 174 cm^{-1}. Considering $\mu_{sHbO_2}(\lambda)$ has components that are also absorption dependent by the Kramers-Kronig relationship [76], we conclude that the spectrum of blood vis-OCT measures is overwhelmingly dominated by absorption instead of scattering.

5.5.3 Influence of number of scattering events on SSF

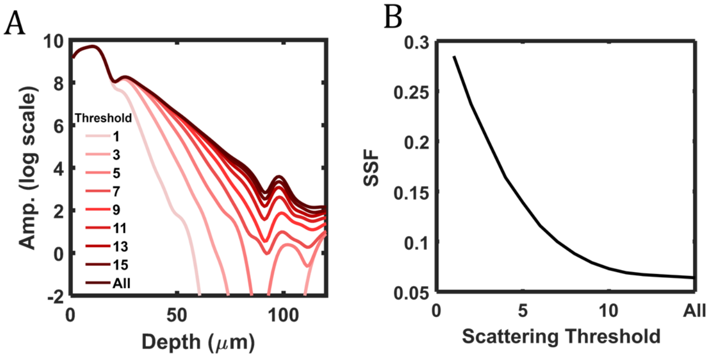

Figure 5.5 (A) Simulated A-line at the center of the vessel after thresholding the number of detected scattering events in blood. Lighter shades indicate a lower threshold of detected scattering events; (B) The SSF value as a function of detected scattering threshold.

To understand how multiple scattering influences SSF, we set a graded threshold to the number of detected scattering events in blood. If a photon packet that entered the blood region is scattered more times than the set threshold, it was not included in the simulated A-line. Fig. 5.5A shows the simulated A-line for different scattering thresholds. The different shades of red plot different scattering threshold levels. The darkest shade has no threshold and collects photon packets from all scattering events (same as Fig. 5.4A). A-line amplitude decays slower with higher threshold levels, consistent with the notion that increased multiple scattering reduces SSF. Specifically, when the threshold level is 1, the A-line is reconstructed by single-scattered Class I photon packets and decays within 20 μm in blood. As sO_2 calculation fits A-lines beyond 20 μm in blood, multiple scattered photons are required for accurate sO_2 measurement *in vivo*.

Additionally, it becomes clear that multiple scattering enables deeper photon penetration necessary for visualizing the PW. The PW becomes weak when the threshold level is less than 7 and invisible when the threshold level is less than 3. This suggests that multiple forward scattering also facilitates the visualization of the PW, a landmark commonly used in vis-OCT oximetry to indirectly measure μ_s [11]. Fig. 5.5B shows the relationship between SSF and the scattering threshold level, which decays approximately exponentially with the scattering threshold, asymptotically approaching 0.064 after threshold > 15. Thresholding 7 scattering events gives SSF = 0.116 and thresholding 2 scattering events gives SSF = 0.285, approaching the set $W = 0.3025$. We measured SSF = 0.424 when thresholding 1 scattering event, although we did not include this data point due to insufficient signal-to-noise-ratio along the measured depths.

5.5.4 Influence of numerical aperture on SSF

As described in photon packet detection in our MC simulation, the detection NA acts as a spatial filter for photon scattering events. The detection aperture (radius) and angle limit an existing photon packet's position and propagation direction. Therefore, the detection criteria can potentially influence the measured SSF.

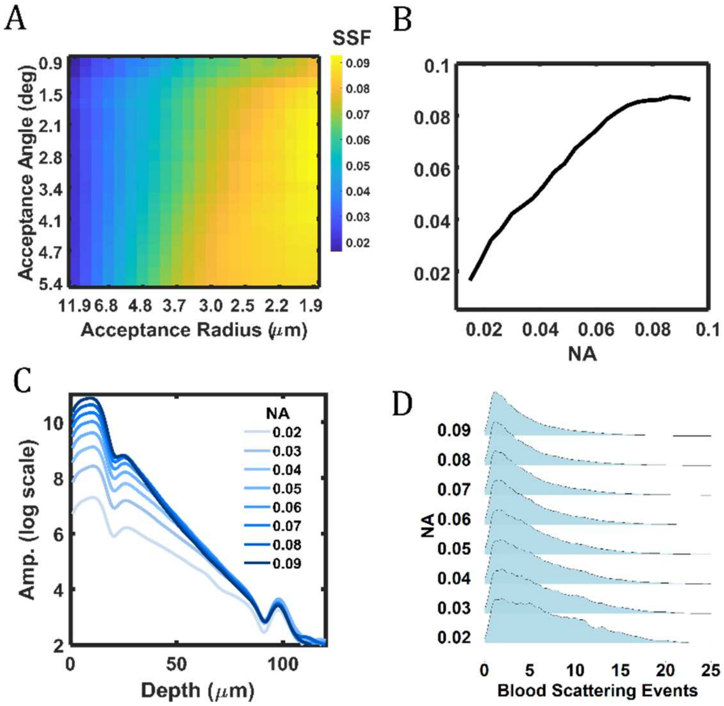

Figure 5.6 (A) The SSF values as a function of optical detection radius and angle; (B) SSF as a function of numerical aperture (NA), which is the diagonal of the matrix in the panel A; (C) Simulated A-line at center of vessel for different NAs; lighter shades indicate lower NA; (D) Normalized distributions of scattering events in blood for different NAs.

We examined the relationship between NA and SFF for $z_0 = 17\ \mu\text{m}$ and $\Delta z = 33\ \mu\text{m}$ based on the conclusion from the above section. The tested NA's are 0.015 to 0.094, which are based on physically reasonable imaging NA's in the human eye. In OCT, retinal imaging NA is almost always less than the maximum possible NA (e.g. 0.2 [116]), since researchers must consider limiting factors like reduced depth-of-focus, aberrations, and eye dilation [102]. Therefore, we varied the acceptance radius from 1.9 μm to 11.9 μm and varied the acceptance angle from 0.9° to 5.4° and found that SSF varied between 0.02 to 0.09 (Fig. 5.6A). We found that SSF reduces with increased acceptance radius, allowing more photon Class II photons (result here). We also found that SSF increased with increased acceptance angles. Photon packets traveling deeper in tissue are less likely to be filtered by the acceptance angle as most photon packets within the acceptance radius for deeply traveling photon packets are within the acceptance angle in deeper tissues.

Fig. 5.6B plots the SSF values for physically possible NA values, which are along the diagonal of the matrix plotted in Fig. 5.6A, and shows that SSF increases with increased NA. However, the relationship between NA and SSF is nonlinear and appears to saturate at the highest NA. For all the tested NA values, SSF is always less than 0.1, which is still less than one third of the literature value $W = 0.3025$. Fig. 5.6C plots the simulated A-line under different NA values. As NA increases, the amplitudes corresponding to AW and BM increase with respect to PW, which intrinsically increases the slope of the blood decay and leads to an increased SSF. Since the number of scattering events increases with imaging depth (Fig. 5.3E), photon packets propagating deeper are less likely to be detected regardless of the NA values. On the other hand, photon packets with shorter propagating depths experienced fewer scattering events and are more likely to be detected under all NA values. This explains why NA influences A-line amplitude more at shorter depths than deeper depths, as shown in Fig. 5.6C.

Fig. 5.6D plots the fitted histograms of scattering events in blood from detected photon packets for different NA values, where each histogram is normalized by its respective maximum value. Fig. 5.6D confirms our previous hypothesis of increased detection of multiply scattered photon packets in Figs. 5.6A-5.6C, where the histogram broadens with reduced NA values. Since the optical properties of blood remain unchanged, this difference is contributed by the changing detection criteria associated with NA.

It is important to note that this simulation presents a simplified view of the influence of OCT detection on SSF. Other variables, including the Gaussian beam profile, longitudinal chromatic aberrations, lateral chromatic aberrations, defocusing, eye geometry, oblique incidence, etc., will collectively influence the illumination and detection criteria as well [122]. However, the above simulation on the relationship between acceptance aperture and angle and SSF establishes a critical foundation for multiple scattering analysis in OCT. Such a relationship suggests no ‘one-size-fits-all’ SSF value exists.

5.5.5 *Ex vivo* experimental results

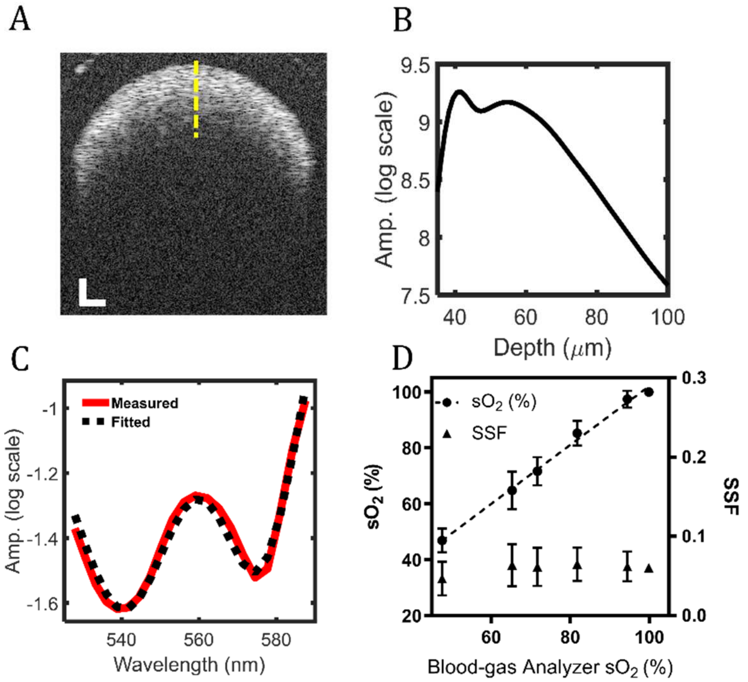

Figure 5.7 (A) vis-OCT B-scan of fully oxygenated blood in a tube phantom; (B) A vis-OCT A-line at the center of tube phantom (yellow-dashed line) in the panel A; (C) Measured attenuation spectrum of fully oxygenated blood; (D) Measured sO_2 and SSF values at different pre-set oxygenation levels.

Fig. 5.7 plots experimental vis-OCT measurements of *ex vivo* blood phantoms. All A-line reconstruction included correction for roll-off and background biases as previously reported [27, 121]. Fig. 5.7A shows a representative B-scan image of the phantom with fully oxygenated ($sO_2 = 100\%$) blood at a hematocrit of 45%, the same as our simulation. The yellow dashed line highlights the location of the A-line plotted in Fig. 5.7B. The A-line is an average of STFT A-lines from 528 nm – 588 nm (central band centered at 558 nm). In Fig. 5.7B, there is a clear delineation between the AW (40 μm depth) and BM (57 μm depth), corresponding to the CFZ.

Attenuation measurement of this A-line using z_0 = 17 μm and Δz = 33 μm, the same as our reference depths in the simulation, gives $\mu_{sHbO_2}(avg)$ = 226 cm^{-1} and SSF = 0.066, agreeing with the simulation.

Fig. 5.7C plots a least-squares fit of the measured attenuation spectrum of fully oxygenated blood (red line) to its theoretical attenuation spectrum (black-dashed line). We performed least-squares fitting using Eq. 5.4 to measure sO_2 using the ratio of the oxygen-dependent coefficients [121] and estimate the SSF. The fitting (R^2 = 0.98) in Fig. 5.7C yields sO_2 = 100%, $\mu_{sHbO_2}(avg)$ = 205 cm^{-1}, and SSF = 0.06, which agrees with the simulated SSF for fully oxygenated blood.

We measured sO_2 and SSF from five sO_2 levels between 40% and 100%. We bootstrapped 100 measurements for each level by shuffling each dataset and randomly selecting 50 B-scans. Fig. 5.7D shows the mean and SD of measured sO_2 (circles) and SSF (triangles). The black dashed line shows the linear best fit relationship ($y = 1.05x - 3.30$) between the blood-gas machine measurements and vis-OCT measurements, indicating excellent agreement between these two independent measurements. The average SSF is 0.060 +/- 0.021, and the average spectroscopic fit R^2 is 0.99. The agreement between simulated and experimentally measured SSF values suggests that our work does not contradict the previously suggested packing factor in whole blood [76] but, instead, adds an additional correction for vis-OCT oximetry.

5.5.4 *In vivo* experimental results

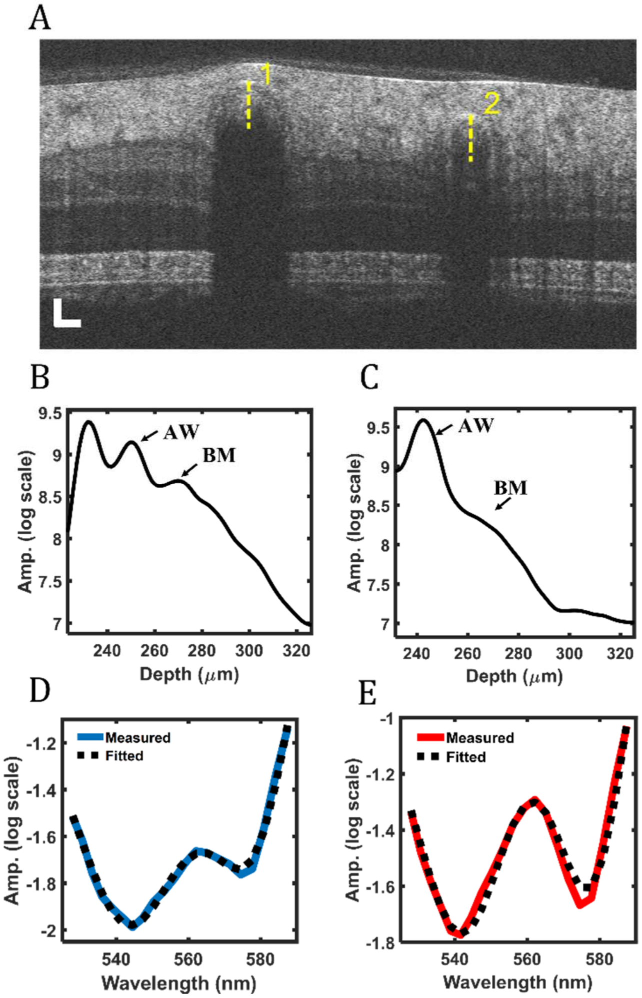

Figure 5.8 (A) Vis-OCT B-scan image of a human retina, where a vein is labeled by 1 and an artery is labeled by 2; (B) Vis-OCT A-line of the vein from the highlighted position in the panel A; (C) Vis-OCT A-line of the artery from the highlighted position in the panel (A); (D) Measured attenuation spectrum from the highlighted vein in the panel A; (E) Measured attenuation spectrum from the highlighted artery in the panel A.

We validated SSF measurement in vis-OCT imaging of human retinas. Fig. 5.8A shows a B-scan image from a 23-year-old male volunteer. We investigated one major vein and one major artery as highlighted by 1 and 2, respectively. The yellow dashed lines highlight the locations of A-lines plotted in Figs. 5.8B & 5.8C. The A-lines are an average of STFT A-lines from 528 nm – 588 nm. The vein plotted in Fig. 5.8B clearly delineated the AW and BM, similar to the simulated A-line (Fig. 5.4A) and ex vivo A-line (Fig. 5.7B). In the artery plotted in Fig. 5.8C, this delineation is less obvious, and there is a change in slope near 260 μm depth where the BM is typically located, which can be caused by higher, pulsatile blood flow in arteries leading to less precise spatial averaging. We also observe a small valley near the center of the vessel in Fig. 5.8C, which may also be associated with more turbulent flow patterns in arteries. Nevertheless, the measured optical properties of blood also agreed with our simulated and e*x vivo* experimental results. Fig. 5.8D shows a least-squares fit of the attenuation spectrum measured in the vein. The best fit yields sO_2 = 59% (R^2 = 0.99) and SSF = 0.07. Fig. 5.8E shows the fitting results for the artery, where sO_2 = 100% (R^2 = 0.97) and SSF = 0.07.

5.6 DISCUSSION AND CONCLUSION

Accurate vis-OCT oximetry remains challenging because of systemic uncertainties introduced by multiple scattering. This work establishes a new correction factor SSF to account for multiply forward scattered photons in blood. Using MC simulation, we found that SSF is near 0.06, significantly smaller than the reported packing factor ($W = 0.3025$) [11, 76, 113]. Documented photon packets' trajectories indicate that most detected photon packets belong to Class I, meaning they are ballistic photon packets and return to the detector with minimal deviation from their incident axis. We found that these Class I photon packets were scattered multiple times, which is only possible if they are primarily forward scattered. We further investigated how different NAs influence the measured SSF. We found that physically reasonable NA values in the human retinal imaging yield SSF values between 0.02 and 0.09, suggesting that NA substantially impacts the measured SSF. As a result, vis-OCT should not use rigid, *a priori* models for retinal oximetry when researchers use different system hardware designs and image different eyes.

We imaged *ex vivo* bovine blood phantoms using vis-OCT as the first validation of our simulation findings. After correcting systemic biases from the background and roll-off, we measured sO_2 and SSF and compared vis-OCT measurements with blood-oxygen analyzer measurements. We found that the average SSF was 0.060 +/- 0.021, almost identical to the simulated results. We further performed vis-OCT sO_2 measurements in the human retina and found that SSF was 0.06 and measured sO_2 values consistent with physiological ranges for arteries and veins. This work is the first comprehensive investigation and validation of blood's attenuation spectrum in vis-OCT using simulation, *ex vivo* phantom imaging, and human retinal imaging.

Using the packing factor to scale the scattering coefficient in our MC simulation resulted in SSF values in excellent agreement with experimental data. As suggested in the literature, the packing factor is the result of correlated scatterings among densely packed RBCs [76, 91, 123, 124]. As RBC concentration increases, coherent interferences can affect the far-field scattered field, which is nonlinearly correlated with RBC density and is likely dependent on the orientations of individual RBCs. While MC simulation does not directly account for orientation-dependent scattering, it can replicate their statistical influence by scaling the input μ_s by W.

Furthermore, previous experimental tests of blood's scattering coefficient were performed using an integration sphere [77, 78, 91, 105, 125], which does not spatially filter detected photons as vis-OCT does. Our SSF combines the influence of scattering effects from blood hemodynamics (e.g., packing factor) and spatial filtering by the imaging modality (e.g., acceptance aperture and angle) on the effective μ_s measured by vis-OCT.

One limitation in our simulation is the assumption of blood as a homogenous medium. In reality, RBC packing density and orientations are affected by blood flow, blood velocity, vessel size, and incident angle [78, 108, 126-128]. These factors can alter scattering cross-section and directionality, changing the optical properties assumed in this work. Although significant spatial averaging may suppress these variations, researchers should carefully monitor the variability of SSF to ensure a suitable oximetry model.

We investigated a suite of parameters influencing vis-OCT detection and conclude that a combination of low NA and multiple forward scattering causes a significant reduction of the measured scattering coefficient of blood. This enables detection of ballistic photons penetrating deep into retinal vessels and absorption-dominated spectroscopic measurements. In the future, researchers should use these conclusions to inform parameters in the sO_2 model.

Chapter 6

Adaptive spectroscopic visible-light optical coherence tomography for human retinal oximetry

6.1 MOTIVATION

Vis-OCT can measure blood's oxygen-dependent spectrum with depth resolution, enabling retinal oximetry. However, current methods fail to separate signals and noises not originating from blood called spectral contaminants (SCs) from the measurement. This harms accuracy and repeatability of retinal oximetry measurements. The statistical consequences of SCs are exaggerated in the human eye, where signals are lower and motions are increased.

6.2 SUMMARY

Retinal oxygen saturation (sO_2) reflects the eye's functional responses to pathological alterations that may lead to vision loss. Visible-light optical coherence tomography (vis-OCT) offers the potential to quantify retinal sO_2 noninvasively in the clinic but is presently unreliable due to unwanted signals referred to as spectral contaminants (SCs). Furthermore, no comprehensive strategy exists to isolate true oxygen-dependent signals from SCs in vis-OCT. Therefore, we developed adaptive spectroscopic vis-OCT (Ads-vis-OCT), which adaptively removes SCs and measures sO_2 under unique conditions of each vessel. We validated Ads-vis-OCT in ex vivo blood phantoms and 125 unique retinal vessels from 18 healthy volunteers. In the human retina, we found high repeatability and accuracy compared to a pulse oximeter, setting the stage for clinical translation of vis-OCT oximetry.

6.3 INTRODUCTION

Visual processing is one of the most oxygen-demanding functions in the human body [129, 130]. Diseases such as glaucoma and diabetic retinopathy cause pathological changes in the eye, leading to irreversible vision loss and even blindness [80, 130]. The retina regulates oxygen supply and extraction in response to pathological changes to satisfy altered metabolic demands [80, 130-135]. Hence, changes in oxygen saturation (sO_2) have been agreed to be a sensitive biomarker for several retinal diseases and may be evident before irreversible vision loss occurs [80, 136].

Optical coherence tomography (OCT) enabled noninvasive retinal imaging at a spatial resolution of a few micrometers [1, 5, 137] and has been considered as the “gold standard” for examining structural damages or therapeutic efficacy in nearly all vision-threatening diseases. However, low optical contrast in blood within the near-infrared (NIR) spectral range confounded OCT’s sO_2 measurements [82, 138, 139]. Recently, visible-light OCT (vis-OCT) [9, 18, 19, 25, 65, 132, 140] showed promise in overcoming the contrast limit because visible light is more sensitive to the optical absorption signatures of blood [30, 82] than NIR light. Researchers obtained blood’s depth-resolved, oxygen-dependent spectrum using a short-time Fourier transform (STFT) [18] of vis-OCT data. Such depth-resolved analysis by vis-OCT has the potential to isolate blood signals from other tissues, offering three-dimensional (3D) oxygenation measurements and improved accuracy, as compared with non-depth-resolved modalities such as fundus photography [141].

However, existing vis-OCT oximetry [18, 19, 93] does not take full advantage of depth information and remains limited in accuracy and repeatability, hampering its clinical impact. One fundamental limitation is the presence of unwanted signals referred to as spectral contaminants (SCs). We define SCs as any erroneous spectra not associated with blood's optical attenuation and classify them into sample-dependent and system-dependent SCs.

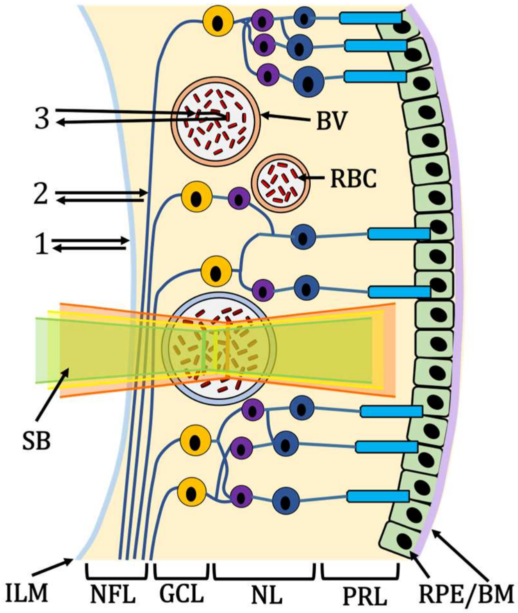

Figure 6.1. Illustration of the human retina composed of inner-limiting-membrane (ILM), Retinal Nerve Fiber Layer (NFL), blood vessels (BV; red is the artery, blue is vein), red blood cells (RBC), ganglion cell layer (GCL), nuclear layers (NL) representing the outer nuclear layer to the outer nuclear layer, photoreceptor layers (PRL) containing rods and cones, and the retinal pigment epithelium and Bruch's membrane (RPE/BM). Number 1 highlights the photon path of a specular reflection; 2 highlights the photon path of backscattering without blood attenuation; 3 highlights the

photon path backscattering from red blood cells. A scanning beam (SB) is composed of visible-light wavelengths (green, yellow, and red illustrate different spectral bands of the beam).

Fig. 6.1 illustrates the human retina and sources of sample-dependent SCs. The spectral signatures of vis-OCT signals contain contributions from three groups of detected photons: specularly-reflected photons (group 1), backscattered photons not interacting with blood (group 2), and backscattered photons interacting with blood (group 3). Various photon interactions with tissues above or in a vessel, such as inner limiting membrane (ILM), retinal nerve fiber layer (RNFL), vessel wall, and red blood cell (RBC) body, can add SCs to sO_2 measurements.

System-dependent SCs come from the optical illumination, detection, and processing of the vis-OCT signals. We identified three key system-dependent SCs: spectrally-dependent roll-off (SDR), spectrally-dependent background bias (SDBG), and longitudinal chromatic aberration (LCA). Recently, we showed how SDR [27] and SDBG [28] contaminate spectroscopic measurements in imaging *ex vivo* blood samples and *in vivo* human retinas. LCA (illustrated by the green, yellow, and red colors in the scanning beam in Fig. 6.1) has also been shown as a contaminant for structural and spectroscopic OCT [22, 46, 63].

Previously, other groups and we analyzed vis-OCT backscattered signals from a vessel's posterior wall (PW) to measure sO_2 in rodents [18, 19, 132, 140] without fully correcting the abovementioned SCs. The fundamental limitation of such measurement is that it does not directly measure the attenuation coefficient of blood and is therefore susceptible to SCs. Furthermore, these methods cannot measure

sO_2 from vessels where the PW is undetectable due to strong blood attenuation in vessels with large diameters.

SCs are increasingly magnified and unpredictable in human imaging compared to small animal imaging due to physical and experimental constraints. In particular, human imaging must contend with reduced illumination powers for ocular laser safety and patient comfort, strong motions from the awake eyes and bodies, and larger variation in retinal anatomies [9, 25, 93, 142]. Ideally, clinical retinal oximetry should be free from SCs and reliable across various vessel diameters.

In this work, we developed adaptive spectroscopic vis-OCT, or Ads-vis-OCT, which isolates blood's oxygen-dependent spectrum by conforming measurements to the unique properties of each vessel. We validated Ads-vis-OCT's accuracy in *ex vivo* samples made from bovine blood at 17 sO_2 levels (Supplementary Section 1). We then measured sO_2 in 125 unique retinal vessels from 18 human volunteers imaged in a clinical environment. Ads-vis-OCT produced highly repeatable sO_2 measurements ($\leq 2.5\%$) across a broad range of vessel types and agreed within 2.1% of pulse oximeter readings in major arteries. Our sO_2 results required no pre or post-calibration to account for any systemic bias, suggesting that Ads-vis-OCT is insensitive to SCs or imaging environment. We compared Ads-vis-OCT to other reported vis-OCT sO_2 techniques and found significant improvements, including a greater than 3-fold increase in measurement repeatability.

6.4 PRINCIPLE OF ADS-VIS-OCT

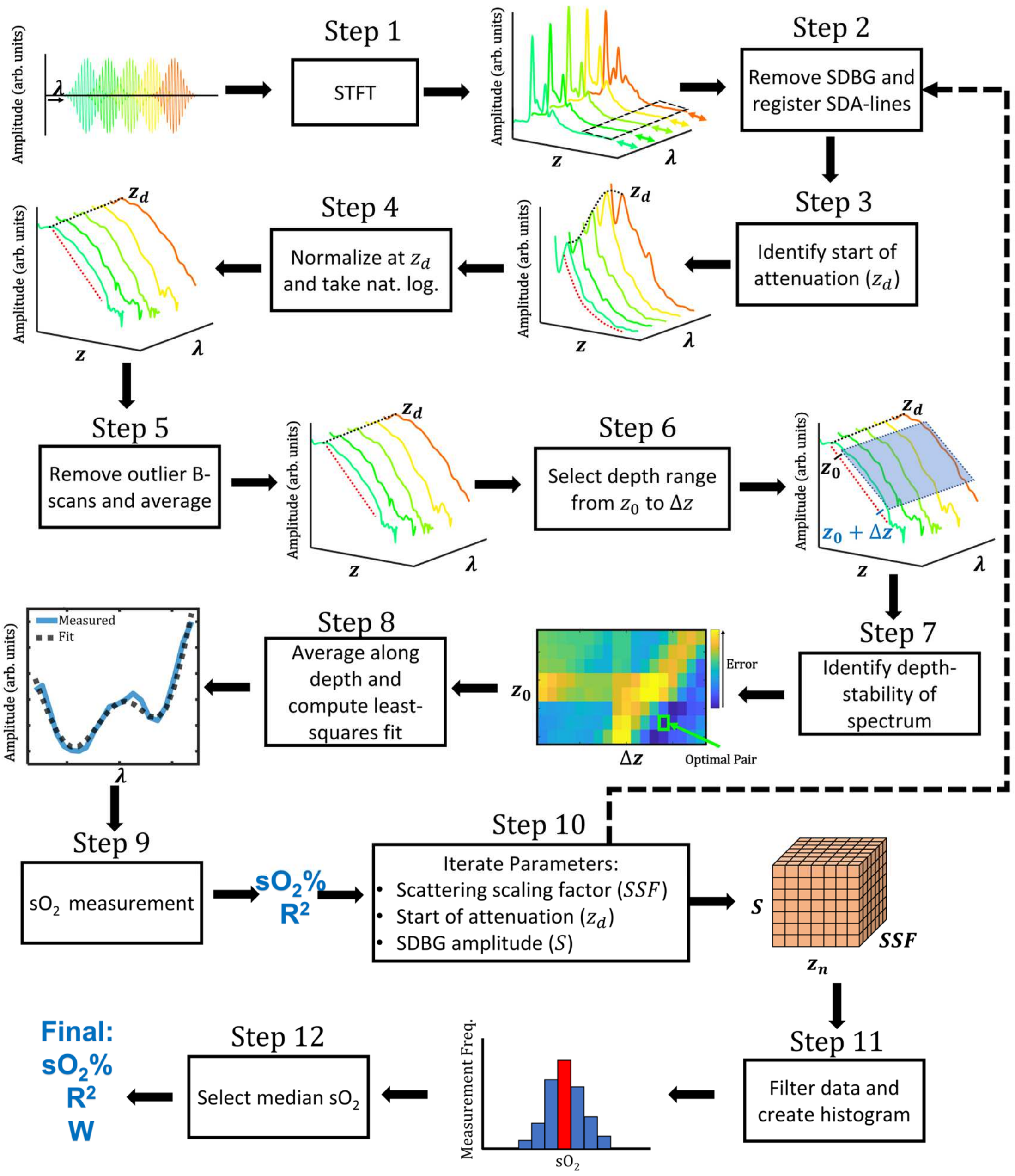

Figure 6.2. Flow chart overview of Ads-vis-OCT processing for retinal oximetry. Arrow direction highlights the input and output of each step.

Fig. 6.2 shows the flow-chart for Ads-vis-OCT, where figures before and after each step depict their respective inputs and outputs. In Step 1, we computed the STFT of the full-band interference fringe to obtain 21 spectrally-dependent A-lines

(SDA-lines) from 528 nm – 588 nm (see Short-time Fourier Transform in Methods). The outputs are the SDA-lines, which encode depth (z-axis) and wavelength (λ-axis). LCA and depth-dependent dispersions [22, 143] wavelength-dependent shifts along the z-axis (colored arrows), and the SDBG causes signal biases along the z and λ-axes (highlighted by black-dashed box). We processed SDA-lines in vessels for each acquired B-scan.

In Step 2, we axially registered the SDA-lines across all B-scans to account for misalignments caused by motions, dispersion, and LCA. We also removed the SDBG bias in the SDA-lines [144].

In Step 3, we automatically identified the depth (z_d) corresponding to the beginning of signal decay in the blood (see Normalization Model for Spectroscopic vis-OCT in Methods). As the Step 3 output, the spectrum at z_d is highlighted by the black dashed line and the blood signal decay is highlighted by the red dashed line.

In Step 4, we normalized the SDA-lines by their amplitude at z_d and computed their natural logarithm (see Normalization Model for Spectroscopic vis-OCT in Methods). The Step 4 output is the natural logarithm SDA-lines (NL-SDA-lines). The black dashed line highlights the spectrum at z_d, which is constant across λ after normalization.

In Step 5, we coarsely measured signal quality in NL-SDA-lines (NL-SDA-lines) in each B-scan (see Supplementary Section 7). After removing outlier B-scans not passing pre-defined quality thresholds, we averaged the remaining B-scans to reduce noise, yielding a single set of NL-SDA-lines.

In Step 6, we selected the depths for spectroscopic measurement. The Step 6 outputs are the starting depth (z_0) and depth range (Δz) for the measurement. The blue box highlights the measurement range for selected depths and spectral sub-bands. We averaged NL-SDA-lines in the blue box along the z-axis, yielding a one-dimensional (1D) STFT spectrum (see Depth Averaging in Methods).

In Step 7, we assessed how the STFT spectrum changed along the depth of the vessel (see Depth Selection in Methods). The Step 7 output is the spectral-stability matrix (SSM), which plots how the spectrum shape changes (error) with depth as a function of z_0 (starting depth) and Δz (depth range). We selected the optimal pair of z_0 and Δz with the smallest error (green box), representing the depth region in the vessel where optical attenuation is most constant.

In Step 8, we averaged the NL-SDA-lines within the optimal depth range and fit the STFT spectrum to a linear combination of oxygenated and deoxygenated blood attenuation spectra (see Oximetry Fitting Model in Methods). The Step 8 output is the least-squares regression fit (black dashed line) to the measured STFT spectrum (blue line). In Step 9, we calculated oxygenation from the regression, outputting sO_2 (%) and coefficient of regression (R^2).

In Step 10, we repeated steps 2-9 for small variations in three parameters, including scattering scaling factor SSF, the start of attenuation depth z_d, and SDBG amplitude scaling factor S (see Supplementary Section 7). The outputs of Step 10 are two three-dimensional (3D) matrixes that store the measured sO_2 and R^2, respectively, where each dimension corresponds to each of the three parameters.

In Step 11, we organized and filtered the data from each iteration (see Supplementary Section 7). In Step 12, we selected a central sO_2 value from the distribution (red bin in the histogram) as the final output and its corresponding R^2 and SSF values.

6.5 RESULTS

6.5.1 Optimal tissue normalization

In Ads-vis-OCT Step 4, we normalize SDA-lines using a reference signal in the tissue to remove SCs. However, there is no consensus in the literature on the optimal location for normalization or even if it is necessary. Here, we highlight four potential tissue normalizations for vis-OCT oximetry: Method 1: no normalization, as reported by Yi *et al.* (17), Chen *et al.* (25), and Pi *et al.* (22); Method 2: normalization by the nerve fiber layer (NFL), which is typically anterior to the retinal vessels, as reported by Song *et al.* (26) and suggested by Chong *et al.* (19, 20); Method 3: normalization by the anterior vessel wall, which can be highly reflective and is immediately above the blood signal; and Method 4: normalization at the start of signal decay in the blood (z_d), which is used in Ads-vis-OCT. We compared the influence of Methods 1-3 with Method 4 on the STFT spectra in human retinal vessels. For a fair comparison, we used the same SDA-lines and vessel measurement depths for all methods.

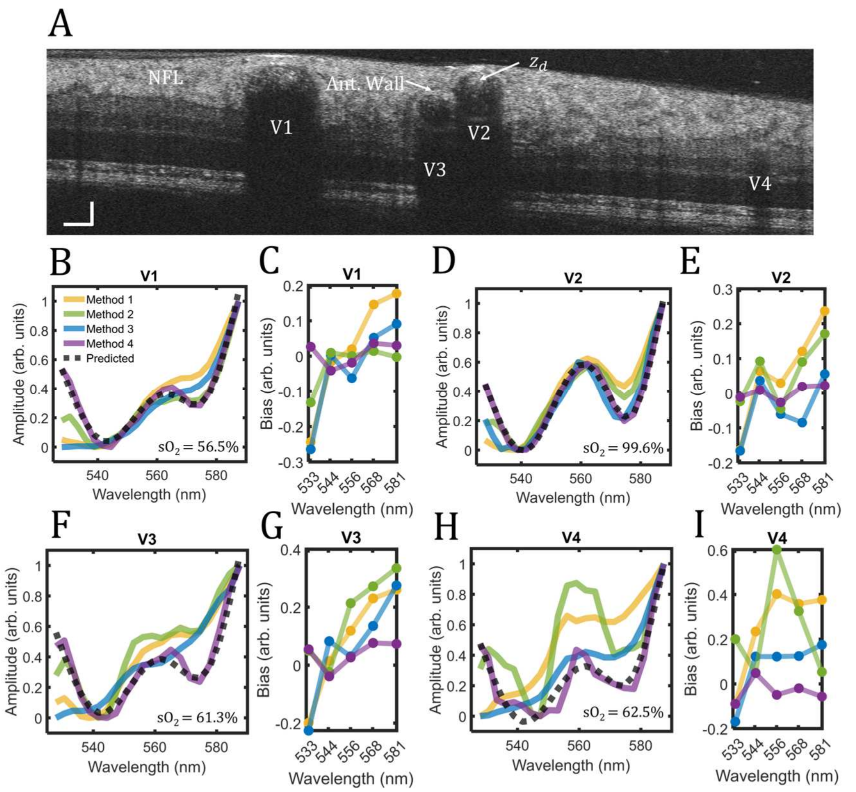

Figure 6.3. Spectroscopic normalizations in the human retina. (A) vis-OCT B-scan of healthy human retina; vessels labeled V1-V4 were identified as vein, artery, vein, and vein, respectively; (B) Measured spectra in V1 with no normalization (yellow), normalization by NFL (green), normalization by the anterior vessel wall (blue), and normalization by the start of signal decay in blood (z_d) (purple), respectively; predicted spectrum for $sO_2 = 99.6\%$ (gray dashed line); (C) Bias for each normalization with respect to predicted spectrum at five wavelengths; (D & E) Same analysis for V2 and $sO_2 = 56.5\%$; (F & G) Same analysis for V3 and $sO_2 = 61.3\%$; (H & I) Same analysis for V4 and $sO_2 = 62.5\ \%$

Fig. 6.3A is a vis-OCT B-scan image acquired 1.7-mm superionasal to the optic disc from a 37-year-old volunteer. We measured STFT spectra in vessels V1-V4 with diameters of 168 μm, 120 μm, 79 μm, and 43 μm, respectively. Fig. 6.3B plots the measured STFT spectra in V1 for all four normalization methods (yellow, green, blue, and purple, respectively). The gray dashed line plots the literature-derived spectrum (see Methods – Oximetry fitting model) predicted using least-squares fit in Ads-vis-OCT (sO_2 = 56.5%). Since we could not guarantee that Methods 1-3 completely removed SCs, it was mathematically inappropriate to fit their STFT spectra with the Ads-vis-OCT fitting model. Instead, we used the Ads-vis-OCT predicted spectrum (gray dashed line) as a reference with which to identify SC-derived errors. We scaled all STFT spectra between 0 and 1 in the plots.

Comparing the normalizations, Methods 1-3 measure STFT spectra that deviate significantly from the predicted spectrum, while Method 4 agrees with the predicted spectrum. We quantified the general trends of the spectral biases from Fig. 6.3B in Fig. 6.3C for five STFT bands with their respective central wavelengths at 533 nm, 544 nm, 556 nm, 568 nm, and 581 nm. The bias is defined as the difference between each measured spectrum in Fig. 6.3B and the predicted spectrum for the specified central wavelengths of the STFT bands. The bias trends for Methods 1-4 highlight different error-inducing SCs, confirming the observation of different spectral features in Fig. 6.3B. Although Methods 1-3 induce larger bias values for the longest wavelengths (581 nm) versus the shortest wavelengths (533 nm), their trends are non-trivial (e.g., non-linear or non-monotonic) with different amplitudes and signs. Such biases may represent either incomplete removal of SCs or the introduction of new SCs after tissue normalization.

Figs. 3D & 3E, 3F & 3G, and 3H & 3I show the same analysis for vessels V2, V3, and V4, respectively. Similar to vessel V1 (Figs. 3B & 3C), biases in vessel V2 (Figs. 3D & 3E) for Methods 1-3 are generally higher at longer wavelengths

(581 nm) than for shorter wavelengths (533 nm), but differ at middle wavelengths (544 nm-568 nm). Also, compared with V1, V2 bias magnitudes are generally increased for Methods 1 & 2 but reduced for Method 3. The unpredictability of SCs becomes particularly noticeable in vessels V3 & V4, which are smaller than V1 & V2 and buried deeper below the NFL. Vessel V3 (Figs. 3F & 3G) has nearly double the bias amplitudes compared with V1 & V2. Also, Method 2 bias is highest at the middle through longer wavelengths (556 nm – 581 nm), a trend not seen in V1 and V2. Finally, vessel V4 demonstrates the most significant biases among all the vessels, with a particularly large bias at the middle wavelength (556 mm).

Fig. 6.3 indicates that normalization Methods 1-3 induce wavelength-dependent biases that vary among vessels and are unpredictable. Method 4 used in Ads-vis-OCT consistently yields the least bias across the entire spectral range and agrees well with the predicted model. The observation that SCs vary with retinal locations, eyes anatomies, and imaging sessions makes proper normalization essential for accurate and repeatable spectroscopic analysis.

6.5.2 Retinal oximetry around the optic disk

An oximetry map of the optic disk can help investigate oxygen delivery or extraction in the entire retina. Fig. 6.4A shows a representative vis-OCT oximetry map of the optic disk with a 4.8×4.8 mm^2 FOV in a 23-year-old volunteer. We measured sO_2 in 17 vessels (10 arteries and seven veins) ranging from 37 μm to 168 μm in diameter.

We pseudo-colored the 17 vessels according to their measured sO_2 values onto a vis-OCT fundus image (Fig. 6.4A) and plotted the sO_2 values in the bar chart (Fig.

6.4B). The measured sO_2 across all arteries was 95.8±4.4% (n = 10) and the measured sO_2 across major arteries (diameter $\geq$ 100 μm) was 97.3%±2.8% (n = 6). The average pulse oximeter measurement from the index finger was 98%, agreeing well with the vis-OCT measured sO_2 from the major arteries. The measured sO_2 across all veins was 59.0±3.2%.

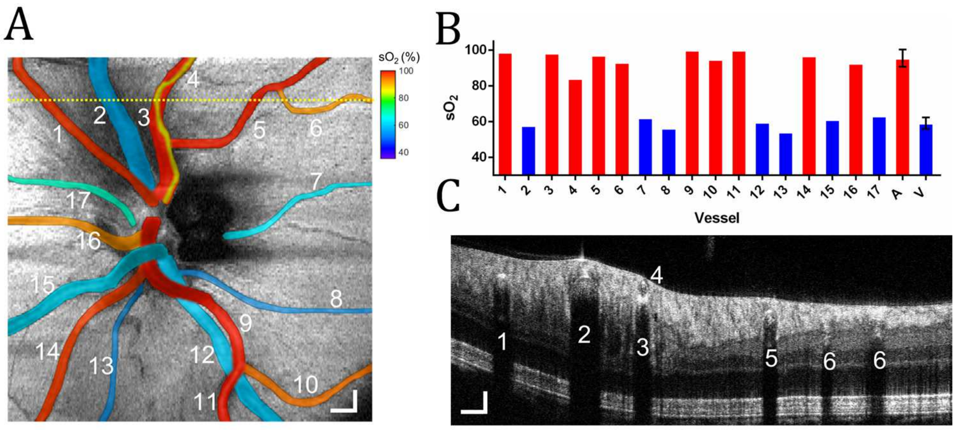

Figure 6.4. Oximetry map of the optic disk. (A) sO_2 measurements in 17 vessels in the optic disk from a healthy 23-year-old. The sO_2 values pseudo-colored and overlaid onto the fundus image. Scale bar: 300 μm; (B) Bar chart plots sO_2 measurements from panel A in individual arteries (red bar) and veins (blue) numbered from 1 to 17, as well as average sO_2 in all arteries and all veins; (C) B-scan from the position highlighted by the yellow dashed line in panel A. Scale bars: 150 μm.

Fig. 6.4C shows a B-scan from the location highlighted by the dashed yellow line in Fig. 6.5A. We can observe a small artery (vessel 4, diameter = 37 μm) directly above a major artery (vessel 3, diameter = 122 μm). The measured sO_2 value in vessel 3 is 98.3%, consistent with pulse oximeter reading (98%); the measured sO_2 value in vessel 4 is 85.8%. We measured sO_2 values from both vessels, demonstrating the unique depth-resolved sO_2 imaging capability permitted by vis-OCT. Axially overlapping vessels in the retina require SC removal since, for example, attenuation from vessel 4 will contaminate that in vessel 3. Vessel 3's agreement with the pulse oximeter, despite sitting below a vessel with significantly lower sO_2, confirms the removal of SCs from posterior tissues *in vivo*. The posterior wall of vessel 4 appears to be in direct contact with the anterior wall of vessel 3. We hypothesize that the lower sO_2 in vessel 4 is partially caused by oxygen diffusion to the contacting vessel or surrounding RNFL.

6.5.3 Retinal oximetry in a healthy volunteer group

We performed Ads-vis-OCT retinal oximetry in 18 volunteers without known ocular diseases. We measured sO_2 in 125 unique vessels (72 arteries and 53 veins) within a 3.4 mm radius of the optic nerve head.

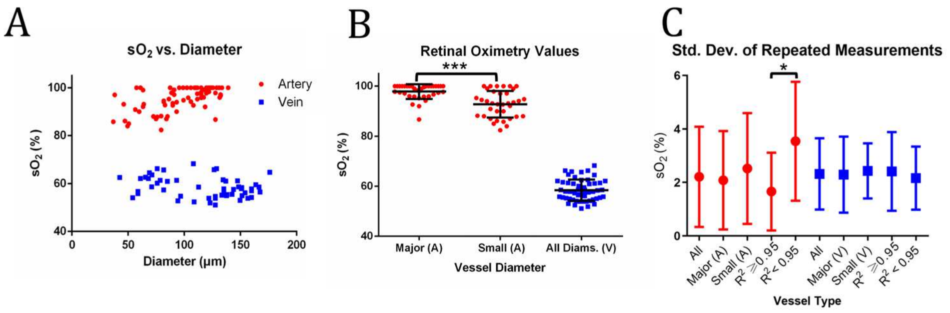

Figure 6.5. Oximetry map of the optic disk. (A) sO_2 measurements in 17 vessels in the optic disk from a healthy 23-year-old. The sO_2 values pseudo-colored and overlaid onto the fundus image. Scale bar: 300 μm; (B) Bar chart plots sO_2 measurements from panel A in individual arteries (red bar) and veins (blue) numbered from 1 to 17, as well as average sO_2 in all arteries and all veins; (C) B-scan from the position highlighted by the yellow dashed line in panel A. Scale bars: 150 μm.

Fig. 6.5A shows sO_2 from unique arteries (red) and veins (blue) plotted as a function of vessel diameter. Arterial sO_2 values show a decreasing trend with decreasing vessel diameter. We determined that vessel diameter was a statistically significant factor (see Methods – Statistical Analysis) in this trend ($p = 4.35 \times 10^{-6}$). The diameter-dependent trend is consistent with oxygen gradients observed in other precapillary arteries [145-151]. Since smaller vessels generally offered less attenuation contrast and fewer-averaged pixels compared to larger vessels, they were potentially more sensitive to noise. We investigated whether the sO_2 decrease was an artifact of lower spectral fit R^2. We determined that R^2 was not a statistically significant factor (see Methods – Statistical Analysis) in this trend ($p = 0.701$). Finally, venous sO_2 slightly increases with decreasing vessel diameter, but the trend is not statistically significant ($p = 0.232$). Spectral fit R^2 is also not significant ($p = 0.070$) in determining sO_2 in veins.

To account for the observed sO_2 gradient with diameter, we computed average sO_2 in arteries across two diameter groups (diameter ≥ 100 μm and diameter < 100 μm). Fig. 6.5B shows sO_2 measurements for major arteries (diameter ≥ 100 μm), small arteries (diameter < 100 μm), and veins with all diameters. Major arteries (n = 36) had sO_2 = 97.9 ± 2.9%. Small arteries (n = 36) had sO_2 = 93.2 ± 5.0%. The difference in sO_2 between the two groups was statistically significant ($p = 4.01 \times 10^{-6}$). Average spectral fits were R^2 = 0.96, 0.93, and 0.95 for major arteries, small arteries, and all veins, respectively.

We acquired repeated scans of 42 unique vessels and calculated their average standard deviations (SDs) (24 unique arteries and 18 unique veins across 12 volunteers). Fig. 6.5C shows average SDs for unique arteries (red) and veins (blue). All arteries and veins had average SDs of 2.2% and 2.3%, respectively. First, we investigated repeatability for arteries and veins of diameters larger and smaller than 100 μm. Larger arteries (n = 17) and smaller arteries (n = 7) had average SDs of 2.1% and 2.5%, respectively. Larger veins (n = 15) and smaller veins (n = 3) had average SDs of 2.3% and 2.4% respectively. There was no statistically significant difference between the average repeatability values for any of the groups (two-sample T-test). Finally, we investigated repeatability for best spectral fits ($R^2 \geq 0.95$) and relatively lower spectral fits ($R^2 < 0.95$). Best fit arteries (n = 17) and lower fit arteries (n = 7) had average SDs of 1.7% and 3.5%, respectively. Best fit veins (n = 11) and lower fit veins (n = 7) had average standard deviations of 2.4% and 2.2%, respectively. The difference between the average SDs for the artery groups was statistically significant ($p = 0.02$), although one analyzed artery with $R^2 < 0.95$ was an outlier (SD = 6.83%). Without the outlier, average SD $R^2 < 0.095$ arteries is 3.0%, not a statistically significant difference ($p = 0.09$). Statistics for each unique vessel in repeatability analysis shown in Supplementary Section 2.

We estimated the ground-truth arterial sO_2 using a pulse oximeter fastened to the finger during imaging and compared it with Ads-vis-OCT measured sO_2 in major arteries (diameter ≥ 100 um) from 12 subjects. Average Ads-vis-OCT sO2 in tested subjects was 98.3%, in very close agreement with that from the pulse oximeter (sO2 = 98.6%). We measured the root-mean-squared-error (RMSE) between pulse oximeter sO_2 and Ads-vis-OCT sO_2 for each unique artery in each respective subject (see Supplementary Section 2). The average RMSE between vis-OCT and the pulse oximeter was 2.1%, the same value as the SD of repeated measurements in major arteries. This suggests that Ads-vis-OCT measured sO_2 may be within noise-limited agreement with the pulse oximeter.

6.5.4 Comparison with non-adaptive retinal sO_2 measurements

To quantify the influence of adaptive processing (Fig. 6.2) on sO_2, we compared measurements using non-adaptive vis-OCT methods. Briefly, we define non-adaptive processing as using fixed algorithms or parameters. To achieve a non-adaptive version of Ads-vis-OCT, we omitted Steps 3, 5, 7, 10, 11, and 12 from the flow chart in Fig. 6.2, which eliminates the adaptive signal normalization, adaptive quality control, adaptive depth selection, and parameter iterations (see Supplementary Section 8 for more detail). The above algorithm is a singular measurement of blood's attenuation coefficient along a predefined depth range, which is basis of all retinal oximetry measurements. Hereon, we refer to this as the 'fixed attenuation method' (FA method). Next, we compared Ads-vis-OCT with the PW method reported previously by Yi *et al.* [18, 152]

Vessel Type	Method	Adaptive	Success %	Mean sO_2 (%)	SD sO_2 (%)	Ves. Rep. (SD %)	Fit R^2
Major Artery (n = 32)	FA	No	89	97.5	5.2	2.3 (n = 15)	0.92
Small Artery (n = 34)	FA	No	94	86.5	10.9	9.1 (n = 7)	0.86
Vein (n = 45)	FA	No	85	52.6	12.5	8.9 (n = 15)	0.87
Major Artery (n = 13)	PW	No	36	90.7	7.5	6.0 (n = 3)	0.94
Small Artery (n = 33)	PW	No	92	89.0	12.8	7.4 (n = 6)	0.95

Vein (n = 17)	PW	No	32	62.4	13.3	Not Enough Data	0.94
Major Artery (n = 36)	Ads	Yes	100	97.9	2.9	2.1 (n = 17)	0.96
Small Artery (n = 36)	Ads	Yes	100	93.2	5.0	2.5 (n = 7)	0.93
Vein (n = 53)	Ads	Yes	100	58.4	4.3	2.3 (n = 18)	0.95

Table 6.1. Comparison of adaptive and non-adaptive vis-OCT oximetry; n is the number of vessels analyzed for each group; FA is the fixed attenuation method; PW is the posterior wall method; Ves. Rep. is the repeatability of unique vessels as defined in Results – Retinal Oximetry in a Healthy Population

Table 6.1 compares sO_2 measurement in the same 125 unique vessels (Fig. 6.5) using the FA method, PW method, and Ads-vis-OCT. Unlike Ads-vis-OCT, the FA and PW methods yielded a handful of extreme outliers (> 7 SDs from the Ads-vis-OCT mean). To highlight the failed measurements while also reducing statistical bias, we report the success rate, defined as the percent of physiologically viable measurements from each group of vessels. Additionally, the PW method also fails when there is insufficient visibility of the PW. Empirically, we determined the bottom wall was visible when its average STFT intensity was at least 1 dB greater than the noise floor; otherwise, the measurement was considered unviable.

Using the FA method, we successfully measured most vessels ($\geq$ 85% success). This yielded mean sO_2 values of 97.5 $\pm$ 5.2% for major arteries, 86.5 $\pm$ 10.9% for small arteries, and 52.6 $\pm$ 12.5% for all veins. Comparing with Ads-vis-

OCT, the FA method measures similar sO_2 for larger arteries, (97.5% vs. 97.9%), but underestimates by 7% for small arteries (86.5% vs. 93.2%) and by 6% for all veins (52.6% vs 58.4%). SDs of each vessel group increase 2-3-fold using the FA method, as compared with Ads-vis-OCT. Individual vessel repeatability is similar for major arteries between the two methods (2.3% and 2.1%) but is nearly 4-fold higher for small arteries (9.1% and 2.5%) and veins (8.9% and 2.3%). The less stable measurements are consistent with their worse spectral fits (R^2). In particular, small arteries and veins have R^2 of 0.86 and 0.87, lower than 0.93 and 0.95 for the same Ads-vis-OCT groups.

The PW method fails to perform viable sO_2 measurements in half of the vessels. Specifically, most major arteries and veins failed due to their larger vessel diameter and insufficient visualization of the posterior wall. PW-measured major arteries yielded an sO_2 of 90.7 ± 7.5%, with 6.0% repeatability. These sO_2 measurements are lower and less stable than in Ads-vis-OCT (97.9 ± 2.9%, with 2.1% repeatability). The mean sO_2 of 90.7% is inconsistent with pulse oximeter readings (e.g., $sO_2 \geq 95\%$). Smaller arteries yielded 92% successful measurement but had 4% sO_2 lower than in Ads-vis-OCT (89.0% and 93.2%), had a broader distribution (SD = 12.8% vs. 5.0%), and were less repeatable (7.4% and 2.5%). Additionally, the mean sO_2 was almost the same between PW-measured major and small arteries, meaning it failed to detect the statistically significant difference measured by Ads-vis-OCT. Finally, all veins measured with the PW method had 4% higher sO_2 than Ads-vis-OCT with a broader distribution (SD = 13.3% vs. 4.3%) (insufficient data to measure repeatability). Interestingly, the PW method has higher spectral fits (R^2) than the FA method, comparable to those in Ads-vis-OCT. However, PW measurements also have significantly increased uncertainties, possibly caused by the sO_2 fitting model [18, 152]. Since the PW method does not properly remove SCs, it can misinterpret SCs as true sO_2-carrying signals. In this case, a high R^2 with high measurement uncertainty indicates the model overfitted the data. Such overfitting can lead to systemic biases and uncertainties intrinsic to the least-squares fit, evident in Table 6.1. On the contrary, the FA method and Ads-vis-OCT directly correlate increased uncertainty with lower R^2 fit using the same regression model developed in this work (see Oximetry fitting model in Methods).

6.6 DISCUSSION

Existing vis-OCT oximetry shows limited repeatability caused by SCs and uniformly applied algorithms to all vessels. To overcome this challenge, we developed a new model for vis-OCT oximetry and an adaptive processing method that optimizes SC removal and sO_2 measurement. In the human retina, sO_2 measurements across all unique arteries and veins were highly repeatable (SD = 2.2% and 2.3%, respectively). Furthermore, the RSME of 2.1% between major artery sO_2 and a pulse oximeter was the same as the average SD of major artery sO_2 after repeated measurements (SD = 2.1%), suggesting that uncertainty was limited by random noise not systemic bias. Across 72 unique arteries from 18 subjects, we found a statistically significant trend between decreased diameter and decreased sO_2. This trend is consistent with previously observed precapillary oxygen gradients [145-151].

In Fig. 6.3, we show that SCs impose biases on vis-OCT STFT spectra. The SCs vary with different vessel locations, sizes, and types (e.g., artery or vein). Normalizing by local, highly reflective tissues like the anterior vessel wall (AW) does not provide repeatable biases. First, most vessels are buried under several layers of retinal tissues like the NFL with varying optical properties [25, 153, 154]. Second, interfaces at the ILM and AW are composed of highly reflective and fibrous tissues. For example, consider vessel V1 in Fig. 6.3. The ILM/NFL interface appears transparent at some parts of the retina but is bright directly above this vessel. Since the brightness is most intense when the interface is orthogonal to the vis-OCT illumination beam, it is likely from specular reflection or high backscattering from the fibrous tissues. A similar trend is seen at the AW interface for V1. While most of the vessel wall has similar intensity to the NFL, the center of the AW exhibits a higher reflectance. Again, this may be a specular reflection or strong backscattering from the fibrous vessel lamina [155, 156]. Meanwhile, V3 in Fig. 6.3 demonstrates no such bright reflectances. Such light-tissue interactions can have spectral profiles dependent upon the incident angle of light, as well as local optical properties such as polarization [154, 156, 157]. We provide an additional example of the unpredictability of retinal backscattering in Supplementary Section 5.

Table 6.1 shows that the current strategies for vis-OCT retinal oximetry fail to achieve desired accuracy and repeatability in sO_2 measurements in our human dataset. Although the FA method attempted to remove SCs, it performed the removal without adapting measurement variables to different vessels and images. Meanwhile, the PW method indirectly measured blood’s attenuation spectrum and did not consider SCs other than the PW itself. Unfortunately, lack of PW visibility in larger vessels (e.g. > 100 μm) prevents this method from measuring sO_2 near the optic disk, a potential limitation to measuring total oxygen delivery and collection in the retina. Additionally, the PW method yielded significantly higher sO_2 uncertainty than Ads-vis-OCT but had comparable spectral fit R^2, meaning it overfitted the measured spectrum. Overfitting not only causes systemic sO_2 bias and uncertainty, but also false confidence (R^2) in the reliability of the results. We suggest a few potential sources of such overfitting below.

First, vis-OCT measures a scattering coefficient of blood lower than that predicted by Mie theory [29, 30]. We can modify the fitted scattering coefficient by multiplying it with the factor SSF. However, the value of SSF in vis-OCT varies significantly among different studies [18, 63, 65, 158]. Recently, we determined using Monte Carlo simulation and experimental validation that our vis-OCT system measures an SSF near 0.06 [29]. However, the PW method uses SSF = 0.2, based on a model-dependent only on hematocrit [18]. We believe the prior conclusion of SSF = 0.2 was the result of incomplete removal of SCs, since a higher SSF results in STFT spectral correlation (see Fig. 3 in Yi et al. [18]) with those measured using Method 1 in Fig. 6.3. Method 1 generally produces a negative bias at shorter wavelengths and a positive bias at longer wavelengths. When the PW method selects SSF = 0.2, it assumes that these biases are all oxygenation-dependent, which may be untrue. Any incorrect assumption of SSF may interact in the fitting model with the power law ($-\alpha \ln(\lambda)$), where α is an arbitrary constant), which exists to correct for the backscattering spectrum from the PW. The power law's monotonic decrease with wavelength is opposite to the bias trend seen in normalization Method 1 and the increased SSF. Therefore, if the predetermined SSF = 0.2 is overestimated, as we predict here, the power law will be overfitted to compensate for this overestimation. In this sense, SSF = 0.2 and the power law both fit common bias trends but incorrectly describe the the physics of the SDA-line (see Eqs. 3.1 & 3.2), leading, in part, to inability to differentiate oxygen-dependent and non-oxygen-dependent variables in the model. We note that the power law are also susceptible to overfitting other SCs such as SDR and SDBG, which typically increase and decrease with wavelength, respectively.

Although the PW model is sensitive to sO_2 values in rodents [19, 132, 152], where SNRs are high, imaging times are extended, and vessels are homogeneous, failure to properly model the light-tissue interaction or remove SCs prevents researchers from predictably assessing sO_2 error or uncertainty in the clinic. Furthermore, such errors and uncertainties may vary with different vis-OCT systems or imaging protocols, challenging reproducibility.

Using Ads-vis-OCT in imaging well-controlled *ex vivo* blood phantoms (Supplementary Section 1), we found spectra consistent with SSF = 0.02-0.10, nearly 10-fold less than the reported SSF = 0.2.The average fitted SSF in the phantom experiment was 0.068 at physiological hematocrit (45%) (Fig. 6.6a). Both of these measurements are consistent with our recent investigation of the scattering coefficient of whole blood in vis-OCT [29]. Since our normalization protocol explicitly isolated the scattering and absorption coefficients of blood from SCs, we anticipated that spectral measurements in the human retina should be comparable to the *ex vivo* phantoms (neglecting any spectral differences between human and bovine blood). We measured the average best-fit W in the human retina as 0.064 (Supplementary Section 1), very close to that value in the *ex vivo* experiments (0.068) and predicted by our simulations [29]. Even though the two experimental conditions were different, we reached nearly identical quantitative conclusions, validating that Ads-vis-OCT removes SCs and appropriately models the measured data.

In summary, we took full advantage of the high-resolution and high contrast in vis-OCT to achieve adaptive, depth-resolved analysis of spectral signatures from light-blood interactions. We developed and validated Ads-vis-OCT for retinal oximetry in 18 healthy volunteers in retinal vessels ranging from 37 μm to 174 μm in diameter in a clinical environment. We found excellent spectral fits, repeatability, and agreements with the pulse oximeter readings, setting the stage for future clinical vis-OCT retinal oximetry applications.

6.6 MATERIALS AND METHODS

6.6.1 Short-time Fourier transform

We multiplied 21 Gaussian windows with the spectral interferogram. Windows were of equal wavenumber (k) full-width at half maximum (FWHM) and spaced equidistantly in k space from 528 to 588 nm. Window FWHM was 11 nm at 558 nm, reducing the average axial resolution to 9 μm in the retina (assuming a refractive index of 1.35).

6.6.2 Normalization model for spectroscopic vis-OCT

To accurately quantify sO2, the oxygen-dependent attenuation spectrum of blood must be isolated from sample-dependent and system-dependent SCs. Eq. 1 describes the generalized SDA-line for a homogenous medium

$$I(\lambda,z) = F(\lambda,z)2\sqrt{I_{samp}(\lambda)I_{ref}(\lambda)}\sqrt{A(\lambda,z)T(\lambda,z_s)\mu_b(\lambda)}e^{-\mu_t(\lambda)(z-z_s)} + B(\lambda,z), \tag{6.1}$$

where λ is the wavelength; z is the depth coordinate; z_s is the surface of the medium with respect to the zero-delay depth z= 0; $\sqrt{I_{samp}(\lambda)}$ and $\sqrt{I_{ref}(\lambda)}$ are the power spectra of the light collected from the sample and reference arms, respectively. The SDR is $F(\lambda,z)$ [27], the LCA transfer function is $A(\lambda,z)$ (see Supplementary Section 4), and the SDBG is $B(\lambda,z)$ [28]. $\mu_b(\lambda)$ is backscattering coefficient of the medium, $\mu_t(\lambda)$ is the attenuation coefficient of the medium, and $T(\lambda,z_s)$ is the double-pass transmission coefficient across the top interface of the medium

The retina-specific model for the SDA-line must consider multi-layered media with different optical properties. After normalizing by the source power spectrum (DC component) and subtracting the SDBG, we write the amplitude of the SDA-line where blood signal decay begins, z_d (Step 3 in Fig. 2), as

$$I(\lambda,z_d) = F(\lambda,z_d)2\sqrt{A(\lambda,z_d)\mu_{b_{blood}}(\lambda)}\prod_{i=1}^{n-1}\left[\sqrt{T(\lambda,z_i)}e^{-\mu_{t_i}(\lambda)(z_{i+1}-z_i)}\right] for\ \ z = z_d, \tag{6.2}$$

where i is the tissue layer and blood is the n^{th} tissue layer. We write the residual SDA-line below z_d as

$$I(\lambda, z) = I(\lambda, z_d) \frac{F(\lambda,z)\sqrt{A(\lambda,z)}}{F(\lambda,z_d)\sqrt{A(\lambda,z_d)}} e^{-\mu_{t_{blood}}(\lambda)(z-z_d)} \; for \;\; z > z_d, \tag{6.3}$$

where $\frac{F(\lambda,z)\sqrt{A(\lambda,z)}}{F(\lambda,z_d)\sqrt{A(\lambda,z_d)}}$ represents the residual LCA and SDR beyond the depth z_d. We divided $I(\lambda, z)$ by $I(\lambda, z_d)$ to yield

$$I(\lambda, z) = \frac{F(\lambda,z)\sqrt{A(\lambda,z)}}{F(\lambda,z_d)\sqrt{A(\lambda,z_d)}} e^{-\mu_{t_{blood}}(\lambda)(z-z_d)} \; for \;\; z > z_d. \tag{6.4}$$

We rejected all vessels from depths greater than 700 μm from the zero-delay. We calculated $\frac{F(\lambda,z)}{F(\lambda,z_d)}$ from the roll-offs of our spectrometer and found the SDR had negligible spectral influence after normalization by $I(\lambda, z_d)$. Therefore, the ratio $\frac{F(\lambda,z)}{F(\lambda,z_d)}$ is set to 1, yielding

$$I(\lambda, z) = \frac{\sqrt{A(\lambda,z)}}{\sqrt{A(\lambda,z_d)}} e^{-\mu_{t_{blood}}(\lambda)(z-z_d)} for \;\; z > z_d. \tag{6.5}$$

We estimated $\frac{\sqrt{A(\lambda,z)}}{\sqrt{A(\lambda,z_d)}}$ for the same depths (see Supplementary Section 4) and concluded that the residual LCA could have a small but non-negligible influence on sO_2 even after normalization. Therefore, we included $\frac{\sqrt{A(\lambda,z)}}{\sqrt{A(\lambda,z_d)}}$ in our model. Finally, taking the natural logarithm of $I(\lambda, z)$, we have a function that is linearly proportional to $\mu_{t_{blood}}(\lambda)$ (Fig. 2, Step 3) as

$$\ln\big(I(\lambda,z)\big) = \tfrac{1}{2}\ln\big(A(\lambda,z)\big) - \ln\big(A(\lambda,z_d)\big) - \mu_{t_{blood}}(\lambda)(z-z_d)\ for\ z > z_d. \qquad (6.6)$$

6.6.3 Depth averaging

To remove noise variations in the speckle and the background, we averaged Eq. 6 across z, which can be written as

$$\frac{1}{\Delta z}\int_{z_0}^{z_0+\Delta z} \ln\big(I(\lambda,z)\big)dz$$

$$= \frac{1}{\Delta z}\int_{z_0}^{z_0+\Delta z} \frac{1}{2}\Big(\ln\big(A(\lambda,z) - A(\lambda,z_d)\big) - \mu_{t_{blood}}(\lambda)(z - z_d)\Big)dz\ for\ z > z_d$$

$$= LCA_{avg}(\lambda,z) - \mu_{t_{blood}}(\lambda)\left[(z_0 - z_d) + \tfrac{\Delta z}{2}\right]\ for\ z > z_d, \qquad (6.7)$$

where LCA_{avg} is the depth-averaged residual LCA (Supplementary Section 4); z_0 is the starting depth for averaging; and Δz is the depth range for averaging. We show the statistical advantages of depth averaging in Supplementary Section 3.

6.6.4 Depth selection

The term $-\mu_{t_{blood}}(\lambda)\left[(z_0 - z_d) + \tfrac{\Delta z}{2}\right]$ is a constant and represents uniform, oxygen-dependent attenuation along the vessel depth. Blood cell packing, orientation, flow, and oxygen diffusion may add variability to this assumption. To reduce variability and outliers in sO_2 measurement, we minimized depth-dependent changes to the attenuation spectrum.

First, we measured the STFT spectrum in a blood vessel according to Eq. 7. We iterated z_0 from 0 to $12\ \mu m$ and Δz from 17 to $40\ \mu m$, both in $1.15\ \mu m$ (depth pixel size) increments. We normalized each spectrum to a minimum of 0 and a maximum of 1. Then, we generated a 3-dimensional (3D) matrix that indexed the spectra according to their respective depth windows. Such a matrix can be written as

$$S(\lambda_k)_{m,\mathrm{n}} = \begin{pmatrix} S(\lambda_k)_{1,1} & \cdots & S(\lambda_k)_{1,20} \\ \vdots & \ddots & \vdots \\ S(\lambda_k)_{10,1} & \cdots & S(\lambda_k)_{1,20} \end{pmatrix}, \tag{6.8}$$

where $S(\lambda_k)_{m,n}$ is the normalized (between 0 and 1) spectrum for each window iteration; m is the iteration index of z_0; n is the iteration index of Δz; and k is the STFT sub-band index. To measure the response of $S(\lambda_k)_{m,n}$ to a shift in depth, we computed the mean-squared-error (MSE) between spectra from 9 adjacent windows in $S(\lambda_k)_{m,n}$ to generate the SSM as

$$SSM_{i,j} = \sum_{k=1}^{21} \sum_{x=-1}^{1} \sum_{y=-1}^{1} \sum_{m=2}^{9} \sum_{n=2}^{19} \left(MSE\left[S(\lambda_k)_{m,\mathrm{n}}, S(\lambda_k)_{m+x,n+y} \right] \right), \tag{6.9}$$

where $MSE\left[S(\lambda_k)_{m,n}, S(\lambda_k)_{m+x,n+y}\right]$ is the MSE between spectra $S(\lambda_k)_{m,n}$ and $S(\lambda_k)_{m+x,n+y}$; and x and y are the indexes of the compared spectra. We show an example $SSM_{m,n}$ from two selected vessels in Supplementary Section

6. We identified the indexes m and n for minimized $SSM_{m,n}$ and used this depth window for sO_2 measurement.

6.6.5 Oximetry fitting model

We fit the spectrum determined by Eqs. 3.7-3.9 to the following model using a non-negative linear least-squares regression

$$LCA_{avg}(\lambda,z) - \Big(\mathrm{sO}_2(\mu_{a_{HbO_2}}(\lambda) + SSF\mu_{s_{HbO_2}}(\lambda)) + (1 - \mathrm{sO}_2)(\mu_{a_{Hb}}(\lambda) + SSF\mu_{s_{Hb}}(\lambda))\Big)\left[(z_0 - z_d) + \frac{\Delta z}{2}\right] \; for\; z > z_d, \tag{6.10}$$

where $\mu_{a_{HbO_2}}(\lambda)$, $\mu_{s_{HbO_2}}(\lambda)$, $\mu_{a_{Hb}}(\lambda)$, and $\mu_{s_{Hb}}(\lambda)$ are the reported absorption and scattering coefficients of oxygenated and deoxygenated blood, respectively. We constrained the fitting for $SS = 0.02 - 0.10$, consistent with our previous findings () and ±100 µm focal shifts in $LCA_{avg}(\lambda, z)$ (see Supplementary Section 4).

We used the reported absorption and Mie-theory-predicted scattering coefficients of blood [30, 82]. We modified the reported spectra to match the post-processing of the vis-OCT signal. First, we cropped wavelengths from the reported spectra within our spectrometer's wavelength range (508 nm – 614 nm). We upsampled the reported spectra by 6-fold to a 12288-element array, the same size as our interference fringe after 6-fold zero-padding. Then, we performed interpolation of the reported spectra to be linear in *k*-space. Finally, we filtered and digitized the reported blood spectra with the same 21 STFT Gaussian windows.

6.6.6 vis-OCT systems

We used vis-OCT systems at NYU Langone Health Center (Aurora X1, Opticent Health, Evanston, IL) and Northwestern Medical Hospital (Laboratory Prototype), which were reported, respectively, in our previous work [142]. We previously characterized spectrometer roll-offs [27].

6.6.7 Imaging protocols

Imaging was performed at NYU Langone Health Center and Northwestern Memorial Hospital. We limited light exposure on the cornea to $< 250\ \mu W$, which is considered eye-safe [45]. The camera line period was set to 40 μs (39 μs exposure + 1 μs data transfer) for a 25 kHz A-line rate. All imaging was approved by respective NYU and Northwestern University Institutional Review Boards and adhered to the Tenants of Helsinki.

We performed three scan types for oximetry measurement: arc scan, small FOV raster scan, and large FOV raster scan. An arc scan is a 120-degree segment of a circular scan with a radius of 1.7 mm acquired with 16 B-scans at 8192 A-lines per B-scan. A small-FOV scan is a 1 mm × 1 mm raster scan acquired containing 16 B-scans with 8192 A-lines per B-scan. A large-FOV scan is a 4.8 mm × 4.8 mm raster scan containing 64 B-scans with 4096 A-lines per B-scan. We found no significant differences in sO_2 values for different scanning modes.

6.6.7 Vessel selection

We measured sO_2 in 176 total retinal vessels (100 arteries and 75 veins) across 18 healthy subjects. We analyzed 125 unique retinal vessels (72 arteries and 53 veins) (see Methods – Retinal oximetry in a healthy cohort). For vessels with more than one measurement, we selected unique vessels by selecting sO_2 measurement with the highest R^2. For repeatability analysis, we selected vessels with at least two repetitions.

6.6.7 Vessel segmentation

We selected the left and right borders of a vessel, guided by its attenuation shadow. To account for different vessel geometries, we automatically segmented the central 36%, 40%, and 42% of A-lines of the vessel. We repeated these three segmentations for a 4% shift left and right of the detected vessel center, totaling 9 segmentations of the same vessels. We treated each of the 9 segmentations as separate B-scans in the analysis.

6.6.8 Statistical analysis

To assess whether the lower sO_2 values were influenced by vessel diameter or were an artifact of poor fitting (lower R^2), we included both parameters in a linear model

$$\mathrm{sO}_2 = a_1 D + a_2 R^2, \tag{6.11}$$

where D is vessel diameter; R^2 is the spectral fit R^2 value; and a_1 and a_2 are arbitrary constants. A two-way ANOVA was performed in MATLAB 2018a. Significance was considered as $p < 0.05$. We compared sO_2 measurement populations in Figs. 5B and 5C. We used the two-sample t-test to determine differences in the mean. Significance was considered as $p < 0.05$. t-tests were performed in MATLAB 2018a.

6.7 SUPPLEMENTARY INFORMATION

6.7.1 *Ex vivo* phantom validation and *in vivo* comparison

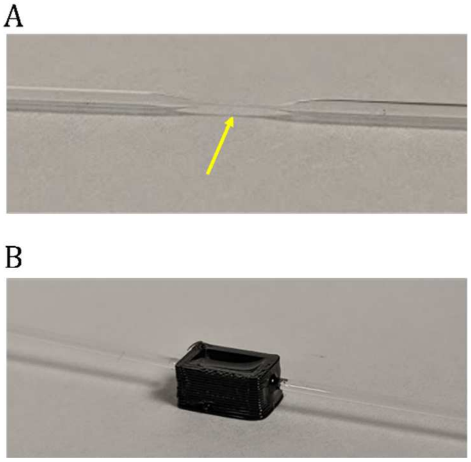

Figure 6.6. Capillary tube phantom for *ex-vivo* vis-OCT oximetry. (A) Glass capillary tube pulled to an inner diameter of ~ 200 μm (arrow); (B) Tube inserted in a homemade well under ~ 500 μm of immersion oil.

We measured sO_2 values in an *ex vivo* bovine blood phantom using vis-OCT and compared them with a blood-gas analyzer (Rapidlab 248, Siemens Healthcare Diagnostics, Malvern, PA). Briefly, we pulled a glass capillary tube to an inner diameter of ~ 200 μm (Fig. 6.6a). We embedded the pulled tube in the middle of a homemade plastic well (Fig. 6.6b). To reduce specular reflections from the air-glass interface, we added immersion oil (refractive index = 1.52) to the well until the tube was covered by ~ 500 μm of oil.

Next, we prepared oxygenated ($sO_2 \approx 100\%$) and deoxygenated ($sO_2 \approx 0\%$) bovine blood (Quadfive, Ryegate, MT). Hematocrit of blood samples was 45%. To oxygenate blood, we exposed it to a constant stream of pure oxygen while mixing with a magnetic stir bar. We verified that the blood was oxygenated using the blood-gas machine. To deoxygenate blood, we added sodium dithionite to the solution [159]. We monitored the partial pressure of oxygen (pO_2), partial pressure of carbon dioxide (pCO_2), pH, and temperature of the mixture using the blood-gas machine and converted to sO_2 [160]. We continued adding sodium dithionite and measuring sO_2 until the blood was sufficiently deoxygenated. Following oxygenation and deoxygenation, we immediately loaded blood samples into syringes to prevent influences from ambient air.

We used oxygenated and deoxygenated samples to make 17 blood samples between $sO_2 \approx 100\%$ and $sO_2 \approx 0\%$. To this end, we mixed oxygenated and deoxygenated samples to create blood of another oxygenation level. We measured sO_2 of the mixed blood using the blood-gas machine. We imaged each blood sample immediately after blood-gas machine measurement.

Before loading blood into the tube, we flushed the tube with a phosphate-buffered saline (PBS) and heparin solution to prevent clotting or sedimentation. Then, we loaded the blood into a syringe, which was connected to the glass tube by ~ 1 m of plastic tubing. We placed the syringe in a syringe pump (Model-Fusion 100, Chemyx, Inc. Stafford, TX), which flowed the blood at ~ 0.03 mm/s inside the glass tube to prevent clotting or sedimentation.

Before imaging, we focused the beam on the tube by adjusting tube height and maximizing the intensity of backscattered light. After reaching best focus, we adjusted the reference arm to place the top of the tube < 100 μm from the zero-delay. Then, we imaged the tube using a 512 x 512 raster scan. Optical power incident on the tube was 1.20 mW. After imaging each blood sample, we re-flushed the tube with the PBS and heparin solution.

We measured sO_2 with vis-OCT in each blood sample using the Ads-OCT processing proposed in this work. Since scattering factor W was not well-agreed upon in the literature, we varied SSF to find the highest spectral fit R^2. We found that best spectral fit R^2 was reached between $0.02 \leq SSF \leq 0.10$.

We computed 100 vis-OCT sO_2 measurements for each tube. Briefly, we processed and stored all 512 B-scans. Then, we randomly selected and averaged 50 different B-scans from this set for sO_2 measurement. Then, we refreshed the 512 B-scans and repeated random selection 100 times to reach 100 sO_2 measurements.

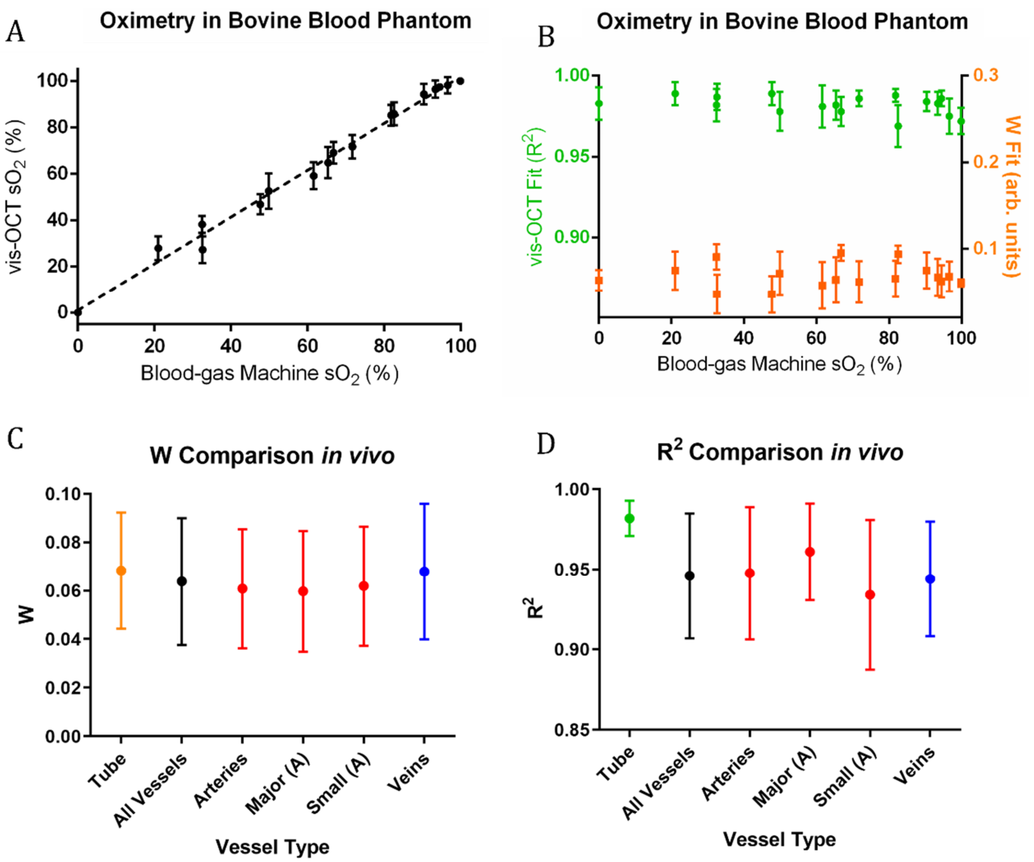

Figure 6.7. Results of vis-OCT oximetry in *ex vivo* phantom and comparison to *in vivo* human eye. (a) vis-OCT sO_2 measurements in phantom plotted against sO_2 measurements from blood-gas machine; (b) Distributions of spectral fit R^2 and best fit W in phantom; (c) Distributions of best fit W in phantom compared to human eye; (d) Distributions of best fit R^2 in phantom compared to human eye

Fig. 6.7a shows tube sO_2 measured by vis-OCT and the blood-gas machine for 17 tubes ranging from $sO_2 \approx 0\%$ to $sO_2 \approx 100\%$. The equation of the best fit line is $y = 1.01x + 1.28$ and the coefficient of regression is $R^2 = 0.97$. The relationship between the blood-gas machine and vis-OCT sO_2 was nearly a slope of 1 with only ~1% bias. This was within our target accuracy, so we did not apply a post-hoc calibration curve to vis-OCT measurements in this work.

Fig. 6.7b shows spectral fits (R^2) and best fit SSF for each tube. Average spectral fit R^2 was 0.98 and average SSF was 0.068. In Fig. 6.7c, we plot the best-fit SSF *ex vivo* and *in vivo*. In the tubes, we measured SSF = 0.068 ± 0.024. For all unique vessels, we measured SSF = 0.064 ± 0.026, agreeing well with the tube data. Specifically, SSF measurements were 0.061 ± 0.025, 0.060 ±0.025, 0.062 ± 0.025, and 0.068 ± 0.028 for all arteries, large arteries, small arteries, and all veins, respectively. In Fig. 6.7d, we plot the spectral fit R^2 *ex vivo* and *in vivo*. In tubes, we measured $R^2 = 0.98 \pm 0.01$. For all unique vessels, we measured average $R^2 = 0.95 \pm 0.04$. R^2 measurements were 0.95 ± 0.04, 0.96 ±0.03, 0.93 ± 0.05, and 0.94 ± 0.04 for all arteries, major (diameter $\geq$ 100 μm) arteries, small arteries (diameter < 100 μm), and all veins, respectively. We anticipated that major arteries would have slightly higher R^2 (0.96) than smaller ones (0.93), considering the increased spatial averaging for larger vessels. Nevertheless, R^2 did not have a significant influence on sO_2 value (see **Retinal oximetry in a healthy cohort**).

6.7.2 sO_2 repeatability and comparison to pulse oximeter

Unique Vessel	Type	Avg. Diameter (μm)	Avg. sO_2 (%)	Repetitions	Repeatability (SD %)	Avg. Spectral Fit R^2
1	A	138	100.0	3	0	0.972
2	A	134	98.9	2	1.63	0.980
3	A	130	100.0	2	0	0.963
4	A	128	97.1	2	1.06	0.961
5	A	124	99.6	2	0.64	0.965
6	A	122	96.2	3	3.75	0.971
7	A	122	97.8	4	3.81	0.962
8	A	121	99.2	2	1.20	0.946
9	A	121	99.9	3	0.23	0.969
10	A	120	100.0	2	0	0.955
11	A	119	95.5	2	4.88	0.948
12	A	116	99.6	2	0.64	0.953
13	A	116	98.4	2	2.26	0.970
14	A	116	98.6	3	2.48	0.943

15	A	113	97.0	2	4.24	0.966
16	A	105	96.1	2	5.59	0.948
17	A	104	97.9	2	2.97	0.964
18	A	93	92.0	2	2.83	0.966
19	A	89	99.6	2	0.64	0.963
20	A	89	96.2	2	1.27	0.932
21	A	86	91.1	2	2.40	0.950
22	A	86	92.0	3	6.83	0.918
23	A	62	92.9	2	1.13	0.958
24	A	48	91.3	2	2.55	0.912
25	V	174	62.3	2	3.46	0.968
26	V	160	57.0	2	2.12	0.953
27	V	160	58.1	2	0.35	0.954
28	V	157	54.8	3	3.07	0.943
29	V	156	60	3	2.31	0.967
30	V	153	55.4	3	2.97	0.957
31	V	149	55.9	4	4.98	0.951
32	V	146	56.0	2	1.41	0.954
33	V	145	61.0	3	2.06	0.927
34	V	139	58.4	3	3.44	0.918
35	V	135	55.0	2	1.20	0.900
36	V	133	60.1	2	1.27	0.974
37	V	131	54.3	2	0.49	0.940
38	V	128	51.5	2	4.45	0.955
39	V	125	50.6	2	0.78	0.980
40	V	80	59.0	2	2.4	0.977
41	V	70	64.1	2	3.46	0.913
42	V	62	57.7	2	1.41	0.904

Table 6.2. All unique vessels analyzed for repeatability. ‘A’ indicates artery and ‘V’ indicates vein.

Subj.	**Avg. Pulse Ox. sO_2 (%)**	**Avg. vis-OCT sO_2 (%)**	**Num. Unique Major Arteries Measured by vis-OCT**	**RMSE Between Pulse Ox. and Unique Artery sO_2 (%)**
1	100	100	2	0
2	98	99.6	2	1.6
3	99.7	98.9	3	2.0
4	99	95.2	1	3.8
5	95	95.8	1	0.8
6	98	100	1	2
7	99	100	1	1
8	100	98	2	2.8
9	98	100	2	2
10	100	96	2	4
14	98	97.6	5	2.6
17	99	99	3	1.4
Avg.	98.6	98.3	2.1	2.1

Table 6.3. All unique major arteries compared with pulse oximeter.

6.7.3 Statistical advantage of depth averaging

	Depth Avg. (A)	**Slope (A)**	**Depth Avg. (V)**	**Slope (V)**
Success %	100 (n = 72)	64 (n = 46)	100 (n = 53)	66 (n = 35)
Average sO_2 (%)	95.1	90.4	58.5	56.8
SD sO_2 (%)	5.1	8.92	4.3	10.71
Average Fit R^2	0.95	0.92	0.94	0.92

Table 6.4. Comparison of depth-averaging and slope methods for vis-OCT retinal oximetry

The depth-resolved slope of NL-SDA-lines (further referred to as the “slope method”) was previously used to extract the attenuation coefficient of OCT signals in **Step 8** in Fig. 6.2 [25, 63, 161]. In this work, we found that the depth-resolved average of NL-SDA-lines (further referred to as “depth-averaging method”) was statistically advantageous to the slope method for retinal oximetry. We compared the two methods for sO_2 measurements in the 125 unique human retinal vessels described above. Both sO_2 measurements used identical AdS-vis-OCT processing with identical depth-selection windows. To implement the slope method, only the depth-averaging step, as depicted by Step 8 in the AS-OCT processing, was replaced with a simple linear regression to estimate the slopes of NL-SDA-lines along the z-axis.

Table 6.4 compares the sO_2 measurement statistics for 125 unique human retinal vessels (72 arteries and 53 veins) for the depth-averaging and slope methods. Success rate indicates the fraction of sO_2 measurements that surpassed Ads-vis-OCT spectral fit R^2 threshold, which is $R^2 > 0.80$ or $R^2 > 0.93$ if $sO_2 = 100\%$. For this analysis, we combine sO_2 across all diameters.

For all tested unique arteries, the depth-averaging method had a success rate of 100 %, while the slope method had a success rate of 64 %. For depth-averaging, all arteries had an average sO_2 of 95.1 ± 5.1 %, while the slope method yielded an average of 90.4 ± 8.92 %. The SD of the slope method was 75% higher than that of the averaging method. The lower average spectral fit R^2 for the slope method (0.92), as compared with the depth-averaged method (0.95), is consistent with its higher SD. Additionally, we anticipated that the R^2 was still inflated for the slope method since we rejected 36% of vessels based on a low R^2.

For all tested unique veins, the depth-averaging method had a success rate of 100%, while the slope method had a success rate of 66%. For depth-averaging, veins had an average sO_2 of 58.5 ± 4.3 %, while the slope method had an average of 56.8 ± 10.71 %. SD of the slope method was 149% higher than that of the depth-averaging method. Similar to arteries, the slope method had a lower average R^2 (0.92), as compared with the depth-averaging method (0.94). Since we rejected 34 % based on low R^2, we anticipate that the venous R^2 for the slope method was still inflated.

The comparisons between the two methods demonstrate that the depth-averaging method greatly improves the stability of vis-OCT retinal oximetry than the slope method. We investigated the improved stability using Monte-Carlo simulation in the **Supplementary Information**.

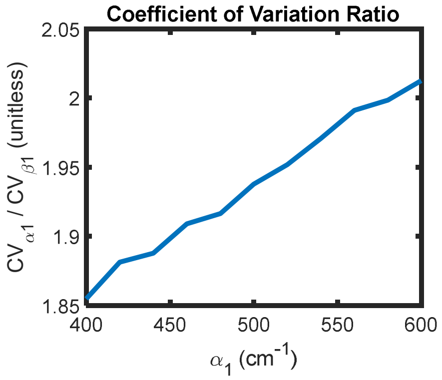

Figure 6.8. Coefficient of variation ratio between slope and depth averaging methods for estimating attenuation coefficient. Exponential decay model from Eq. 6.14 is used for calculations. α_1 is attenuation coefficient estimated by slope method; β_1 is proportional to α_1 and estimated by depth averaging method.

Empirically, we found that depth-averaging the natural logarithm of the SDA-lines yielded less noisy spectra, as compared with the slope method (Table 6.3). We verified these empirical observations by Monte Carlo simulation. To begin, we applied the slope method and depth-averaging method to the equation of a line, which is predicted by Eqn. 6.7 in **Methods**. (for simplification, removing small effect of LCA):

$$y(x) = -\alpha_1 x + \sigma_N, \tag{6.12}$$

where α_1 is an arbitrary constant and σ_N is random, normally distributed noise. x was a 30-pixel vector ranging from 0 to 35 μm for the depth selection window. We used the slope method to compute the slope of Eq. 6.12 and directly find α_1. We used the depth-averaging method to compute the average value of Eq. 6.12 (similar to Eq. 6.8) to find the constant $\beta_1 \propto \alpha_1$. We computed 10^5 iterations of such measurements, and then measured their coefficients of variation:

$$CV_{method} = \frac{\sigma_{method}}{|\mu_{method}|}, \tag{6.13}$$

where CV_{method} is the coefficient of variation of the measured α_1 or β_1 from each respective method, σ_{method} is the SD of the measured α_1 or β_1 from each respective method, and μ_{method} is the average of the measured α_1 or β_1 from each respective method. We computed CV_{method} for $\alpha_1 = 400$ cm^{-1} to $\alpha_1 = 600$ cm^{-1} in an increment of 20 cm^{-1}, which covered the reported attenuation coefficients of blood in the visible-light spectral range for $W = 0.064$. We used normally distributed noise with amplitude $\sigma_N = 0.02$ (arb. units), which was a relative noise typically observed *in vivo*. For each value of α_1, we calculated $\frac{CV_{\alpha_1}}{CV_{\beta_1}}$, which compared the relative uncertainty of the slope method to the depth-averaging method. For all values of α_1, $\frac{CV_{\alpha_1}}{CV_{\beta_1}}$ converged to 1.67. In general, we found that value of $\frac{CV_{\alpha_1}}{CV_{\beta_1}}$ was independent of α_1 and σ_N. This suggested that the depth-averaging method had an intrinsic noise reduction advantage of 67% over the slope method for additive, normally distributed noise.

In reality, however, the SDA-lines follow an exponential decay with the additive noise. We applied a natural logarithm to this function:

$$y_2(x) = \ln\left(e^{-\alpha_1 x} + \sigma_N\right). \tag{6.14}$$

One frequent assumption by the slope method is that signal is significantly greater than noise, or $e^{-\alpha_1 x} \gg \sigma_N$, after which Eq. 6.14 would converge to a noiseless version of Eq. 6.12. However, in the human retina, SNR is often low, and this assumption might not be correct. To this end, the noise in Eq. 6.14 after the natural logarithm is less trivial than in Eq. 6.12 since there is no longer a linear relationship between α_1 and σ_N. We repeated the simulation described above, except we generated the signal and noise using Eq. 6.14. Fig. 6.8 plots $\frac{CV_{\alpha_1}}{CV_{\beta_1}}$ for this simulation. Like the analysis from Eq. 6.12, the coefficient of variation using the slope method is always higher than that using the depth averaging method. However, the $\frac{CV_{\alpha_1}}{CV_{\beta_1}}$ is not constant and increases with increased α_1. This is because the relationship between α_1 and σ_N is nonlinear in Eq. 6.14. This has important implications for the slope method in sO_2 calculation, since the measured blood spectrum can have different noise levels for different wavelengths and for different depth selection windows. In this work, we demonstrated empirically that depth averaging is statistically advantageous over the slope method for sO_2 calculation, consistent with the simulation.

6.7.4 Longitudinal chromatic aberration in vis-OCT retinal oximetry

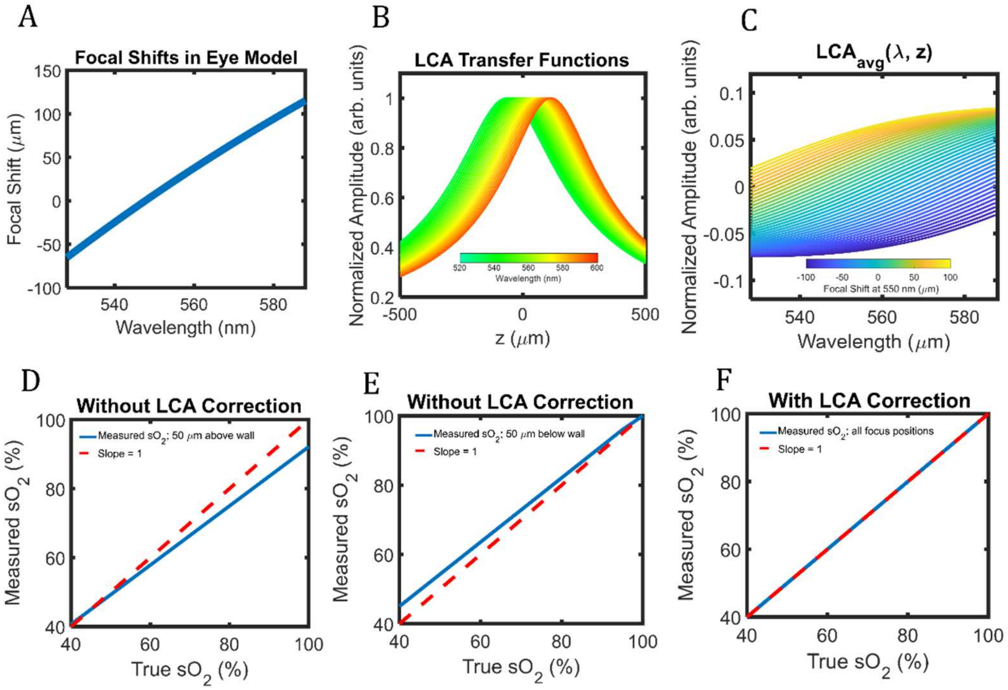

Figure 6.9. Simulation of LCA in human eye and influence on vis-OCT retinal oximetry. (a) CFS in human eye simulated by Zemax software; (b) Transfer function of the LCA on vis-OCT SDA-lines. Colors depict central wavelength of STFT window; (c) Simulated LCA contribution to measured spectrum after Ads-OCT processing; (d) Simulated sO_2 measurement without LCA correction when focus at 550 nm is 50 μm above the anterior vessel wall; (e) Simulated sO_2 measurement without LCA correction when focus at 550 nm is 50 μm below the anterior vessel wall; (f) Simulated sO_2 measurement with LCA correction for all focus positions

We developed an approach for fitting LCA transfer functions to sO_2 measurement using the physical optics of the human eye. First, we simulated the CFS in the human eye model from Polans et al. [162] using Optic Studio 16 (Zemax, Kirkland, Washington). Since the wavelength ranges and lateral resolutions of the vis-OCT systems used in this study were approximately the same (see **Methods – Vis-OCT Systems**), we used the same CFS for both systems (Fig. 6.9). The simulated chromatic focal shift (CFS) CFS is consistent with that previously measured in the human eye [163]. Then, we calculated potential LCA transfer functions using a modified version of the equation used in [164] to account for spectroscopic analysis:

$$A(\lambda, z) = \frac{1}{\left(\frac{z - z_{f_{550}} - CFS(\lambda, z)}{2z_r(\lambda)}\right)^2 + 1} \tag{6.15}$$

where $z_{f_{550}}$ is the reference focusing depth at 550 nm, $CFS(\lambda, z)$ are the chromatic focal shifts, and $z_r(\lambda)$ are the wavelength-dependent Rayleigh lengths (assumed refractive index = 1.35 and $1/e^2$ spot size = 7 μm). We calculated 41 LCA transfer functions up to $z_{f_{550}}$ = 100 μm above and below the anterior wall of a simulated vessel in 5 μm increments. Fig. 6.9b illustrates a simulated LCA transfer function ($\sqrt{A(\lambda, z)}$) for $z_{f_{550}}$ focused at the anterior vessel wall. Then, we normalized $\sqrt{A(\lambda, z)}$ by its spectral profile at z_n = 12 μm into the simulated vessel lumen, consistent with typical sO_2 measurements, and took its natural logarithm. We found $LCA_{avg}(\lambda, z)$ by averaging the normalized ln $\left(\sqrt{A(\lambda, z)}\right)$ from z_0 = 16 μm to $z_0 + \Delta z = 46$ μm into the vessel lumen (Eqn. 6.7), also consistent with typical sO_2 measurements. To create the LCA lookup table, we saved $LCA_{avg}(\lambda, z)$ for each of the 41 focal positions (Fig. 6.9c).

To understand potential influence of LCA on sO_2 measurement, we simulated SDA-lines in a vessel consistent with the Beer-Lambert law and the attenuation spectra in Faber et. al [30]. We multiplied $\sqrt{A(\lambda, z)}$ at each focal position with the SDA-lines to account for LCA and took its natural logarithm. We averaged the spectrum at the same depths used to find $LCA_{avg}(\lambda, z)$ (Eqn. 6.7 in **Methods**). We noted that for all simulated physiological sO_2 measurements (sO_2 = 40% to sO_2 = 100%) and focal positions, the peak-to-peak amplitude of $LCA_{avg}(\lambda, z)$ was less than 0.25 times the peak-to-peak amplitude of $\mu_{t_{blood}}(\lambda)\left[(z_0 - z_n) + \frac{\Delta z}{2}\right]$. We used this relationship to constrain physically reasonable $LCA_{avg}(\lambda, z)$ to avoid overfitting this parameter in the sO_2 measurement. Furthermore, since the above constraint described relative amplitudes only, it was independent optical power incident on the vessel.

We measured sO_2 in the above simulation without and with LCA fitting described in **Methods – Oximetry Fitting Model**. We measured sO_2 for up to $z_{f_{550}}$ = 100 μm above and below the anterior wall of a simulated vessel in 5 μm increments. Measurements were derived from simulated SDA-lines of oxygen-dependent spectra from sO_2 = 40% to 100%. Figs. 6.9d and 6.9e plot sO_2 measurements without fitting the contribution of $LCA_{avg}(\lambda, z)$. Fig. 6.9d shows sO_2 measurements for $z_{f_{550}}$ = 50 μm above the vessel anterior wall and Fig. 6.9e shows sO_2 measurements for $z_{f_{550}}$ = 50 μm below the anterior wall. When $z_{f_{550}}$ = 50 μm above the anterior wall, sO_2 is underestimated. When $z_{f_{550}}$ = 50 μm below the anterior wall, sO_2 is overestimated. Fig. 6.9f plots sO_2 measurements with fitting the contribution of $LCA_{avg}(\lambda, z)$, as described in **Methods – Oximetry Fitting Model**. For all values of $z_{f_{550}}$, measured sO_2 matches the ground truth sO_2 with a slope of 1.

We recognize this is a simplified approach may not have fully appreciated the exact influence of LCA in each recorded image. Nevertheless, such corrections are based on the well-verified aberrations and defocusing in the human eye. More precise LCA correction may be reached with a wavefront sensor and adaptive optics to directly measure wavelength-dependent aberrations, although they add expense and complexity to the vis-OCT system. The influence of LCA can also be reduced by employing an achromatizing lens [46] in the sample arm of the system. Additionally, our vis-OCT systems used a focusing beam diameter ($1/e^2$) of 7 μm. Decreasing beam diameter at the cornea and increasing depth of focus can also reduce influence of LCA on sO_2 calculation, although it may challenge laterally resolving smaller vessels.

6.7.5 Example SDA-lines

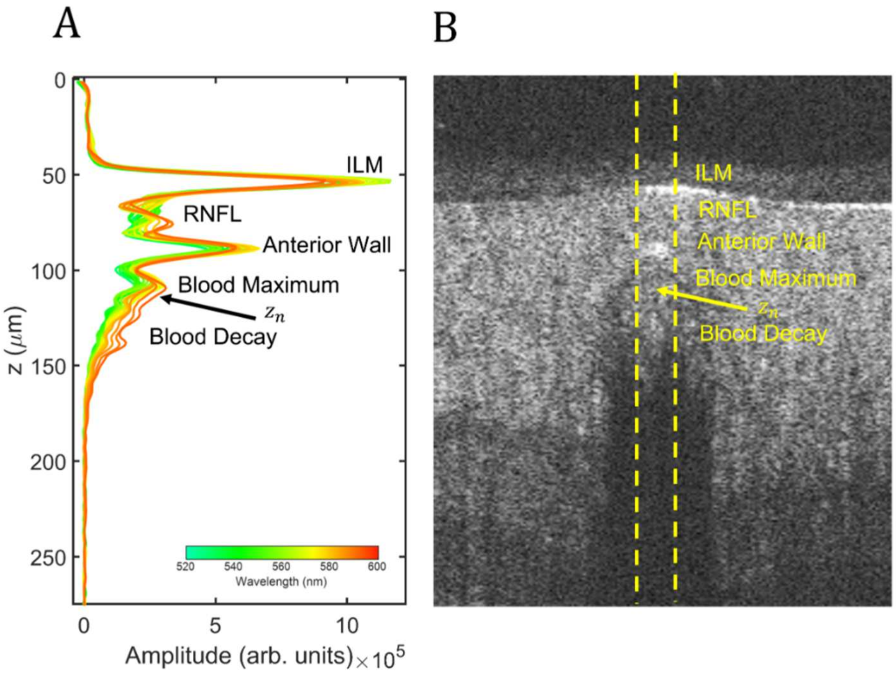

Figure 6.10. SDA-lines features. (a) SDA-lines from vein in human retina (after SDBG correction). Color bar represents central wavelength of STFT window. z_d indicates depth of normalization where SDA-lines start to decay in amplitude; (b) Magnified B-scan where SDA-lines in (a) were measured. SDA-lines were averaged laterally within yellow dashed lines

6.7.6 Accounting for depth-dependent spectra within retinal vessels

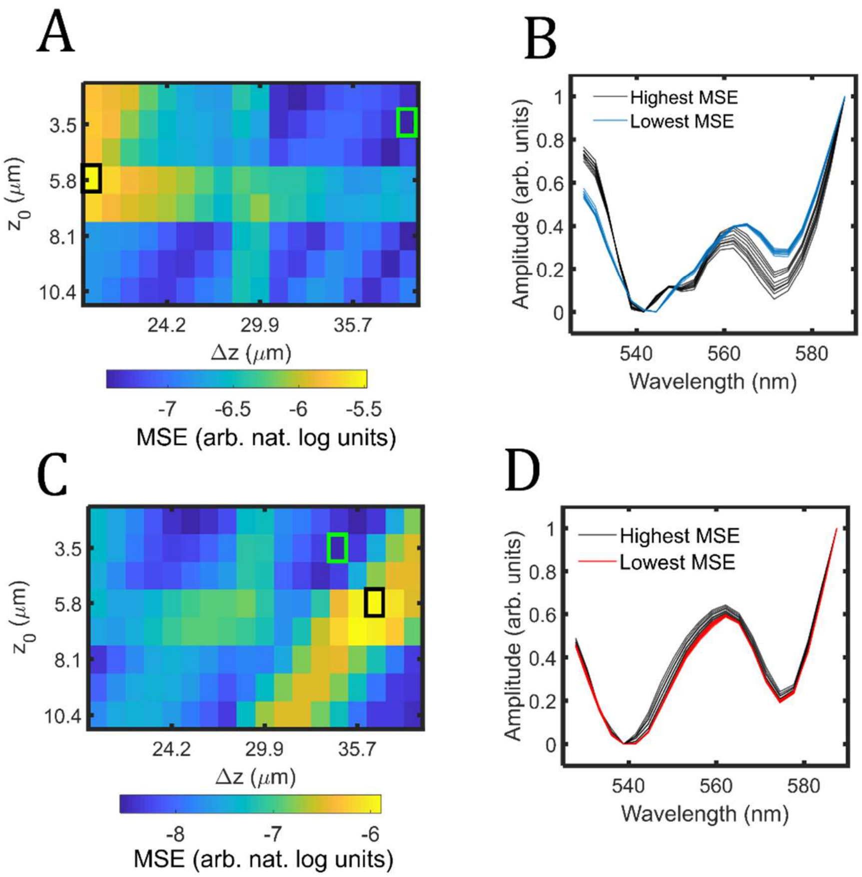

Figure 6.11. Spectral stability analysis in human retinal vessels. (a) Spectral stability matrix (SSM) for vessel V3 from Fig. 6.3. Green box highlights lowest mean-squared-error (MSE) and black box highlights highest MSE; (b) Spectra in V3 after nine depth perturbations for the lowest MSE (blue lines) and highest MSE (black lines), respectively. (c) SSM for vessel V2 from Fig. 6.3. Green box highlights MSE and black box highlights highest MSE. (d) Spectra in V4 after nine depth perturbations for the lowest MSE (red lines) and highest MSE (black lines)

Fig. 6.11A shows the spectral stability matrix (SSM) for vessel V1, a vein, in Fig. 6.3. The SSM plots how the measured STFT spectrum changes with depth as a function of the selected starting depth z_0 and depth range Δz (see Step 7 in Fig.

6.2 & Methods – Depth Selection). A lower mean-squared error (MSE) indicates that the measured STFT spectrum has less depth variation. The green box in Fig. 6.11A highlights the pair of z_0 and Δz where MSE is the lowest, and the black box highlights where it is highest.). In V3, the spectrum is most depth-stable for longest Δz and least depth-stable for shortest Δz. Fig. 6.11B plots measured spectra (normalized between 0 and 1) from the locations of the highest MSEs (black lines) and lowest MSEs (blue lines) in Fig. 6.11A. There are 9 plots from each of the two regions, each representing 9 small shifts in depth (see Methods – Depth Selection). Following the MSE calculation, the spectra plotted in blue change significantly with depth than those plotted in black.

Optimally selected z_0 and Δz varied across the veins investigated in this study. The average selected Δz for veins (n = 53) was 33 μm out of a maximum value of 40 μm. Selected Δz ranged from Δz = 22 μm to Δz = 40 μm.

Fig. 6.11C shows the SSM for V2 from Fig. 6.3. Unlike in Fig. 6.11A, the lowest MSE (green box) is actually at a shorter depth than the highest MSE (black box). Arteries are generally pulsatile and have higher flow velocity than veins, perhaps introducing different flow-dependent SCs at deeper vessel depths. Nevertheless, we show that by finding the z_0 and Δz with the lowest MSE, we selected the most depth-stable spectrum (Fig. 6.11D; highest MSE plotted in black, lowest MSE plotted in red).

Like veins, depths with minimized MSE varied across arteries in this study. The average selected Δz in arteries (n = 72) was 33 μm out of a maximum of 40 μm and selected Δz ranged from Δz = 17 μm to Δz = 40 μm.

6.7.7 Adaptive filtering (Stage 1)

We averaged NL-SDA-lines along a 32 μm depth region beyond z_n for each respective B-scan to obtain a 1D STFT spectrum. We calculated sO_2 and spectral fit R^2 from NL-SDA-lines in each B-scan by least-squares fit (see **Methods – Oximetry fitting model**). Then, we applied a threshold of $sO_2 > 15\%$ and $R^2 > 0.40$ and removed B-scans that did not pass. For the smallest analyzed vessels (diameter < 60 μm), we did not perform this step, due to increased noises in individual B-scans.

6.7.8 Adaptive filtering (Stage 2)

First, we rejected all sO_2 iterations where the spectral fit $R^2 < 0.80$. We found that noisier arterial spectra resulted in $sO_2 = 100\%$, which saturates at the maximum possible value. Therefore, we also rejected iterations where $sO_2 = 100\%$ and $R^2 < 0.93$. Next, we sorted the iterations in ascending order of sO_2 and selected the 20 central indexes, acting as a pseudo-median measurement. Among these values, we selected the iteration where the R^2 was the highest. We saved the z_n, W, and S for the selected iteration and accepted the sO_2 with these parameters.

6.7.9 Parameter iterations

We introduced small variations in three parameters we identified as sensitive to sO_2. The first parameter is z_d, the identified depth where blood signal begins to decay. After STFT, the axial resolution of ~ 9 μm and spatial averaging between B-scans broadens the peak blood backscattering signal, adding uncertainty to its localization. Furthermore, random, or unknown parameters, such as speckle noise, erythrocyte spatial distributions, and vis-OCT illumination beam's incidence angle, may contribute to depth-dependent spectroscopic signal differences in vessels. Therefore, we tuned z_d from 6 μm to 14 μm in 8 equidistant steps below the identified peak blood signal and computed sO_2 for each iteration. If a single peak could not be found, perhaps due to noise or spatial averaging, we then tuned z_d from 16 μm to 24 μm in 8 equidistant steps from the peak amplitude of the anterior vessel wall. The second parameter is the scattering scaling factor SSF, which can vary with erythrocyte spatial distributions and multiple scatterings [29]. Based on *ex-vivo* bovine blood sO_2 measurements (see **Supplementary Information**) and human retinal sO_2 measurements, we determined that the strongest regression fits (R^2) were found between SSF $= 0.02$ and SSF $= 0.10$. This is consistent with our previous findings [29]. Therefore, we computed 8 iterations of sO_2 for SSF in this range with a step size of 0.01. The third parameter S scales the SDBG amplitude by a small value. Briefly, we measured the SDBG where the vis-OCT signal was attenuated to the noise floor and extrapolated its amplitude at the vessel location by fitting an exponential curve to the SDBG. Due to the low SNR of the measured spectrum relative to the SDBG, small errors in this extrapolation could alter the measured spectrum. To account for these potential errors, we applied a small correction factor S to the SDBG, $B(\lambda, z)$, before SDBG subtraction from Eq. 1. We tuned S between 0.96 and 1.04 in 9 steps with a step size of 0.01. We measured sO_2 for each iteration (Fig. 6.2, Step 8). In total, we calculated sO_2 for $8 \times 8 \times 9 = 576$

iterations. We stored measured sO_2 and spectral fit R^2 for each parameter iteration in 3D matrixes.

6.7.10 Fixed-attenuation measurement parameters

We computed sO_2 measurments for a non-adaptive method referred to as ‘fixed attenuation’ (FA Method; see Results - Comparison with non-adaptive retinal oximetries). Rather than compute optimal depths for normalization and spectroscopic measurement, we used rigid parameters. For z_d, normalization depth, we selected 23 μm below the peak signal from the anterior vessel wall; for z_0, starting depth of spectroscopic measurement, we selected 8 μm after z_d; for Δz, spectroscopic measurement range, we selected 36 μm below z_0. If the rigid parameters did not fit inside of a smaller vessel (diam < 60 μm), we manually reduced the depth range to fit inside the vessel. These parameters were all within the ranges specified in Ads-vis-OCT.

Chapter 7

High-speed balanced detection visible-light optical coherence tomography in the human retina using sub-pixel spectrometer calibration

7.1 MOTIVATION

Vis-OCT relies on supercontinuum lasers to generate broadband visible-light. However, these lasers are susceptible to rapid intensity fluctuations called relative intensity noise, or RIN. RIN negatively affects image quality and becomes more prevalent with increased imaging speed. This fundamentally limits image quality and imaging speed in the clinic. Failure to visualize the retina due to RIN or head and eye motions is the presently greatest limiting factor for vis-OCT applications in humans.

7.2 SUMMARY

Increases in speed and sensitivity enabled rapid clinical adoption of optical coherence tomography (OCT) in ophthalmology. Recently, visible-light OCT (vis-OCT) achieved ultrahigh axial resolution, improved tissue contrast, and provided new functional imaging capabilities, demonstrating the potential to improve clinical care further. However, limited speed and sensitivity caused by the high relative intensity noise (RIN) in supercontinuum lasers impeded the clinical adoption of vis-OCT. To overcome these limitations, we developed balanced-detection vis-

OCT (BD-vis-OCT), which uses two calibrated spectrometers to cancel RIN and other noises. We analyzed the RIN to achieve robust subpixel calibration between the two spectrometers and showed that BD-vis-OCT reduced the A-line noise floor by up to 20.5 dB. Metrics comparing signal-to-noise-ratios showed similar image qualities across multiple reference arm powers, a hallmark of operation near the shot-noise limit. We imaged healthy human retinas at an A-line rate of 125 kHz and a field-of-view up to 10 mm × 4 mm. We found that BD-vis-OCT revealed retinal anatomical features previously obscured by the noise floor.

7.3 INTRODUCTION

Optical coherence tomography (OCT) images the living human retina noninvasively at micrometer-scale volumetric resolutions [1, 2]. Since its first demonstration in the early 1990s, OCT has rapidly become the clinical imaging standard for diagnosing, treating, and monitoring nearly all retinal diseases [2, 5]. The clinical adoption of OCT can be partially attributed to technical advancements in imaging speed and sensitivity. Development of spectral-domain OCT enabled high-speed imaging at 100s of kHz with increased sensitivity [2, 5, 137, 165]. Traditionally, spectral-domain OCT has operated in the near-infrared (NIR) wavelength range (800 nm-1300 nm).

The recent development of visible-light OCT (vis-OCT) [9], which operates near 500 nm – 600 nm, has shown promise for providing valuable information not available in NIR OCT. Using shorter wavelengths, vis-OCT enables an axial resolution < 2 μm [9, 24, 46, 57], at least 2-fold higher than clinical NIR systems. Hence vis-OCT revealed or enhanced retinal structures previously inaccessible by

NIR OCT by taking advantage of its high axial resolution and increased tissue scattering contrast. For example, recent studies have found that vis-OCT can delineate Bruch's membrane (BM) [24, 46, 166], a structural origin of macular degeneration, and the inner plexiform layer (IPL) sublayers [16, 167], which contains scattering information from dendritic connections that may be a biomarker for glaucoma. Additionally, vis-OCT achieved retinal oximetry by analyzing spectral contrast between oxygenated and deoxygenated blood [18], opening a new window for functional retinal imaging.

Although vis-OCT enhances structural and functional information in the retina, it has unique limits that hamper its clinical adoption. Perhaps the most significant limitation is the light source. Unlike NIR-OCTs, which use low-noise superluminescent diodes (SLDs), vis-OCT relies on supercontinuum lasers. Supercontinuum lasers have intrinsic power fluctuations referred to as relative intensity noise (RIN) [9, 23, 168]. After the Fourier transform, the RIN increases the image background's average amplitude (noise floor) and variation (noise). The increased noise floor amplitude degrades vis-OCT's image contrast, while the increased noise variation increases the uncertainty of vis-OCT's pixel amplitudes. RIN can be suppressed by increasing the exposure time of the spectrometer's camera (decreasing A-line rate) to average out intensity fluctuations [23]. Therefore, vis-OCT researchers often limited A-line rates near or below 30 kHz in human retinal imaging [16, 24, 46, 166, 169, 170]. Such low A-line rates induce two challenges. First, head and eye motions [24, 47] make optical alignment, large field-of-view (FOV) volumetric imaging, and image registrations for frame averaging more challenging. Second, prolonged imaging time increases light exposure in the eye. Although within the ANSI laser safety standards [170], the visible-light illumination may be distracting and uncomfortable, inducing additional eye motions. Eye motions and high RIN reduce vis-OCT's ability to resolve minute retinal anatomical features, such as IPL sublayers and BM, and measure functional parameters, particularly challenging because it reduces image contrast and, unlike noise variation, it cannot be removed by frame averaging or filtering. Our solution is to develop a balanced-detection (BD) vis-OCT, which uses two calibrated spectrometers to cancel noises (including RIN) [5, 171, 172]. BD has been well-demonstrated in swept-source OCT [2, 5], where two single-element detectors record interference sweeping through the entire bandwidth to reject influences from light source energy instability. BD was also tested in spectrometer-based OCT systems [172-177]. A comprehensive study by Bradu et al. found no noise floor reduction, partially attributed to poor calibration between the two spectrometers [173]. Other demonstrations also showed limited success, where researchers routinely reported 3–6 dB increases in signal intensity but no significant reduction in the noise floor [172, 174-177]. Because BD equally splits the interference signals into two separate paths before being recombined, the reported improvement in signal amplitude is not obvious when compared with a single spectrometer detection without splitting the interference signal [173]. One study circumvented the calibration problem by interleaving detection of fringes in time on the same spectrometer [177], but degraded the effective A-line rate by 50%. Reducing RIN should be a key goal of BD but is particularly constrained by the inability to calibrate two spectrometers precisely.

Recently, Kho et al. [178] reported that excess noise (dominated by RIN) from a supercontinuum source is spectrally encoded on the spectrometer. This allowed for accurate pixel-to-wavelength mapping using only the RIN. Since the goal of BD is to subtract RIN commonly measured across two spectrometers, we hypothesize that it is optimal to calibrate spectrometers using the RIN itself. This new calibration differs from previous calibrations [172-174, 176], which make overly simplified assumptions that careful optical alignment, finding overlap in the OCT fringes or background spectra, or linear wavenumber (k) interpolation can achieve efficient noise reduction in BD SD-OCT.

In this work, we show for the first time that creating a subpixel map between two spectrometers using RIN correlation, polynomial fitting such map, and using the map to interpolate OCT fringes greatly improves the efficiency of BD and significantly reduces the OCT noise floor. First, we developed BD-vis-OCT based on a Mach-Zehnder interferometer and calibrated two spectrometers using the spectrally-encoded RIN. After calibrating two spectrometers with subpixel accuracy, we subtracted their interference fringes to reject the RIN. Subsequently, we investigated BD performance as a function of calibration errors and found that subpixel accuracy is necessary for optimal RIN rejection. We validated RIN rejection in a retinal phantom at multiple reference arm power levels by tuning spectrometer camera gain and found up to 20.5 dB reduction in the noise floor. In addition, we imaged the retinas of five healthy human volunteers at 125 kHz A-line rate using BD SD-OCT. BD vis-OCT revealed anatomical features previously obscured by the noise floor, opening a new window for high-speed SD-OCT ophthalmic imaging using high RIN light sources.

7.4 METHODS AND MATERIALS

7.4.1 Experimental setup

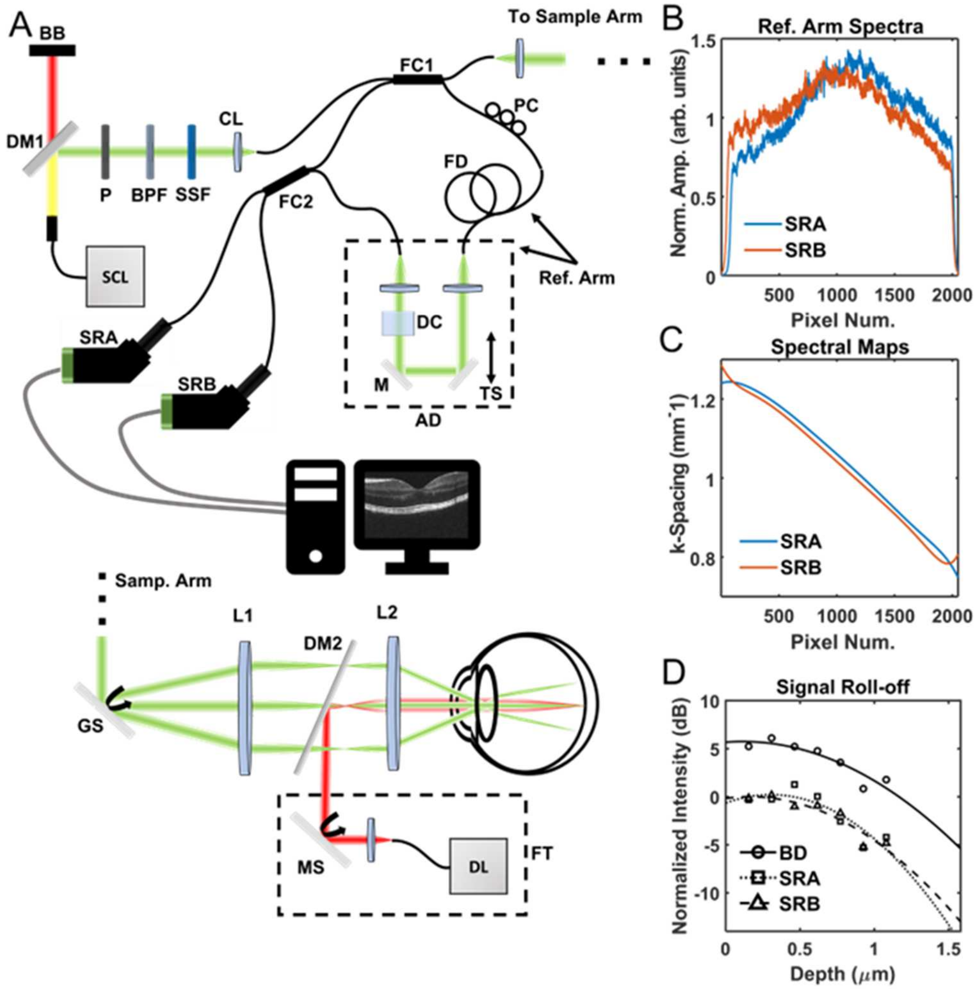

Figure 7.1. (A) Schematic of BD-vis-OCT system. SCL: supercontinuum laser; DM: dichroic mirror; BB: beam block; P: polarizer; BPF: bandpass filter; SSF: spectral shaping filter; CL: collimating lens; PC: polarization controller; FC: fiber coupler; FD: fiber delay; TS: translation stage; M: mirror; DC: dispersion compensation; AD: air delay; SRA: spectrometer A; SRB: spectrometer B; GS: galvanometric scanner; L: lens; MS: microelectromechanical scanner; DL: diode laser; FT: fixation target; (B) reference arm spectra; (C) spectrometer wavenumber (k) maps; (D) Signal roll-offs normalized with respect to the first depth

measurement in SRB. Circle, square, and triangle show actual measurements for SRA, SRB and balanced detection (BD); corresponding lines show best fits

Fig. 7.1A illustrates the BD-vis-OCT system based on a modified Mach-Zehnder interferometer (MZI) configuration. The MZI's transmission-based configuration minimizes the number of fiber couplers in the light paths to reduce losses. A supercontinuum laser (SCL, SuperK 78 MHz EXW-6, NKT Photonics, Denmark) delivered light to a multistage filter set consisting of a dichroic mirror (DM1, DMSP650, Thorlabs, NJ), polarizer (P, WP25M-VIS, Thorlabs), bandpass filter (BPF, FF01-560/94-25, Semrock, NY), and spectral shaping filter (Hoya B-460, Edmund Optics, NJ). We coupled the light into a 10:90 fiber coupler (FC1, TW560R3A2, Thorlabs). The 10% output of FS1 delivered light to the sample arm (Fig. 7.1A, bottom). A collimating lens (CL) collimated a 2.5-mm diameter beam incident on a galvanometer scanner (Cambridge Technology, MA). A two-lens telescopic system (L1 and L2) with a 3:2 magnification ratio delivered 240 μW to the eye. Meanwhile, a red diode laser (DL, LPS-675-FC, Thorlabs) delivered 5 μW to the eye for fixation. We separated the fixation light from the vis-OCT path using a dichroic mirror (DM2, 3114-666, Alluxa, CA). A microelectromechanical scanner (MS, Mirrorcle, Richmond, CA) scanned a 'star-shaped' fixation pattern on the retina during vis-OCT imaging. The 90% output of FC1 was input to a transmission-type reference arm, consisting of a polarization controller (PC), a fiber delay line (FD), and an adjustable air delay (AD) line. The AD and dispersion compensation (DC) matched the double-pass path length in the free space part of the sample arm, while the FD matched the double-pass fiber path length in the sample arm. Backscattered light from the sample arm and transmitted light from the reference arm interfered in a 50:50 fiber coupler (FC2, TW560R5A2, Thorlabs). We collected the interfered light from both output arms using two spectrometers (SRA and SRB, Blizzard SR, Opticent Inc.,) which offer a maximum A-line rate of 135 kHz using a 1D CCD camera (OctoPlus, Teledyne e2v). SRA covers 509.1 nm to 613.7 nm and SRB covers 507.5 nm to 613.1 nm. The BPF slightly reduces the usable range to 513 nm to 607 nm. We subtracted the SRA detection from the SRB detection for BD. Due to manufacturing imperfection, the splitting ratio of FC2 was slightly asymmetric, as shown in Fig. 7.1B, which did not significantly compromise the BD performance. SRA and SRB have alignment differences as indicated by their different wavenumber (k) [27] spacings in Fig. 7.1C. The k-spacings show that the spectrometer alignments are nonlinear with respect to pixel index and nonlinear with respect to each other, making hardware-based calibration impractical and software-based calibration non-trivial. We measured an *in vivo* axial resolution of 1.7 μm with SRB alone (single detection, or SD) and with SRA & SRB for BD (see Supplementary Materials)[1]. At 1-mm imaging depth, SRA & SRB have signal roll-offs of -4.3 dB and -3.6 dB, respectively, and a combined BD (SRB-SRA) signal roll-off of -4.0 dB (Fig. 7.1D). At a 125 kHz A-line rate and minimal camera amplification, we measured sensitivities of 73.1 dB and 99.6 dB near the zero-delay for SRB and BD, respectively. System performance for *in vivo* and *ex vivo* imaging are shown in Section III.

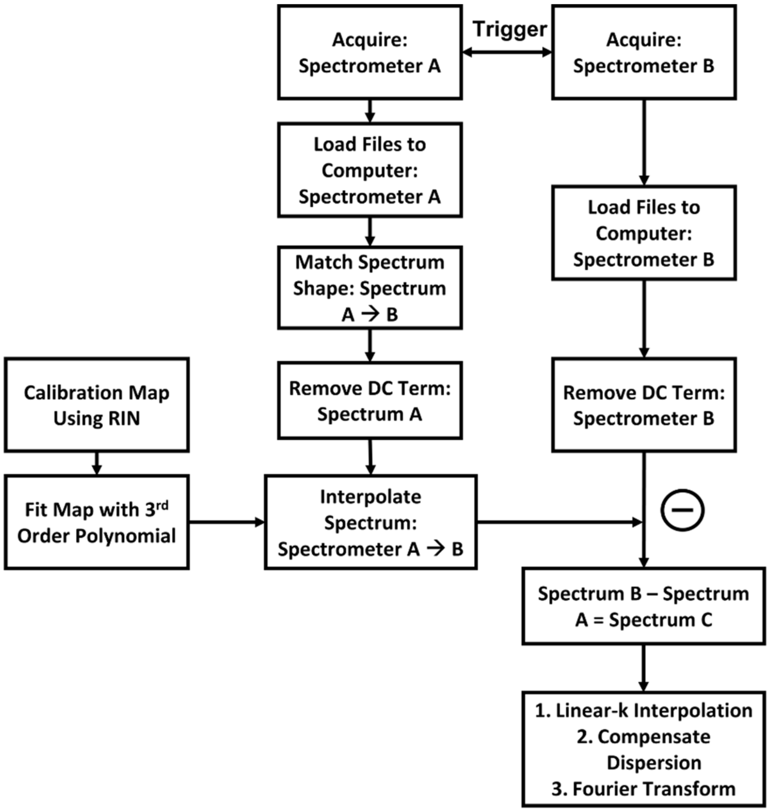

Figure 7.2. Flowchart for BD vis-OCT. The sequence follows arrows from top to bottom.

Fig. 7.2 shows the flowchart detailing the steps for BD from acquisition to image reconstruction. Briefly, we acquired A-lines in SRA and SRB simultaneously. In pre-processing, we scaled the spectrum in SRA by its ratio with that in SRB to digitally match their DC shapes. This did not enhance image quality but allowed for a more unbiased comparison of image quality metrics considering any deviations from an ideal 50:50 splitting ratio (Fig. 7.1B). Then, we removed the DC components from the respective fringes. After pre-processing the fringes, we applied a calibration map generated by the maximum RIN correlations between SRA and SRB [178]. We fitted a third-order polynomial to the map to reduce undersampling artifacts caused by the finite pixel number of the camera. The calibration and its performance are detailed later in Section III-A. We used the calibration map to interpolate the fringes from SRA to linear with respect to SRB. After calibration, we subtracted the respective fringes between SRB and SRA. Finally, we performed traditional OCT image reconstruction, including k-space interpolation, compensation for dispersion mismatch, and the Fourier transform.

7.4.2 Phantom eye imaging

We imaged a phantom eye (OCT Model Eye, Rowe Technical Design) using a rectangular scan consisting of 512 A-lines × 64 B-scans at an A-line rate of 125 kHz (7.7 μs exposure time, 0.3 μs readout time). The total acquisition time was 0.26 seconds. We imaged at the highest and lowest camera gain levels.

7.4.3 Human imaging

We imaged the eyes of four healthy volunteers between 25 and 47 years of age. The imaging procedure was approved by the Northwestern University institutional review board (IRB), and volunteers provided informed consent before imaging. Imaging was performed at an A-line rate of 125 kHz (7.7 μs exposure time, 0.3 μs readout time) using the highest camera gain. Vis-OCT illumination light power was no higher than 240 μW on the cornea. We scanned multiple patterns: small FOV with a 4 mm × 4 mm scanning range and 512 A-lines × 256 B-scans (total acquisition time: 1 second); medium FOV with a 7 mm × 4 mm scanning range and 1024 A-lines × 256 B-scans (total acquisition time: 2 seconds); large FOV with a 10 mm × 4 mm scanning range and 1024 A-lines × 256 B-scans (total acquisition time: 2 seconds); and high-density speckle reduction (HDSR) [24] with either a 12 mm × 3 mm or 8 mm × 3 mm scanning range and 32768 A-lines × 16 B-scans (total acquisition time: 4 seconds). HDSR scans consisted of 16 scans orthogonal to the B-scan axis [24]. All respective scans in this work were acquired within 4 seconds or less.

7.4.4 Image quality metrics

Noise floor amplitude and variation, which increase with RIN, degrade image quality. We adopted three commonly-used metrics to compare image quality between SD and BD.

OCT image sensitivity was previously defined as the ratio of the signal to the noise floor [2]. Here, we use a similar metric called peak-signal-to-noise-floor-ratio

$$PSNFR = 20\log_{10}\frac{A_{sig_m}}{A_{floor}}, \tag{7.1}$$

where A_{sig_m} is the maximum amplitude of the selected signal and A_{floor} is the average amplitude of the noise floor near A_{sig_m}. PSNFR describes the range where a signal can be differentiated from A_{floor}. Increased PSNFR results in higher imaging sensitivity and contrast between the signal and noise floor. Previous reports showed A_{sig_m} is biased when it is not sufficiently larger than A_{floor}, thereby biasing PSNFR [61]. We found empirically in our images that this bias becomes small when PSNFR > 10 dB. Rather than make assumptions about the exact influence of this bias, we measured PSNFR in regions with PSNFR > 10 dB.

Next, we measured image peak-signal-noise-ratio [39]

$$PSNR = 20\log_{10}\frac{A_{sig_m}}{\sigma_{floor}}, \tag{7.2}$$

where σ_{floor} is the standard deviation of the noise floor near A_{sig_m}. PSNR highlights pixel uncertainty relative to the peak signal. Due to the potential bias in A_{sig_m}, we measured PSNFR in the same brightly reflecting regions as PSNFR.

Finally, we measured contrast-to-noise ratio [39]

$$CNR = 10\log_{10}\frac{A_{sig}-A_{floor}}{\sqrt{\sigma_{sig}^2+\sigma_{floor}^2}} , \tag{7.3}$$

where A_{sig} is the selected signal amplitude (not necessarily maximum); and σ_{sig} is the standard deviation of the selected signal. CNR highlights limitations from both contrast and pixel uncertainty. For a weak vis-OCT signal in SD, $A_{sig} - A_{floor}$ could be close to zero or negative, yielding an extremely negative (< -10 dB) or complex CNR. We considered these cases as 'noise floor limited'.

7.5 RESULTS

7.5.1 Spectrometer noise analysis

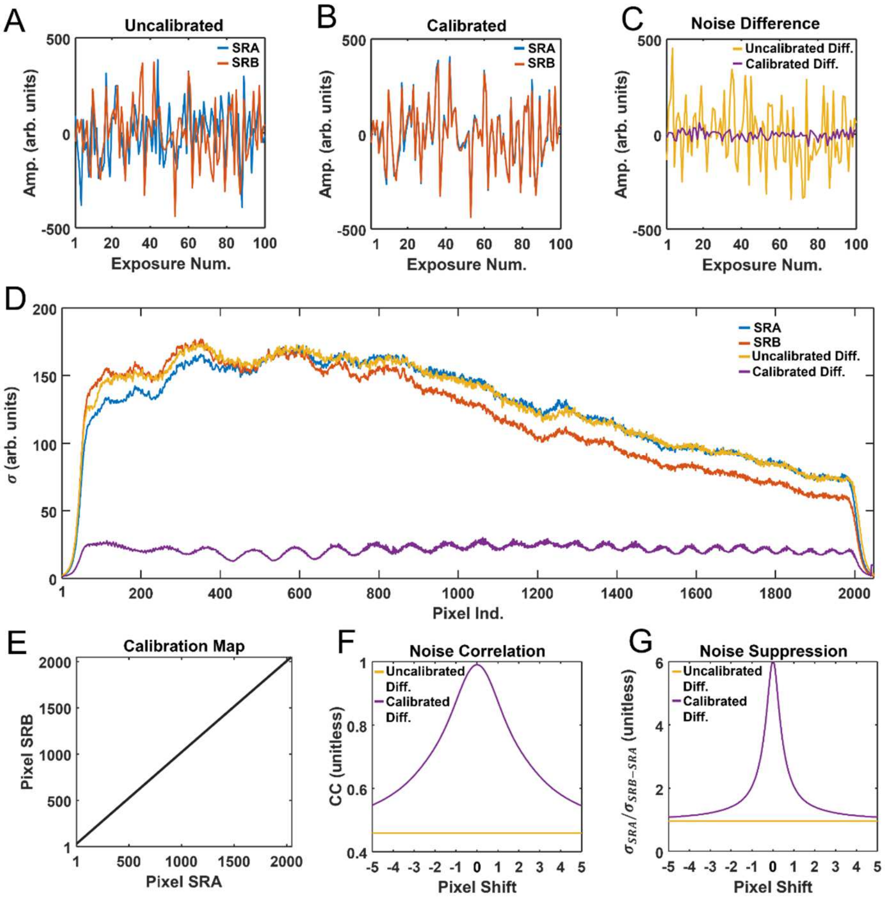

Figure 7.3. Spectrometer noises in 100 continuous camera exposures for the camera pixel 500 without calibration (A), with calibration (B), and after subtraction between spectrometer B (SRB) and A (SRA) (C); (D) Standard deviations of noises across the entire camera array; (E) Calibration map relating pixels in SRB to pixels in SRA. The map is nonlinear and displayed after fitting by a third-order polynomial; (F) Correlation coefficient as a function of shifting the map in (E). (G) Average ratio of standard deviation between SRA and the difference of SRA and SRB as a function of shifting the map in (E). Higher ratio indicates better noise suppression. In (F) & (G), pixel shift = 0 represents the optimal calibration map.

We compared noises in the spectrometers before and after BD calibration in the 1D CCD camera array. Figs. 7.3A-7.3C show the noises at camera pixel index 500 acquired across 100 continuous camera exposures. Fig. 7.3A shows noises in SRA (orange) and SRB (blue) before the calibration procedure. The standard deviation (σ, [arb. units]) of noises is 160.6 for SRA and 160.4 for SRB. The noises do not overlap, which is a result of their alignment differences. The difference is quantified by their correlation coefficient (CC) of 0.49. Fig. 7.3B plots the same noises after calibration. After calibration, the noises overlap almost identically with a CC of 0.99. Fig. 7.3C plots the difference between the noises from SRA and SRB before and after calibration. The noise subtraction without calibration has a significantly higher standard deviation ($\sigma = 157.6$) than after calibration ($\sigma = 19.6$).

We validated these trends for each pixel in the spectrometer. Fig. 7.3D plots the σ of noises from SRA and SRB and the σ of their difference before and after calibration for 5000 camera exposures. The average σ across all pixels (neglecting edges of the camera where there is no light) is 131.1 for SRA and 123.9 for SRB. The average σ across all pixels after taking the difference of the spectrometers is 21.7 with calibration and 133.1 without calibration. The average CC between SRA and SRB is 0.46 before calibration and 0.99 after calibration. As shown in Fig. 7.3D, calibration effectively reduces noise across all camera pixels (all wavelengths). Furthermore, there is a spectral dependence in noises before calibration (orange and blue lines) and in their difference without calibration (yellow line), indicating the spectral dependence of RIN [9]. After calibration, the noises are mostly flat across all pixels (wavelengths), indicating an effective RIN rejection. We note a small oscillation in the calibrated noise difference. This is associated with aliasing by the finite pixel sampling of the camera. This artifact is mostly suppressed by fitting a third-order polynomial to the calibration map (Fig. 7.3E) to estimate continuous subpixel mapping. In the Supplementary Materials, we show the impact of fitting the calibration map on noise subtraction.

As seen in previous BD SD-OCT results [172-177], hardware and software calibrations are non-trivial and susceptible to errors. We show that accurate subpixel calibration is necessary for optimal noise rejection. To assess the impact of a potential miscalibration, we added constant subpixel shifts to each pixel in the calibration map in Fig. 7.3E. Fig. 7.3F plots the correlation between noises in SRA and SRB as a function of pixel shift. The purple line shows the average CC across all pixels when the shifted calibration map is applied, and the yellow line shows the average CC when no calibration is applied (CC = 0.46). The optimal calibration map yields a CC = 0.99 at 0 pixel shift. Meanwhile, noise correlation decays exponentially for nonzero pixel shifts. The average CC drops to 0.96 at ±0.5 pixel shift, 0.87 at ±1 pixel shift, and 0.64 at ±3 pixel shift.

Fig. 7.3G plots the noise suppression by taking the ratio of average σ from SRA and the σ difference of SRA and SRB $\left(\frac{\sigma_{SRA}}{\sigma_{SRB}-\sigma_{SRA}}\right)$. When this ratio is 1, the average σ after BD is the same as SRA. The purple line shows the average noise suppression across all pixels when the shifted calibration map is applied. The yellow line shows the average noise suppression when no calibration is applied (noise suppression ratio = 0.99, which is noisier than SRA alone). The optimal calibration map yields a noise suppression ratio of 6.0 at 0 pixel shift. The average noise suppression ratio is 3.3 at ±0.5 pixel shift, 2.1 at ±1 pixel shift, and 1.2 at ±3 pixel shift. The majority (67%) of noise suppression inefficiency occurs when the pixel shift is < 1, and about half (45%) of the noise suppression inefficiency occurs when the pixel shift < 0.5.

This means that the subpixel calibration accuracy demonstrated in our work is critical for balanced detection to be effective. Such high sensitivity to subpixel shift is further emphasized by the average CC, where only a 3% drop in the CC at ± 0.5 pixel shift (Fig. 7.3F) corresponds to a 45% drop in noise suppression (Fig. 7.3G).

As a comparison, Kuo et al. [172] performed hardware and software-based calibration for BD SD-OCT by finding overlapping features in the spectra detected by the two spectrometers. They estimated ~ 40% inefficiency in their noise subtraction and did not demonstrate any noise floor reduction. Such a method is not necessarily sensitive to subpixel differences or nonlinearities between the spectrometers. The spectrometer noise analysis presented here provides a quantitative explanation of and solution for the inefficiencies of BD SD-OCT. We note that the potential miscalibrations tested here (constant pixel shift across camera array) are likely overly simplified. In reality, the nonlinear nature of spectrometer alignment (e.g., Fig. 7.1C and also reported by Kuo et al.) can introduce additional non-linear pixel errors across the camera array, making the subpixel sensitivities shown here conservative estimations.

7.5.2 Imaging phantom eyeball

We imaged a phantom eyeball to assess BD-vis-OCT retinal imaging in a well-controlled environment. We compared SD and BD images using the spectrometer camera's highest and lowest gains and measured PSNFR, PSNR, and CNR. Reference arm powers were set to ~ 67% of the saturation limit of the camera.

Figs. 7.3A & 7.3B show SD and BD B-scans (five-times averaging) of the phantom at the highest manufacturer-specified camera gain. The images are plotted on the same contrast scales (2% of pixel outliers at extremes removed, square root scale, normalized between 0 and 1). All vis-OCT images in this work are plotted on this contrast scale. Fig. 7.3C plots A-lines from the regions highlighted by the red and green dashed lines in Figs. 7.3A and 7.3B, respectively. The peak near 200 μm depth from BD (green line) is ~ 6 dB higher than that from SD (red line), consistent with the addition of two fringes from SRA and SRB. The noise floor (near 100 μm depth) is 9.5 dB lower for BD than SD.

To measure PSNFR and PSNR in the phantom eye, we used the homogeneous brightly reflecting region at the top of the phantom (Figs. 7.3A & 7.3B) to minimize the bias potential bias. We averaged five adjacent A-lines and automatically used the maximum amplitude at the selected bright reflection as A_{sig_m}. We used the average of a 20-pixel (depth) × 20-pixel (lateral) window centered 70 pixels above A_{sig_m} as A_{floor}. We measured PSNFR and PSNR for A-lines 25 through 425 (of 512), avoiding the edges of the image, which were too close to the zero-delay to measure the noise floor accurately. To measure CNR in the phantom retina, we used the average of a 20-pixel (depth) × 20-pixel (lateral) region below the bright line as A_{sig} and the average of a 20-pixel (depth) × 20-pixel (lateral) window centered 70 pixels above the bright line at the same lateral location as A_{floor}.

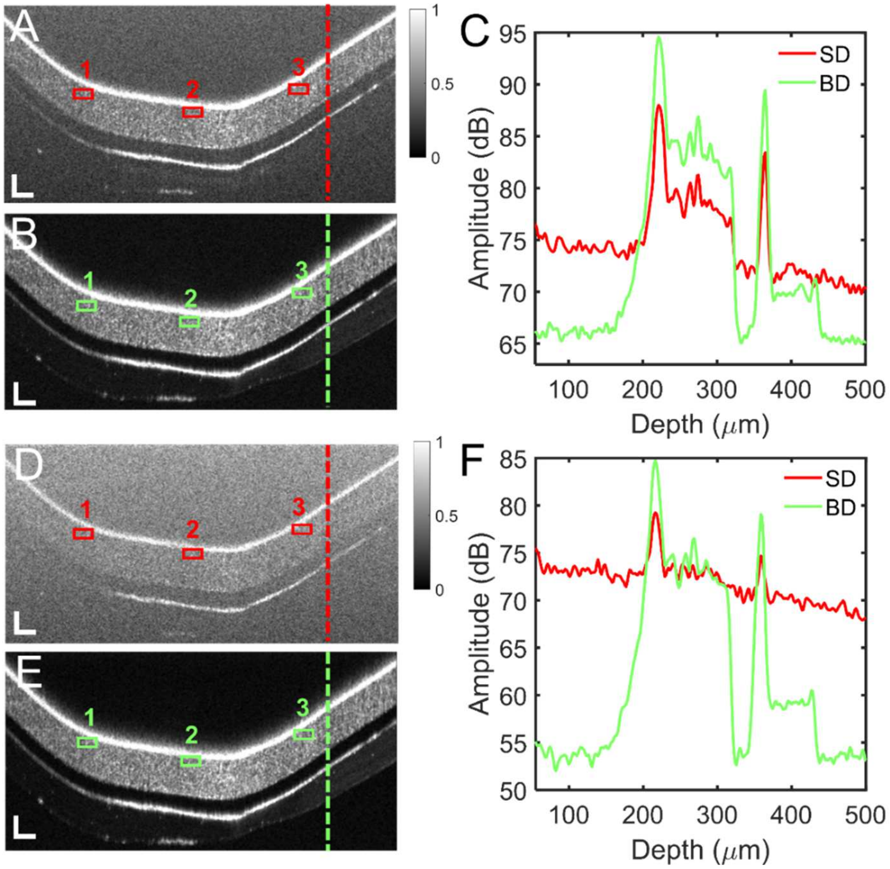

Fig. 7.4. (A) Single detection and (B) balanced detection B-scans of phantom eye at lowest camera amplification level. Red and green boxes highlight measurement locations of CNR. Red and green dashed lines highlight locations of A-lines plotted in (C); (D-F) Following same layout as (A-C) but for maximum camera amplification level. B-scans magnified to show detail. Scale bars 50 μm (vertical) × 225 μm (horizontal).

Image metrics for Figs. 7.4A & 7.4B are summarized in Table 7.1. After BD, PSNFR increases by 14.8 dB and PSNR increases by 14.6 dB. For boxes labeled 1-3, after BD, CNR increases from ~ 1 dB or less to 3-4 dB.

Figs. 7.4D & 7.4E show SD and BD B-scans (five-times B-scan averaging) of the phantom at the lowest manufacturer-specified spectrometer camera gain. Reducing the camera gain increased its photon detection capacity. Reaching the same detection amplitude as the highest camera gain (shown by noise floor amplitude ~75 dB in Figs. 7.4C & 7.4F) while maintaining the same sample arm power required increasing reference arm power, which also increased contribution of RIN. While SD failed to resolve the phantom structure clearly, BD fully revealed all the structural details. Fig. 7.4C plots the A-lines from the locations highlighted by the red and green dashed lines in Figs. 7.4A and 7.4B, respectively. The peak near 200 µm depicts the bright layer on the top of the phantom, which is is ~ 5 dB higher for BD (green line) than SD (red line). The expected BD increase is 6 dB from the addition of the two interference fringes; the lower value (5 dB vs. 6 dB) is associated with noise bias in the SD. The noise floor (near 100 µm) is ~ 20.5 dB lower for BD than SD.

Image metrics for Figs. 7.4D & 7.4E are also summarized in Table 7.1. Using BD, PSNFR increases by 25.3 dB and PSNR increases by 25.6 dB. For boxes labeled 1-3, after BD, CNR increases from noise floor limited or very negative to 3-4 dB.

In spectral domain OCT, assuming reference arm power is much greater than sample arm power, A-line intensity scales linearly with reference arm power [2, 172]. For a shot-noise limited system, A-line noise variance scales linearly with the reference arm power; for a RIN-dominated system, it scales with the square of the reference arm power [172]. Therefore, PSNFR and PSNR are sensitive to reference arm power increases in a RIN-dominated system but are insensitive to reference arm power increases in a shot-noise limited system [23, 172, 173]. For SD, image quality metrics are highly sensitive to the camera gain-determined reference arm power. The lower gain level has 8.6 dB lower PSNFR and 8.8 dB lower PSNR. The majority of this difference can be attributed to RIN. Comparatively, BD is significantly less sensitive to the camera gain-determined reference arm power (the lower gain level has 1.9 dB higher PSNFR and 2.2 dB higher PSNR). Small changes to PSNFR and PSNR in response to a near 3-fold increase in RIN suggests that BD-vis-OCT removes nearly all RIN and operates near the shot-

noise limit. The slightly better performance of the lower amplification level may be attributed to the slightly lower electronic noises or increased reference arm power.

Image	Method	PSNFR (dB)	PSNR (dB)	CNR 1 (dB)	CNR 2 (dB)	CNR 3 (dB)
Phantom, High Amp.	SD	13.9	26	0.3	1.5	0.3
Phantom, High Amp.	BD	28.7	40.6	3.3	3.9	3.7
Difference SD → BD		14.8	14.6	3.0	2.4	3.4
Phantom, Low Amp.	SD	5.3	17.2	NFL	-7.2	NFL
Phantom, Low Amp.	BD	30.6	42.8	3.4	3.8	3.6
Difference SD → BD		25.3	25.6	NFL → 3.4	11	NFL → 3.6

Table 7.1 SD: Single Detection; BD: Balanced Detection; NFL: Noise Floor Limited

7.5.3 Imaging human retina with small field-of-view

Fig. 7.5 shows the small FOV scan located near the fovea of the right eye of a healthy, 47-year-old male volunteer (Eye 1). Figs. 7.5A & 7.5B show *en-face* images for SD and BD, respectively. We generated the *en-face* images by taking the mean intensity projection of the retinal volume after cropping out the first 20 pixels along the depth direction. The red and green dashed boxes in Figs. 7.5A & 7.5B highlight regions that are magnified by Figs. 7.5C and 7.5D, respectively. Fig. 7.5D reveals small vessels (highlighted by green stars) buried in the noise floor with SD in Fig. 7.5C (highlighted by red stars). Figs. 7.5E & 7.5F show B-scans (registered and averaged five times) at the locations highlighted by the red and green dashed lines in Figs. 7.5A & 7.5B, respectively. Comparing with SD (Fig. 7.5E), where the high noise floor obscures the anatomical details [166, 179], the BD resolves them. To highlight the qualitative difference in structural visibility between SD and BD, we overlaid A-lines (log scale) on their respective locations in Figs 7.5E and 7.5F. A-line 1 highlights a blood vessel at its respective location in the SD (red A-line) and BD (green A-line). For SD, the signal within the blood vessel is buried in the noise floor. Meanwhile, the reduced noise floor in BD reveals the characteristic blood signal decay [63, 161]. The attenuation is visible across the entire depth of the vessel. A-line 2 highlights the retinal anatomical layers resolved by SD and BD, respectively. BD reveals the inner plexiform layer (IPL) sublayers, which has three distinct bright laminations and is a promising biomarker for glaucoma [16, 167]. In SD image and A-line, IPL is invisible.

Image	Method	Scan	PSNFR (dB)	PSNR (dB)	CNR 1 (dB)	CNR 2 (dB)
Eye 1	SD	Small FOV	11.1	23.7	-6.0	-3.8
Eye 1	BD	Small FOV	26.2	38.8	4.4	3.7
Difference SD → BD			15.1	15.1	10.4	7.5
Eye 2	SD	Med. FOV	16.1	28.6	-6.7	-9.7
Eye 2	BD	Med. FOV	31.8	43.8	3.4	3.8

Difference SD → BD			15.7	15.2	10.1	13.5
Eye 3	SD	Small FOV	1.4	12.8	NFL	-6.1
Eye 3	BD	Small FOV	15.5	28.1	4.0	3.0
Difference SD → BD			14.1	15.3	NFL → 4.0	9.1
Eye 4	SD	Med. FOV	8.1	20.9	NFL	-6.6
Eye 4	BD	Med. FOV	22.5	35	1.3	1.2
Difference SD → BD			14.4	14.1	NFL → 1.3	7.8
Eye 5	SD	Med. FOV	8.7	21.3	NFL	NFL
Eye 5	SD	Med. FOV	22.3	35.1	2.2	2.1
Difference SD → BD			13.6	13.8	NFL → 2.2	NFL → 2.1

Table 7.2 SD: Single Detection; BD: Balanced Detection; NFL: Noise Floor Limited; Eyes 3-5 shown in Supplementary Materials

To measure PSNFR and PSNR in the human retina, we identified brightly reflecting regions at the internal limiting membrane (ILM). We averaged 5 adjacent A-lines and automatically used the maximum amplitude at the selected bright reflection as A_{sig_m}. Since such bright reflections are sparse in the human retina, we measured PSNFR and PSNR only in discrete regions. We used the average of a 20-pixel (depth) × 20-pixel (lateral) window centered 50 pixels above A_{sig_m} as A_{floor}. To measure CNR in the human retina, we used the average of a 20-pixel (depth) × 20-pixel (lateral) region in the nerve fiber layer (NFL) as A_{sig} and the average of a 20-pixel (depth) × 20-pixel (lateral) window centered 50 pixels above the ILM at the same lateral location as A_{floor}.

We measured PSNFR and PSNR at an ILM reflection (highlighted by red and green arrows in Figs. 7.5E & 7.5F, respectively). We measured CNRs in the RNFL highlighted by the red and green boxes labeled 1 and 2. Image metrics for Figs. 7.5E & 7.5F (Eye 1) and all volunteers (Eyes 2-5) are summarized in Table 7.2. In Figs. 7.5E & 7.5F, PSNFR increases by 15.1 dB and PSNR increases by 15.1 dB. CNR in boxes 1 & 2 increase from negative to 4.4 dB and 3.7 dB, respectively.

There are minimal motion artifacts in the small FOV volume. We did not perform any registrations for the *en face* projections. At 125-kHz A-line rate, the small FOV volumes were acquired in 1 second, overcoming many fundamental limitations from eye motions, where, for example, involuntary saccades occur on the order of 1 Hz [18]. Additional images with small FOV from other volunteers are shown in Supplementary Materials.

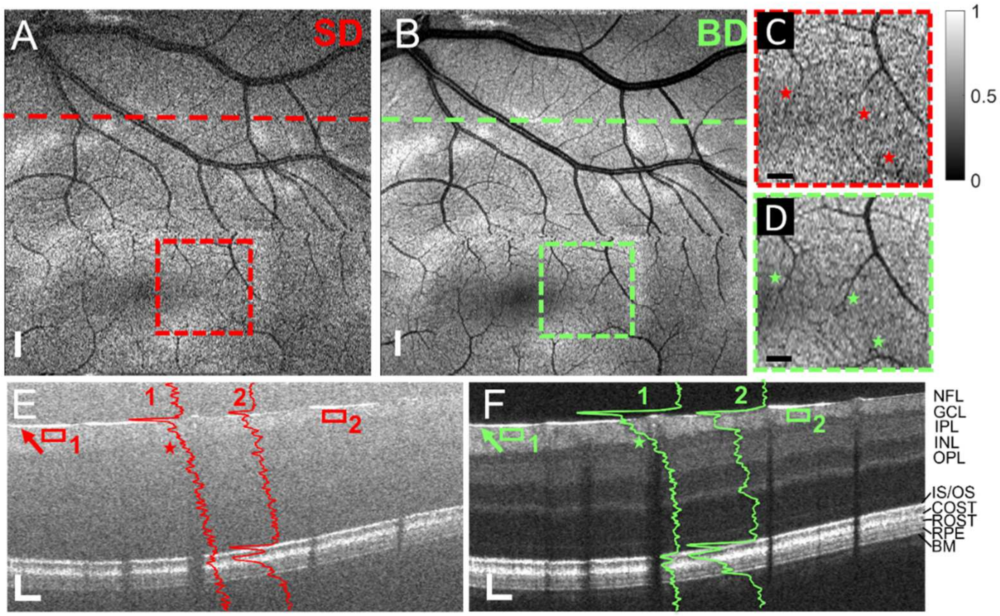

Figure 7.5. Small field-of-view vis-OCT images of the retina of a healthy 47-year-old male (Eye 1); (A) En-face image near the fovea for SD; (B) En-face projection near the fovea for BD; (C) Magnified view of area highlighted by the red dashed box in panel A; red stars highlight small blood vessels; (D) Magnified view of the area highlighted by the green dashed box in panel B; green stars highlight small blood vessels; (E) B-scan image from the location highlighted by the dashed line in panel A; (F) B-scan image from the location highlighted by the dashed line in panel B; Red and green A-lines overlay their respective locations; stars near A-line 1 highlight blood attenuation; red and green arrows highlight locations of PSNFR and PSNR measurement; solid red and green boxes highlight locations of CNR measurement. Scale bars in (A) & (B) are 275 μm (isometric); scale bars in (C) & (D) are 150 μm (isometric); scale bars in (E) & (F) are 60 μm (vertical) × 225 μm (horizontal). NFL: nerve fiber layer; GCL: ganglion cell layer; IPL: inner plexiform layer; INL: inner nuclear layer; OPL: outer plexiform layer; ELM: external limiting membrane; IS/OS: inner segment/outer segment; COST: cone outer segment tips; ROST: rod outer segment tips; RPE: retinal pigment epithelium; BM: Bruch's membrane.

7.5.4 Imaging human retina with medium field-of-view

Fig. 7.6 compares SD and BD vis-OCT image with medium FOV from the left eye of a 24-year-old male volunteer (Eye 2). En face projections (Figs. 7.6A and 7.6B) cover the fovea and optic disc (OD) in a single scan with minimal motions. In the BD image (Fig. 7.6B), as compared with SD, vessels from the OD to the fovea are visible at the capillary level thanks to the improved optical contrast within the visible-light spectral range. Figs. 7.6C and 7.6D are magnified views of the areas highlighted by the red and green dashed boxes in Figs. 7.6A and 7.6B, respectively, where capillaries are better visualized by BD.

Figs. 7.6E and 7.6F show B-scans (registered and averaged five times) from respective locations highlighted by the red and green dashed in Figs. 7.6A and 7.6B. Similar to the small FOV B-scans, BD reveals the retinal anatomical layers with much higher contrast than SD. In previous work by Rubinoff et al. [9], we showed that B-scans acquired at an A-line rate of 25 kHz could not be registered and directly averaged without significant blurring. Here, we show that with a 125 kHz A-line rate and near the same scanning range, five B-scans can be registered and averaged with nearly no blurring. We previously limited vis-OCT's A-line rate at 25 kHz to reduce the influence of RIN and increase image quality in human imaging. BD achieved comparable image quality at a 5-fold increased A-line rate. In Figs. 7.6E and 7.6F, we overlay two A-lines (log scale) that highlight retinal structures and a blood vessel at their respective locations (highlighted 1 & 2). We measured PSNFR and PSNR at the regions highlighted by the red and green arrows, respectively. For SD, PSNFR and PSNR are 16.1 dB and 28.6 dB, respectively. For BD, PSNFR and PSNR are 31.4 dB and 43.8 dB, respectively. PSNFR and PSNR increased by 15.3 dB and 15.2 dB, respectively. We measured CNR in the areas highlighted by the red and green boxed regions labeled 1 and 2 in Figs. 7.6E and 7.6F. In Fig. 7.6E, CNRs are - 6.7 dB in box 1 and -9.7 dB in box 2. In Fig. 7.6F, CNRs are 3.3 dB in box 1 and 3.8 dB in box 2. Additional images with medium FOV are shown in Supplementary Materials.

E. Imaging Human Retina with Large Field-of-View with High-Density Speckle Reduction

Figs. 7A and 7B respectively show en-face SD and BD vis-OCT images from Eye 2 with large FOV and Figs. 7C and 7D respectively show high-density speckle reduction (HDSR) [9] SD and BD B-scan image from the positions highlighted by red and green dashed lines in Figs 7A and 7B, respectively. The large FOV scan enables vis-OCT to provide an unprecedented view of the retina beyond the macula and optic disc while exhibiting minimal motions thanks to the 125-kHz A-line rate. We combined the large FOV scan with an HDSR scan. A benefit of the HDSR scan is that it can combine dense A-line scanning, speckle reduction, and wide scanning range without registrations [9]. Dense A-line scanning can also help reduce fringe washout from the scanner across a long scanning range. At a 125 kHz A-line rate, we can increase HDSR A-line density without sacrificing the total scanning time. Here, we acquired HDSR B-scans with 32768 A-lines (0.26 s per B-scan) and laterally averaged them 32 times, allowing many more averages than in the medium FOV (five averages) while scanning a larger range.

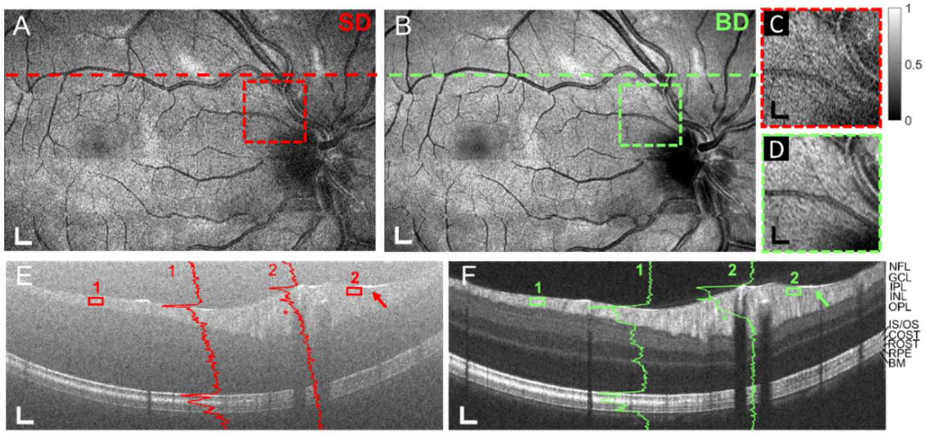

Fig. 7.6. Medium FOV vis-OCT images of the retina of a healthy 24-year-old male (Eye 2); (A) En-face image near the fovea for SD; (B) En-face image near the fovea for BD; (C) Magnified view of the region highlighted by the red dashed box in panel A; (D) Magnified view of the region highlighted by the green dashed box in panel B; (E) B-scan image from the location highlighted by the dashed line in panel A; (F) B-scan image from the location highlighted by the dashed line in panel B; Red and green A-lines overlay their respective locations; stars near A-line 2 highlight blood attenuations; red and green arrows highlight locations of SNFR measurement; solid red and green boxes highlight locations of CNR measurement. Scale bars in (A) & (B): 275 μm (vertical) × 325 μm (horizontal); scale bars in (C) & (D): 150 μm (vertical) × 175 μm; scale bars in (E) & (F): 50 μm (vertical) × 275 μm (horizontal).

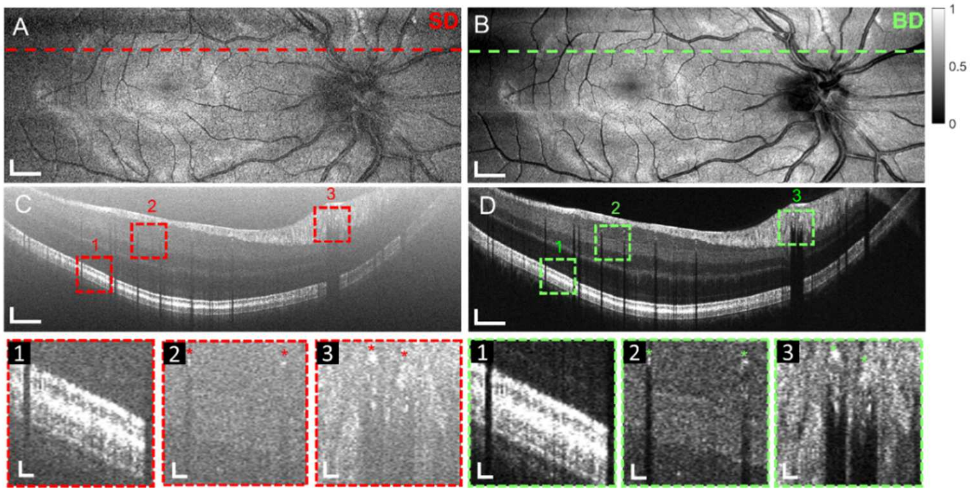

Figure 7.7. (A-D) Large FOV scans in 24-year-old male (Eye 2); (A) En face projection for SD; (B) En face projection for BD; (C) High-density speckle reduction (HDSR) scan at location of red dashed line in (A); (D) High-density speckle reduction (HDSR) scan at location of green dashed line in (B). Red and green dashed boxes in (C) & (D) labeled 1-3 highlight regions for magnification in SD and BD, respectively. Magnifications for respective boxes are shown below. Red and green stars in boxes 1 & 2 highlight blood vessels. Scale bars in (A) & (B): 350 μm (vertical)× 500 μm (horizontal); scale bars in (C) & (D): 100 μm × 700 μm; scale bars in magnification boxes 1-3: 40 μm × 100 μm.

The red and green dashed boxes (labeled 1-3) in Figs. 7C and 7D highlight three retinal regions in the HDSR B-scan image, and their magnified views are shown below the B-scan images. Following the pattern in Figs. 7.5 & 7.6, BD, but not SD, reveals retinal layers (boxes 1 & 2) and blood vessels (boxes 2 & 3, highlighted by stars) across the retina. As seen in Fig. 7D and magnified by green boxes 1 & 2, IPL, RPE, and BM (see Figs. 7.5 & 7.6) are delineated across nearly the entire scanning range. vis-OCT imaging across a large FOV can be useful for mapping structures like IPL, RPE, and BM, providing new information for the diagnosis, monitoring, and treatment of blinding diseases. An additional example of an HDSR scan is available in Supplementary Materials.

7.6 DISCUSSION

We demonstrated BD in vis-OCT for the first time after a subpixel calibration of two spectrometers using the RIN itself. We showed in a phantom retina that BD reduces the noise floor up to 20.5 dB and reaches nearly identical image quality metrics under both highest and lowest camera gains, despite RIN being significantly at the lowest camera gain. This implies that BD is highly effective in removing high levels of RIN and that vis-OCT can afford shorter spectrometer exposure times, higher A-line rates, and cheaper light sources. Based on our *in vivo* results, we anticipate that BD-vis-OCT can reach A-line rates higher than 200 kHz, although one potential limitation is fringe washout caused by optical scanning.

We overcame discrete sampling limitations by fitting our calibration map with a third-order polynomial. This enabled subpixel calibration accuracy, giving an average CC = 0.99 between noises in the two spectrometers. Calibration accuracy may be further improved by either increasing the camera sampling density (pixel number) or reducing the k-spacing (smaller bandwidth), although additional technical complications may have diminishing benefits, given the high CC already found in the fitting approach.

We investigated the importance of subpixel calibration accuracy in BD for the first time. We showed a steep decay in noise suppression efficiency for even small pixel inaccuracies (Fig. 7.3G). For example, 67% of potential noise reduction is lost for average calibration errors of < 1 pixel, and 45% of potential noise reduction is lost for average calibration errors of < 0.5 pixels. Practical hardware tolerances, human errors, and wavelength-dependent nonlinearities make hardware-based calibrations infeasible and other software-based calibrations extremely challenging and inefficient. The high calibration accuracy required for complete RIN rejection better explains why previous demonstrations of BD SD-OCT were generally ineffective at reducing the noise floor and overall signal quality, despite increasing signal 3-6 dB. It also informs researchers the upper limitations of RIN rejection and the methods and tolerances necessary to achieve in BD SD-OCT.

In our phantom measurements, we found small image quality enhancements using the lower camera amplification compared with the higher camera amplification. This may be associated with lower electronic noises in the lower amplification, or perhaps the increased dynamic range of the detector, which merits a future, systemic investigation. Since each camera's amplification settings are set by the manufacturer and are not necessarily ubiquitous, we recommend that researchers optimize the unique settings of their cameras to maximize PSNFR and SNFR.

We found *in vivo* in five volunteers aged 25-47 that PSNFR and PSNR increases are near those found in the retinal phantom (~14-15 dB). We found CNR increases from negative to up to 4.4 dB. Most importantly, we found that retinal features entirely obscured by RIN in SD are revealed by BD. Based on roll-off measurements and image comparisons, we did not observe any significant signal decay, artifacts, or resolution loss that may be attributed to poor calibration. RIN was previously suppressed in vis-OCT by reducing the A-line rate to perform increased temporal averaging of the interference fringe. When combined with the distraction and potential discomfort of a visible-light beam, low speed is perhaps the critical limiting factor for translating vis-OCT to the clinics. BD enables high-speed vis-OCT without significantly sacrificing image quality, resolution, or spectroscopic bandwidth. Additionally, supercontinuum lasers are more costly than SLDs, and technology improvements to reduce RIN in supercontinuum lasers may add additional costs. BD-vis-OCT significantly reduces the influence of RIN, permits high-speed, high-quality human imaging, and imposes fewer performance requirements on supercontinuum lasers, all of which may bring down the overall vis-OCT cost. Although we focus on vis-OCT here, it is not the only OCT technology where BD is applicable. Other OCTs use supercontinuum sources to achieve broad bandwidths to increase axial resolution [180], or operate in the far-infrared range for deep penetration [181].

The recent development of ANDi fiber supercontinuum lasers [182] presented a positive step forward in low RIN supercontinuum-based OCT. However, its demonstration for OCT is limited to the NIR wavelength range and is not yet commercially available. Unlike introducing a new source, BD requires no new laser technologies or expertise and is immediately compatible with all existing high-RIN supercontinuum sources across any wavelength range. Robust and simple subpixel calibration enables using two spectrometers with different hardware alignments, removing a major technical hurdle that previously prevented noise rejection. Since calibration only requires spectrometer detection of reference arm power, it can be performed without additional alignments, making operation feasible in a closed box in a clinical setting by non-technical experts. Since calibration can be performed after each acquisition, BD is robust against any hardware misalignments over time. As scanning speeds continuously increase, less temporal averaging will increase RIN, perhaps even in a low RIN ANDi supercontinuum source. BD maintains at least equivalent performances despite significantly increased RIN, which we validated (Fig. 7.4) by minimizing camera amplification. Our RIN-rejection methods enable supercontinuum light sources to be suitable for much broader OCT applications beyond visible-light spectral range.

7.7 CONCLUSION

We developed BD-vis-OCT based on an MZI. Using BD, we demonstrated high-quality human retinal imaging at an A-line rate of 125 kHz, the fastest with vis-OCT so far. In a phantom eyeball, we demonstrated at high RIN levels that

PSNFR increases by up to 25.3 dB and PSNR up to 25.6 dB. We demonstrated such increases *in vivo* by up to 15.3 dB and 15.2 dB, respectively. For both the phantom and *in vivo* images, CNRs were mostly negative or noise floor limited in SD, but increased up to 3-4 dB after BD. Most of these increases came from the reduction of RIN. Qualitatively, BD revealed more structural features *in vivo* than SD. We anticipate that BD will enable broad and immediate clinical applications of vis-OCT and other OCTs using supercontinuum sources.

7.8 SUPPLEMENTARY MATERIALS

7.8.1 *In vivo* axial resolution measurement for single and balanced detections

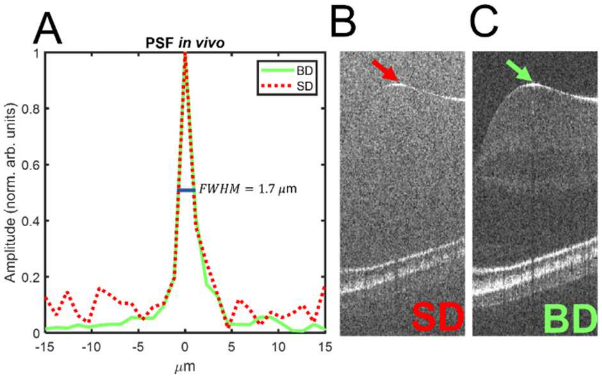

Figure 7.8. Resolution measurement for BD and SD; (A) Point spread functions (PSF) from specular reflection at ILM. The solid green line represents PSF from BD, and the red dashed line represents PSF from SD. Both PSFs overlap and have a measured full-width and half maximum (FWHM) of 1.7 μm. (B) (B) Location of PSF for SD (highlighted by red arrow); (C) Location of PSF for BD (highlighted by green arrow)

7.8.2 Additional examples of human retinal imaging

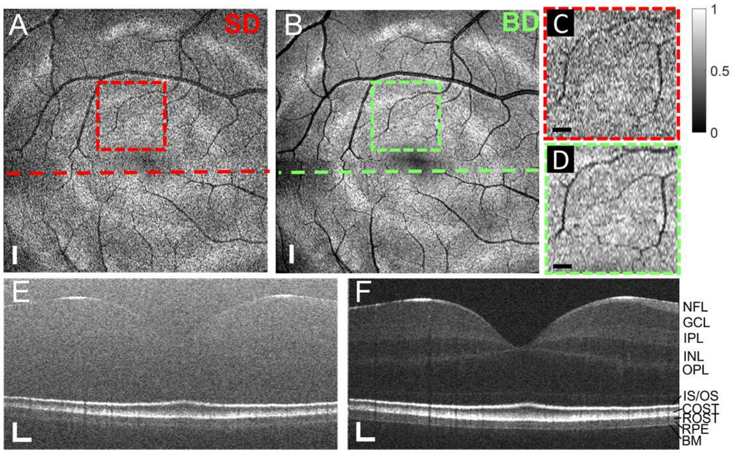

Figure 7.9. (A-F) Small field-of-view vis-OCT images of the retina of a healthy 24-year-old male (Eye 2); (A) *En face* projection near fovea for single detection; (B) *En face* projection near fovea for balanced detection; (C) Magnification from red dashed box in (A); (D) Magnification from green dashed box in (B); (E) B-scan from the location of the dashed line in (A); (F) B-scan from the location of the dashed line in (B); Red and green A-lines overlay their respective locations Scale bars in (A & B) are 275 μm (isometric); scale bars in (C & D) are 150 μm (isometric); scale bars in (E & F) are 60 μm (vertical) × 225 μm (horizontal). NFL: nerve fiber layer; GCL: ganglion cell layer; IPL: inner plexiform layer; INL: inner nuclear layer; OPL: outer plexiform layer; ELM: external limiting membrane; IS/OS: inner segment/outer segment; COST: cone outer segment tips; ROST: rod outer segment tips; RPE: retinal pigment epithelium; BM: Bruch's membrane

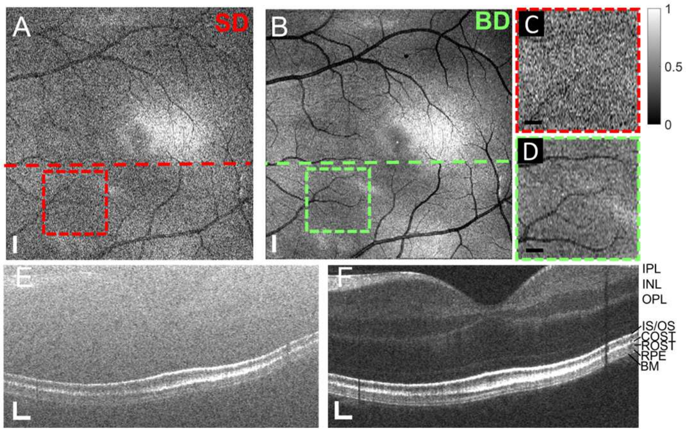

Figure 7.10. (A-F) Small field-of-view vis-OCT images of the retina of a healthy 27-year-old female (Eye 3); Figure layout and scale bars are same as in Fig. 7.9.

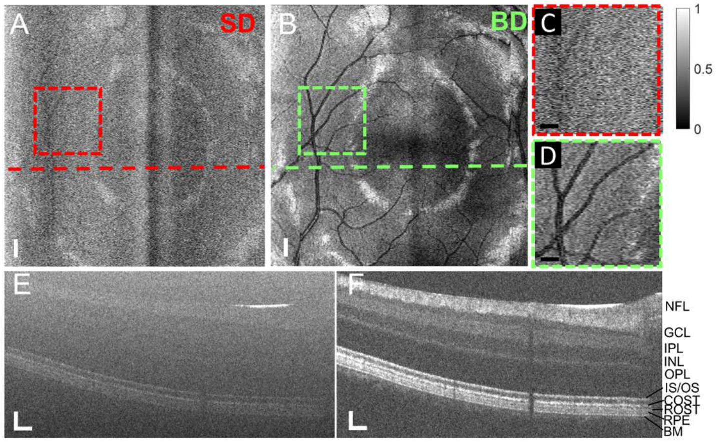

Figure 7.11. (A-F) Small field-of-view vis-OCT images of the retina of a healthy 25-year-old male (Eye 5); Figure layout and scale bars are same as in Fig. 7.9.

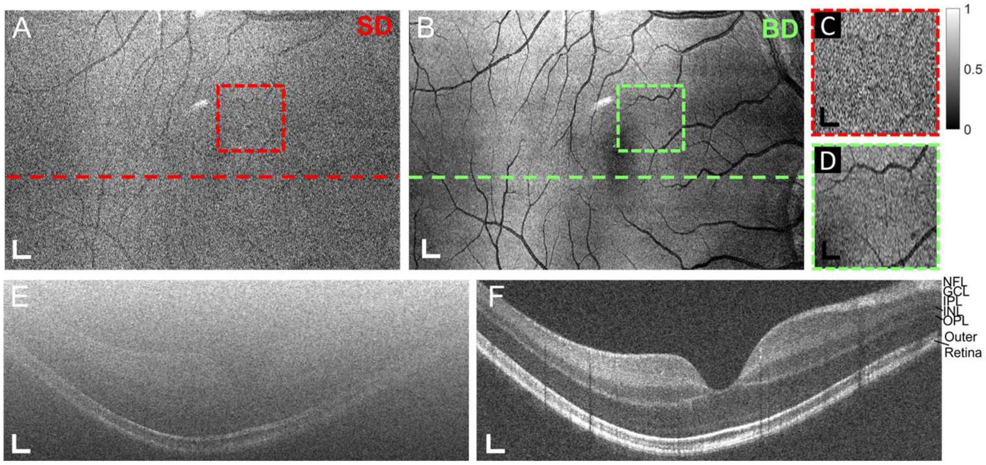

Figure 7.12. (A-F) Medium field-of-view vis-OCT images of the retina of a healthy 25-year-old male (Eye 4); (A) *En face* projection near fovea for single detection; (B) *En face* projection near fovea for balanced detection; (C) Magnification from red dashed box in (A); (D) Magnification from green dashed box in (B); (E) B-scan from the location of the dashed line in (A); (F) B-scan from the location of the dashed line in (B); Scale bars in (A & B) are 365 μm (horizontal) × 275 μm (vertical); scale bars in (C & D) are 200 μm ×150 μm; scale bars in (E&F) are 50 μm × 275 μm. B-scans magnified to show detail. NFL: nerve fiber layer; GCL: ganglion cell layer; IPL: inner plexiform layer; INL: inner nuclear layer; OPL: outer plexiform layer

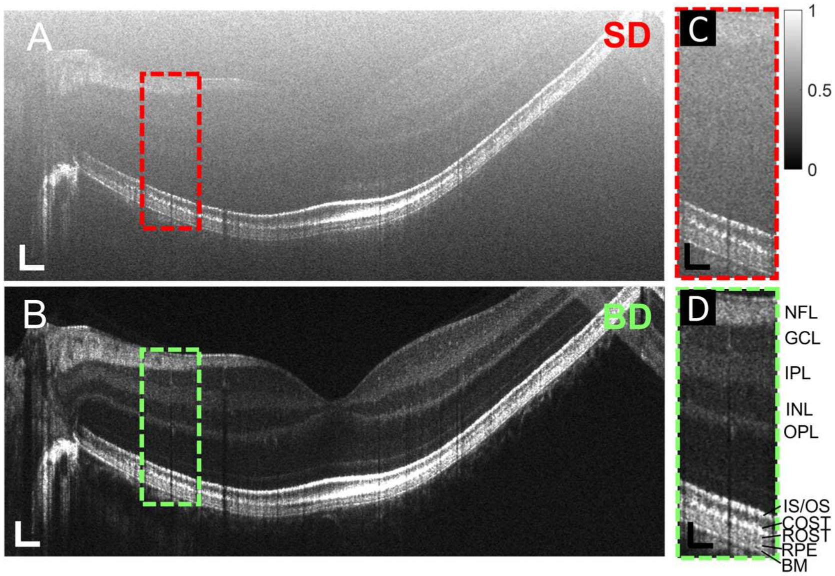

Figure 7.13. (A-D) High-definition speckle reduction (HDSR) vis-OCT image of the retina of a healthy 27-year-old female (Eye 3). (A) B-scan for SD; (B) B-scan for BD; (C) Magnification from red dashed box in (A); (D) Magnification from green dashed box in (B); Scale bars in (A & B) are 60 μm (vertical)× 235 μm (horizontal); scale bars in (C & D) are 70 µm × 150 µm

7.8.3 Spectrometer noises before and after calibration fitting

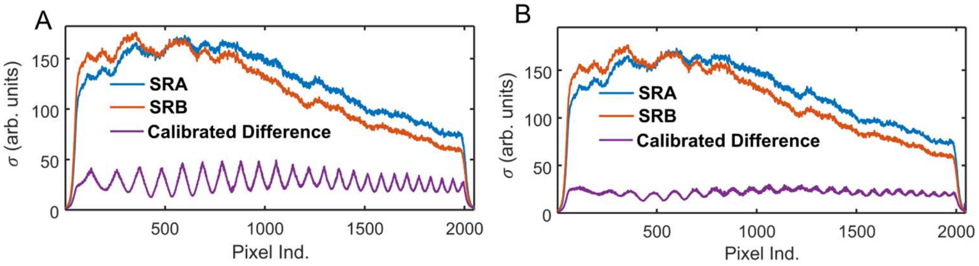

Figure 7.14. Balanced detection noise reduction (A) before and (B) after fitting the calibration with a third-order polynomial and subpixel mapping.

7.8.4 System characterization

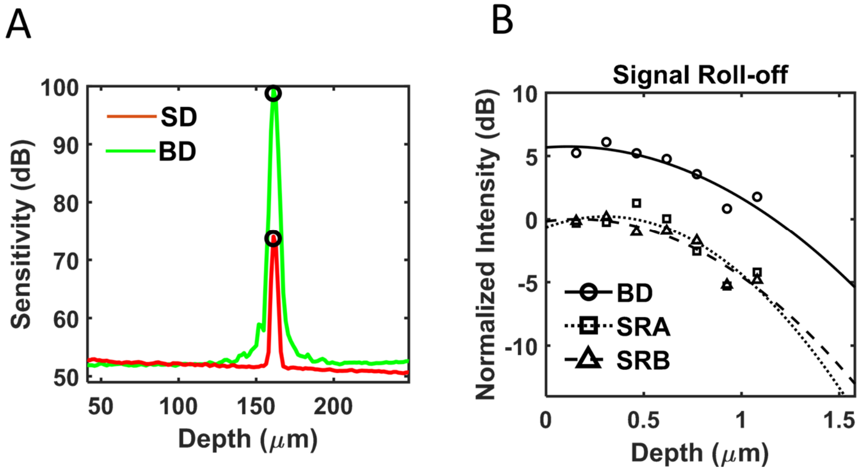

Figure 7.15. (A) Maximum sensitivity measurement for balanced detection (BD) and single detection (SD); (B) Roll-off measurement for balanced detection (BD), spectrometer A (SRA), and spectrometer B (SRB)

Chapter 8

Summary, perspectives, and future applications

8.1 SUMMARY AND PERSPECTIVES

Yi et. al first demonstrated vis-OCT retinal oximetry in 2013. Prior to this work, the field of vis-OCT was relatively unexplored and underdeveloped. Since then, a handful of talented groups around the world found new and creative ways to apply this technology towards the prevention of vision loss. By leveraging key advantages of visible-light, researchers noninvasively revealed micrometer-scale neuronal structures and seemingly invisible metabolic functions in living eye. Nevertheless, gaps in vis-OCT signal modeling and hardware performance fundamentally limited applications in humans. This dissertation develops the technical advances necessary to translate vis-OCT to the clinic.

In Chapter 1, we introduced the history and scientific principles behind OCT. We investigated each step of the signal formation process, and how they enabled 3D, high-resolution, non-invasive imaging. Then, we introduced vis-OCT and its benefits and limitations. We described the steps necessary to translate vis-OCT to the clinic, which were implemented in Chapters 2-7.

In Chapter 2, we designed and implemented a new scanning pattern that redistributed A-line acquisitions orthogonal to the B-scan axis. This enabled averaging of decorrelated speckle noises without blurring from motions, overcoming vis-OCT's speed limitations. We demonstrated human retinal imaging with unprecedented detail, including visualization of Bruch's membrane. Since publication of these results, similar methods were used in vis-OCT to visualize fine retinal details like IPL [16, 26] and ganglion cell bodies [14].

In Chapter 3, we investigated spectrally dependent roll-off (SDR), which describes spectrally dependent attenuations of the vis-OCT signal caused by spectrometer detection. This phenomenon multiplies an image with a spectrum not associated with the optical properties of the sample. By dividing the image by the SDR transfer function, we offset its influence. This work not only improved accuracy of spectroscopic vis-OCT, but also emphasized the need to define how optical detection influences signal measurement.

Chapter 4 is a closely related follow-up to Chapter 3. Here, we investigated how non-uniform spectrometer detection and the numerical resampling causes a systemic, spectrally dependent background noise (SDBG). This work highlighted the spectroscopic influence of common, often overlooked step in vis-OCT image reconstruction. Like the SDR, the SDBG is the result of a non-sample-based ‘signal’. Both the SDR and SDBG are part of a larger class of signals and noises that must be corrected before performing quantitative vis-OCT spectroscopy like sO_2.

Taking inspiration from Chapters 3 & 4, Chapter 5 recognized that vis-OCT measures an altered version of the true optical properties of tissues. In this case, we investigated how vis-OCT hardware detection influenced measurement of the scattering coefficient of blood. Owing to blood’s high optical scattering coefficient and high probability of forward scattering, we hypothesized that vis-OCT was sensitive to multiple forward scattered photons in blood. Detection of uniaxial multiple scattering could allow for sensitivity to photons travelling deeper than previously predicted. Using Monte Carlo simulation, we found that vis-OCT signal in blood was almost exclusively derived from multiple forward scattered photons. This led to a reduction of the predicted scattering coefficient of blood by the scattering scaling factor (SSF). The simulated SSF was ~ 5-fold smaller than predicted by the literature. We proceeded to measure the SSF *ex vivo* and *in vivo* and found nearly identical values to the simulation, validating our hypothesis. Further modeling indicated that the vis-OCT system’s optical illumination could influence the SSF, indicating the importance of a flexible sO_2 model. The results of this work contradicted previous vis-OCT retinal oximetry models used by us and others and emphasized the need for new, evidence-based approaches.

In Chapter 6, we identified and modeled a special class of signals and noises disrupting spectroscopic vis-OCT measurements called spectral contaminants (SCs). SCs come from the OCT system, like those described in Chapters 3 & 4, and from the sample itself. We applied knowledge of SCs and the SSF from Chapter 5 to develop a new model for sO_2 measurement. Then, we recognized SCs could change with each unique image, requiring an adaptive measurement approach. This led to the development of adaptive spectroscopic vis-OCT (Ads-vis-OCT), which found the optimal sO_2 measurement parameters for each vessel. First, we tested Ads-vis-OCT in phantom blood vessels and found excellent agreement with the ground truth. Then we used Ads-vis-OCT to measure sO_2 in 18 healthy human retinas in vessels as small as small as 37 μm and as large as 168 μm. We found $\leq$ 2.5% sO_2 repeatability in all vessels and noise-limited sO_2 accuracy with respect to a pulse oximeter in major arteries. We found a statistically significant decrease in sO_2 with decreasing arterial vessel diameter, suggesting sensitivity to diffusion or metabolic effects. Finally, we compared Ads-vis-OCT to alternative approaches and found significant accuracy and repeatability improvements. Unlike these alternative approaches, which made many assumptions and simplifications, Ads-vis-OCT was driven by known scientific principles and empirical evidence. This chapter depicted the largest and most comprehensive test of vis-OCT retinal oximetry in humans or animal models.

Chapter 7 addressed perhaps vis-OCT's greatest obstacle towards clinical translation: RIN. As detailed in Chapter 1, RIN is intrinsic to vis-OCT and prevents high-speed and high-SNR performance simultaneously. This limitation is detrimental to many of the new applications provided by vis-OCT here and in other studies. To overcome this limitation, we employed a dual-spectrometer detection scheme called balanced-detection (BD), which simultaneously sensed and removed RIN without degrading signal. Although researchers previously attempted BD with two spectrometers, they never demonstrated significant noise reduction. We approached this problem differently by focusing on spectrometer cross-calibration. Contrary to previous works, this work performed a relative calibration between the two spectrometers, removing any error propagation between two discrete calibrations. Furthermore, it used the RIN itself to map light distribution on the spectrometers. This heuristic approach calibrated the spectrometers with the very noise we wished to cancel. Next, we addressed errors in RIN removal by investigating and applying subpixel calibration. This analysis found that most of the noise removal occurred at calibration accuracies less than 1 pixel. Taking all these improvements together, we demonstrated up to 25.6 dB SNR improvement and performed the fastest ever vis-OCT human retinal imaging at 125 kHz A-line rate. This reduced typical acquisition time from 5-seconds to 1-second, a transformative difference for imaging human subjects. Finally, and most importantly, it revealed key anatomical features previously obscured by noise.

Each chapter in this thesis not only helped advance vis-OCT technology, but also taught critical lessons informing future chapters. In Chapter 1, we applied a new vis-OCT scan pattern to overcome speed limitations. Investigations of how motions negatively impacted image quality in humans inspired high-speed BD in Chapter 7. In Chapters 3 & 4, we investigated spectrometer-based contaminations of spectroscopic vis-OCT. These works inspired the larger concept of spectral contaminants, whose understanding was critical for accurate and repeatable retinal oximetry in Chapter 6. The theory and simulation for nonuniform spectrometer sampling in Chapters 3 & 4 also informed BD in Chapter 7, where correction of nonuniform sampling was critical for RIN removal. Chapter 5 recognized from Chapters 3 & 4 that vis-OCT spectroscopic measurement of blood was not representative of its literature definition. Rather than make simplified assumptions, as done in the past, we used knowledge of spectral contaminants, physical principles, and Monte Carlo simulation to redefine how vis-OCT measured blood. This new definition informed the Ads-vis-OCT model in Chapter 6 and validated its accuracy. Taken together, Chapters 2-5 built new concepts and techniques that were realized in Chapter 6 & 7, which directly improved sO_2 reliability and imaging speed and quality, respectively.

8.2 FUTURE APPLICATIONS

All medical imaging modalities, particularly ophthalmic OCT, should strive towards direct, human impact. Prior to the works outlined in this dissertation, vis-OCT's applications were limited to small animal models or few, healthy human volunteers. By addressing three key limitations: imaging speed, image quality, and sO_2 reliability, we can now expand these applications to the clinic across larger healthy and diseased populations. Specifically, improved imaging speed and quality will enable translation proof-of-concept studies like full, 3D visualization of Schlemm's canal [12] or discrete nerve fiber analysis [13] in humans for the first time. Speckle reduction developed in Chapter 2 can expand visualization of IPL or Bruch's membrane across larger fields of view and increase subject participation in studies like those by Ghassabi et. al [26] or Zhang et. al [16]. Increased speeds can also enable reliable angiography, expanding retinal oximetry from few vessels-per-subject towards depth resolved maps from the optic disk to the fovea. Such oximetry maps will finally achieve the long-term goal of geometrically mapping oxygen metabolism to retinal disease. Technologically speaking, researchers should continually push the boundaries of speed and image quality, which will ultimately enhance vision care. As one example, we demonstrated vis-OCT human retinal imaging at 125 kHz, which was limited not limited by image quality, but the camera's data transfer rate. State-of-the-art linear array cameras can now acquire data as fast as 600 kHz [183]. Integrating BD with higher speed cameras will improve the above-mentioned applications and likely to enable new ones, such as dynamic contrast [183], which converts cellular movements to contrasts invisible in typical images.

Today, vis-OCT can match or exceed most imaging capabilities offered by clinical NIR OCTs. Full clinical adoption will require significant attention towards commercialization and usability. Researchers, engineers, companies, and clinicians must aim their sights towards agile, user-friendly software and hardware designs. Indeed, the future of vis-OCT is bright.

References

1. D. Huang, E. A. Swanson, C. P. Lin, J. S. Schuman, W. G. Stinson, W. Chang, M. R. Hee, T. Flotte, K. Gregory, C. A. Puliafito, and J. G. Fujimoto, "Optical Coherence Tomography," Science **254**, 1178-1181 (1991).
2. J. F. de Boer, R. Leitgeb, and M. Wojtkowski, "Twenty-five years of optical coherence tomography: the paradigm shift in sensitivity and speed provided by Fourier domain OCT [Invited]," Biomed Opt Express **8**, 3248-3280 (2017).
3. A. Ng and J. Swanevelder, "Resolution in ultrasound imaging," Bja Educ **11**, 186-192 (2011).
4. J. M. Schmitt, "Optical coherence tomography (OCT): a review," IEEE Journal of selected topics in quantum electronics **5**, 1205-1215 (1999).
5. M. Wojtkowski, "High-speed optical coherence tomography: basics and applications," Appl Optics **49**, D30-D61 (2010).
6. A. V. Oppenheim and R. W. Schafer, *Discrete-time signal processing,* 3rd ed. (Pearson, Upper Saddle River, 2010), pp. xxviii, 1108 p.
7. J. W. Goodman, *Statistical optics*, Wiley series in pure and applied optics (Wiley, New York, 1985), pp. xvii, 550 p.
8. A. L. Oldenburg, C. Y. Xu, and S. A. Boppart, "Spectroscopic optical coherence tomography and microscopy," Ieee J Sel Top Quant **13**, 1629-1640 (2007).
9. X. Shu, L. Beckmann, and H. F. Zhang, "Visible-light optical coherence tomography: a review," J Biomed Opt **22**(2017).
10. S. L. Jacques, "Optical properties of biological tissues: a review (vol 58, pg R37, 2013)," Phys Med Biol **58**, 5007-5008 (2013).
11. J. Yi, Q. Wei, W. Liu, V. Backman, and H. F. Zhang, "Visible-light optical coherence tomography for retinal oximetry," Optics letters **38**, 1796-1798 (2013).
12. X. Zhang, L. Beckmann, D. A. Miller, G. Shao, Z. Cai, C. Sun, N. Sheibani, X. Liu, J. Schuman, and M. Johnson, "In vivo imaging of Schlemm's canal and limbal vascular network in mouse using visible-light OCT," Investigative ophthalmology & visual science **61**, 23-23 (2020).
13. M. Grannonico, D. A. Miller, M. N. Liu, P. Norat, C. D. Deppmann, P. A. Netland, H. F. Zhang, and X. R. Liu, "Global and Regional Damages in Retinal Ganglion Cell Axon Bundles Monitored Non-Invasively by Visible-Light Optical Coherence Tomography Fibergraphy," J Neurosci **41**, 10179-10193 (2021).
14. S. H. Pi, T. T. Hormel, X. Wei, W. Cepurna, J. C. Morrison, and Y. L. Jia, "Imaging retinal structures at cellular-level resolution by visible-light optical coherence tomography," Opt Lett **45**, 2107-2110 (2020).
15. Z. Ghassabi, R. V. Kuranov, J. S. Schuman, R. Zambrano, M. Wu, M. Liu, B. Tayebi, Y. Wang, I. Rubinoff, X. Liu, G. Wollstein, H. F. Zhang, and H. Ishikawa, "In Vivo Sublayer Analysis of Human Retinal Inner Plexiform Layer Obtained by Visible-Light Optical Coherence Tomography," Invest Ophthalmol Vis Sci **63**, 18 (2022).

16. T. Zhang, A. M. Kho, and V. J. Srinivasan, "In vivo Morphometry of Inner Plexiform Layer (IPL) Stratification in the Human Retina With Visible Light Optical Coherence Tomography," Frontiers in Cellular Neuroscience **15**(2021).
17. W. Y. Song, S. P. Fu, S. S. Song, S. Zhang, L. Zhang, S. Ness, M. Desai, and J. Yi, "Longitudinal detection of retinal alterations by visible and near-infrared optical coherence tomography in a dexamethasone-induced ocular hypertension mouse model," Neurophotonics **6**(2019).
18. J. Yi, Q. Wei, W. Z. Liu, V. Backman, and H. F. Zhang, "Visible-light optical coherence tomography for retinal oximetry," Opt Lett **38**, 1796-1798 (2013).
19. S. H. Pi, T. T. Hormel, X. Wei, W. Cepurna, B. J. Wang, J. C. Morrison, and Y. L. Jia, "Retinal capillary oximetry with visible light optical coherence tomography," P Natl Acad Sci USA **117**, 11658-11666 (2020).
20. I. Rubinoff, R. V. Kuranov, Z. Ghassabi, Y. Wang, L. Beckmann, D. A. Miller, B. Tayebi, G. Wollstein, H. Ishikawa, J. S. Schuman, and H. F. Zhang, "Adaptive spectroscopic visible-light optical coherence tomography for human retinal oximetry," bioRxiv (2021).
21. F. E. Robles, C. Wilson, G. Grant, and A. Wax, "Molecular imaging true-colour spectroscopic optical coherence tomography," Nat Photonics **5**, 744-747 (2011).
22. E. Yuan, P. Si, Y. Winetraub, S. Shevidi, and A. de la Zerda, "A Spectral Demixing Model for Triplex In Vivo Imaging of Optical Coherence Tomography Contrast Agents," Acs Photonics **7**, 893-900 (2020).
23. M. Jensen, I. B. Gonzalo, R. D. Engelsholm, M. Maria, N. M. Israelsen, A. Podoleanu, and O. Bang, "Noise of supercontinuum sources in spectral domain optical coherence tomography," J Opt Soc Am B **36**, A154-A160 (2019).
24. I. Rubinoff, L. Beckmann, Y. B. Wang, A. A. Fawzi, X. R. Liu, J. Tauber, K. Jones, H. Ishikawa, J. S. Schuman, R. Kuranov, and H. F. Zhang, "Speckle reduction in visible-light optical coherence tomography using scan modulation," Neurophotonics **6**(2019).
25. S. P. Chong, M. Bernucci, H. Radhakrishnan, and V. J. Srinivasan, "Structural and functional human retinal imaging with a fiber-based visible light OCT ophthalmoscope," Biomed Opt Express **8**, 323-337 (2017).
26. Z. Ghassabi, R. V. Kuranov, M. Wu, B. Tayebi, Y. Wang, I. Rubinoff, X. Liu, G. Wollstein, J. S. Schuman, H. F. Zhang, and H. Ishikawa, "In Vivo Sublayer Analysis Of Human Retinal Inner Plexiform Layer Obtained By Visible-Light Optical Coherence Tomography," bioRxiv (2021).
27. I. Rubinoff, B. Soetikno, D. A. Miller, I. Rischall, A. Fawzi, R. Kuranov, and H. F. Zhang, "Spectrally dependent roll-off in visible-light optical coherence tomography," Optics letters **45**, 2680-2683 (2020).
28. I. Rubinoff, R. V. Kuranov, and H. F. Zhang, "Intrinsic spectrally-dependent background in spectroscopic visible-light optical coherence tomography," Biomed Opt Express **12**, 110-124 (2021).
29. R. Fang, I. Rubinoff, and H. F. Zhang, "Multiple forward scattering reduces the measured scattering coefficient of blood in visible-light optical coherence tomography," bioRxiv, 2022.2003.2020.485063 (2022).

30. D. J. Faber, M. C. G. Aalders, E. G. Mik, B. A. Hooper, M. J. C. van Gemert, and T. G. van Leeuwen, "Oxygen saturation-dependent absorption and scattering of blood," Phys Rev Lett **93**(2004).
31. I. Rubinoff, D. A. Miller, R. Kuranov, Y. Wang, R. Fang, N. J. Volpe, and H. F. Zhang, "High-speed balanced-detection visible-light optical coherence tomography in the human retina using subpixel spectrometer calibration," IEEE Trans Med Imaging **PP**(2022).
32. M. R. Hee, J. A. Izatt, E. A. Swanson, D. Huang, J. S. Schuman, C. P. Lin, C. A. Puliafito, and J. G. Fujimoto, "Optical Coherence Tomography of the Human Retina," Arch Ophthalmol-Chic **113**, 325-332 (1995).
33. J. M. Schmitt, S. H. Xiang, and K. M. Yung, "Speckle in optical coherence tomography," J Biomed Opt **4**, 95-105 (1999).
34. M. R. Hee, C. R. Baumal, C. A. Puliafito, J. S. Duker, E. Reichel, J. R. Wilkins, J. G. Coker, J. S. Schuman, E. A. Swanson, and J. G. Fujimoto, "Optical coherence tomography of age-related macular degeneration and choroidal neovascularization," Ophthalmology **103**, 1260-1270 (1996).
35. M. R. Hee, C. A. Puliafito, C. Wong, E. Reichel, J. S. Duker, J. S. Schuman, E. A. Swanson, and J. G. Fujimoto, "Optical Coherence Tomography of Central Serous Chorioretinopathy," Am J Ophthalmol **120**, 65-74 (1995).
36. A. Ozcan, A. Bilenca, A. E. Desjardins, B. E. Bouma, and G. J. Tearney, "Speckle reduction in optical coherence tomography images using digital filtering," J Opt Soc Am A **24**, 1901-1910 (2007).
37. M. Bashkansky and J. Reintjes, "Statistics and reduction of speckle in optical coherence tomography," Opt Lett **25**, 545-547 (2000).
38. A. Sakamoto, M. Hangai, and N. Yoshimura, "Spectral-domain optical coherence tomography with multiple B-scan averaging for enhanced imaging of retinal diseases," Ophthalmology **115**, 1071-1078 (2008).
39. M. Szkulmowski, I. Gorczynska, D. Szlag, M. Sylwestrzak, A. Kowalczyk, and M. Wojtkowski, "Efficient reduction of speckle noise in Optical Coherence Tomography," Opt Express **20**, 1337-1359 (2012).
40. A. E. Desjardins, B. J. Vakoc, G. J. Tearney, and B. E. Bouma, "Speckle reduction in OCT using massively-parallel detection and frequency-domain ranging," Opt Express **14**, 4736-4745 (2006).
41. M. Pircher, E. Gotzinger, R. Leitgeb, A. F. Fercher, and C. K. Hitzenberger, "Speckle reduction in optical coherence tomography by frequency compounding," J Biomed Opt **8**, 565-569 (2003).
42. Y. Zhao, K. K. Chu, W. J. Eldridge, E. T. Jelly, M. Crose, and A. Wax, "Real-time speckle reduction in optical coherence tomography using the dual window method," Biomed Opt Express **9**, 616-622 (2018).
43. O. Liba, M. D. Lew, E. D. SoRelle, R. Dutta, D. Sen, D. M. Moshfeghi, S. Chu, and A. de la Zerda, "Speckle-modulating optical coherence tomography in living mice and humans," Nat Commun **8**(2017).
44. C. Cuartas-Velez, R. Restrepo, B. E. Bouma, and N. Uribe-Patarroyo, "Volumetric non-local-means based speckle reduction for optical coherence tomography," Biomed Opt Express **9**, 3354-3372 (2018).

45. J. Yi, S. Y. Chen, X. Shu, A. A. Fawzi, and H. F. Zhang, "Human retinal imaging using visible-light optical coherence tomography guided by scanning laser ophthalmoscopy," Biomed Opt Express **6**, 3701-3713 (2015).
46. S. P. Chong, T. W. Zhang, A. Kho, M. T. Bernucci, A. Dubra, and V. J. Srinivasan, "Ultrahigh resolution retinal imaging by visible light OCT with longitudinal achromatization," Biomed Opt Express **9**, 1477-1491 (2018).
47. S. Martinez-Conde, S. L. Macknik, and D. H. Hubel, "The role of fixational eye movements in visual perception," Nat Rev Neurosci **5**, 229-240 (2004).
48. D. C. Adler, T. H. Ko, and J. G. Fujimoto, "Speckle reduction in optical coherence tomography images by use of a spatially adaptive wavelet filter," Opt Lett **29**, 2878-2880 (2004).
49. B. T. Soetikno, L. Beckmann, X. Zhang, A. A. Fawzi, and H. F. Zhang, "Visible-light optical coherence tomography oximetry based on circumpapillary scan and graph-search segmentation," Biomed Opt Express **9**(2018).
50. J. C. Booij, D. C. Baas, J. Beisekeeva, T. G. M. F. Gorgels, and A. A. B. Bergen, "The dynamic nature of Bruch's membrane," Prog Retin Eye Res **29**, 1-18 (2010).
51. C. A. Curcio, M. Johnson, M. Rudolf, and J. D. Huang, "The oil spill in ageing Bruch membrane," Brit J Ophthalmol **95**, 1638-1645 (2011).
52. M. Guizar-Sicairos, S. T. Thurman, and J. R. Fienup, "Efficient subpixel image registration algorithms," Opt Lett **33**, 156-158 (2008).
53. S. H. Yun, G. J. Tearney, J. F. de Boer, and B. E. Bouma, "Motion artifacts in optical coherence tomography with frequency-domain ranging," Opt Express **12**, 2977-2998 (2004).
54. C. E. Riva, J. E. Grunwald, S. H. Sinclair, and B. L. Petrig, "Blood Velocity and Volumetric Flow-Rate in Human Retinal-Vessels," Invest Ophth Vis Sci **26**, 1124-1132 (1985).
55. J. A. Izatt and M. A. Choma, "Theory of Optical Coherence Tomography," Optical Coherence Tomography: Technology and Applications, 47-72 (2008).
56. R. R. Liu, J. A. Winkelmann, G. Spicer, Y. X. Zhu, A. Eid, G. A. Ameer, V. Backman, and J. Yi, "Single capillary oximetry and tissue ultrastructural sensing by dual-band dual-scan inverse spectroscopic optical coherence tomography," Light-Sci Appl **7**(2018).
57. L. Beckmann, X. Zhang, N. A. Nadkarni, Z. Cai, A. Batra, D. P. Sullivan, W. A. Muller, C. Sun, R. Kuranov, and H. F. Zhang, "Longitudinal deep-brain imaging in mouse using visible-light optical coherence tomography through chronic microprism cranial window," Biomedical Optics Express **10**, 5235-5250 (2019).
58. A. Lichtenegger, D. J. Harper, M. Augustin, P. Eugui, M. Muck, J. Gesperger, C. K. Hitzenberger, A. Woehrer, and B. Baumann, "Spectroscopic imaging with spectral domain visible light optical coherence microscopy in Alzheimer's disease brain samples," Biomed Opt Express **8**, 4007-4025 (2017).
59. Z. L. Hu, Y. S. Pan, and A. M. Rollins, "Analytical model of spectrometer-based two-beam spectral interferometry," Applied Optics **46**, 8499-8505 (2007).
60. C. Dorrer, N. Belabas, J. P. Likforman, and M. Joffre, "Spectral resolution and sampling issues in Fourier-transform spectral interferometry," J Opt Soc Am B **17**, 1795-1802 (2000).

61. B. Baumann, C. W. Merkle, R. A. Leitgeb, M. Augustin, A. Wartak, M. Pircher, and C. Hitzenberger, "Signal averaging improves signal-to-noise in OCT images: But which approach works best, and when?," Biomed Opt Express **10**, 5755-5775 (2019).
62. B. Baumann, M. Augustin, A. Lichtenegger, D. J. Harper, M. Muck, P. Eugui, A. Wartak, M. Pircher, and C. K. Hitzenberger, "Polarization-sensitive optical coherence tomography imaging of the anterior mouse eye," J Biomed Opt **23**(2018).
63. C. Veenstra, S. Kruitwagen, D. Groener, W. Petersen, W. Steenbergen, and N. Bosschaart, "Quantification of total haemoglobin concentrations in human whole blood by spectroscopic visible-light optical coherence tomography," Sci Rep-Uk **9**(2019).
64. M. Szkulmowski and M. Wojtkowski, "Averaging techniques for OCT imaging," Opt Express **21**, 9757-9773 (2013).
65. S. P. Chong, C. W. Merkle, C. Leahy, H. Radhakrishnan, and V. J. Srinivasan, "Quantitative microvascular hemoglobin mapping using visible light spectroscopic Optical Coherence Tomography," Biomed Opt Express **6**, 1429-1450 (2015).
66. N. Uribe-Patarroyo, S. H. Kassani, M. Villiger, and B. E. Bouma, "Robust wavenumber and dispersion calibration for Fourier-domain optical coherence tomography," Opt Express **26**, 9081-9094 (2018).
67. S. W. Lee, H. W. Jeong, B. M. Kim, Y. C. Ahn, W. Jung, and Z. P. Chen, "Optimization for Axial Resolution, Depth Range, and Sensitivity of Spectral Domain Optical Coherence Tomography at 1.3 mu m," J Korean Phys Soc **55**, 2354-2360 (2009).
68. P. Laguna, G. B. Moody, and R. G. Mark, "Power spectral density of unevenly sampled data by least-square analysis: Performance and application to heart rate signals," Ieee T Bio-Med Eng **45**, 698-715 (1998).
69. J. Yi, A. J. Radosevich, J. D. Rogers, S. C. P. Norris, I. R. Capoglu, A. Taflove, and V. Backman, "Can OCT be sensitive to nanoscale structural alterations in biological tissue?," Optics Express **21**, 9043-9059 (2013).
70. G. P. Lan and G. Q. Li, "Design of a k-space spectrometer for ultra-broad waveband spectral domain optical coherence tomography," Sci Rep-Uk **7**(2017).
71. J. G. Fujimoto, W. Drexler, J. S. Schuman, and C. K. Hitzenberger, "Optical Coherence Tomography (OCT) in ophthalmology: introduction," Optics express **17**, 3978-3979 (2009).
72. M. Almasian, N. Bosschaart, T. G. van Leeuwen, and D. J. Faber, "Validation of quantitative attenuation and backscattering coefficient measurements by optical coherence tomography in the concentration-dependent and multiple scattering regime," Journal of biomedical optics **20**, 121314 (2015).
73. P. Gong, M. Almasian, G. Van Soest, D. M. De Bruin, T. G. Van Leeuwen, D. D. Sampson, and D. J. Faber, "Parametric imaging of attenuation by optical coherence tomography: review of models, methods, and clinical translation," Journal of biomedical optics **25**, 040901 (2020).
74. S. Liu, Y. Sotomi, J. Eggermont, G. Nakazawa, S. Torii, T. Ijichi, Y. Onuma, P. W. Serruys, B. P. Lelieveldt, and J. Dijkstra, "Tissue characterization with depth-

resolved attenuation coefficient and backscatter term in intravascular optical coherence tomography images," Journal of biomedical optics **22**, 096004 (2017).

75. D. J. Smithies, T. Lindmo, Z. Chen, J. S. Nelson, and T. E. Milner, "Signal attenuation and localization in optical coherence tomography studied by Monte Carlo simulation," Physics in Medicine & Biology **43**, 3025 (1998).
76. N. Bosschaart, G. J. Edelman, M. C. Aalders, T. G. van Leeuwen, and D. J. Faber, "A literature review and novel theoretical approach on the optical properties of whole blood," Lasers in medical science **29**, 453-479 (2014).
77. M. Friebel, J. Helfmann, U. J. Netz, and M. C. Meinke, "Influence of oxygen saturation on the optical scattering properties of human red blood cells in the spectral range 250 to 2000 nm," Journal of biomedical optics **14**, 034001 (2009).
78. A. Roggan, M. Friebel, K. Dörschel, A. Hahn, and G. J. Mueller, "Optical properties of circulating human blood in the wavelength range 400-2500 nm," Journal of biomedical optics **4**, 36-46 (1999).
79. C. W. Lu, C. K. Lee, M. T. Tsai, Y. M. Wang, and C. C. Yang, "Measurement of the hemoglobin oxygen saturation level with spectroscopic spectral-domain optical coherence tomography," Opt Lett **33**, 416-418 (2008).
80. R. A. Linsenmeier and H. F. Zhang, "Retinal oxygen: from animals to humans," Prog Retin Eye Res **58**, 115-151 (2017).
81. W. Z. Liu, S. J. Wang, B. Soetikno, J. Yi, K. V. Zhang, S. Y. Chen, R. A. Linsenmeier, C. M. Sorenson, N. Sheibani, and H. F. Zhang, "Increased Retinal Oxygen Metabolism Precedes Microvascular Alterations in Type 1 Diabetic Mice," Invest Ophth Vis Sci **58**(2017).
82. S. Y. Chen, J. Yi, W. Z. Liu, V. Backman, and H. F. Zhang, "Monte Carlo Investigation of Optical Coherence Tomography Retinal Oximetry," Ieee T Bio-Med Eng **62**, 2308-2315 (2015).
83. S. Chen, J. Yi, and H. F. Zhang, "Measuring oxygen saturation in retinal and choroidal circulations in rats using visible light optical coherence tomography angiography," Biomedical optics express **6**, 2840-2853 (2015).
84. J. Yi, W. Liu, S. Chen, V. Backman, N. Sheibani, C. M. Sorenson, A. A. Fawzi, R. A. Linsenmeier, and H. F. Zhang, "Visible light optical coherence tomography measures retinal oxygen metabolic response to systemic oxygenation," Light: Science & Applications **4**, e334-e334 (2015).
85. S. Pi, A. Camino, X. Wei, J. Simonett, W. Cepurna, D. Huang, J. C. Morrison, and Y. Jia, "Rodent retinal circulation organization and oxygen metabolism revealed by visible-light optical coherence tomography," Biomedical optics express **9**, 5851-5862 (2018).
86. S. Pi, A. Camino, W. Cepurna, X. Wei, M. Zhang, D. Huang, J. Morrison, and Y. Jia, "Automated spectroscopic retinal oximetry with visible-light optical coherence tomography," Biomedical optics express **9**, 2056-2067 (2018).
87. S. Chen, X. Shu, P. L. Nesper, W. Liu, A. A. Fawzi, and H. F. Zhang, "Retinal oximetry in humans using visible-light optical coherence tomography," Biomedical optics express **8**, 1415-1429 (2017).

88. S. Pi, T. T. Hormel, X. Wei, W. Cepurna, B. Wang, J. C. Morrison, and Y. Jia, "Retinal capillary oximetry with visible light optical coherence tomography," Proceedings of the National Academy of Sciences **117**, 11658-11666 (2020).
89. S. Chen, J. Yi, W. Liu, V. Backman, and H. F. Zhang, "Monte Carlo investigation of optical coherence tomography retinal oximetry," IEEE transactions on biomedical engineering **62**, 2308-2315 (2015).
90. D. J. Faber, E. G. Mik, M. C. Aalders, and T. G. van Leeuwen, "Toward assessment of blood oxygen saturation by spectroscopic optical coherence tomography," Optics letters **30**, 1015-1017 (2005).
91. M. Meinke, G. Müller, J. Helfmann, and M. Friebel, "Empirical model functions to calculate hematocrit-dependent optical properties of human blood," Applied optics **46**, 1742-1753 (2007).
92. W. G. Zijlstra, A. Buursma, and O. W. van Assendelft, *Visible and near infrared absorption spectra of human and animal haemoglobin: determination and application* (VSP, 2000).
93. W. Song, W. Shao, W. Yi, R. Liu, M. Desai, S. Ness, and J. Yi, "Visible light optical coherence tomography angiography (vis-OCTA) facilitates local microvascular oximetry in the human retina," Biomedical Optics Express **11**, 4037-4051 (2020).
94. C. Veenstra, S. Kruitwagen, D. Groener, W. Petersen, W. Steenbergen, and N. Bosschaart, "Quantification of total haemoglobin concentrations in human whole blood by spectroscopic visible-light optical coherence tomography," Scientific reports **9**, 1-8 (2019).
95. S. P. Chong, C. W. Merkle, H. Radhakrishnan, C. Leahy, A. Dubra, Y. N. Sulai, and V. J. Srinivasan, "Optical coherence imaging of microvascular oxygenation and hemodynamics," in *CLEO: Applications and Technology*, (Optical Society of America, 2014), ATh1O. 2.
96. R. Liu, W. Song, V. Backman, and J. Yi, "Quantitative quality-control metrics for in vivo oximetry in small vessels by visible light optical coherence tomography angiography," Biomedical optics express **10**, 465-486 (2019).
97. G. Yao and L. V. Wang, "Monte Carlo simulation of an optical coherence tomography signal in homogeneous turbid media," Physics in Medicine & Biology **44**, 2307 (1999).
98. L. Wang, S. L. Jacques, and L. Zheng, "MCML—Monte Carlo modeling of light transport in multi-layered tissues," Computer methods and programs in biomedicine **47**, 131-146 (1995).
99. B. G. Yust, L. C. Mimun, and D. K. Sardar, "Optical absorption and scattering of bovine cornea, lens, and retina in the near-infrared region," Lasers in medical science **27**, 413-422 (2012).
100. S. Aumann, S. Donner, J. Fischer, and F. Müller, "Optical coherence tomography (OCT): principle and technical realization," High Resolution Imaging in Microscopy and Ophthalmology, 59-85 (2019).
101. S. Farsiu, J. Christofferson, B. Eriksson, P. Milanfar, B. Friedlander, A. Shakouri, and R. Nowak, "Statistical detection and imaging of objects hidden in turbid media using ballistic photons," Applied optics **46**, 5805-5822 (2007).

102. F. L. Pedrotti, L. M. Pedrotti, and L. S. Pedrotti, *Introduction to optics* (Cambridge University Press, 2017).
103. D. F. Swinehart, "The beer-lambert law," Journal of chemical education **39**, 333 (1962).
104. L. Durak and O. Arikan, "Short-time Fourier transform: two fundamental properties and an optimal implementation," IEEE Transactions on Signal Processing **51**, 1231-1242 (2003).
105. M. Friebel, A. Roggan, G. J. Müller, and M. C. Meinke, "Determination of optical properties of human blood in the spectral range 250 to 1100 nm using Monte Carlo simulations with hematocrit-dependent effective scattering phase functions," Journal of biomedical optics **11**, 034021 (2006).
106. H. Nilsson and G. E. Nilsson, "Monte Carlo simulations of light interaction with blood vessels in human skin in the red-wavelength region," in *Optical Diagnostics of Biological Fluids III*, (International Society for Optics and Photonics, 1998), 44-53.
107. M. Hammer, A. Roggan, D. Schweitzer, and G. Muller, "Optical properties of ocular fundus tissues-an in vitro study using the double-integrating-sphere technique and inverse Monte Carlo simulation," Physics in Medicine & Biology **40**, 963 (1995).
108. D. Sakota and S. Takatani, "Quantitative analysis of optical properties of flowing blood using a photon-cell interactive Monte Carlo code: effects of red blood cells' orientation on light scattering," Journal of biomedical optics **17**, 057007 (2012).
109. M. Kirillin, I. Meglinski, V. Kuzmin, E. Sergeeva, and R. Myllylä, "Simulation of optical coherence tomography images by Monte Carlo modeling based on polarization vector approach," Optics express **18**, 21714-21724 (2010).
110. H. L. Goldsmith, G. R. Cokelet, and P. Gaehtgens, "Robin Fahraeus: evolution of his concepts in cardiovascular physiology," American Journal of Physiology-Heart and Circulatory Physiology **257**, H1005-H1015 (1989).
111. J. Lauri, A. Bykov, and T. Fabritius, "Quantification of cell-free layer thickness and cell distribution of blood by optical coherence tomography," Journal of biomedical optics **21**, 040501 (2016).
112. M. C. Meinke, G. J. Müller, J. Helfmann, and M. Friebel, "Optical properties of platelets and blood plasma and their influence on the optical behavior of whole blood in the visible to near infrared wavelength range," Journal of Biomedical Optics **12**, 014024 (2007).
113. H. H. Billett, "Hemoglobin and hematocrit," Clinical Methods: The History, Physical, and Laboratory Examinations. 3rd edition (1990).
114. D. Toublanc, "Henyey–Greenstein and Mie phase functions in Monte Carlo radiative transfer computations," Applied optics **35**, 3270-3274 (1996).
115. J. Skaar, "Fresnel equations and the refractive index of active media," Physical Review E **73**, 026605 (2006).
116. D. A. Atchison, G. Smith, and G. Smith, *Optics of the human eye* (Butterworth-Heinemann Oxford, 2000), Vol. 2.
117. D. Van Norren and L. Tiemeijer, "Spectral reflectance of the human eye," Vision research **26**, 313-320 (1986).

118. ThorLabs, "400 to 700 nm Wavelength Range" (2022), retrieved https://www.thorlabs.com/newgrouppage9.cfm?objectgroup_id=2910&pn=LSM03-VIS#.

119. R. V. Kuranov, J. Qiu, A. B. McElroy, A. Estrada, A. Salvaggio, J. Kiel, A. K. Dunn, T. Q. Duong, and T. E. Milner, "Depth-resolved blood oxygen saturation measurement by dual-wavelength photothermal (DWP) optical coherence tomography," Biomedical optics express **2**, 491-504 (2011).

120. G. R. Kelman, "Digital computer procedure for the conversion of PCO2, into blood CO2 content," Respiration physiology **3**, 111-115 (1967).

121. R. V. K. Ian Rubinoff, Zeinab Ghassabi, Yuanbo Wang, Lisa Beckmann, David A. Miller, Behnam Tayebi, Gadi Wollstein, Hiroshi Ishikawa, Joel S. Schuman, Hao F. Zhang, "Adaptive spectroscopic visible-light optical coherence tomography for human retinal oximetry," bioRxiv (2021).

122. Y. Pan, E. Lankenou, J. Welzel, R. Birngruber, and R. Engelhardt, "Optical coherence-gated imaging of biological tissues," IEEE Journal of selected topics in Quantum Electronics **2**, 1029-1034 (1996).

123. V. Twersky, "Absorption and multiple scattering by biological suspensions," JOSA **60**, 1084-1093 (1970).

124. A. Ishiniaru and Y. Kuga, "Attenuation constant of a coherent field in a dense distribution of particles," JOSA **72**, 1317-1320 (1982).

125. A. N. Yaroslavsky, I. V. Yaroslavsky, T. Goldbach, and H.-J. Schwarzmaier, "Optical properties of blood in the near-infrared spectral range," in *Optical Diagnostics of Living Cells and Biofluids*, (International Society for Optics and Photonics, 1996), 314-324.

126. M. Friebel, J. Helfmann, G. J. Müller, and M. C. Meinke, "Influence of shear rate on the optical properties of human blood in the spectral range 250 to 1100 nm," Journal of biomedical optics **12**, 054005 (2007).

127. W. Steenbergen, R. Kolkman, and F. de Mul, "Light-scattering properties of undiluted human blood subjected to simple shear," JOSA A **16**, 2959-2967 (1999).

128. A. M. Enejder, J. Swartling, P. Aruna, and S. Andersson-Engels, "Influence of cell shape and aggregate formation on the optical properties of flowing whole blood," Applied optics **42**, 1384-1394 (2003).

129. Y. Sun and L. E. H. Smith, "Retinal Vasculature in Development and Diseases," Annu Rev Vis Sci **4**, 101-122 (2018).

130. J. Kur, E. A. Newman, and T. Chan-Ling, "Cellular and physiological mechanisms underlying blood flow regulation in the retina and choroid in health and disease," Prog Retin Eye Res **31**, 377-406 (2012).

131. D. Y. Yu and S. J. Cringle, "Oxygen distribution and consumption within the retina in vascularised and avascular retinas and in animal models of retinal disease," Prog Retin Eye Res **20**, 175-208 (2001).

132. J. Yi, W. Z. Liu, S. Y. Chen, V. Backman, N. Sheibani, C. M. Sorenson, A. A. Fawzi, R. A. Linsenmeier, and H. F. Zhang, "Visible light optical coherence tomography measures retinal oxygen metabolic response to systemic oxygenation," Light-Sci Appl **4**(2015).

133. B. T. Soetikno, J. Yi, R. Shah, W. Z. Liu, P. Purta, H. F. Zhang, and A. A. Fawzi, "Inner retinal oxygen metabolism in the 50/10 oxygen-induced retinopathy model," Sci Rep-Uk **5**(2015).
134. K. Fondi, P. A. Wozniak, K. Howorka, A. M. Bata, G. C. Aschinger, A. Popa-Cherecheanu, K. J. Witkowska, A. Hommer, D. Schmidl, R. M. Werkmeister, G. Garhofer, and L. Schmetterer, "Retinal oxygen extraction in individuals with type 1 diabetes with no or mild diabetic retinopathy," Diabetologia **60**, 1534-1540 (2017).
135. C. M. Jorgensen, S. H. Hardarson, and T. Bek, "The oxygen saturation in retinal vessels from diabetic patients depends on the severity and type of vision-threatening retinopathy," Acta Ophthalmol **92**, 34-39 (2014).
136. A. Shughoury, S. Mathew, J. Arciero, P. Wurster, S. Adjei, T. Ciulla, B. Siesky, and A. Harris, "Retinal oximetry in glaucoma: investigations and findings reviewed," Acta Ophthalmol **98**, 559-571 (2020).
137. N. Nassif, B. Cense, B. H. Park, S. H. Yun, T. C. Chen, B. E. Bouma, G. J. Tearney, and J. F. de Boer, "In vivo human retinal imaging by ultrahigh-speed spectral domain optical coherence tomography," Opt Lett **29**, 480-482 (2004).
138. B. W. Yin, R. V. Kuranov, A. B. McElroy, S. Kazmi, A. K. Dunn, T. Q. Duong, and T. E. Milner, "Dual-wavelength photothermal optical coherence tomography for imaging microvasculature blood oxygen saturation," J Biomed Opt **18**(2013).
139. L. Kagemann, G. Wollstein, M. Wojtkowski, H. Ishikawa, K. A. Townsend, M. L. Gabriele, V. J. Srinivasan, J. G. Fujimoto, and J. S. Schuman, "Spectral oximetry assessed with high-speed ultra-high-resolution optical coherence tomography," J Biomed Opt **12**(2007).
140. S. H. Pi, A. Camino, X. Wei, J. Simonett, W. Cepurna, D. Huang, J. C. Morrison, and Y. L. Jia, "Rodent retinal circulation organization and oxygen metabolism revealed by visible-light optical coherence tomography," Biomed Opt Express **9**, 5851-5862 (2018).
141. M. Hammer, W. Vilser, T. Riemer, and D. Schweitzer, "Retinal vessel oximetry-calibration, compensation for vessel diameter and fundus pigmentation, and reproducibility," J Biomed Opt **13**(2008).
142. R. V. Kuranov, I. Rubinoff, Y. B. Wang, L. Beckmann, X. Zhang, A. A. Fawzi, H. Ishikawa, J. Schuman, and H. F. Zhang, "Enhanced imaging of the outer retina layers using speckle-reduced visible-light optical coherence tomography," Invest Ophth Vis Sci **60**(2019).
143. A. Kho and V. J. Srinivasan, "Compensating spatially dependent dispersion in visible light OCT," Opt Lett **44**, 775-778 (2019).
144. J. Kfir, Z. Ghassabi, M. F. Wu, I. Rubinoff, R. V. Kuranov, Y. B. Wang, B. Davis, B. Tayebi, J. Schuman, H. Zhang, H. Ishikawa, and G. Wollstein, "Visible-Light OCT Captures In-vivo Changes in Retinal Oximetry in Ischemic Retinal Diseases," Invest Ophth Vis Sci **61**(2020).
145. H. de Carvalho and R. N. Pittman, "Longitudinal and radial variation of PO2 in the hamster cheek pouch microcirculation.," Faseb J **15**, A47-A47 (2001).
146. R. N. Pittman, "Oxygen gradients in the microcirculation," Acta Physiol **202**, 311-322 (2011).

147. S. Sakadzic, E. T. Mandeville, L. Gagnon, J. J. Musacchia, M. A. Yaseen, M. A. Yucel, J. Lefebvre, F. Lesage, A. M. Dale, K. Eikermann-Haerter, C. Ayata, V. J. Srinivasan, E. H. Lo, A. Devor, and D. A. Boas, "Large arteriolar component of oxygen delivery implies a safe margin of oxygen supply to cerebral tissue," Nat Commun **5**(2014).
148. B. R. Duling and R. M. Berne, "Longitudinal Gradients in Periarteriolar Oxygen Tension in Hamster Cheek Pouch," Fed Proc **29**, A320-& (1970).
149. M. Sharan, E. P. Vovenko, A. Vadapalli, A. S. Popel, and R. N. Pittman, "Experimental and theoretical studies of oxygen gradients in rat pial microvessels," J Cerebr Blood F Met **28**, 1597-1604 (2008).
150. R. N. Pittman and B. R. Duling, "Effects of Altered Carbon-Dioxide Tension on Hemoglobin Oxygenation in Hamster Cheek Pouch Microvessels," Microvasc Res **13**, 211-224 (1977).
151. A. G. Tsai, P. C. Johnson, and M. Intaglietta, "Oxygen gradients in the microcirculation," Physiol Rev **83**, 933-963 (2003).
152. J. Yi, Q. Wei, W. Liu, V. Backman, and H. F. Zhang, "Visible-light optical coherence tomography for retinal oximetry," Opt Lett **38**, 1796-1798 (2013).
153. M. Prasse, F. G. Rauscher, P. Wiedemann, A. Reichenbach, and M. Francke, "Optical properties of retinal tissue and the potential of adaptive optics to visualize retinal ganglion cells in vivo," Cell Tissue Res **353**, 269-278 (2013).
154. X. Ge, H. Y. Tang, X. H. Wang, X. Y. Liu, S. Chen, N. S. Wang, G. M. Ni, X. J. Yu, S. F. Chen, H. T. Liang, E. Bo, L. L. Wang, C. S. Braganza, C. J. Xu, S. M. Rowe, G. J. Tearney, and L. B. Liu, "Geometry-Dependent Spectroscopic Contrast in Deep Tissues," Iscience **19**, 965-+ (2019).
155. J. Y. Xu and G. P. Shi, "Vascular wall extracellular matrix proteins and vascular diseases," Bba-Mol Basis Dis **1842**, 2106-2119 (2014).
156. H. Afsharan, M. J. Hackmann, Q. Wang, F. Navaeipour, S. V. K. Jayasree, R. J. Zawadzki, D. Silva, C. Joo, and B. Cense, "Polarization properties of retinal blood vessel walls measured with polarization sensitive optical coherence tomography," Biomed Opt Express **12**, 4340-4362 (2021).
157. G. M. Ni, X. Ge, L. Liu, J. Zhang, X. Z. Wang, J. X. Liu, L. B. Liu, and Y. Liu, "Towards Indicating Human Skin State In Vivo Using Geometry-Dependent Spectroscopic Contrast Imaging," Ieee Photonic Tech L **32**, 697-700 (2020).
158. R. R. Liu, W. Y. Song, V. Backman, and J. Yi, "Quantitative quality-control metrics for in vivo oximetry in small vessels by visible light optical coherence tomography angiography," Biomed Opt Express **10**, 465-486 (2019).
159. R. V. Kuranov, J. Z. Qiu, A. B. McElroy, A. Estrada, A. Salvaggio, J. Kiel, A. K. Dunn, T. Q. Duong, and T. E. Milner, "Depth-resolved blood oxygen saturation measurement by dual-wavelength photothermal (DWP) optical coherence tomography," Biomed Opt Express **2**, 491-504 (2011).
160. G. R. Kelman, "Digital Computer Procedure for Conversion of Pco2 into Blood Co2 Content," Resp Physiol **3**, 111-+ (1967).
161. Y. Y. Huang, S. Q. Wang, Q. Y. Guo, S. Kessel, I. Rubinoff, L. L. Y. Chan, P. Li, Y. L. Liu, J. Qiu, and C. Zhou, "Optical Coherence Tomography Detects Necrotic

Regions and Volumetrically Quantifies Multicellular Tumor Spheroids," Cancer Res **77**, 6011-6020 (2017).

162. J. Polans, B. Jaeken, R. P. McNabb, P. Artal, and J. A. Izatt, "Wide-field optical model of the human eye with asymmetrically tilted and decentered lens that reproduces measured ocular aberrations," Optica **2**, 124-134 (2015).
163. M. Vinas, C. Dorronsoro, L. Sawides, D. Cortes, D. Pascual, A. Radhakrishnan, and S. Marcos, "Longitudinal Chromatic Aberration of the human eye in the visible and near infrared from Hartmann-Shack wavefront sensing, double-pass and psychophysics," Invest Ophth Vis Sci **55**(2014).
164. D. J. Faber, F. J. van der Meer, M. C. G. Aalders, and T. G. van Leeuwen, "Quantitative measurement of attenuation coefficients of weakly scattering media using optical coherence tomography," Opt Express **12**, 4353-4365 (2004).
165. M. A. Choma, M. V. Sarunic, C. H. Yang, and J. A. Izatt, "Sensitivity advantage of swept source and Fourier domain optical coherence tomography," Opt Express **11**, 2183-2189 (2003).
166. T. W. Zhang, A. M. Kho, G. Yiu, and V. J. Srinivasan, "Visible Light Optical Coherence Tomography (OCT) Quantifies Subcellular Contributions to Outer Retinal Band 4," Transl Vis Sci Techn **10**(2021).
167. Z. Ghassabi, R. V. Kuranov, M. Wu, B. Tayebi, Y. Wang, I. Rubinoff, X. Liu, G. Wollstein, J. S. Schuman, H. F. Zhang, and H. Ishikawa, "In Vivo Sublayer Analysis Of Human Retinal Inner Plexiform Layer Obtained By Visible-Light Optical Coherence Tomography," bioRxiv, 2021.2001.2008.425925 (2021).
168. S. Shin, U. Sharma, H. H. Tu, W. Jung, and S. A. Boppart, "Characterization and Analysis of Relative Intensity Noise in Broadband Optical Sources for Optical Coherence Tomography," Ieee Photonic Tech L **22**, 1057-1059 (2010).
169. T. W. Zhang, A. M. Kho, and V. J. Srinivasan, "Improving visible light OCT of the human retina with rapid spectral shaping and axial tracking," Biomed Opt Express **10**, 2918-2931 (2019).
170. S. Y. Chen, X. Shu, P. L. Nesper, W. Z. Liu, A. A. Fawzi, and H. F. Zhang, "Retinal oximetry in humans using visible-light optical coherence tomography [Invited]," Biomed Opt Express **8**, 1415-1429 (2017).
171. A. G. Podoleanu, "Unbalanced versus balanced operation in an optical coherence tomography system," Appl Optics **39**, 173-182 (2000).
172. W. C. Kuo, C. M. Lai, Y. S. Huang, C. Y. Chang, and Y. M. Kuo, "Balanced detection for spectral domain optical coherence tomography," Opt Express **21**, 19280-19291 (2013).
173. A. Bradu and A. G. Podoleanu, "Fourier domain optical coherence tomography system with balance detection," Opt Express **20**, 17522-17538 (2012).
174. W. C. Kuo, Y. S. Lai, C. M. Lai, and Y. S. Huang, "Balanced detection spectral domain optical coherence tomography with a multiline single camera for signal-to-noise ratio enhancement," Appl Optics **51**, 5936-5940 (2012).
175. A. J. Black and T. Akkin, "Polarization-based balanced detection for spectral-domain optical coherence tomography," Appl Optics **54**, 7252-7257 (2015).

176. E. Bo, X. Y. Liu, S. Chen, X. J. Yu, X. H. Wang, and L. B. Liu, "Spectral-domain optical coherence tomography with dual-balanced detection for auto-correlation artifacts reduction," Opt Express **23**, 28050-28058 (2015).
177. M. G. Hyeon, H. J. Kim, B. M. Kim, and T. J. Eom, "Spectral domain optical coherence tomography with balanced detection using single line-scan camera and optical delay line," Opt Express **23**, 23079-23091 (2015).
178. A. M. Kho, T. W. Zhang, J. Zhu, C. W. Merkle, and V. J. Srinivasan, "Incoherent excess noise spectrally encodes broadband light sources," Light-Sci Appl **9**(2020).
179. W. Drexler, U. Morgner, R. K. Ghanta, F. X. Kartner, J. S. Schuman, and J. G. Fujimoto, "Ultrahigh-resolution ophthalmic optical coherence tomography," Nat Med **7**, 502-507 (2001).
180. T. A. Wang, M. C. Chan, H. C. Lee, C. Y. Lee, and M. T. Tsai, "Ultrahigh-resolution optical coherence tomography/angiography with an economic and compact supercontinuum laser," Biomed Opt Express **10**, 5687-5702 (2019).
181. N. M. Israelsen, C. R. Petersen, A. Barh, D. Jain, M. Jensen, G. Hannesschlager, P. Tidemand-Lichtenberg, C. Pedersen, A. Podoleanu, and O. Bang, "Real-time high-resolution mid-infrared optical coherence tomography," Light-Sci Appl **8**(2019).
182. S. Rao D. S, M. Jensen, L. Grüner-Nielsen, J. T. Olsen, P. Heiduschka, B. Kemper, J. Schnekenburger, M. Glud, M. Mogensen, N. M. Israelsen, and O. Bang, "Shot-noise limited, supercontinuum-based optical coherence tomography," Light: Science & Applications **10**, 133 (2021).
183. M. Munter, M. Pieper, T. Kohlfaerber, E. Bodenstorfer, M. Ahrens, C. Winter, R. Huber, P. Konig, G. Huttmann, and H. Schulz-Hildebrandt, "Microscopic optical coherence tomography (mOCT) at 600 kHz for 4D volumetric imaging and dynamic contrast," Biomed Opt Express **12**, 6024-6039 (2021).

Vita

Education

2017	BS, Electrical Engineering Lehigh University, Bethlehem, PA
2019	MS in Biomedical Engineering Northwestern University, Evanston, IL
2022	PhD in Biomedical Engineering Northwestern University, Evanston, IL

Awards and Honors

2022	Dissertation Award, Department of Biomedical Engineering, Northwestern
2022	Student Paper Award Finalist, Optical Biophotonics Congress
2021	Research Progress Award in Imaging, Northwestern University
2020-2021	Travel Grant, Association for Research in Vision and Ophthalmology (ARVO)
2018-2021	NIH T32 Multidisciplinary Visual Sciences Training Grant
2017	Walter P. Murphy Fellowship, Northwestern University